Study of $W\gamma\gamma$ tri-boson production in proton-proton collisions with the ATLAS detector

Auriane Canesse

Department of Physics

McGill University, Montreal

October 2021

A thesis submitted to McGill University in partial fulfillment of the

requirements of the degree of Doctor of Philosophy

Abstract

From 2015 to 2018, the Large Hadron Collider (LHC) collided protons at an unprecedented centre of mass energy of $\sqrt{s} = 13$ TeV. The ATLAS detector recorded an integrated luminosity of 139 fb^{-1} of these collisions hence offering an unprecedented opportunity to test the Standard Model (SM) of particle physics by measuring predicted but yet unobserved rare processes. The tri-boson $W\gamma\gamma$ production is one of these unobserved processes. Its sensitivity to the electroweak trilinear and quartic gauge couplings make it a great probe of new physics phenomena as Beyond Standard Model processes could affect the effective strength of these couplings. This thesis presents the study of the $W\gamma\gamma$ process. Backgrounds are estimated from a combination of Monte Carlo (MC) simulations and data-driven techniques. The dominant source of background to the search for $W\gamma\gamma$ production are jets being misidentified as photons. The advanced data-driven technique used to estimate this background is presented in details. Finally thorough examination of the systematic uncertainties affecting the measurement of the $W\gamma\gamma$ production cross-section are presented. Taking into account all statistical and systematic uncertainties, the expected statistical significance of the measurement is of 5.1 σ for the differential measurement and 7.8 σ for the total cross-section.

Abrégé

De 2015 à 2018, le Grand Collisionneur de Hadron (en anglais : Large Hadron Collider – LHC) a accéléré des faisceaux de protons à une énergie de centre de masse inédite de $\sqrt{s} = 13$ TeV pour les faire entrer en collision. Le détecteur ATLAS a enregistré une luminosité intégrée de 139fb^{-1} de ces collisions. Ces données offrent une opportunité unique permettant aux physicien·ne·s de tester le Modèle Standard de la physique des particules en mesurant des processus rares encore jamais observés. La production tri-bosonique $W\gamma\gamma$ est l'un de ces processus rares. Sa sensitivité aux couplages trilinéaire et quartique de jauge électrofaible en fait un outil parfait pour découvrir de nouveaux phénomènes physiques. En effet, des processus au delà du Modèle Standard pourraient affecter la valeur effective de ces couplages. Cette thèse présente l'étude du processus $pp \to W\gamma\gamma$. Les bruits de fond sont estimés grâce à une combinaison de simulations Monte Carlo (MC) et de techniques basées sur les données. La source de bruit principale provient de jets hadroniques mal-identifiés comme étant des photons. Une technique avancée basée sur les données est utilisée pour estimer ce bruit et est présentée en détails. Finalement, une étude approfondie des erreurs systématiques est présentée. La mesure de la section-efficace du processus a une signifiance statistique attendue de 5.1 σ pour la mesure différentielle et de 7.8 σ pour mesure totale.

Author's Contribution

ATLAS is an international collaboration of physicists, engineers and technicians. It is composed of over 5000 members and almost 3000 scientific authors. The detector construction and operation, the recording and reconstruction of data, and the generation of simulations all used in this thesis are therefore the work of many individuals spanning over decades. Additionally, the analysis softwares and tools used for calibration, event reconstruction and selection, and uncertainty estimation are developed by specialised working groups within the collaboration. The work presented here uses these tools after having validated them for the $W\gamma\gamma$ analysis use case.

The study of the $W\gamma\gamma$ tri-boson production is the work of a small team: two PhD candidates (Alessandro Ambler and Auriane Canesse), two post-doctoral researchers (Dr. Heather Russell, Dr. Tony Kwan) and one professor (Prof. Brigitte Vachon). All members have contributed to the development of the analysis framework and the validation of the analysis methods.

The $W\gamma\gamma$ process has never been observed before and the results presented in this thesis therefore constitute an original and distinct contribution to knowledge. A summary of the contributions of the author is presented for each chapter as well as the contributions of co-authors.

Ch. 1: The author summarizes the context and motivation for the measurement of the $W\gamma\gamma$ production cross section.

Ch. 2: The author gives an overview of the theoretical framework of particle physics to which the thesis is contributing.

Ch. 3: The author describes the Large Hadron Collider (LHC) machine and ATLAS detector which was built and operated by ATLAS co-authors.
The author has contributed to the operation and upgrade of the ATLAS trigger and contributed to the commissioning of small-Strip Thin Gap Chamber (sTGC) detectors for the ATLAS New Small Wheel (NSW) upgrade which will replace the current Small Wheels.

Ch. 4: The author presents the physics object reconstruction process used by the ATLAS collaboration, which was carried out by ATLAS co-authors.

The following chapters have been developed by the author and the $W\gamma\gamma$ analysis co-authors Alessandro Ambler, Dr. Hearther Russell under the supervision of Prof. Brigitte Vachon. They constitute original scholarship and distinct contributions to knowledge.

Ch. 5: The author presents the event selection defined by the author and the $W\gamma\gamma$ co-authors.

Ch. 6: The author presents the analysis backgrounds:

- The fake photon background estimation (and associated appendices) was derived by the author.
- The fake lepton background was derived by Alessandro Ambler.
- The pile-up background was derived by Dr. Heather Russell.
- The simulated backgrounds were studied by the author and co-authors.

Ch. 7: The author gives the estimate of the systematic uncertainties. The theoretical uncertainties were derived by the author using tools developed by ATLAS co-authors. Experimental uncertainties were estimated by the author and co-authors.

Ch. 8: The author has computed the expected significance of the analysis.

Ch. 9: The author presents the work remaining to achieve the $W\gamma\gamma$ observation. This includes the unfolding of the measurement currently being worked on by Dr. Tony Kwan.

Acknowledgements

This doctoral thesis would not have been possible without the support of many people and these few word are far from exhaustive.

I would first like to thank my supervisor, Prof. Brigitte Vachon, for guiding me through my PhD both while at McGill and at CERN, including through a major pandemic. Your advice both in physics and in life has been invaluable to my growth as a physicist and a person.

I will never be able to thank Dr. Heather Russell enough for her guidance in the development of the $W\gamma\gamma$ analysis. It is thanks to your incredible patience and expertise that I was able to achieve this thesis. Many thanks also go to Alessandro Ambler with whom I worked along side with on this analysis.

I want to express my gratitude to the rest of McGill ATLAS group professors Andreas, François and Steve; postdocs Jona, Tamara and Tony; and current and former students Anabelle, Benoit, Sébastien, Christina, John, Lia, Shreya, for their support and feedback during these four years at McGill.

My work at McGill also extended beyond the ATLAS group and I would like to thank the professors, staff, and peers I had the opportunity to work with, including the outreach group, the Equity Diversity & Inclusion (EDI) committee and McGill Graduate Association of Physics Students MGAPS.

Although my contributions to the sTGC commissioning is not presented here, I would also like to thank all the ATLAS New Small Wheel (NSW) commissioning team for the work we achieved together at CERN. Special thanks go to the guidance and patience of Dr. Aimilianos Koulouris and Dr. Gerardo Vasquez.

Last but not least I would like to thank all my friends and family for their emotional support and encouragement throughout my years of study.

Contents

Chapter 1

Introduction

The Standard Model (SM) of particle physics is the theory describing matter and its interaction at the smallest distance scale. The reliability of this theoretical framework has been shown by many measurements over several decades and its last missing piece, the Higgs boson, was observed in 2012 by the ATLAS [1] and CMS [2] collaborations at the Large Hadron Collider (LHC). Despite its successes, the SM does not incorporate a description of some other observed phenomena of nature such as the non-zero neutrino masses, Dark Matter (DM), the matter-anti-matter asymmetry or even the fourth force of nature, gravity. Several models describing Beyond Standard Model (BSM) physics have been developed to explain these observations, and some of them have been investigated at the LHC. As the LHC reaches unprecedented centre-of-mass energies, it naturally offers a unique opportunity to search for new BSM physics phenomena.

The 139 fb^{-1} of proton-proton collisions recorded at $\sqrt{s} = 13$ TeV by the ATLAS detector during Run 2 offer a unique opportunity to test the Standard Model by searching for predicted, but yet unobserved, rare processes. The $W\gamma\gamma$ tri-boson production is one of these rare processes: due to its low cross-section, it has remained out of reach at previous high energy colliders. Its sensitivity to electroweak Quartic Gauge Coupling (QGC) makes it a particularly powerful probe of new physics phenomena. Evidence for the process was found by ATLAS during Run 1 [3] and CMS recently published evidence for the process

using its full Run 2 dataset [4].

The goal of this analysis is to measure the cross-section of $W\gamma\gamma$ tri-boson production in proton-proton collisions for the first time at a statistical significance greater than 5 σ. The process is noted $pp \rightarrow W\gamma\gamma + X$ where X represents other particles produced in the proton-proton interaction, or simply $pp \rightarrow W\gamma\gamma$. This physics reaction is studied in the final states where the W boson decays to either an electron or a muon: $pp \rightarrow W(\rightarrow e\nu)\gamma\gamma$ and $pp \rightarrow W(\rightarrow \mu\nu)\gamma\gamma$. These channels have been chosen because these final states particles can be identified with high efficiency in the ATLAS experiment. The W boson decay to a tau lepton (τ) is more complex since tau leptons promptly decay within the volume of the detector to several different final states. The process $pp \rightarrow W(\rightarrow \tau\nu)\gamma\gamma$ is therefore treated as a background. The observed final state signal photons can be produced in several ways: they can be radiated directly off the W boson thanks to the trilinear $WW\gamma$ and quartic $WW\gamma\gamma$ gauge couplings; they can be emitted from the Initial State Radiation (ISR) or from the final state charged leptons (Final State Radiation (FSR)). Examples of these processes are shown in Figure 1.1

To achieve a first observation of this physics process, background processes with signatures similar to $W\gamma\gamma$ must be precisely estimated. While some can be simulated, other are poorly modelled and must be estimated using data-driven techniques. Hadronic jets misidentified as photons constitute the largest source of background. It is estimated using a data-driven 2D template fit method. Two more backgrounds are estimated using data-driven methods: jets mimicking leptons and the pile-up background, where one or both photons come from another separate hard scatter in the same bunch crossing. The remaining backgrounds are estimated using Monte Carlo (MC) simulations. Systematic effects impacting the measurement of the $W\gamma\gamma$ cross section are studied and estimated.

At the time of writing, the $W\gamma\gamma$ analysis is still *blinded*. A blinding procedure allows the development of an analysis framework without being biased by the expected results. It is required for all ATLAS analyses. In order to finalise the measurement and compute the

final observed $W\gamma\gamma$ cross-section, formal approval from the ATLAS collaboration has to be requested and granted. The blinding procedure is described in Section 5.1. The final results presented in this thesis are the expected statistical significance for both a differential and total cross-section measurements.

The structure of this thesis goes as follows: first, an overview of the theoretical framework is given in Chapter 2 followed by a description of the LHC and of the ATLAS detector in Chapter 3. Then the physics object reconstruction process, common to all ATLAS analyses, is summarised in Chapter 4. It is followed by the description of the object and event selection in Chapter 5. Chapter 6 gives the details description of the analysis backgrounds, which are estimated with a combination of data-driven techniques and MC simulations. The systematic uncertainties affecting the estimation of those backgrounds are then detailed in Chapter 7. Finally, Chapter 8 presents the results of the $W\gamma\gamma$ measurement, followed by the summary and outlook of the thesis, Chapter 9.

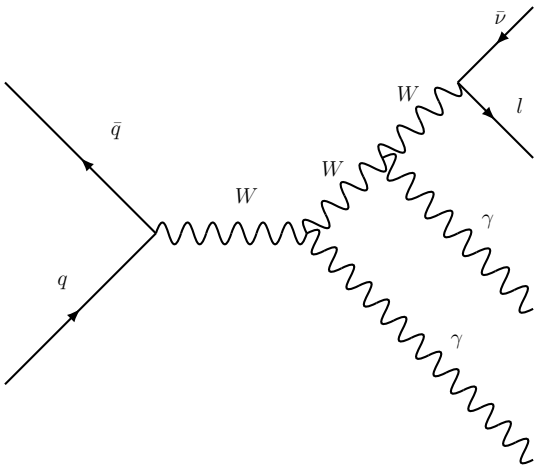

(a) Trilinear Gauge Coupling.

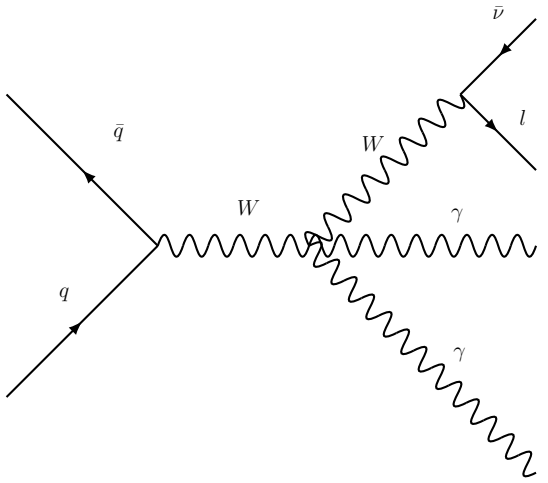

(b) Quartic Gauge Coupling (QGC).

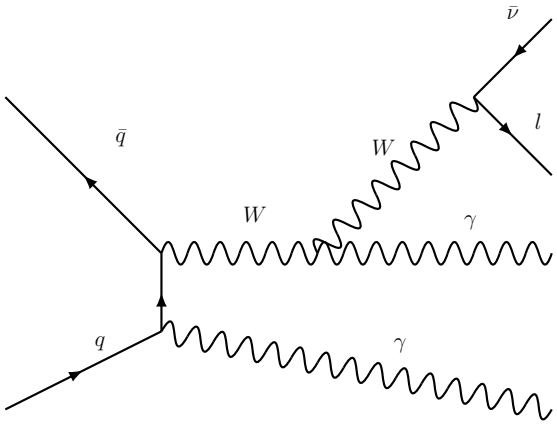

(c) Initial State Radiation (ISR) (+Trilinear Gauge Coupling).

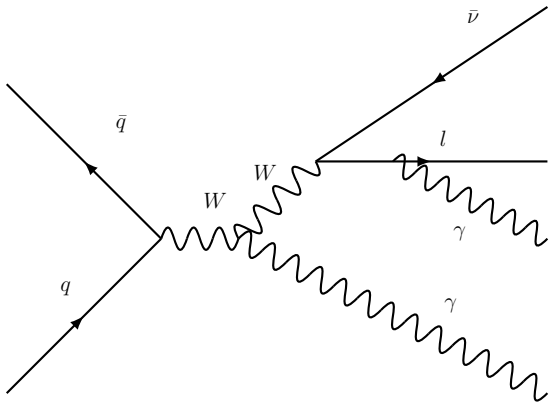

(d) Final State Radiation (FSR) (+Trilinear Gauge Coupling).

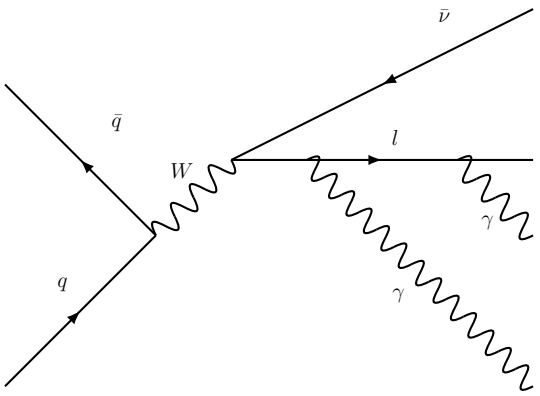

(e) FSR only.

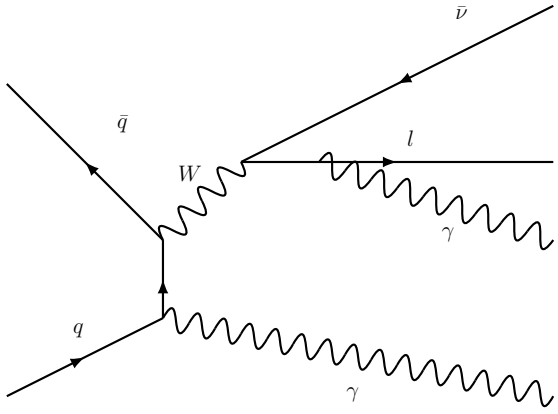

(f) ISR +FSR.

Figure 1.1: Examples of Feynman diagrams contributing to the $W\gamma\gamma$ process.

Chapter 2

Theoretical Background

This chapter presents the theoretical background needed to understand the results and discussions presented in this thesis.

Section 2.1 gives a brief overview of the Standard Model (SM) of particle physics including its particle content, its general mathematical formulation and especially a description of the Higgs sector (Sec. 2.1.3) which is relevant for the study of the $W\gamma\gamma$ process. The Standard Model unfortunately has its limitations too and an Effective Field Theory (EFT) will be presented in Section 2.2 as a way to look for new physical phenomena. Finally, Section 2.3 gives an overview of the latest electroweak precision measurements complementary to the study of the $W\gamma\gamma$ production, and their corresponding EFT constraints on possible contributions from new physical phenomena.

2.1 The Standard Model

2.1.1 Particle content

The Standard Model (SM) is the relativistic quantum field theory describing elementary particles and their interactions at scales of about 10^{-15} m and below [6]. It describes three of the four fundamental interactions: the strong, weak and electromagnetic interactions, which are described as resulting from the exchange of vector bosons between elementary

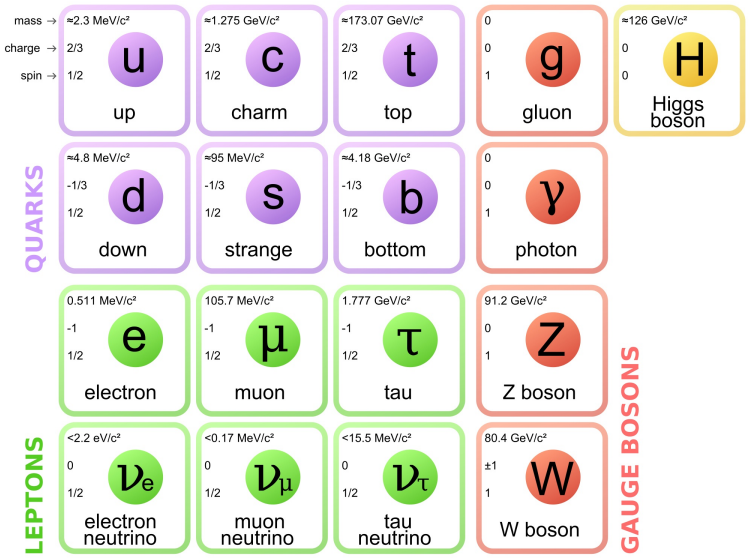

Figure 2.1: Standard Model elementary particles with some of their properties. They are split into two main categories: fermions that make up matter and bosons that mediate interactions [5].

particles.

The known elementary particles that make up matter are 12 spin-1/2 fermions and their corresponding anti-particles (see Figure 2.1). Fermions are divided into two categories: six quarks that interact strongly and six leptons that do not. Leptons are further split into neutrinos (ν_e, ν_μ, ν_τ) that only interact weakly and charged leptons (e, μ, τ) that interact both weakly and electromagnetically. Quarks (u, d, c, s, t, b) carry an additional charge called colour that makes them interact strongly. However, only colourless states are observed in nature and free quarks have never been detected. This is explained by the phenomena of colour confinement which results in quarks being bound to each other and forming color-neutral composite particles: mesons (two quarks with a colour/anti-colour pair) or baryons, like the proton (three quarks with three different colours/anti-coulours). Mesons and baryons are collectively referred to as hadrons. The strong interaction is mediated by eight coloured bosons called gluons (g), the weak interaction by the $W^\pm$ and Z bosons, and the electromagnetic interaction by the photon (γ). Finally, the Higgs boson (H) is the spin-0 boson that gives their mass to all fermions but neutrinos, and to W and

Z boson. The Brout-Engelert-Higgs mechanism, through which this is understood to take place, will be described in Section 2.1.3. Note that the origin of the neutrino mass is an open topic in particle physics that will not be discussed here.

2.1.2 Lagrangian

This section introduces the theoretical formalism of the Standard Model. A more detailed description can be found in references [6] and [7].

The SM describes quantum fields denoted as follows: spinors ψ for fermion fields, vector fields $B,\ W_i$ for electroweak gauge bosons, G_a for gluons and finally a scalar field ϕ for the Higgs. The dynamics and interactions of these fields is given by the SM compact Lagrangian:

$$\mathcal{L}_{SM} = -\frac{1}{4}F_{\mu\nu}F^{\mu\nu} + i\bar{\psi}D\psi + \psi_i y_{ij}\psi_j\phi + |D_\mu\phi|^2 - V(\phi) \tag{2.1}$$

The meaning of each term will be explained in this section. Furthermore, the SM is a gauge theory: its Lagrangian is invariant under $SU(3) \otimes SU(2) \otimes U(1)$ local transformations. This means that for each of the groups generators, a corresponding gauge field is included in the Lagrangian to insure its invariance. This process will be demonstrated in the case of the $U(1)$ symmetry for Quantum Electrodynamics (QED).
To understand the interactions described by Equation 2.1, the compact form of the Lagrangian should be expanded. This will be done in the coming paragraphs treating separately the case of QED, Quantum Chromodynamics (QCD) and the electroweak interaction. The Higgs sector and Electroweak Symmetry Breaking (EWSB) will be detailed in Section 2.1.3.

QED

The first part of the SM to be developed was Quantum Electrodynamics (QED) which describes the electromagnetic interaction [8]. The electromagnetic interaction is invariant under a change of phase or scale, which corresponds to invariance under a global $U(1)_{\mathrm{EM}}$ transformation: $\psi(x) \to e^{i\alpha}\psi(x)$. Starting from the Dirac Lagrangian for a free fermion of

mass m where γ^μ is Dirac matrix:

$$\mathcal{L}_0 = \bar{\psi}(i\gamma^\mu \partial_\mu - m)\psi \tag{2.2}$$

if we apply a local $U(1)_{\text{EM}}$ transformation: $\psi(x) \rightarrow e^{i\alpha(x)}\psi(x)$, with $\alpha(x)$ an arbitrary real function of x, the Lagrangian $\mathcal{L}_0$ is not invariant anymore. To obtain an invariant Lagrangian, a new degree of freedom, the vector field A_μ, must be introduced. It transforms as $A_\mu \rightarrow A'_\mu = A_\mu - \frac{1}{e}\partial_\mu \alpha(x)$ with e the electric charge. The partial derivative ∂_μ in Equation 2.2 must then be replaced by the covariant derivative:

$$D_\mu \psi(x) = (\partial_\mu + ieA_\mu)\psi(x) \tag{2.3}$$

With this new derivative, the Lagrangian is invariant. To obtain the final QED Lagrangian, the inner product of the field strength tensor ($F_{\mu\nu} = \partial_\mu A_\nu - \partial_\nu A_\mu$) describing the photon field dynamics must be added:

$$\mathcal{L}_{QED} = \bar{\psi}(i\gamma^\mu D_\mu - m)\psi - \frac{1}{4}F_{\mu\nu}F^{\mu\nu} \tag{2.4}$$

Here we recognise the structure of three of the terms of equation 2.1: $\bar{\psi}i\gamma^\mu D_\mu \psi$ describes the dynamics of the fermion fields and their interaction with the photon field A_μ, then $\bar{\psi}m\psi$ is the mass term that will be described in more details in Section 2.1.3 and $\frac{1}{4}F_{\mu\nu}F^{\mu\nu}$ describes the fields dynamics (first term of equation 2.1).

QCD

Quantum Chromodynamics (QCD) is the part of the SM describing the strong interaction. It is a gauge theory invariant under the $SU(3)$ group, which has eight generators. QCD is therefore mediated by eight gauge fields (gluons) noted G^a_μ where $a = (1, ..., 8)$ is the colour index. The QCD Lagrangian is expressed as a function of quark colour triplets of fermion fields $q = (q_1, q_2, q_3)^T$ for each quark flavour ($q = u, d, s, c, b, t$):

$$\mathcal{L}_{\text{QCD}} = \sum_q \bar{q}(i\gamma^\mu \partial_\mu - m_q)q + \sum_q g_s \bar{q}\gamma^\mu \frac{\lambda^a}{2} q G^a_\mu - \frac{1}{4}G^a_{\mu\nu}G^{a,\mu\nu} \tag{2.5}$$

where λ^a are the Gell-Mann matrices. The first sum term describes the quark's kinematics and the second sum term the interactions between quarks and gluons, and the last term the interactions between gluons. Note that the strong coupling constant is often noted as $\alpha_s \equiv \frac{g_s^2}{4\pi}$ and that the quark mass m_q has an electroweak origin which will be explained in Section 2.1.3.

Electroweak interactions

At high energies, the electromagnetic and weak interactions are unified into the electroweak interaction, symmetric under the $SU(2)_L \otimes U(1)_Y$ group. The $SU(2)_L$ part is called the weak isospin group which only acts on left handed fermions and has three gauge fields: W_μ^a with $a = 1, 2, 3$ an isospin charge noted I_3. The $_L$ subscript means "left" as the transformation only affects left-handed fermions ψ_L[1].

The $U(1)_Y$ part is the hypercharge group and it has one corresponding gauge field B_μ and a corresponding hypercharge Y. The hyper charge is distinct from the electric charge of the electromagnetic interaction but the electromagnetic gauge group $U(1)_{\mathrm{EM}}$ is a subgroup of $SU(2)_L \otimes U(1)_Y$. The electric charge of a particle Q is given by the Gell-Mann-Nishijima relation $Q = I_3 + \frac{Y}{2}$ At low enough energies, the $SU(2)_L \otimes U(1)_Y$ symmetry is broken through the Brout-Englert-Higgs mechanism hence giving a mass to the weak bosons $W^\pm$ and Z, and resulting in the electromagnetic interaction mediated by the photon.

The electroweak Lagrangian is composed of four terms: $\mathcal{L}_{EW} = \mathcal{L}_{WB} + \mathcal{L}_F + \mathcal{L}_H + \mathcal{L}_Y$ which are respectively the gauge, fermion, Higgs and Yukawa terms. The two first terms are given by:

$$\mathcal{L}_{WB} = -\frac{1}{4} W^a_{\mu\nu} W^{\mu\nu,a} - \frac{1}{4} B_{\mu\nu} B^{\mu\nu} \tag{2.6}$$

$$\mathcal{L}_F = \sum_{j=1}^{6} \bar{\psi}_L^j i\gamma^\mu (\partial_\mu - i g_2 \frac{\sigma^a}{2} W_\mu^a + i g_1 \frac{Y}{2} B_\mu) \psi_L^j + \sum_{j=1}^{9} \bar{\psi}_R^j i\gamma_\mu (\partial_\mu + i g_1 \frac{Y}{2} B_\mu) \psi_R^j \tag{2.7}$$

[1] $\psi_L = \frac{1-\gamma_5}{2}\psi$ with $\gamma_5 = i\gamma_0\gamma_1\gamma_2\gamma_3$ defined from the Dirac matrices, and $\psi_R = \frac{1+\gamma_5}{2}\psi$ the right handed fermions .

Here $W^a_{\mu\nu}$ and $B^{\mu\nu}$ are the field strength tensors are constructed from the electroweak vector fields[2]. The charges g_1 and g_2 are the charges of the $U(1)_Y$ and $SU(2)_L$ respectively, σ^a are the Pauli matrices.

The first Lagrangian $\mathcal{L}_{WB}$ describes the vector field dynamics. In $\mathcal{L}_F$, the term with the partial derivative gives the fermion' dynamics and the other terms the interaction between the fermions and the vector fields. Note here the absence of a mass term.

2.1.3 Brout-Englert-Higgs mechanism

So far the fermions and gauge bosons introduced have been massless and their mass terms need to be added to the Lagrangian. However, adding a simple mass term of the form $m\psi\bar{\psi} = m(\bar{\psi_L}\psi_R + \bar{\psi_R}\psi_L)$ would not respect gauge invariance as left-handed and right-handed fields do no transform in the same way. A more complex process is required to explain the origin of the particle masses: the Brout-Englert-Higgs mechanism [9, 10]. Introduced in 1964, the mechanism explains how the coupling between a scalar field and the fermion and gauge bosons leads to gauge invariant mass terms.

The Higgs field in the Standard Model consists of an isospin doublet of complex scalar fields defined as:

$$\phi(x) = \begin{pmatrix} \phi^+(x) \\ \phi^0(x) \end{pmatrix} = \frac{1}{\sqrt{2}} \begin{pmatrix} \phi_1(x) + i\phi_2(x) \\ \phi_3(x) + i\phi_4(x) \end{pmatrix} \tag{2.8}$$

where $\phi_i(x)$ are real valued scalar fields. Its Lagrangian is given the following equation [6]. Note that these terms correspond to the fourth and fifth terms of equation 2.1.

$$\mathcal{L}_{\text{Higgs}} = (D_\mu\phi)^\dagger(D_\mu\phi) - V(\phi)\,, \tag{2.9}$$

$$\text{with :} \quad D_\mu\phi = \left(\partial_\mu - ig_2\frac{\sigma^a}{2}W^a_\mu + i\frac{1}{2}g_1B_\mu\right)\phi \tag{2.10}$$

$$\text{and :} \quad V(\phi) = \mu^2\phi^\dagger\phi + \frac{\lambda}{4}(\phi^\dagger\phi)^2 \tag{2.11}$$

[2] $W^a_{\mu\nu} = \partial_\mu W^a_\nu - \partial_\nu W^a_\mu + g_2\epsilon^{abc}W^b_\mu W^c_\nu$ and $B^{\mu\nu} = \partial_\mu B^\nu - \partial_\nu B^\mu$

Where $V(\phi)$ is the gauge invariant Higgs potential with μ and λ being scalar constants. The behaviour of the potential depends of the sign of μ^2: if $\mu > 0$, V has one global minimum at $\phi = 0$. But if $\mu < 0$, $\phi = 0$ is a local maximum and the potential has an infinite set of minima as shown in Figure 2.2 and given by:

$$\phi^\dagger \phi = -\frac{2\mu^2}{\lambda} = v^2 \tag{2.12}$$

where v is called the vacuum expectation value (vev). The Higgs doublet's vacuum expectation value can then be expressed as: $\langle \phi \rangle = \frac{1}{\sqrt{2}} \begin{pmatrix} 0 \\ v \end{pmatrix}$. It is not invariant under gauge transformations and the $SU(2)_L \times U(1)_Y$ symmetry is hence spontaneously broken. Note that $< \phi^+(x) >= 0$ and the electrically neutral component $< \phi^0(x) >$ is invariant under an electromagnetic gauge transformation. The electromagnetic gauge symmetry $U(1)_{\mathrm{EM}}$ is therefore preserved. To make the Higgs boson apparent, the doublet can be rewritten in the unitary gauge as $\phi(x) = \frac{1}{\sqrt{2}} \begin{pmatrix} 0 \\ v+H(x) \end{pmatrix}$ where $H(x)$ is the Higgs particle field. Equation 2.11 then becomes:

$$V = \frac{M_H^2}{2} H^2 + \frac{M_H^2}{2v} H^3 + \frac{M_H^2}{8v^2} H^4 \tag{2.13}$$

which yields the Higgs particle mass term (first term) and self interactions (second and third terms).

Now one can derive how the $W^\pm$ and Z boson acquire their masses. The Higgs Lagrangian from Equation 2.9 can now be rewritten as a function of $H(x)$ and the kinetic term can be expanded as:

$$\frac{1}{2} \left(\frac{g_2}{2} v \right)^2 (W_\mu^1 W^{\mu,1} + W_\mu^2 W^{\mu,2}) + \frac{1}{2} \left(\frac{1}{2} v \right)^2 (W_\mu^3, B_\mu) \begin{pmatrix} g_2^2 & g_1 g_2 \\ g_1 g_2 & g_1^2 \end{pmatrix} \begin{pmatrix} W^{3,\mu} \\ B^\mu \end{pmatrix} \tag{2.14}$$

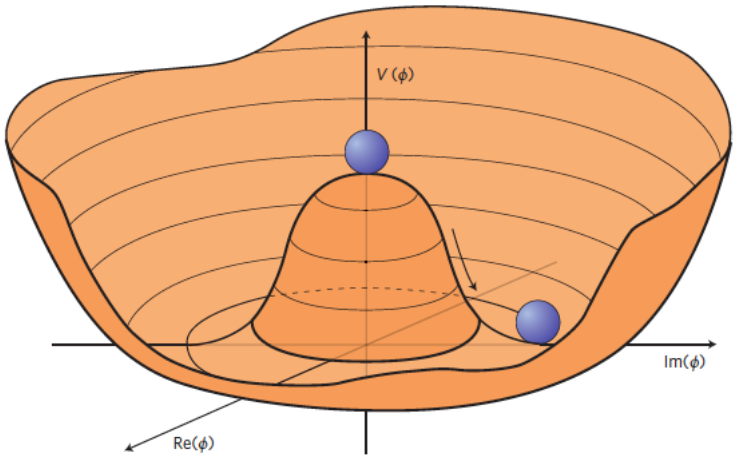

Figure 2.2: An illustration of the Higgs potential in the case that $\mu^2 < 0$, in which case the minimum is at $|\phi|^2 = -\frac{\mu^2}{2\lambda}$. Choosing any of the points at the bottom of the potential breaks spontaneously the rotational $U(1)$ symmetry. [11]

This equation can be re-expressed in terms of the physical gauge bosons defined as:

$$W_\mu^\pm = \frac{1}{\sqrt{2}}(W_\mu^1 \mp iW_\mu^2) \tag{2.15}$$

$$\begin{pmatrix} Z_\mu \\ A_\mu \end{pmatrix} = \begin{pmatrix} \cos\theta_W & \sin\theta_W \\ -\sin\theta_W & \cos\theta_W \end{pmatrix} \begin{pmatrix} W_\mu^3 \\ B_\mu \end{pmatrix} \tag{2.16}$$

Using the definition of the physical gauge bosons (Equations 2.15 and 2.16), Equation 2.14 can be rewritten in a simpler form that reveals the W and Z boson mass terms:

$$M_W^2 W_\mu^+ W^{-,\mu} + \frac{1}{2}(Z_\mu, A_\mu) \begin{pmatrix} M_Z^2 & 0 \\ 0 & 0 \end{pmatrix} \begin{pmatrix} Z_\mu \\ A_\mu \end{pmatrix} \tag{2.17}$$

$$\text{Where} \quad M_W = \frac{g_2}{2}, \quad \text{and} \quad M_Z = \frac{\sqrt{g_1^2 + g_2^2}}{2}\, v \tag{2.18}$$

Note that the field A_μ remains massless and corresponds to the photon fields.

Trilinear and quartic gauge couplings:

The couplings between the electroweak gauge bosons arise from the covariant derivative

term in Equation 2.9. Expanding that term using the physical W, Z and A fields yields the following couplings: $WW\gamma$, $WW\gamma\gamma$, WWZ, $WWWW$, $WWZZ$, $WWZ\gamma$. The Lagrangian for the couplings of interest between the W bosons and photons are:

$$\mathcal{L}_{WW\gamma} = ig_2 \sin\theta_W \left(W^+_{\mu\nu}W^{-\mu}A^\nu - W^-_{\mu\nu}W^{+\mu}A^\nu + W^+_\mu W^-_\nu F^{\mu\nu}\right) \quad (2.19)$$

$$\mathcal{L}_{WW\gamma\gamma} = -g_2^2 \sin\theta_W{}^2 \left[(W^+_\mu W^{-\mu})(A_\nu A^\nu) - (W^+_\mu A^\mu)(W^-_\nu A^\nu)\right] \quad (2.20)$$

The trilinear and quartic gauge couplings are hence fully fixed by the $SU(2)_L \times U(1)_Y$ symmetry of the SM.

Yukawa interactions:

The fermion masses also arise from the spontaneous symmetry breaking of the $SU(2)_L \times U(1)_Y$ gauge symmetry and come from the so called Yukawa Langrangian:

$$\mathcal{L}_Y = -y_l \bar{L_L}\phi l_R - y_d \bar{Q_L}\phi d_R - y_u \bar{Q_L}\phi^c u_R + \text{h.c} \quad (2.21)$$

where the left handed leptons are arranged in a neutrino-charged lepton doublet $L_L = \binom{\nu_L}{l_l}$ as well as left handed quarks: $Q_L = \binom{u_L}{d_L}$. The y_i coefficients are called Yukawa couplings. These are free parameters and their values are not determined by the theory. This Lagrangian corresponds to the third term of equation 2.1. The fermions mass terms are obtained by expanding the Lagrangian in the unitary gauge which yields:

$$\mathcal{L}_Y = -\sum_{f=l,u,d} \left(m_f \bar{\psi}_f \psi_f + \frac{m_f}{v} H \bar{\psi}_f \psi_f\right) \quad (2.22)$$

$$\text{with :} \quad m_f = y_f \frac{v}{\sqrt{2}} \quad (2.23)$$

This form of the Lagrangian reveals the interaction between the Higgs and fermions. As a final remark, note the absence of a neutrino mass term as the field ν_R (equivalent of the u_R term in Equation 2.21) does not exist in the Standard model.

2.1.4 Limitations of the Standard Model

The Standard Model describes very well the phenomena observed in high energy collisions. However, it is known to have numerous shortcomings which will be briefly discussed here.

First the SM suffers from a fundamental problem: the *hierarchy problem* or *fine-tuning* problem [6]. The scale of the electroweak symmetry breaking is of the order of 100 GeV (Higgs mass) but it is expected to receive corrections of the order of the Planck scale (10^{19} GeV) or of a Grand Unified Theory (GUT) scale. The low Higgs mass is explained by a fine tuning of the tree level and loop contribution to the Higgs mass in such a way they almost cancel out. The SM also requires 19 numerical constants that have to be measured (masses, mixing angles, couplings) and that are not predicted by theory. Moreover, the range of the parameters has a huge spread with no obvious explanation, for example $m_e = 0.511$ GeV to $m_t = 170$ GeV without even mentioning the neutrino masses of a few meV.

The nature of the neutrino masses is still unclear and the Standard Model only describes massless neutrinos. Due to their electric neutrality, neutrinos could be their own anti-particle (Majorana neutrino) or have a right-handed anti-neutrinos component existing in nature making them Dirac neutrinos.

The Standard Model is also inconsistent with the λ-CDM model of cosmology [12]. Several astrophysical and cosmological observations [13] suggest that the universe is made up of $\sim$25% of an unknown type of matter called Dark Matter (DM), the nature of which is not described by the SM. The rest would be made of Dark energy (70%) and baryonic matter, studied in this thesis, would make up only 5% of the universe's mass. The SM does not explain the reason for the observed matter-antimatter asymmetry. Finally, gravity is just not described at the quantum level.

Many Beyond Standard Model (BSM) theories have been developed to try to explain these phenomena. Supersymmetry for instance offers an elegant solution to the hierarchy problem while predicting the existence of new particles which could explain the nature of the DM. However no new BSM particle has been observed at the LHC so far and BSM theories will not be covered in this thesis. Instead, another approach to look for new phenomena is using an Effective Field Theory (EFT) approach which is a model independent way of parametrizing new physics. Moreover, any BSM model can be compared to the latests limits set on EFTs which is a key tool for theorists to compare their models with experimental results.

2.2 Effective Field Theory Approach

In an Effective Field Theory (EFT), particles much heavier than the scale of a physical problem do not appear explicitly. Their effect is incorporated in the coupling constants, masses, or possibly new operators of the Lagrangian.

A good example of a successful EFT is Fermi's theory of beta decay [14]. The weak decay of a proton or neutron happens at a scale $p \ll M_W$ and it can be described as a single point interaction between four fermions currents (see Figure 2.3):

$$\mathcal{L}_F = \frac{G_F}{\sqrt{2}}(\bar{p}n\bar{e}\nu + \bar{n}p\bar{\nu}e) \tag{2.24}$$

where $G_F = \frac{\sqrt{2}g_2^2}{8M_W^2}$ is the Fermi constant and p and n are the proton and neutron currents respectively. This description of weak interactions breaks down at higher energies and is already a few percent off in the description of τ decays. The interaction must then be described by the SM as being mediated by a W boson. It is described by the term of the electroweak Lagrangian (see Equation 2.7):

$$\mathcal{L} = -ig_2 \sum_{j=1}^{6} \bar{\psi}_L^j i\gamma^\mu (\frac{\sigma^a}{2} W_\mu^a) \psi_L^j \tag{2.25}$$

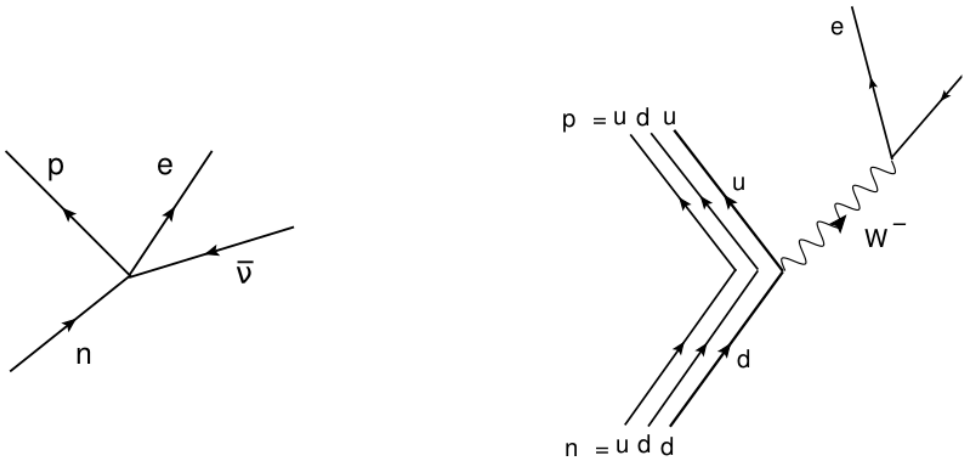

Figure 2.3: Feynman diagrams showing the beta decay as described in Fermi's effective weak theory (left) and in the Standard Model (right).

Similarly, the Standard Model itself can be viewed as an EFT valid at the vev scale: $v = 246$ GeV. Potential new heavy particles within a higher energy description of nature would then generate tree level contributions to gauge boson couplings, leading to so-called *anomalous couplings*, i.e. couplings different than those predicted to exist by the SM. These couplings can be parametrised in a generic way and in that case the SM Lagrangian introduced earlier can be extended to an EFT Lagrangian of the form [15]:

$$\mathcal{L}_{\mathrm{EFT}} = \mathcal{L}_{\mathrm{SM}} + \sum_{n=5}^{\infty} \frac{f_n}{\Lambda^{n-4}} \mathcal{O}_n \tag{2.26}$$

where Λ is the characteristic scale of new physics, f_n are the anomalous coupling constants and $\mathcal{O}_n$ are n-dimension operators [3]. These operators must be Lorentz structures that are invariant under the SM symmetries and are are built from powers of the SM fields and their derivatives. In our previous example, the four fermion current in Fermi theory's of beta decay is an operator of dimension 6.

Anomalous trilinear and quartic gauge couplings, including the aQGC affecting the $WW\gamma\gamma$ vertex are derived in reference [15]. These anomalous contributions are expected to affect both the total cross-section and the cross-section dependence on various kinematic

[3] Note that in natural units $[\phi], [W], [B] = 1,\ [\psi] = \frac{3}{2},\ [m] = 1$ and the Lagrangian is of dimension 4

variables. The observation of the $W\gamma\gamma$ process is therefore useful to set constraints on the possible existence of aQGC. It can also be combined with other precision measurements in global EFT fits, hence allowing the exhaustive search for deviations from the SM.

2.3 Latest multi-boson measurements

Bosonic gauge self-interactions are fully determined in the Standard Model and their precise measurement serves both to establish the SM when agreement is found but also to indicate the possible existence of new physics in case of a deviation. Though the W boson was studied during almost four decades, its production in some multi-boson final states hasn't been observed yet due to their low cross-section and studies are ongoing at the LHC.

The trilinear gauge-boson couplings, easier to probe, have been shown to agree with the SM within a few percent [15]. For instance the $WW\gamma$ triple gauge coupling has been probed by several ATLAS Run 1 analyses: $W\gamma$ and $Z\gamma$ analysis at 7 TeV [16] and the WW analysis at 7 TeV [17]. The $W\gamma$ production has been observed by the CMS collaboration in 13 TeV collisions as well and limits were set on anomalous triple-gauge couplings [18]

The study of Quartic Gauge Coupling (QGC) requires either the production of three bosons in the final state or the pair production of gauge boson via Vector Boson Fusion (VBF). The first QGC measurements were carried out at LEP where the processes $e^+e^- \to W^+W^-\gamma$ and $e^+e^- \to Z\gamma\gamma$ were studied [19, 20].
Studies have been continued at the LHC and several new observations have been made. The inclusive weak tri-boson production (VVV with $V = Z$ or $W^{\pm}$), was observed recently by the CMS collaboration in 2020 [21], while ATLAS recently observed the simultaneous production of three W bosons [22]. The tri-boson final state $WW\gamma$ and $WZ\gamma$ was observed at 8 TeV [23] and used to constraint both TGC and QGC.
Vector boson fusion has been extensively studied as well and the process $\gamma\gamma \to WW$ was observed at 13 TeV by the ATLAS collaboration [24] as well as the electroweak production

of a Z pair [25] and a W pair [26]. However, the tri-boson $W\gamma\gamma$ production has not been observed yet: evidence of the process (3 σ significance) was found by ATLAS [27] during the LHC Run 1 and by CMS with the Run 1 [28]. The CMS collaboration has also released their Run 2 results: the $W\gamma\gamma$ production was measured with an observed (expected) 3.1 (4.5) σ significance [4].

The work presented in this thesis aims at observing for the first time at a statistical significance superior to 5 σ the $W\gamma\gamma$ process using the full Run 2 data recorded by the ATLAS detector.

Chapter 3

Experimental Setup

This chapter gives an overview of the experimental setup used to acquire the data used in this thesis. First, the LHC and the CERN accelerator complex is described in Section 3.1. Then the ATLAS detector and its various sub-modules are described in Section 3.2. Finally the process and detectors used to measure luminosity are described in Section 3.3 followed by an overview of the ATLAS triggering system in Section 3.4.

3.1 The LHC

The Large Hadron Collider (LHC) is a 27 km long circular particle accelerator and collider used to collide hadrons [29]. It is located about 100 m below ground under the French-Swiss border at CERN, near Geneva. Four detectors are located at different interaction points along the LHC tunnel: ATLAS [30], ALICE [31], CMS [32] and LHCb [33], as shown in Figure 3.1. The LHC was designed to collide protons at a maximum centre of mass energy of $\sqrt{s} = 14$ TeV and a luminosity[1] of $L = 10^{34}\ \mathrm{cm}^{-2}\,\mathrm{s}^{-1}$; and to collide heavy ions (lead) at the centre of mass energy of 2.5 TeV. The goal of the proton collisions is to look for new physics phenomena at the highest energy ever reached in a lab. The study of these kind of proton collisions has already led to the discovery of the Higgs boson in 2012. The heavy ion collisions provide an environment to study the properties of a state

[1] Luminosity is collider parameter that relates the production rate of a process to its cross-section, see Section 3.3

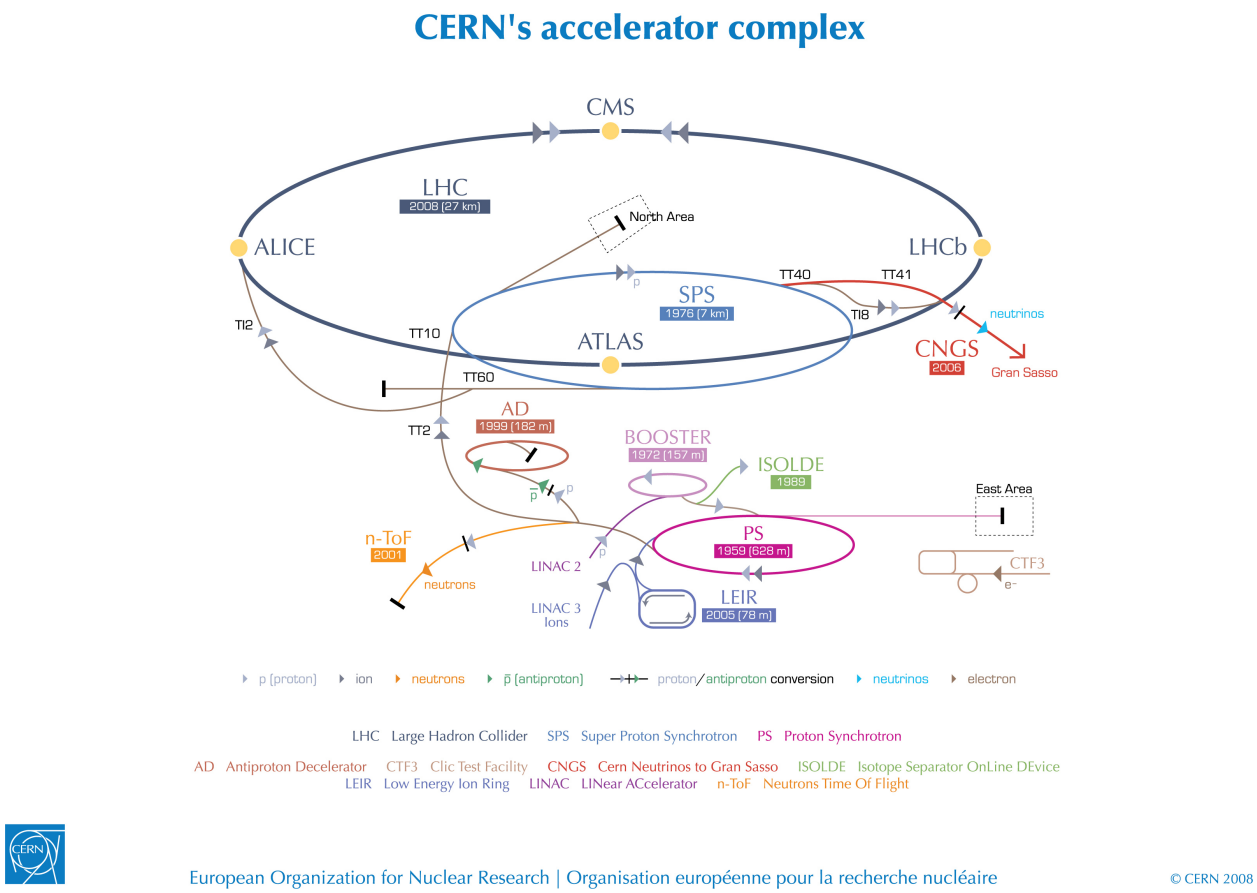

Figure 3.1: Schematic diagram of the CERN accelerator complex. The LHC injector chain is composed of the Linac 2, Booster, PS, SPS and LHC [34]. Note that since 2020, the Linac 2 was replaced by the new Linear accelerator 4 (Linac 4) which boosts negative hydrogen atoms to 160 MeV before injecting them into the Booster. CERN's accelerator complex consists of more accelerators that deliver various types of beam to other experiments.

of matter called *quark-gluon plasma*, momentarily reproducing conditions similar to those that existed in the very early universe.

The LHC consists of two rings of counter-rotating particle beams travelling in vacuum. The beams are bent and focused using superconducting magnets and accelerated using radio frequency (RF) cavities. A chain of several other accelerators, showed in Figure 3.1 is used to deliver 450 GeV protons to the LHC. The protons come from hydrogen gas which is ionised in an electric field. They are pulsed in bunches into the Linear accelera-

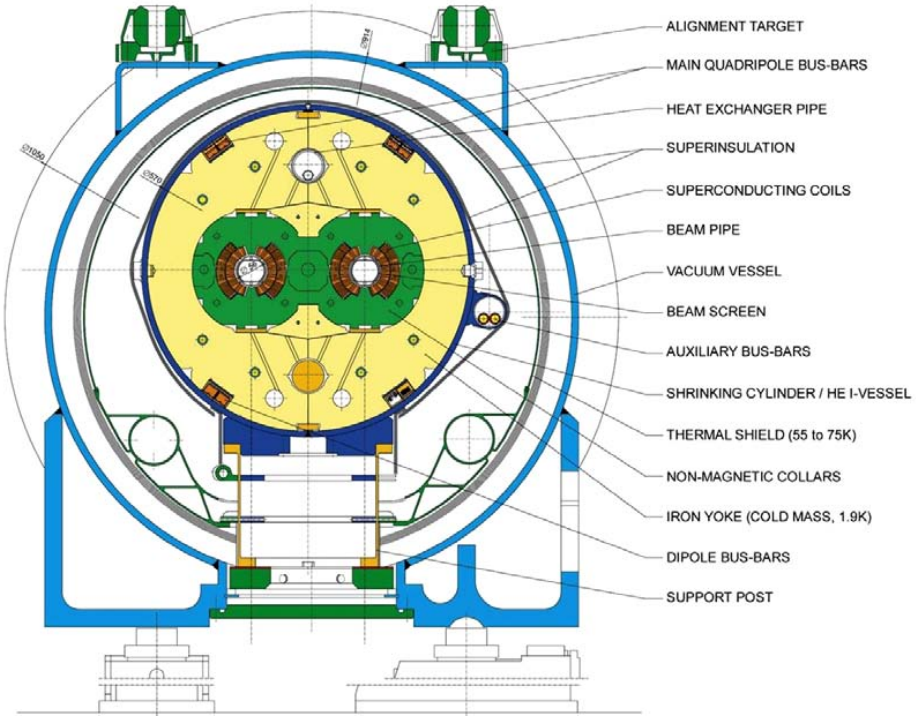

Figure 3.2: Cross section of a LHC dipole magnet and its cryostat [29].

tor 2 (Linac 2) which boosts the proton bunches energy to 50 MeV. The proton bunches are then injected into the four rings of the Proton Synchrotron Booster (Booster) where they are accelerated to an energy of 1.4 GeV. The next stage of acceleration is the Proton Synchrotron (PS) where the proton bunches reach an energy of 25 GeV. Finally the protons enter the Super Proton Synchrotron (SPS) and are accelerated to an energy of 450 GeV prior to being injected into the LHC.

Multiple acceleration cycles are required to fill the LHC and bunches of protons from the SPS are injected consecutively. Once filled, the energy of the protons in the LHC is ramped up from 450 GeV to 6.5 TeV. The collisions can then start and last from a few minutes in case of beam instabilities up to a dozen hours. Over time, collisions reduce the amount of protons in the bunches and at some point it becomes more efficient to dump the beam in a dedicated area and refill the LHC for another data taking period, than continuing to collide protons at a much reduced rate.

Superconducting magnets

The LHC requires 1232 dipole magnets to bend the beam's trajectory, about 450 quadrupole magnets to focus the beam, and several thousand corrector magnets that correct the beam's focus and orbit. Dedicated magnets called kickers are also used to extract proton bunches from the SPS accelerator to the LHC. The dipole magnets bending power is one of the factors limiting the maximum energy the accelerator can reach. Other limiting factors include the power of accelerating RF cavities and energy loss by radiation (bremsstrahlung). To operate with protons at an energy of 7 TeV, the LHC requires magnetic fields of an intensity surpassing 8 T, which can only be reached by superconducting magnets. LHC magnets are made from a Niobium-Titanium alloy (NbT), operated at a temperature of 2 K, and cooled down using superfluid helium in a cryostat showed in Figure 3.2. Due to the limited space available in the LHC tunnel, a novel magnet *twin bore* design was adopted. It accommodates the windings of the two beam channels into one common cryostat, which complicates the magnet structure as both magnets are coupled. Superconducting magnets can *quench*, which means they suddenly transition back to a normally conducting mode. The process releases huge amounts of heat due to the Joule effect and can lead to serious damages if proper safety mechanisms are not put in place. In order to reach the their nominal operation magnetic field, the LHC superconducting magnets must be *trained* to be able to sustain the high current required. The electrical current in the magnet coils is slowly ramped up until the magnet quenches, and the process is repeated until all magnets are able to sustain the high current. This training process takes several months.

RF systems

The LHC proton beams are accelerated and maintained at maximum energy thanks to 16 superconducting radio frequency (RF) cavities. The cavities are metallic chambers coated with Niobium that are operated in the superconducting regime [35]. An oscillating electric field of 400 MHz with a amplitude varying from 8 to 16 MV is created in the cavity. It accelerates each proton beam from its injection energy to the current operational maximum energy of 6.5 TeV. The RF cavities also help to shape the beam longitudinally and

keep the proton bunches separated. Outlier protons that arrive in advance compared to the main bunch receive less acceleration and conversely, late protons are accelerated more strongly. The RF cavity chamber length constrains the maximum bunch length allowed.

3.1.1 LHC evolution

Constructing and operating the world's largest and most energetic collider hasn't come without challenges. Adjustments to the initial LHC project plan and schedule were made over the years, and future machine upgrades are planned and promise an increased reach for research in the decades to come. The historical development and future of the LHC is briefly discussed in here.

- **1994:** The LHC project was approved as the next accelerator meant to replace CERN's Large Electron Positron collider (LEP).
- **1998:** Construction began and lasted a decade.
- **2008:** A major magnet quench incident damaged the infrastructure in a section of the accelerator. The repair and component modifications required to avoid such incident in the future led to a one year delay. Furthermore, the decision was taken to initially operate the LHC at sub-nominal energy and luminosity.
- **2009-2013:** Run 1 physics data taking period during which the LHC was operated at a centre of mass energy of $\sqrt{s} = 7$ TeV then $\sqrt{s} = 8$ TeV.
- **2013-2015:** Long shutdown 1: operation stopped for machine consolidation work to reach original design beam energy.
- **2015-2018:** Run 2 physics data taking period during which the centre of mass energy was increased to $\sqrt{s} = 13$ TeV.
- **2019-2022:** Long shutdown 2: consolidation work to prepare running at design collision energy of $\sqrt{s} = 14$ TeV. Some accelerator and detector upgrades are scheduled in preparation for the future High Luminosity LHC (HL-LHC) operation.

- **2022-2024**: The LHC Run 3 is expect to double the integrated luminosity delivered to the experiments compared to Run 1 and Run 2 combined [36].
- **2025-2027:** Long shutdown 3: final machine and detectors upgrade in preparation for HL-LHC operation.
- **2027**: HL-LHC operation that will see the LHC beams intensity increased by a factor of 10 beyond the original design value.

Pushing the exploration of the energy frontier further will require a next generation collider; a project that requires long term planning. Therefore, discussions have already started within the physics community to design the next accelerator that will take over after the LHC. The European Particle Physics Strategy committee has concluded that "An electron-positron Higgs factory is the highest-priority next collider". This next collider could take the form of the electron-positron International Linear Collider (ILC) currently under consideration in Japan, or a circular electron-positron collider implemented as a first stage of the Futur Circular Collider (FCC) project being developed at CERN [37].

3.2 The ATLAS detector

The ATLAS detector [30] is a multi-purpose detector operating at the LHC at CERN. It is designed to search for new physics phenomena in LHC collisions and to make precise measurements of Standard Model parameters and known physics processes. In order to identify the nature of the secondary particles produced in the proton-proton collisions, the ATLAS detector requires fast, radiation hard sensors and electronics, a high granularity and a good hermeticity. To meet all these requirements, ATLAS is composed of different detector sub-systems shown in Figure 3.3 that are each optimised for different tasks. The different detector sub-systems are described here starting from the location closest to the interaction region, and moving outward.

- The Inner Detector (ID), described in Section 3.2.1, is used to measure the trajectory of charged particles and precisely reconstruct the location of primary and secondary interaction vertices.

- The calorimeter system described in Section 3.2.2, is then used to measure the energy of electrons, photons and hadrons.
- Muons are not stopped in the calorimeters and measuring their momentum requires an additional dedicated Muon Spectrometer (MS) system, described in Section 3.2.3.
- The detector sub-systems are complemented by a complex magnet system that bends the trajectory of charged particles in order to identify their charge and measure their momentum. The ATLAS magnet system is composed of one thin superconducting solenoid magnet of 5.3 m long and 2.4 m diameter providing a 2 T axial magnetic field for the ID; one barrel toroid and two end-caps toroids superconducting magnets producing a field of 0.5 and 1 T respectively in the central and end-cap regions of the muon spectrometer.

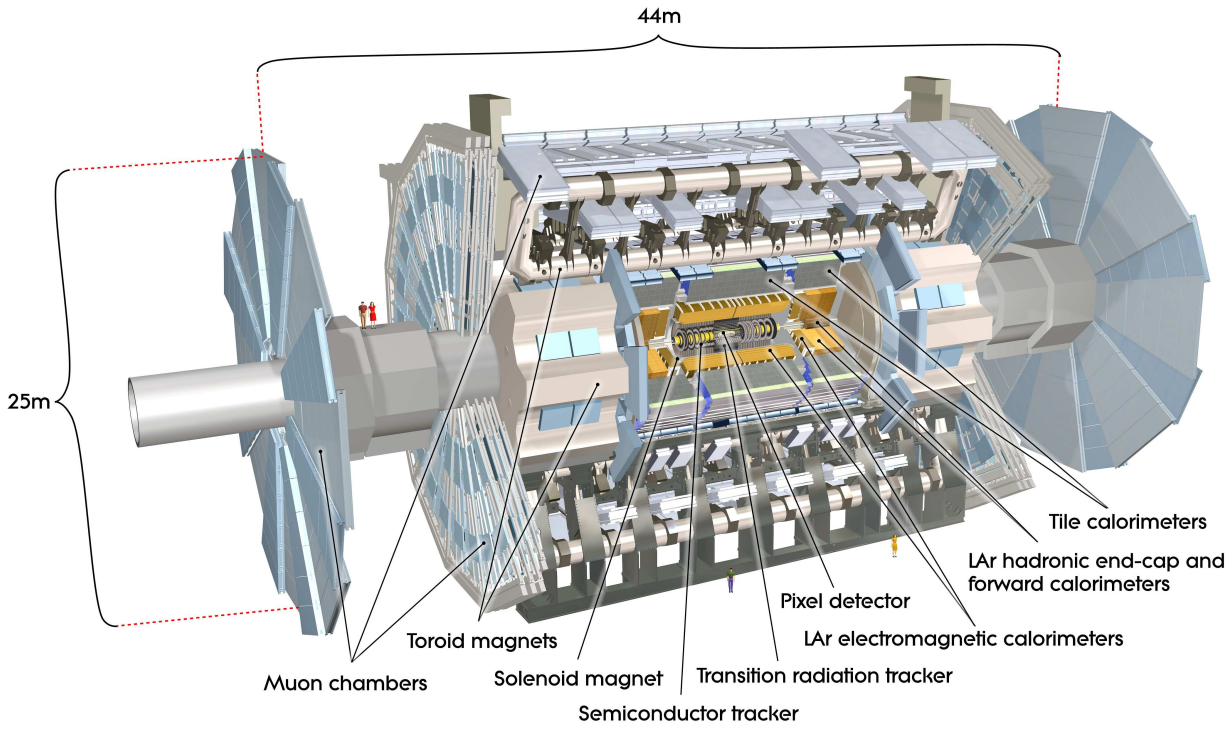

Figure 3.3: Schematic view of the ATLAS detector showing the location of the different detector sub-systems [30]. ATLAS measures 44 m long by 25 m wide and weighs around 7000 tons.

ATLAS coordinate system

The coordinate system used to describe the ATLAS detector is defined as follows: the interaction point is taken as the origin of the coordinate system. The x-axis points towards the centre of the LHC ring, the y-axis points upward and the z-axis is defined by the direction of the beam pipe. The azimuthal angle ϕ is measured around the beam z-axis, and the polar angle θ is the angle as measured from the beam axis. Two additional variables are of interest here: the pseudorapidity $\eta = -\ln\tan\frac{\theta}{2}$ and the angle in the pseudorapidity-azimuthal angle space: $\Delta R = \sqrt{\Delta\eta^2 + \Delta\theta^2}$ which quantifies the distance between two particles trajectories in the detector.

The pseudorapidity η tends towards rapidity[1] y when a particle's momentum is much greater than its mass, which is the case for the final state photons and leptons studied in this thesis. Rapidity is preferred over angular measurements as differences in rapidity are invariant quantities under Lorentz boosts. Although the proton-proton collisions are stationary in the lab frame, the high energy interactions studied here occur between partons (quarks and gluons making up protons) which carry a varying fraction of the proton's momentum. These parton-parton collisions therefore have a variable Lorentz boost along the z-axis. Note that pseudorapidity varies from 0 (direction along the y-axis) to infinity (direction tending toward z-axis beam).

3.2.1 Inner Detector

The ATLAS Inner Detector (ID) [38, 39] is used to measure the trajectory of charged particles and their point of origin over the pseudo rapidity range $|\eta| < 2.5$. Located inside the volume of the solenoid magnet, the ID operates in a 2 T magnetic field which bends the trajectory of charged particles in the transverse x-y plane, enabling the measurement of their electric charge and momentum. The ID must have a fast response, offer excellent transverse momentum resolution for particles with transverse momentum $p_T > 0.5$ GeV, while operating in a high-radiation environment, and while having a low material budget to minimize multiple scattering of particles travelling through its volume. To do so, it

[1] Rapidity is defined as $y \equiv \frac{1}{2}\ln\left(\frac{E+p_z}{E-p_z}\right)$

combines discrete, high-resolution semiconductor pixel and strip detectors and a straw-tube Transition Radiation Tracker (TRT) in its outer layer as shown in Figure 3.4. The ID spacial resolution in the bending plane is 15 µm in the silicon detectors and 150 µm in the TRT. The corresponding transverse momentum resolution is momentum dependent and can be parametrised as:

$$\frac{\sigma_{p_T}}{p_T} = a \oplus b \times p_T \tag{3.1}$$

where a is related to multiple scatterings and b corresponds to the ID intrinsic resolution. The momentum resolution was measured to be 1.6% at low transverse momentum ($p_T < 5$ GeV) and around 50% at 1 TeV [40].

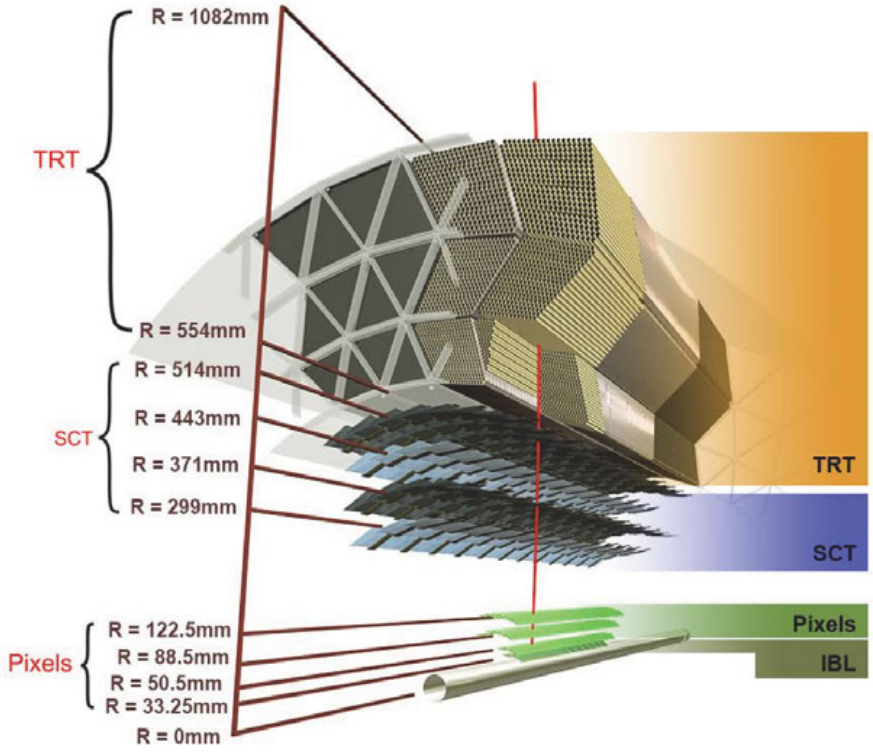

Figure 3.4: Schematic view of the ATLAS Inner Detector (ID) showing the different sub-modules being traversed by a charged particle of transverse momentum $p_T = 10$ GeV (red) [41].

Pixel detector

The pixel detector is composed of 3 layers of pixel sensors in the barrel and end-cap

regions. The pixels are silicon p-n junctions, operated in a reverse bias voltage, in which a small current pulse is created upon the passage of a charged particle. Each pixel measures 50×400 µm in $\phi - z$. There are approximatively 67 million pixels in the barrel and 13 million in the end-caps, covering a total active area of about 1.7 m^2 and corresponding to 80 million readout channels [42]. The intrinsic spacial resolution for a module is 10 µm in the $r - \phi$ plane and 115 µm in z.

Semi-Conductor Tracker (SCT)

The SCT [38] is the next detector sub-module. It uses similar technology as the pixel detector but the sensors are microstrips of 285 µm wide by 6 cm long with a 80 µm pitch. They are arranged into 4 layers in the barrel region and 9 layers in the end-caps. The intrinsic spacial resolution for a module is of 17 µm in the $r - \phi$ plane and 580 µm in z.

Transition Radiation Tracker (TRT)

The TRT [43] is a straw-tube tracker covering the pseudorapidity range $|\eta| < 2$ in the outer part of the ID. It is a ionisation gas detector made of 52 544 drift tubes measuring 4 $\mathrm{mm}\times$ 39 cm with a central anode wire. The straws are filled with a mixture of $Xe/CO_2/O_2$ and a 1.5 kV voltage is applied between the straw wall and anode wire. Charged particles traversing the volume of the straws ionize the gas, the ionization charge is then amplified by the electric field with a gain of 2.5×10^4 and the resulting signal is read out via a central anode wire. Its intrinsic single-point resolution is of 120 µm.

In addition to its role of measuring the trajectory of charged particles, the TRT also assists in the identification of different particle types. The volume between straws is filled with with material designed to enhance the creation of transition radiation (soft x-ray photons) which occurs when a highly relativistic charged particle traverses a material boundary. This effect is proportional to the relativistic γ-factor $\gamma = \frac{E}{m}$ of a given particle and is therefore strongest for electrons. These soft x-ray photon are absorbed by the xenon atoms which deposits additional energy in the gas. This leads to significantly higher readout signals which enables electron identification.

Inner b-Layer (IBL)

The IBL [44,45] is a fourth layer added to the pixel detector in 2014 at a radius of 3.3 cm . It was added to improve ATLAS vertexing and b-tagging performance. It is made of 26880 pixels consisting of 3D sensors fabricated with CMOS 130 nm technology and covers the range $|\eta| < 3$.

3.2.2 Calorimeters

Calorimeters are detectors designed to measure the total energy of electromagnetic and hadronic *showers*[2] created by incoming electrons, photons or hadrons. They come in two categories: homogeneous and sampling calorimeters. The ATLAS detector only uses sampling calorimeters which are made of alternating active layers that generate a signal, and absorber layers that trigger the further showering of secondary particles in the calorimeter until all the energy is completely absorbed. The energy resolution of a calorimeter can be parametrised as [46]:

$$\frac{\sigma_E}{E} = \frac{a}{\sqrt{E}} \oplus \frac{b}{E} \oplus c \tag{3.2}$$

where a is the stochastic term coming mostly from intrinsic shower fluctuations, b is the noise term coming from the electronic noise of the readout chain, and c is the constant term which depends on calorimeter geometry, imperfections and calibration. Note that the full containment of the shower is necessary in order to obtain an accurate measurement of the incoming particle initial energy. ATLAS has several calorimeters designed to differentiate electrons and photons from hadrons and to measure their energy: the electomagnetic (EM) calorimeter closer to the interaction point, and hadronic calorimeters surrounding it. The latter is further subdivided into the Tile calorimeter (Tile) in the barrel region and the Hadronic End-cap Calorimeter (HEC). Finally, the Forward Calorimeter (FCAL) covers high pseudorapidity regions to ensure a good hermeticity. The calorimeters are shown in Figure 3.5.

[2]Showers are cascades of secondary particles produced when a high energy particle interacts with dense matter

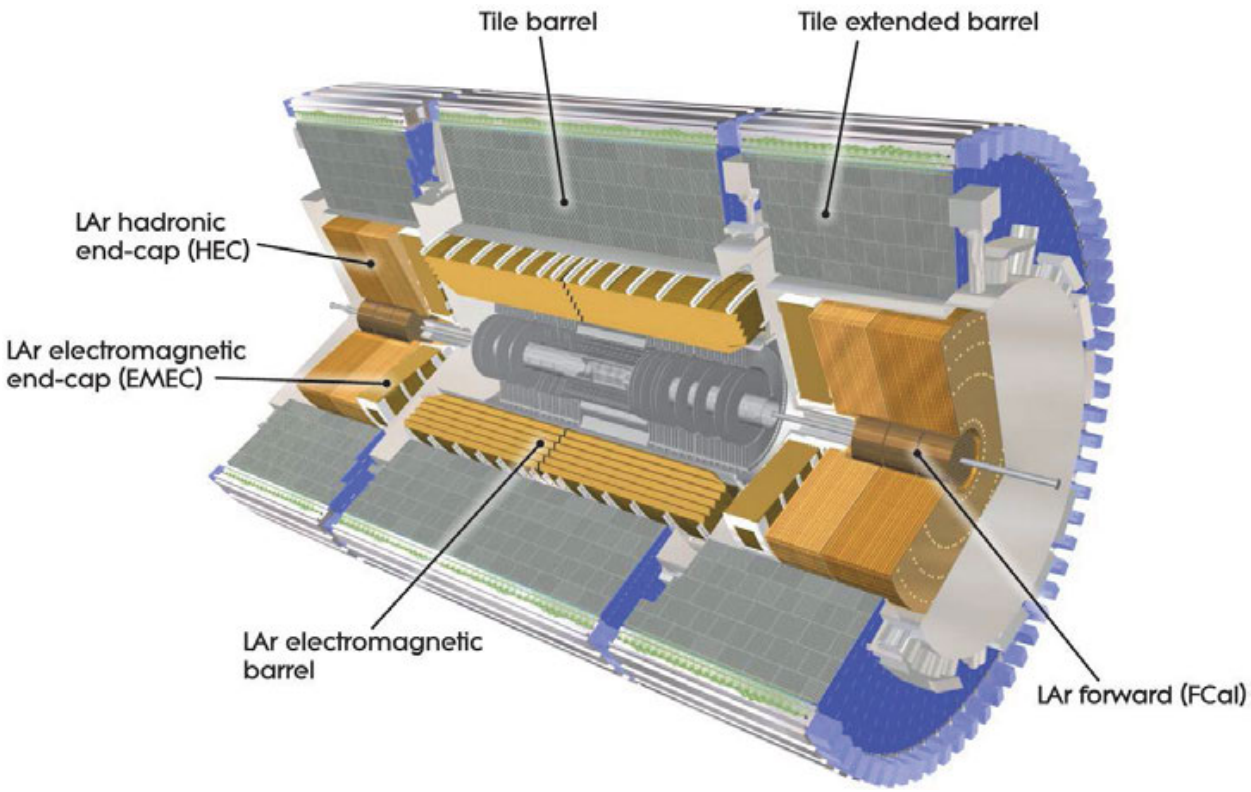

Figure 3.5: ATLAS calorimeter system: the EM calorimeter, HCAL and FCAL have different designs adapted to their radiation environment and physics process of interest [30]

EM calorimeter

The electomagnetic (EM) calorimeter [47] is split up into a barrel section ($|\eta| < 1.46$) located from $r = 1.15$ m to $r = 2.25$ m and an end-cap section (EMEC) at $|z|$ = 3.6 m that covers the region $1.36 < |\eta| < 3.2$. It uses an accordion geometry shown in Figure 3.6. The active material is liquid argon (LAr) contained in 2.1 mm wide gaps between lead-stainless steel absorbers (1.13-2.2 mm thick). The absorber's thickness varies with η so that all particles cross the same amount of material. Charged particles produced in the showers triggered by the absorber ionise the liquid argon and the charge is collected on an anode thanks to a 2 kV electric potential within a drift time of 450 ns. In the barrel region, the EM calorimeter is subdivided into layers of decreasing granularity: the first layer must be fine enough to differentiate single photons from the decay of neutral pions $\pi_0 \to \gamma\gamma$. The natural widening of the showers allows for larger cells further from the interaction point. The resolution of the EM calorimeter is given by $\frac{\sigma_E}{E} = \frac{10\%}{\sqrt{E}} \oplus c$ with c =

1% in the barrel region and 1-2% in the end-caps (with E measured in GeV) [48]. The total EM calorimeter thickness is 22 times its *radiation length*[1] χ_0 and 9.7 times its *interaction length*[2] λ in the barrel region, and 24 χ_0 (10 λ) in the end-caps.

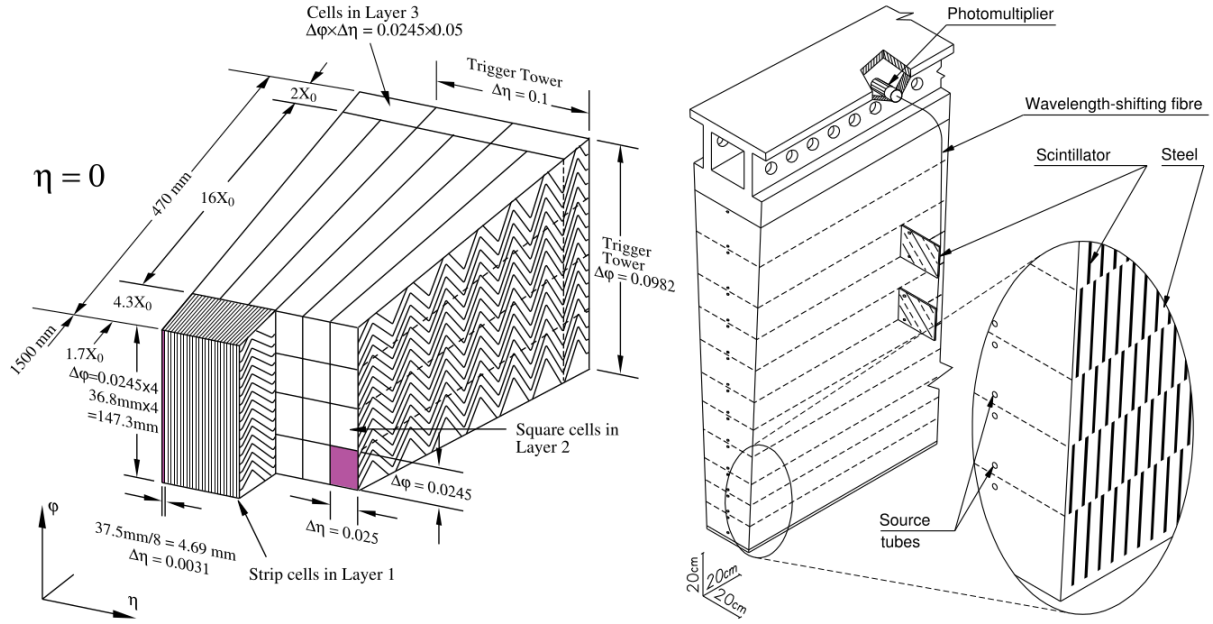

Figure 3.6: Structure of the barrel electromagnetic LAr calorimeter (left) and of a tower of the hadronic Tile Calorimeter (right) [47].

Hadronic calorimeters

The hadronic calorimeters [47, 49] surround the EM calorimeter and are designed to absorb hadrons that pass through the EM calorimeter. They are divided into the Tile calorimeter in the barrel section ($|\eta| < 1.7$ and $2.28 < r < 4.25$ m) and the Hadronic End-cap Calorimeter (HEC) in the end-cap region ($1.7 < |\eta| < 3.2$ and $0.475 < r < 2.03$ m). The Tile calorimeter is made of steel and polystyrene scintillator tiles stacked into towers. Secondary charged particles in a hadronic shower will cause the scintillator to emit UV light,

[1] When passing through matter, high-energy electrons lose energy mostly by bremsstrahlung, and high-energy photons by pair production. The radiation length is a characteristic of a material: it is the mean distance over which electrons lose all but $\frac{1}{e}$ of their energy by bremsstrahlung. It is usually expressed in $\mathrm{g\,cm^{-2}}$.

[2] The interaction length λ is the mean free path hadronic particles travel in matter before undergoing an inelastic nuclear interaction.

which is carried by wave-length shifting fibres to Photomultiplier Tubes (PMTs) located on the outer layer of the Tile calorimeter (Figure 3.6).

The HEC is located in a region of higher radiation and is therefore made of a copper-LAr sampling calorimeter, following the design of the EM calorimeter. Each end-cap section is composed of two wheels built from first 25 mm then 50 mm copper plates.

The hadronic calorimeters energy resolution is worse than that of the EM calorimeter due to greater fluctuations in the particle showers. Its resolution is $\frac{\sigma_E}{E} = \frac{52\%}{\sqrt{E}} \oplus 5.7\%$ (with E measured in GeV) [50]. The Tile calorimeters thickness corresponds to 7.4 times its interaction lengths at $\eta = 0$.

FCAL

The Forward Calorimeter (FCAL) covers the region of pseudorapidity $3.1 < \eta < 4.9$ [51]. It is located in a region of particularly high radiation and uses LAr as active material. It is composed of three layers: the first layer uses copper as absorber which yields good energy resolution to reconstruct the energy of electrons and photons. The two outer layers use tungsten as an absorber, which is denser and better suited to contain hadronic showers. The FCAL is crucial to the measurement of missing transverse energy ($E_{\mathrm{T}}^{\mathrm{miss}}$) as it ensures the good hermeticity of the ATLAS calorimeter system.

3.2.3 Muon spectrometers

Muons have a mean lifetime of about 2 $\mu\mathrm{s}$ and behave like Minimum Ionizing Particles (MIPs)[1] for a large energy range. They therefore traverse ATLAS inner detector and calorimeters while losing only little of their energy through ionisation. The ID can measure muons transverse momentum up to an energy of the order of 100 GeV. For higher energies, the particle trajectories are not curved enough within the ID volume to allow for a good transverse momentum measurement. The Muon Spectrometer (MS) with its much larger volume has a longer lever arm to measure the bending trajectory of muons above 100 GeV. Detecting muons outside of the calorimeters is also used to uniquely identify

[1]The rate of energy loss of a particle going through matter is energy dependent. Minimum Ionizing Particles (MIPs) are particles whose energy loss rate is minimum.

particles as muons.

The ATLAS Muon Spectrometer (MS) surrounds the rest of the detector sub-systems and is composed of separate trigger and high-precision tracking chambers designed to measure the trajectories of muons [52]. In the barrel region for $|\eta| < 1.4$, magnetic bending is provided by the large barrel toroid magnet (1 T) and in the end-cap region ($1.6 < |\eta| < 2.7$), muon trajectories are bent by two smaller end-cap toroid magnets (0.5 T). The MS is composed of three concentric stations of muon chambers in the barrel at ($r = 5$ m, 7.5 m, 10 m) and four disks in each end-caps at approximatively $|z| = 7.4$ m, 10.8 m, 14 m, and 21.5 m as shown in Figure 3.7. The muon spectrometer must operate over a wide range of muon transverse momentum (100 MeV-1 TeV), be adapted to a high level of particle flux at high η, and provide a fast response used for triggering. To satisfy these requirements, the MS is composed of four different technologies, optimised for either precision tracking or triggering purposes.

Monitored Drift Tubes (MDTs)

The MDTs [53] are precision detectors made of cathode tubes of 30 mm diameter with a central wire anode. The use of drift tubes ensures a good mechanical strength and makes it possible to cover large areas at low cost. The tubes are filled with a 90/10 mixture of Argon and CO_2 at a pressure of 3 bar, operated at a voltage of 3 kV. Drift tubes are stacked in layers and arranged into multi-layer chambers. Three concentric stations of MDTs make up the barrel region and two stations are present in each end-cap, covering up to $|\eta| < 2.4$. The maximum ionisation drift time is of about 700 ns and the track sagitta resolution of the combined stations is of 45 µm, corresponding to a transverse momentum resolution of 10% at 1 TeV.

Cathode strip chambers (CSCs)

MDTs can only operate up to a count rate of 150 Hz cm^{-2} so in the end-cap first station innermost section ($2 < |\eta| < 2.7$) where the particle flux is highest, Cathode strip chambers (CSCs) are used [54]. The CSCs are multi-wire proportional chambers with cathodes

segmented into strips, operated at 1.9 kV with a gas mixture of Argon and CO_2. The position at which a muon traversed the chamber is obtained by reading out the charge on neighbouring cathode strips and fitting the cluster position. The wires are not read out. The CSCs can achieve a spatial resolution of 60 $\mu\mathrm{m}$ per CSC plane, and 5 mm in the non bending plane.

Resistive Plate Chambers (RPCs)

The RPCs [55] are fast detectors used for triggering. They are located in the middle and outer stations of the MS barrel region ($|\eta| < 2$). A RPC is a gaseous parallel electrode-plate detector where amplification occurs simultaneously for all ionisation clusters. The gas gap is 2 mm thick and the RPCs are operated at a voltage of 9.8 kV with a gas mixture of: $C_2H_2F_4$/iso-C_4H_{10}/SF_6. Each RPC module has two detector layers. In the barrel region, there are in total 3 layers of RPC modules, and a muon will therefore typically cross 6 RPC layers, enabling a 3 out out of 4 coincidence requirement for the trigger. The timing and spatial resolution of RPCs is approximately 1.5 ns and 1 cm respectively.

Thin Gap Chamberss (TGCs)

The TGCs [56] are multiwire chambers operating in the quasi-saturated mode. They provide the trigger and the azimuthal coordinate of muons in the end-cap regions. The chambers gas gap is 2.8 mm thick with an anode wire pitch of 1.8 mm and they are operated at 3.1 kV with a gas mixture of CO_2 and n-pentane. One of the cathodes is segmented into readout strips used to measure the azimuthal coordinate of the position at which a muon traversed the chamber. The azimuthal angular resolution achieved using the information from the strip readout is of approximately 2-3 mrad. Anode wires are read out in groups of 6 to 31 wires in order to optimise the detector granularity as a function of pseudorapidity. They provide the muon trajectory position in the bending plane. The TGCs are assembled into multiplets of two of three layers which allows for redundancy and electrode staggering which improves the spatial resolution. The TGCs also have an adequate time resolution to provide bunch-crossing identification.

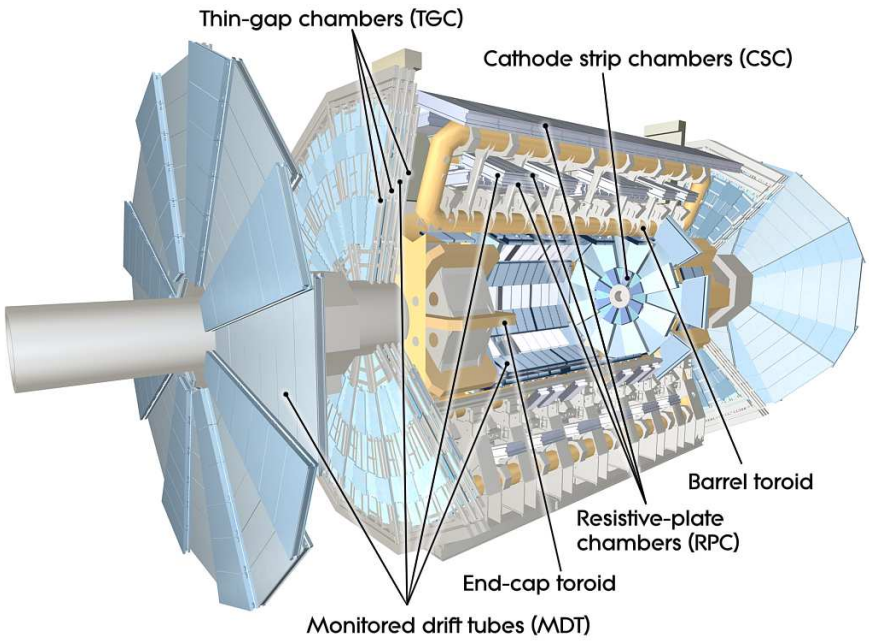

Figure 3.7: Structure of the Muon Spectrometer (MS) [30].

3.3 Luminosity measurement

The instantaneous luminosity is a parameter of the particle collider that relates the production rate of a process to its cross-section using the following formula:

$$L = \frac{1}{\sigma}\frac{dN}{dt} \tag{3.3}$$

where σ is the interaction cross-section of a specific physics process and N is the number of events recorded during a given time t. Instantaneous luminosity is measured in units of $\mathrm{cm}^{-2}\,\mathrm{s}^{-1}$. The precise knowledge of the LHC instantaneous luminosity as function of time is necessary to the measurement of a process cross-section, such as that presented in this thesis. The instantaneous luminosity of a collider depends on its beam structure as described by the following equation:

$$L = f_{rev}\frac{N_1 N_2 N_b}{4\pi\sigma_x\sigma_y}S \tag{3.4}$$

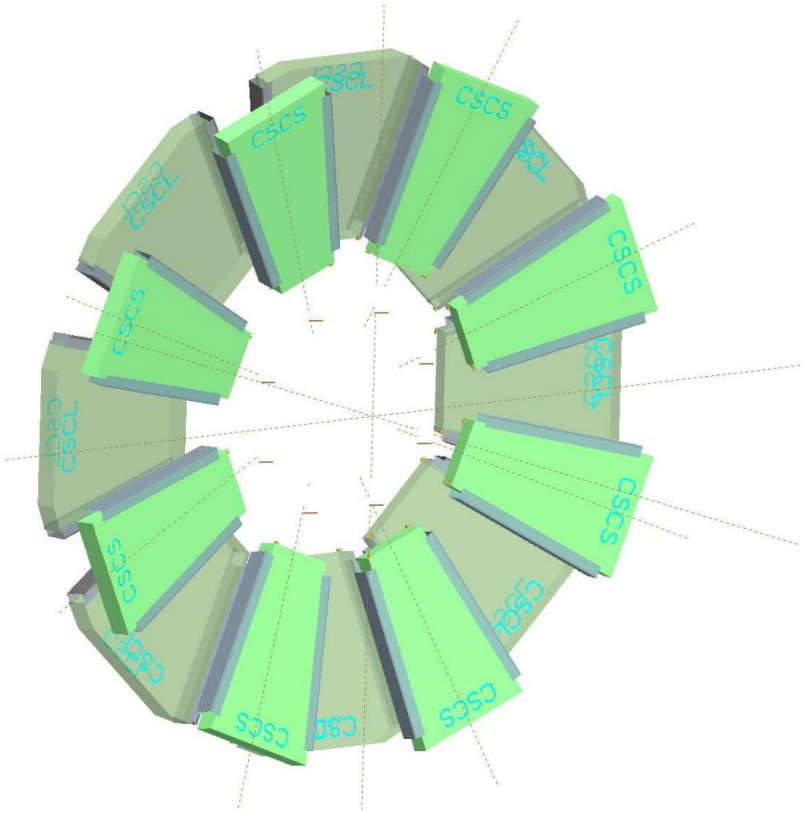

Figure 3.8: Each CSC wheel is made of 8 small and 8 Large sectors of 8 CSC layers each. THe cathode pitch is of 5.31 mm and 5.56 mm for the large and small chambers respectively [30].

where $N_1,\ N_2$ are the number of particles in each colliding bunch, N_b is the number of bunches per beam, and f_{rev} is the revolution frequency of the bunches. The denominator corresponds to the transverse area of the beam with σ_x and σ_y representing the root-mean-square transverse beam size at the collision point, and S is a geometric factor accounting for the crossing angle and finite bunch length [46].

To measure the instantaneous luminosity, the LHC experiments use dedicated detectors called luminometers. The ATLAS experiment relies on the measurements obtained from different types of luminometers in order to reduce measurement bias [57]. For the Run 2 period, the LUCID2 detector [58] provided the primary bunch by bunch luminosity measurement for ATLAS. It is a Cherenkov detector located on both sides of the interaction point at $z = \pm 17\ \mathrm{m}$. Complementary information is provided by the beam condition mon-

itor (BCM) [59] which is made of diamond sensors. The LUCID2 and BCM raw hit counts are converted into the visible rate per bunch crossing μ_{vis} which is itself proportional to the instantaneous luminosity [46]:

$$L = \frac{\mu_{vis} f_{rev}}{\sigma_{vis}} \tag{3.5}$$

where σ_{vis} is a calibration constant corresponding to the visible cross-section. The calibration is performed each year during special LHC runs using van der Meer (vdM) scans [60]. During a van der Meer scan, the overlap of the two beams in the $x - y$ plane is scanned to measure the relative interaction rates as a function of the transverse beam separation, and to measure the shape and size of the interaction region. During Run 2, the LHC maximum instantaneous luminosity achieved during data taking varied from 5 to $19 \times 10^{33}\ \mathrm{cm}^{-2}\,\mathrm{s}^{-1}$ [57].

Another important quantity for physics analyses is the *integrated luminosity* which is simply $\mathcal{L} = \int L dt$, where the instantaneous luminosity is integrated over the full data taking period. During the Run 2 data taking period, the LHC delivered 156 fb^{-1} , 147 fb^{-1} of which were recorded by the ATLAS detector. Not all recorded data is dedicated to proton-proton physics analyses and a total of 139 fb^{-1} of data are used in this thesis.

3.4 Trigger system

The LHC 40 MHz collision rate corresponds to a bunch crossing every 25 ns. Recording the raw data for each bunch crossing would correspond to a rate of roughly 60 $\mathrm{TB/s}$ which is not technically possible both in terms of output bandwidth and storage space. Furthermore, not all bunch crossings produce interesting high energy particles and the ATLAS detector only records events showing specific signatures. The ATLAS trigger [62] is the system that selects in real time the events to be recorded. It is split into two levels: the Level 1 trigger (L1) and the High Level Trigger (HLT). The trigger path runs in parallel to the regular data acquisition path as shown in Figure 3.9. The full detector data is

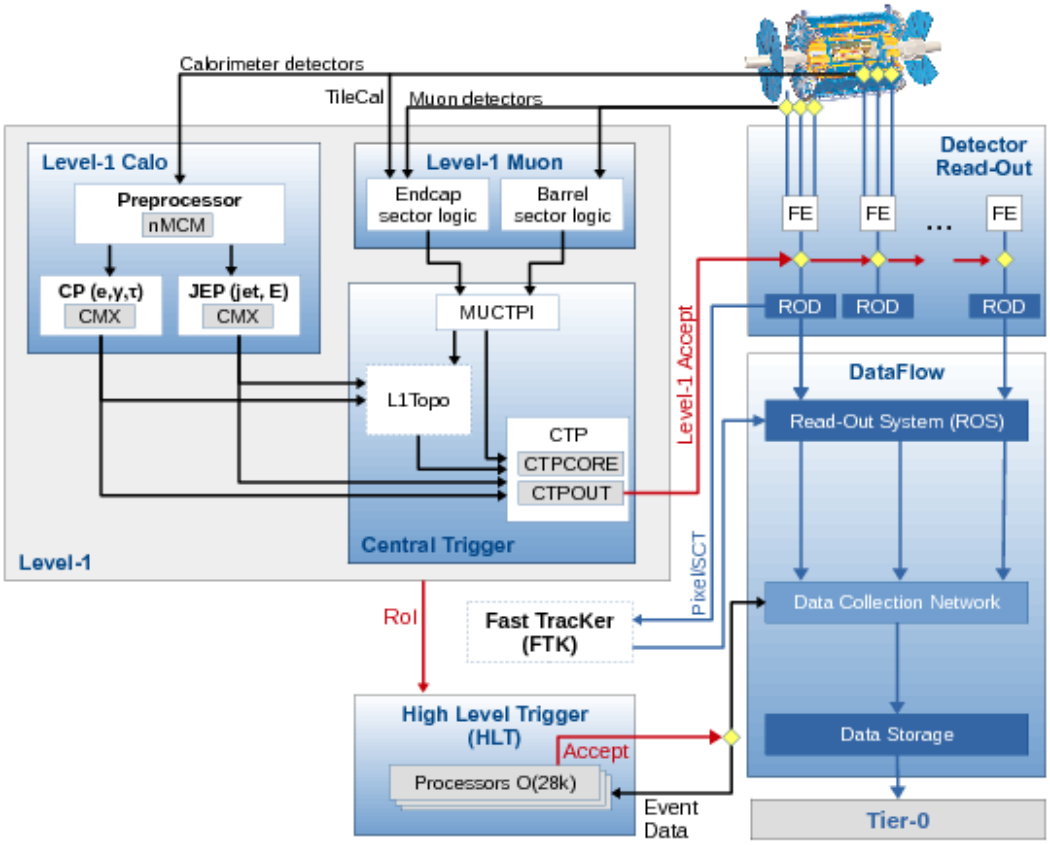

Figure 3.9: Schematic layout of the ATLAS trigger and data acquisition system in Run 2 [61].

buffered until the trigger reaches a decision, at which point the raw detector information sent to permanent storage.

The L1 trigger system is a hardware based trigger built with fast custom-made electronics. It uses information from the calorimeters and muon spectrometers to find potential Regions of Interest (RoI). The L1Calo looks for regions with high energy deposits in the EM calorimeter and the L1Muon independently searches for coinciding hits in the muon RPC and TGC that are compatible with a muon coming from the interaction point. If a region of interest is found, the L1 trigger system sends an accept command and the RoI characteristics to the HLT for further processing. This is done within 2.5 µs of the bunch

crossing and the event rate is reduced to 100 kHz.

The HLT is a software based trigger running on a farm of of-the-shell CPUs on the surface above the ATLAS detector. The HLT uses information from the inner detector, calorimeters and muon spectrometers to reconstruct more complex objects, such as tracks,in order to identify the type of physics objects produced (electron, jet, etc...) and to estimate their transverse energy. The decision making process follows a list of selection and decision chains defined in the trigger menu. The trigger menu can be updated between LHC runs and contains chains targetting various physics processes but also chains used for calibration and detector performance measurements. The HLT reduces the incoming L1 trigger rate to approximately 1 kHz and processes events within 200 $\mu\mathrm{s}$.

Chapter 4

Object reconstruction

The reconstruction of the various physics objects from detector signals is a crucial part of any ATLAS analysis. Depending on their properties, the particles created in the proton-proton collisions will leave specific signatures in the different sub-systems of the ATLAS detector, which are used for particle identification. Figure 4.1 gives an overview of the typical signatures left by particles in the ATLAS detector. The raw signals coming from the detector are combined using dedicated algorithms to recreate tracks and energy deposits as described in Section 4.1. Interaction vertices can then be reconstructed, followed by particle identification. This section will describe the different steps involved in the reconstruction of photons & electrons (Section 4.2), muons (Section 4.3), jets[1] (Section 4.4) and missing transverse energy $E_{\mathrm{T}}^{\mathrm{miss}}$ (Section 4.5). Note that since taus (τ) are not used in this thesis, their reconstruction process is not described.

4.1 Intermediate objects

Tracks and energy clusters are the first building blocs of the reconstruction process. These intermediate objects will be used for the reconstruction of the various physics objects.

[1] Jets are collimated bunches of hadrons created by the hadronization of quarks and gluons.

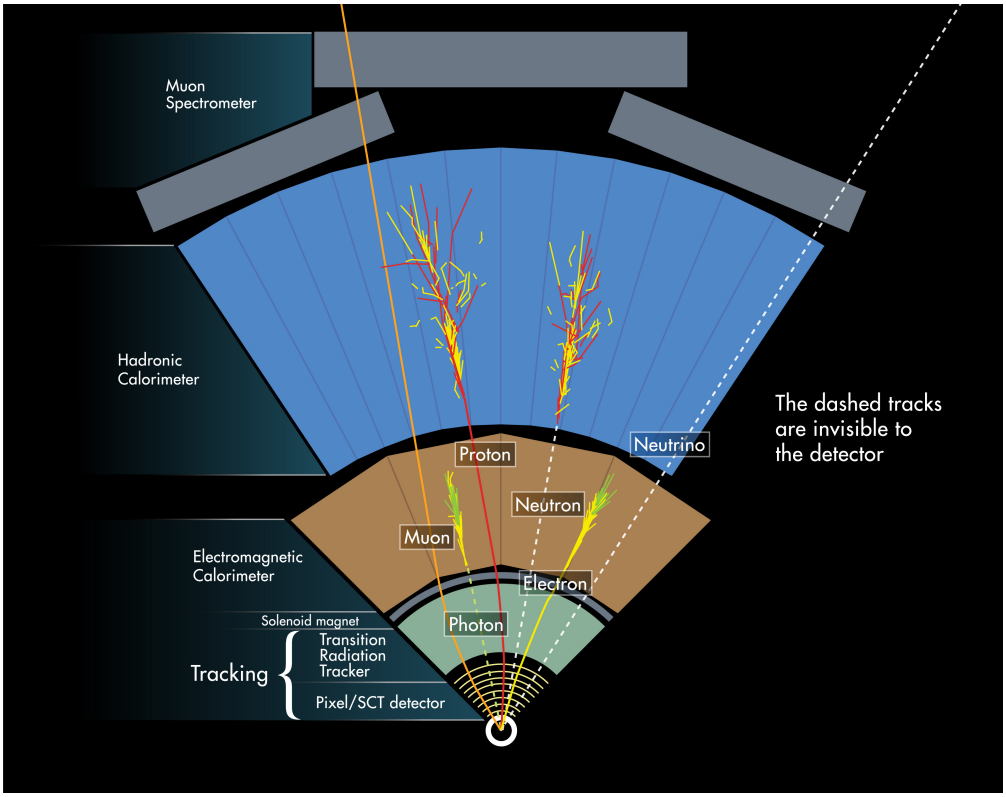

Figure 4.1: Schematic diagram representing the different signatures expected from different types of particles travelling through the ATLAS detector sub-systems. [63]

4.1.1 Inner detector tracks

Charged particle trajectories are reconstructed from the pixel and SCT detectors in four main steps: clusterization, track finding, ambiguity solving and precision fitting. In the first step, clusters are created by grouping adjacent pixels or strips sensors that recorded deposited energy above threshold. In the Run 2 dense environment, the typical distance between particles is only a few pixels so clusters can correspond to several particle hits [64]. A cluster 3D position is referred to as *space-point*. Track candidates are then computed using an iterative process starting with seeds of three space points. Plausible seeds are extrapolated using a Kalman filter [65] to add space-points to the track candidates. Next, track candidates are ranked according to their quality using a track score based on: number of hits and χ^2 fit of the track. Ambiguous or overlapping tracks with the lowest score are dropped. Higher momentum tracks are kept over low momentum ones and only the tracks satisfying basic requirements such as $p_T > 400$ MeV (for an assumed pion

mass), and a minimum of 7 pixel and SCT clusters within $|\eta| < 2.5$ are kept. Finally, a high resolution fit of the track is performed in which the position and uncertainty of each cluster is determined using a neural network [64].

4.1.2 Vertices

Several proton-proton interactions can occur in the same bunch crossing. Vertex reconstruction is the process in which tracks are grouped according to their point of origin. The vertex with the highest p_{T} tracks is called the Primary Vertex (PV) and the other vertices are considered coming from pile-up[2] events. Only good quality tracks are considered for vertex reconstruction. They must satisfy the following requirements to be added to the track pool [66]:

- $p_{\mathrm{T}} > 400$ MeV and $|\eta| < 2.5$.
- At least 9 silicon hits if $|\eta| \leq 1.65$ or 11 hits if $|\eta| > 1.65$.
- At least 1 hit in the IBL.
- A maximum of 1 shared module (1 shared pixel hit or 2 shared SCT hits).
- Zero pixel holes and a maximum of 1 SCT hole (missing a hit in a ID layer).

The reconstruction is then done in two stages: vertex finding and vertex fitting [67]. First a seed position for the vertex is defined. The tracks and seed are then used to estimate the vertex position via an iterative fitting procedure. During the fit, the tracks are weighted and the less compatible tracks are given less impact. Once the vertex position is defined, incompatible tracks are removed and allowed to be used for other vertices. The procedure is repeated for the remaining tracks in the event. All vertices with at least two associated tracks are kept as valid primary vertex candidates.

[2] In one proton bunch crossing, several proton collisions happen. The collision with the highest transverse energy is taken as the hard scatter and all the other collisions constitute pile-up.

4.1.3 Calorimeter clusters

The fine segmentation of both the electromagnetic and hadronic calorimeters enables three-dimensional reconstruction of particle showers. Two different algorithms are used to construct clusters from the raw energy deposits: the sliding-window method [68], used mostly to reconstruct electromagnetic showers and the topological method, used mostly to reconstruct hadronic showers [69].

Sliding-window clusters

In this method, calorimeter clusters are seeded using a sliding window of 3×5 cells in $\eta \times \phi$, looking for energy deposits exceeding 2.5 GeV in the EM calorimeter [68]. It is used by default for electron and photons reconstruction. The EM calorimeter is divided into a grid of 200×256 towers in $\eta \times \phi$ which corresponds to a cell size of $\Delta\eta \times \Delta\phi = 0.025 \times 0.025$. The fixed cluster size allows for precise energy calibration. If two cluster candidates are too close, the candidate with the highest transverse energy is kept. The cluster reconstruction efficiency is above 99% for deposited transverse energy E_{T} greater than 15 GeV.

Topological clusters

Topo-clusters are seeded by high energy cells where $|E|$ exceeds the expected noise by four times its standard deviation. The cluster is then expanded both laterally and longitudinally by adding all the adjacent cells with $|E| > 2\sigma_{\mathrm{noise}}$. Finally all neighbouring cells surrounding the proto-cluster are added. This is followed by a potential splitting step where at most two local energy maxima are separated into two different clusters. This algorithm is designed to separate showers of different nature (electromagnetic vs hadronic).

Calorimeter cluster calibration

Cell-level calibration constants are applied to raw calorimeter cell signals to convert the amplitude of the signal into units of energy (GeV). These cell-level calibration constants were measured in test beam and are defined with respect to the calorimeter response to

electron/photons [70]. The total energy of an electromagnetic cluster is the sum of the energy from each cell belonging to the cluster. The ATLAS calorimeters are however non-compensating, i.e. the signal recorded as a result of a hadronic shower is lower than that recorded from an electromagnetic shower of the same energy. Hadronic showers used as a basis for jet reconstruction span both the electromagnetic and hadronic calorimeters. As a result, the energy of these clusters must be further calibrated to the so-called jet energy scale.

To do so, a cluster-level calibration correction is derived using Monte Carlo (MC) simulations of single pions. It is done cluster by cluster and accounts for the non-compensating calorimeter response but also for potential signal loss during the clustering procedure and signal loss in passive materials.

4.2 Photons & electrons

Electrons and photons produce similar electromagnetic showers in the EM calorimeter; their reconstruction is therefore run in parallel [71,72].

Electrons

Electron candidates are created by matching electron-track candidates with EM cluster seeds as shown in Figure 4.2. Electrons are likely to radiate bremsstrahlung photons and their track reconstruction uses a special algorithm, the Gaussian Sum Filter (GSF) [73] which allows for up to 30% energy loss at each intersection with the detector material. Once a track is matched to a cluster seed, the cluster is extended to a window size of 3×7 in $\eta \times \phi$ (or 5×5 in the end-caps) and the energy of the cluster is further calibrated to correspond to that of an electron using multivariate techniques [70]. The track candidate must point to the primary vertex for the object to be considered as an electron. For E_{T} > 15 GeV, the electron reconstruction efficiency ranges from 96% to 99% for $|\eta| < 2.47$ [71].

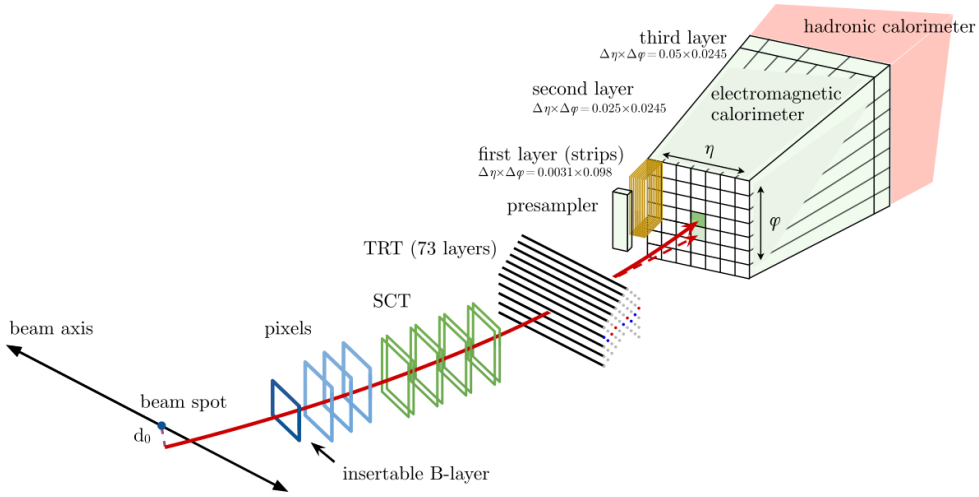

Figure 4.2: Schematic diagram showing an electron path through the different detector sub-systems. The electron first traverses the tracking system (pixel, SCT and TRT detectors) and then enters the electromagnetic calorimeter. The dashed trajectory indicates the path of a radiative photon produced by the interaction of the electron with the detector material. The radiated photon energy will be associated to the electron's EM calorimeter cluster. [71]

Photons

Photons are 50% likely to convert into electron-positron pairs before reaching the EM calorimeter and their reconstruction has to take into account all possible photon conversion scenarios. Tracks loosely matched to calorimeter clusters are used as input for conversion vertex reconstruction. Both tracks with silicon hits (Si tracks) and tracks reconstructed only in the TRT (TRT tracks) are used; one or two tracks can point back to the conversion vertex. Calorimeter clusters with no matching conversion vertex candidate nor associated tracks are considered to be unconverted photon candidates. The final step is to resolve any potential ambiguities on the object's nature, i.e. whether the reconstructed object should be identified as a photon or an electron. In cases where a calorimeter cluster belongs to both a converted photon and electron candidate, an arbitration based on the track and vertex quality is performed to decide the final type of the reconstructed object.

The photon reconstruction efficiency $\epsilon = \frac{n^{reco}}{n^{true}}$ using the Tight ID criteria [72] varies from from 45-60% at $E_T = 10$ GeV to 95-98% for $E_T > 100$GeV, depending on the photon's pseudorapidity region conversion status.

4.3 Muons

Muon track reconstruction is first performed independently in the Inner Detector (ID) and Muon Spectrometer (MS) detectors before being combined [74]. In the ID, the muon tracks are reconstructed as described in Section 4.1.1.

In the MS, the search for hit patterns is done separately in the different muon sub-systems with dedicated algorithms that produce track *segments*. Segments that are loosely matched with the interaction point are combined into track candidates. The combination process starts with the segments from MS middle stations, then adding segments from the outer and inner stations. In the barrel region, at least two matching segments are required to build a track candidate and at least one segment is required in the end-cap regions. The track candidates obtained are then fitted using a global χ^2 fit.

From there, information from the ID, calorimeters and MS can be combined to define four muon types:

- Combined (CB) muons are the default and most accurate type of reconstructed muons. The CB track is obtained by re-fitting the combined hits from both the ID and MS sub-detectors.

- Segment-tagged (ST) muons are used at low p_{T} or in case the muon falls into a region of reduced MS acceptance. An ID track is reconstructed as muon if it can be associated with at least one local track segment in the MDT or CSC detectors.

- Calorimeter-tagged (CT) muons are defined in the MS crack region for $|\eta| < 0.1$ and for $15 < p_T < 100$ GeV. An ID track is reconstructed as muon if it can be matched with a MIP compatible cluster in the calorimeters.

- Extrapolated (ME) muons are used to increase the muon acceptance onto the region $2.5 < |\eta| < 2.7$ which is not covered by the ID. MS tracks are required to match loosely the interaction point. Two MS layers are required to provide track measurements in the barrel and three layers are required in the forward region.

To be considered a prompt muon, candidates are required to pass additional selection criteria on variables offering good discrimination between prompt muons and background muons (mainly from pion and kaon decays). Three different working points are defined: Loose ID with a reconstruction efficiency of 98.1% for prompt and 0.76% for fake muons, Medium ID with an efficiency of 96.1% for prompt and 0.17% for fake muons, and finally Tight ID with an efficiency of 91.8% for prompt and 0.11% for fake muons. Muons used in this analysis have to pass the medium ID selection.

4.4 Jets & *b*-tagging

4.4.1 Jets

Jets are collimated bunches of stable hadrons created by the hadronization of quarks and gluons. Two different jet reconstruction algorithms are used in ATLAS and are described in this section.

Topo jets

Jets are traditionally reconstructed by first defining topological clusters in the calorimeters and by then combining the clusters into jet objects using the anti-k_T algorithm [75] with a distance or radius parameter $R = 0.4$. The anti-k_T algorithm is an iterative procedure in which the energy clusters are associated to form jets. It relies on d_{ij} the distance between two clusters, and the the distance d_{iB} between the i-th cluster and the jet axis (B):

$$d_{ij} = \min\left(k_{T,i}^{-2}, k_{T,j}^{-2}\right)\frac{\Delta_{ij}}{R} \quad (4.1)$$

$$d_{iB} = k_{T,i}^{-2} \quad (4.2)$$

with $k_{T,i}$ the transverse momentum of cluster i, and $\Delta_{ij}^2 = (\gamma_i - \gamma_j)^2 + (\phi_i - \phi_j)^2$ the distance between the two clusters in the rapidity $\times$ azimuthal angle space. At each iteration, the two distances are computed and compared: if $d_{iB} < d_{ij}$, the cluster i is considered as a belonging to a new independent jet and is removed, if $d_{iB} > d_{ij}$ the i-th cluster is merged into the jet. Once jets are reconstructed, they need to be cleaned and calibrated as described in Section 5.3.1 before being used for analysis.

Particle flow jets

The topo jets defined above only use calorimeter information but data from the ID can be used in complement to define *pFlow* jets [76], which are the jets used in this analysis. In a pFlow jet, the calorimeter energy deposits due to charged hadrons of $p_T < 40$ GeV are removed from the topo cluster set used for jet reconstruction. The momenta from the removed particles is instead estimated from their tracks in the ID. To be removed, clusters must be matched with a good quality track coming from the Primary Vertex (PV) and not identified as a muon or electron. If the matched track does not come from the PV, the corresponding object is considered as originating from a pile-up collision and removed entirely before the jet reconstruction starts. Once all candidate tracks have been treated, the remaining topo clusters and the matched good tracks are associated into jets using the same anti-k_T algorithm as for topo jets. For low-energy charged particles, the momentum resolution of the tracker is significantly better than the calorimeter energy resolution, therefore the pFlow algorithm overall improves the jet energy and angular resolution. It also extends the detector acceptance to softer particles with a minimum transverse momentum of $p_T > 400$ MeV. Once the jets are reconstructed, the remaining pile-up from neutral hadrons and out of time events is removed using the jet-area method [77].

4.4.2 *b*-tagging

Jets coming from the decay of a b-quark are referred to as b-jets and are identified through a process called b-tagging. Various algorithm can be used to identify b-jets. They rely on the long lifetime, high mass and high decay multiplicity of b-hadrons. b-hadrons typically

travel about 3 mm before decaying, resulting in a displaced secondary vertex detectable in the ID. The ATLAS b-tagging procedure uses a two stage approach [78]. First, low level algorithms are used to reconstruct the characteristic features of b-jets: the IP2D and IP3D [79] algorithms use the large impact parameters of b-jet tracks, the SV1 [80] algorithm reconstructs explicitly the secondary vertices and finally the JETFITTER [81] algorithm reconstructs the full b-hadron to c-hadron decay chain. The results of these algorithms are then combined using high level, machine learning based, algorithms that yield as output the probability of a jet coming from a b-hadron decay or not. The algorithm used in this analysis is the DL1 [79] algorithm. It uses a deep neural network and has a multidimensional output corresponding to the probabilities for a jet to come from a b decay, a c decay, or to be a light-flavour jet. Using the output probabilities, several working points are defined, corresponding to a certain b-jet tagging efficiency: 60%, 70%, 77% and 85% b-jet tagging efficiencies. This analysis uses the 77% working point. It corresponds to a rejection factor of 4.9 for c-jets, 15 for τ-jets , and 110 for light flavoured jets.

4.5 Missing transverse momentum

Undetectable particles such as neutrinos (ν) go through the entire ATLAS detector without interacting and do not leave any direct signal. Their potential production in the hard scatter can only be deduced indirectly from missing transverse momentum ($E_{\mathrm{T}}^{\mathrm{miss}}$) in a fully reconstructed collision event. Transverse momentum is a conserved quantity and its sum for all particles coming from a given proton-proton collision is expected to be zero as the colliding protons have no transverse momentum. When significantly different from zero, $E_{\mathrm{T}}^{\mathrm{miss}}$ indicates that undetectable particle(s) have been produced. In ATLAS, $E_{\mathrm{T}}^{\mathrm{miss}}$ is reconstructed from two contributions [82]:

- The reconstructed and calibrated particles from the hard scatter: electrons, photons, τ-leptons, jets and muons.
- The soft-events signals reconstructed from low energy tracks associated with the hard scatter vertex.

Note that particles coming from pile-up events should not be taken into account.

A key step in $E_{\mathrm{T}}^{\mathrm{miss}}$ reconstruction is the signal ambiguity resolution: since particles are reconstructed independently, the same energy deposits can be associated to several different physics objects, yet only one should be used to avoid double counting. A rejection procedure is applied: electrons are taken into account first, followed by photons, then τ-leptons, then jets and finally muons. Objects overlapping with the previous category are discarded. For final states with neutrinos, the $E_{\mathrm{T}}^{\mathrm{miss}}$ resolution has been measured using $W \to l\nu$ Monte Carlo (MC) simulations and show a reconstructed resolution of $E_{\mathrm{T}}^{\mathrm{miss}}$ ~ 15 GeV to 20 GeV for a true $E_{\mathrm{T}}^{\mathrm{miss}}$ range of 0 to 500 GeV.

Chapter 5

Object and event Selection

This chapter describes the event selection criteria specific to the $W\gamma\gamma$ measurement. The overall workflow used to select the final events used in this analysis is summarised in Figure 5.1. The first step, not shown in the diagram, was to define the analysis strategy, which is described in Section 5.1. It is a crucial step in order to then define the data, MC simulation and triggers to use, which are described in Section 5.2. Identifying the sources of background is also required in order to define the object and event selection defined in Section 5.3.

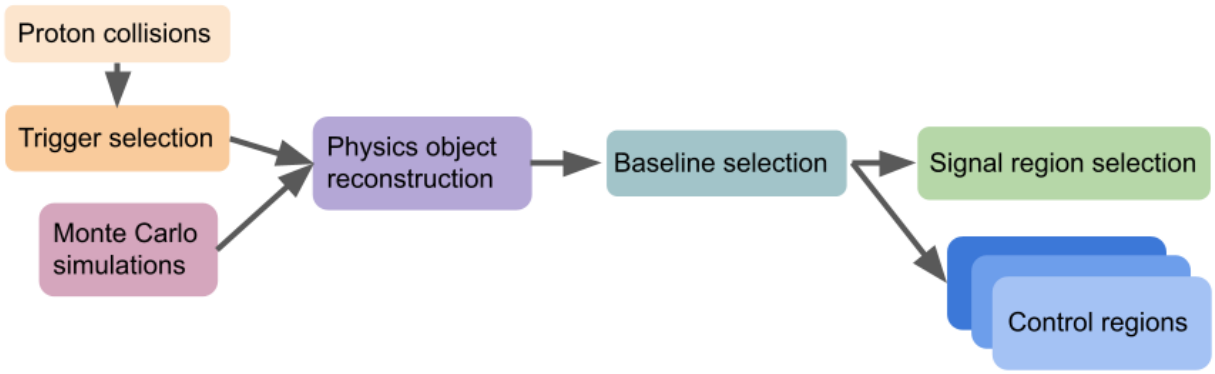

Figure 5.1: General event selection workflow. The physics object reconstruction is common to all ATLAS analysis and has been covered in Chapter 4.

5.1 Analysis strategy

The goal of the analysis presented in this thesis is to measure the tri-boson $W\gamma\gamma$ production cross-section in proton-proton collisions: $pp \to W\gamma\gamma$. To do so, the process is studied in the W electron and muon decay channels: $pp \to W(\to e\nu)\gamma\gamma$ and $pp \to W(\to \mu\nu)\gamma\gamma$. Although the W boson leptonic branching ratios are smaller than its hadronic branching ratio, leptonic decays were chosen as they result in event final states that offer a much better background discrimination power than hadronic decays. The reconstruction of tau particles being more complex and resulting in worse signal-to-background ratio, the process $pp \to W(\to \tau\nu)\gamma\gamma$ is treated here as a background. Signal events of interest are therefore expected to contain at least two isolated photons, one electron or muon, and a significant amount of missing transverse energy ($E_{\mathrm{T}}^{\mathrm{miss}}$) associated with the production of a neutrino in the W decay. For simplicity, electrons and muons are collectively referred too as *leptons* in the rest of this thesis, following the convention typically used within the ATLAS collaboration. Neutrinos (ν) and tau particles (τ) will be explicitly named when required.

As the $W\gamma\gamma$ tri-boson production is rare, the challenge of this analysis is to achieve a sufficient level of discrimination between signal and background. Many background processes, listed in Table 6.1, can result in event signatures in the ATLAS detector that are similar to the signature expected from true signal events. The first step to reduce background contributions is to define an appropriate signal region (SR) using appropriate selection criteria applied to reconstructed objects and the event as a whole. This analysis step is presented in the current chapter. Section 5.2 first introduces the dataset used for the analysis. Then Section 5.3 details the selection process used to identify the final state object of interest in the data. Finally, signal region, optimised to maximise the signal over background ratio is defined in Section 5.3.4.

Even after carefully optimized event selection is applied, some background events are still present in the signal region. To extract a signal yield, the number of background events

is estimated as described in Chapter 6. While some sources of background are estimated from simulated data, others are estimated directly from the data set. To do so, various kinematical control regions (CRs) are defined, some are used to estimate the contribution of different background sources, others are used to verify the estimated background contributions.

Finally, the estimation of uncertainties on the object reconstruction efficiencies, background estimations, statistical fluctuation is then needed to estimated the precision of the final result and is described in Chapter 7. The final cross-section extraction procedure and result is given in Chapter 8.

5.1.1 Blinding procedure

During the development of the analysis framework the data is *blinded* to avoid any human biases. The blinding procedure applied in this analysis has two requirements:

- The ATLAS data in the signal region is not looked at.
- Data-driven background estimation methods using control regions overlapping with the signal region (e.g. 2D template fit method for fake photon estimation) use only half of the data in the sensitive control regions.

Note that however, the full available Monte Carlo simulations are used and all data is used in control regions which are orthogonal to the signal region.

At the time of writing, the analysis is still blinded. This unblinding procedure will be carried out in the coming months with the approval of the ATLAS collaboration.

5.2 Dataset definition

5.2.1 Data

This analysis uses proton-proton collision data recorded at $\sqrt{s} = 13$ TeV by the ATLAS detector between 2015 and 2018, referred to as the Run 2 dataset. Before being used for physics, ATLAS data is checked for potential hardware or software issues through the monitoring of detector-level quantities and event characteristics. A total of 95.6% of the recorded data from 2015 to 2018 satisfies the standard data quality requirements [83]. The total good quality data used in this analysis corresponds to an integrated luminosity of 139 fb^{-1} , measured with a global 1.7% uncertainty [57]. During Run 2, the average number of pile-up interactions varied from $\langle\mu\rangle = 20$ in 2015-2016 to $\langle\mu\rangle = 38(37)$ in 2017(2018).

5.2.2 Trigger selection

Signal trigger

As discussed in Chapter 3 the ATLAS experiment does not record all proton-proton collisions but only a fraction that are deemed interesting for physics analysis, or for monitoring purposes. What is interesting for different analyses can vary greatly and ATLAS possesses a wide range of triggers optimised to select a variety of different types of events. Event selection therefore starts with the choice of a set of trigger selection criteria that will determine data to be further analysed. Combined triggers are used for this analysis: they require the signature of several particles at the same time, in our case two photons and one lepton. The advantage of requiring the simultaneous presence of several physics objects at the trigger level is that the required minimum energy threshold on each physics object can be chosen to be quite low due to lower rate of background events satisfying complex trigger signatures. Two sets of trigger selection criteria are used for this analysis, one for each of the leptonic decay channels of the W boson:

- The $\mu\gamma\gamma$ trigger section requires the presence of at least two photons of energy greater than 10 GeV along with at least one muon of energy greater than 20 GeV.

- The $e\gamma\gamma$ trigger selection varied slightly during the Run 2 data taking period. In 2015-2016, the $e\gamma\gamma$ trigger selection required the presence of at least two photons with energy greater than 10 GeV along with an electron of energy greater than 20 GeV. In 2017-2018, the minimum photon energy requirement was increased to 12 GeV.

Control regions

The control region used for the data-driven estimate of the jets misidentified as electrons or muons (Section 6.4) requires a different set of events and the following set of triggers are used as well:

- For the muon channel, the lowest energy, Loose ID, single muon trigger is used. In 2015 the energy threshold was at 20 GeV and for 2016-2018 the threshold was increased to 26 GeV due to the increase in luminosity.

- For the electron channel, Medium trigger ID are used with a threshold of 24 GeV in 2015 and 26 GeV in 2016-2018.

The detailed list of all triggers used is given in Appendix A.

5.2.3 Event simulations

Simulated events are used in this analysis to optimise the event selection, determine the kinematic distributions of the expected signal and some of the background sources, and to estimate the uncertainty on these distributions. The data-driven background estimations also require some input from simulations datasets.

In each LHC proton-proton collision, hundreds of particles are typically produced and their momenta range over several orders of magnitude. The simulation of such complex processes is possible thanks to the factorisation of the simulation procedure which allows the treatment of the processes of interest into different regimes [84]:

- First, the Standard Model matrix elements are computed by an event generator for a given approximation scheme: leading order (LO), next-to-leading order (NLO), etc...

- Non-perturbative QCD processes are described with a phenomenological approach. The generation of parton showers and their hadronization into outgoing hadrons is done in this second step.

- The interaction of the particles with the detector material is simulated using the GEANT4 software [85]. The output of this simulation step results in simulated detector signals identical in format to real data.

- Finally physics objects are reconstructed using the algorithms described in Chapter 4 as is done in real data.

The detailed list of all simulated samples used for this analysis is given in Appendix B. It includes three different simulations of the $W\gamma\gamma$ signal process: two samples generated at next-to-leading order with the SHERPA [86] and MADGRAPH5_aMC@NLO [87, 88] (referred to as MadGraph) generators, and one last sample generated at leading order with SHERPA.

5.3 Event selection

All analysis objects must satisfy strict selection requirements to ensure they are compatible with the $W\gamma\gamma$ signal event signature and to minimize background contamination. A first baseline selection is defined to preselect the physics objects and events to be considered for further analysis. This first selection is quite inclusive in order to maximize signal event acceptance at this point of the analysis. As discussed in Chapter 4, the output from the ATLAS reconstruction algorithms may be sometimes ambiguous. Resolving identification ambiguities and removing overlapping objects is done in the baseline selection described in this section. The loose baseline selection is also used to reject certain backgrounds such as $Z\gamma\gamma$ which produces a second lepton that is not expected for

signal events. A second stricter selection is then applied to define the signal region (Section 5.3.4). In the signal region, physics objects considered in the analysis are required to pass a much tighter selection to suppress backgrounds from other processes such as fake photons or $t\bar{t}$ events. Finally, some of the background estimations described in Chapter 6 will be data-driven or normalised using data. Each background estimation method uses dedicated control regions defined from baseline objects and designed to be orthogonal to the signal region.

5.3.1 Object selection

This section describes the object level selection for photons, leptons, jets and $E_{\mathrm{T}}^{\mathrm{miss}}$ used in the analysis.

5.3.1.1 Photons

To pass the baseline selection, photons should have a transverse momentum greater than 20 GeV, be identified within the detector acceptance (see Table 5.2), and must satisfy the LoosePrime5 identification working point. Photon identification (ID) is based on a series of variables related to the calorimeter shower shapes and EM calorimeter strip variables which are listed in Table 5.1.

To pass the signal selection, baseline photons should pass the Tight ID selection and should be isolated. The photon isolation energy (E_{iso}) used here is computed using topo-clusters in the electromagnetic and hadronic calorimeters, defined with a cone radius of $R = 0.4$ by:

$$E_{\mathrm{iso}} = E_T^{\mathrm{topo,cone40}} - 0.022 \times p_T \tag{5.1}$$

This quantity represents the amount of activity in the calorimeter around the photon due to the passage of other particles. The isolation energy is used for the determination for the fake photon background described lated in Section 6.2. It is also used to define the isolation working point "FixedCutTightCaloOnly" used in this thesis which requires $E_{\mathrm{iso}} < 2.45$ GeV for a photon to be considered as tightly isolated. These photon cuts are

Variable name	Definition	LP5	Tight
Calorimeter variables:			
R_{had}	Ratio of E_T deposited in the first layer of the EM calorimeter compared to the energy in the first layer of the hadronic calorimeter.	✓	✓
R_η	In the middle layer of the EM calorimeter: energy ratio in the $3 \times 7(\eta \times \phi)$ cells to the 7×7 cells cluster.	✓	✓
R_ϕ	In the middle layer of the EM calorimeter: energy ratio in the $3 \times 3(\eta \times \phi)$ cells to the 7×3 cells cluster.	✓	✓
w_2	Lateral width on the shower (EM middle layer)	✓	✓
Strip variable:			
w_{s3}	Shower width for three EM calorimeter strips around maximum strip, using the energy weighted sum over the total energy contained in the three EM calorimeter strips.	×	✓
w_{stot}	Total lateral shower width determined with the energy weighted sum over cells in a window corresponding to the cluster size.	×	✓
F_{side}	Fraction of energy outside a core of 3 central EM calorimeter strips, but within 7 EM calorimeter strips	×	✓
ΔE	Difference between the energy of the strip with the second largest energy deposited and the energy of the strip with the smallest energy deposit between the two leading EM calorimeter strips	×	✓
E_{ratio}	Ratio of the energy difference between the largest and second largest energy deposits over the sum of these energies.	×	✓

Table 5.1: List of the variables used to identify photons. The Tight identification working point requires the photon to pass the cuts on all of these variables. The LoosePrime5 working point is a relaxed version of the Tight ID where the cuts on up to all five EM calorimeter strips variables are allowed to fail [72].

meant to reduce the non-prompt photon background coming from jets and pile-up. The baseline and signal photon selection is summarized in Table 5.2.

5.3.1.2 Leptons

As previously mentioned, *lepton* (l) refers here to either an electron (e) or a muon (μ). Leptons are selected in three stages: first they are first preselected with very loose cuts. The

Parameter	Photon	
	baseline	signal
Transverse momentum	$p_{\mathrm{T}} < 20$ GeV	
Pseudo rapidity	$\lvert\eta\rvert < 1.37$ or $1.52 < \lvert\eta\rvert < 2.37$	
Particle identification	LoosePrime5	Tight
Particle isolation	none	FixedCutTight

Table 5.2: Summary of the baseline and signal photon selection cuts

lepton transverse momentum should be greater than 6 GeV and the lepton track should be compatible with the primary vertex: $|z_0 \sin\theta| < 0.5$ mm, where z_0 is the longitudinal impact parameter[1]. For electrons, the LHLooseBL [71] identification (ID) working point is used along with the acceptance cuts: $\eta < 1.37$ or $1.52 < \eta < 2.37$. For muons, the ID working point used is medium [74] and the acceptance cut is $|\eta| < 2.4$.
Events with more than one preselected lepton are discarded to suppress the background from Z decays. Preselect leptons are used for overlap removal as described in Section 5.3.3.

Then baseline leptons are defined as preselect lepton with a higher p_{T} cut at 25 GeV. For electrons, the ID working point is tightened and the MediumLH [71] is used. Finally signal leptons are defined from baseline leptons by requiring them to be isolated and to have a transverse impact parameter significance of $|d_0|/\sigma_0 < 5$ for electrons and $|d_0|/\sigma_0 < 3$ for muons.

5.3.1.3 $E_{\mathrm{T}}^{\mathrm{miss}}$ & Jets

Jets are not part of the $W\gamma\gamma$ final state studied here, however they can constitute a source of background and their reconstruction is required for the computation of $E_{\mathrm{T}}^{\mathrm{miss}}$. The jets are reconstructed using the pFlow method and anti-k_T algorithm with a radius of $\Delta R = 0.4$. They are then calibrated using E_T and η dependent corrections derived from MC simulations [89]. Baseline jets are required to have a transverse momentum

[1]The impact parameter corresponds to the distance between the primary vertex of an event and the point of origin of a given particle's track. Its projection on the z-axis is the longitudinal impact parameter z_0 and its projection on the x-y plane is the transverse impact parameter d_0.

Parameter	Electron			Muon		
	preselect	baseline	signal	preselect	baseline	signal
Transverse momentum	$p_{\mathrm{T}} < 6$ GeV	$p_{\mathrm{T}} < 25$ GeV		$p_{\mathrm{T}} < 6$ GeV	$p_{\mathrm{T}} < 25$ GeV	
Pseudo rapidity	$\lvert\eta\rvert < 1.37$ or $1.52 < \lvert\eta\rvert < 2.47$			$\lvert\eta\rvert < 2.4$		
Transverse impact parameter	none		$\lvert d_0\rvert/\sigma_0 < 5$	none		$\lvert d_0\rvert/\sigma_0 < 3$
Longitudinal impact parameter	$\lvert z_0 \sin\theta\rvert < 0.5mm$			$\lvert z_0 \sin\theta\rvert < 0.5mm$		
Particle identification	LHLooseBL	MediumLH		medium		
Particle isolation	none		Tight	none		Tight

Table 5.3: Summary of the lepton selection cuts

$p_T > 20$ GeV and a pseudo rapidity $|\eta| < 4.5$. They are used in the physics object overlap removal procedure.

To suppress jets coming from pile-up events, signal jets have to pass additional Jet Vertex Tagger (JVT) requirements. The JVT is a multivariate discriminant based on associating the jets tracks to the primary vertex [90]. The JVT Tight working point is used which has an efficiency of 96%. Note that light-flavour jets are neither required nor excluded but a b-jet veto is applied in the signal region to reduce contributions from processes involving top quark decays. The jet selection criteria are summarised in Table 5.4.

Missing transverse energy ($E_{\mathrm{T}}^{\mathrm{miss}}$) is computed from calibrated electrons, muons, photons, jets and soft hadronic activity (charged-particle tracks not associated with the physics objects) [91]. Missing transverse energy of at least 25 GeV is required to select events likely to have a neutrino from the leptonic W decay. The corrections applied to the analysis objects (leptons, photons, jets) are taken into account for the $E_{\mathrm{T}}^{\mathrm{miss}}$ computation. The $E_{\mathrm{T}}^{\mathrm{miss}}$ is reconstructed before physics object overlap removal is applied using the METMaker tool [92].

Parameter	Jet	
	baseline	signal
Transverse momentum	$p_{\mathrm{T}} < 20$ GeV	
Pseudo rapidity	$\lvert\eta\rvert < 4.5$	
Jet Vertex Tagger	none	pass

Table 5.4: Summary of the baseline and signal Jet and $E_{\mathrm{T}}^{\mathrm{miss}}$ selection cuts

Particles overlapping	**conditions**	**particle kept**
Photon - electron/muon	$\Delta R < 0.4$	electron/muon
Electron - jet	$\Delta R < 0.2$ $0.2 < \Delta R < 0.4$	electron jet
Muon - jet	$\Delta R < 0.4$ & $N_{tracks}^{jet} < 3$ or $\Delta R < 0.2$ $\Delta R < 0.4$ & $N_{tracks}^{jet} \geq 3$	muon jet
photon - jet	$\Delta R < 0.4$	jet

Table 5.5: The ATLAS experiment overlap removal procedure. The steps are carried out in order of appearance, from top to bottom of the table.

5.3.2 Overlap removal

Physics object overlap removal addresses the challenges of object duplication and isolation. The ATLAS reconstruction process can sometimes create several different types of physics objects from the same energy deposits, resulting into two very close by objects at analysis level (duplication). To avoid double counting these objects, an overlap removal procedure is applied. This procedure also deals with cases of two separate but close-by objects (isolation) [93].

The ATLAS recommended removal procedure is applied using the standard approach described in: [94]. Objects taken as input are pre-selected leptons and baseline photons and jets. The cuts are summarized in Table 5.5 and are applied depending on the geometrical proximity of objects define as ΔR, using the value of rapidity y of the objects: $\Delta R = \sqrt{(\Delta\phi)^2 + (\Delta y)^2}$.

5.3.3 Baseline selection

The baseline event selection is meant to preselect signal-like events. It is used as input to define the signal region and various control regions as well as to carry out various studies of the selection efficiency. Selected $W\gamma\gamma$ event candidates must contain at least two baseline photons, exactly one baseline electron or one muon. The lepton and two photons must be matched to the same type of physics object as identified by the trigger system. Sufficient missing transverse energy should be present as well: $E_{\mathrm{T}}^{\mathrm{miss}} > 25$ GeV. Additional cuts are added to select events with a W boson and to veto events coming from a Z boson decay. A b-jet veto is applied to reduce the background from $t\bar{t}$ decays. The event level cuts defining the $W\gamma\gamma$ baseline selection are summarized in Table 5.6

Physics objects:	Baseline selection	Signal selection
Photon	≥ 2 baseline	2 signal photons
Lepton	exactly 1 baseline	1 signal lepton
$E_{\mathrm{T}}^{\mathrm{miss}}$	> 25 GeV	″
b-jets	no requirement	$n_{b-jet} = 0$
W boson	$m_T^W > 40$ GeV	″
Z veto:	$p_T^{l\gamma\gamma} < 30$ GeV	″
	$m_{l\gamma\gamma} \notin [81, 100]$ GeV	
	$m_{l\gamma_1} \notin [81, 100]$ GeV	
	$m_{l\gamma_2} \notin [81, 100]$ GeV	
Overlap removal:	$\Delta R_{\gamma,\gamma}$, $\Delta R_{\gamma,jet}$, $\Delta R_{\gamma,l}$, $\Delta R_{jet,l} < 0.4$	″

Table 5.6: The $W\gamma\gamma$ baseline and signal selections.

5.3.4 Signal region selection

The signal region (SR) is defined as the subset of the baseline selection which has the highest signal purity while keeping reasonable statistics. From the baseline selection described in Table 5.6, cuts on the photons and leptons are tightened, requiring them to satisfy their

respective signal object selections. If more than 2 baseline photons are present, the 2 highest p_{T} photons are kept as signal photons. If an event contains both a signal electron and a signal muon, the event is discarded. A b-jet veto is applied to reduce the contributions from top quark backgrounds, as top quarks mostly decay as $t \to bW$.

Chapter 6

Background estimation

Even after the strict signal selection, some background events will still end up in the signal region. In order to extract the number of signal events in the signal region, all sources of background listed in Table 6.1 must be precisely estimated. While some can be simulated, other are poorly modelled and must be estimated using data-driven techniques.

Three types of backgrounds are estimated using data-driven methods. First, hadronic jets misidentified as photons are estimated using a 2D template fit method described in Section 6.2. They constitute the largest source of background. Then hadronic jets can also be misidentified as electrons or muons (referred to as fake leptons) and the estimation of this source of background is described in Section 6.4. Finally the pile-up background, where one or both photons come from separate hard scatters in the same bunch crossing is estimated in Section 6.3.

Other backgrounds are estimated using Monte Carlo (MC) simulation and described in Section 6.1. Note that two backgrounds have to be normalised using data control region (CR)[1] as the uncertainty on their cross section is large: the processes involving top quarks ($t\bar{t}$, $t\bar{t}\gamma$ and $tW\gamma$) which represent the second largest background, and the $Z\gamma$ background that consists mostly of leptons misidentified as photons.

[1]Control Regions and Validation Regions are regions of phase space defined in such a way as to contain events with similar characteristics to the Signal Region but containing different events.

Background	Final state	How it can misidentified as signal
Jets	$W\gamma + j$ $E_{\mathrm{T}}^{\mathrm{miss}} + j + \gamma\gamma$	Fluctuations in jet shape and size can lead a jet to be misidentified as an electron/muon or a photon resulting in an event signature similar to signal events. Several final states are possible.
Pile-up	$W(l\nu)\gamma + \gamma_{\mathrm{pile-up}}$	One reconstructed photon originates from a different in-time proton-proton collision (pile-up).
$Z\gamma$	$l\bar{l}\gamma$	One of the Z leptonic decay products is misidentified as a photon. Various sources of object misreconstruction lead to the presence of $E_{\mathrm{T}}^{\mathrm{miss}}$.
$Z\gamma\gamma$	$l\bar{l}\gamma\gamma$	One of the Z leptonic decay products is not reconstructed of falls outside of the detector acceptance, leading to $E_{\mathrm{T}}^{\mathrm{miss}}$.
$t\bar{t}$ $t\bar{t} + \gamma$	$l\nu l\nu bb$ $(+\gamma)$, $l\nu jjbb$ $(+\gamma)$, $jjjjbb$ $(+\gamma)$	Jets can be misidentified as photons or leptons, and electrons can be misidentified as photons. One or two real photons can also be radiated from charged particles produced in this process.
$tW\gamma$	$l\nu bl\nu\gamma, jjbl\nu\gamma$	Similar mechanisms at mimicking signal events as described for the $t\bar{t}$ process.
WW, WZ, ZZ	$l\nu l\nu, l\nu ll, llll$	Diboson processes can have leptons misreconstructed as photons and some of the final state particles can fall outside of the detector acceptance leading to sizeable values of $E_{\mathrm{T}}^{\mathrm{miss}}$, and photons can be radiated from charged particles in the event.
$W(\tau\nu)\gamma\gamma$	$l\nu\nu\gamma\gamma, \nu jj\gamma\gamma$	Tau leptons can decay leptonically and in that case the event final state is almost identical to signal. In the case of tau hadronic decay, a jet can fake signal.
$WH(\gamma\gamma)$	$l\nu\gamma\gamma$	To be consistent with other electroweak analyses for future combinations, the WH process where the Higgs decays as two photons is treated as background. The final state is identical to $W\gamma\gamma$ signal.

Table 6.1: Summary of the different sources backgrounds that are considered in the analysis presented in this thesis. The final states are given as examples, some processes can have additional final states that may occasionally mimic an event signature. The different particles are noted as: l either electron or neutrino, ν any flavour of neutrino, j jets, b jet originating from a b-quark decay, γ photons and t top quarks.

6.1 Simulated backgrounds

The following backgrounds are estimated using MC simulations:

- Z backgrounds:
  - $Z\gamma$
  - $Z\gamma\gamma$
- Top backgrounds:
  - $t\bar{t}$
  - $tX\gamma$: $t\bar{t}\gamma$ and $tW\gamma$
- W backgrounds:
  - $W(\tau\nu)\gamma\gamma$
  - $WH(\gamma\gamma)$
  - diboson: WW, WZ, ZZ

The detailed list of all MC samples and their generators details is given in Appendix B. The number of events estimated for each source of background is given in Table 6.2. Even with a Z veto, the dominant simulated background comes from Z processes. The top quark processes come second and finally the diboson, $W(\tau\nu)\gamma\gamma$ and $WH(\gamma\gamma)$ processes represent the smallest source of background.

Normalisation

The normalisation of the simulated background distributions can be obtained in two different ways: using a theoretical calculation of the total fiducial cross-section of the process or by normalising the simulated kinematic distributions to data in an appropriate control region. Here, most background processes are normalised using the most accurate theoretical cross-section predictions currently available, except for the top and $Z\gamma$ backgrounds which are normalised to data due to higher uncertainties on the processes cross-sections. The normalisation of the top backgrounds is carried out using a likelihood fit described later in Section 8.2.1. The $Z\gamma$ background is normalised in a data control region by a procedure described in Section 6.1.1.

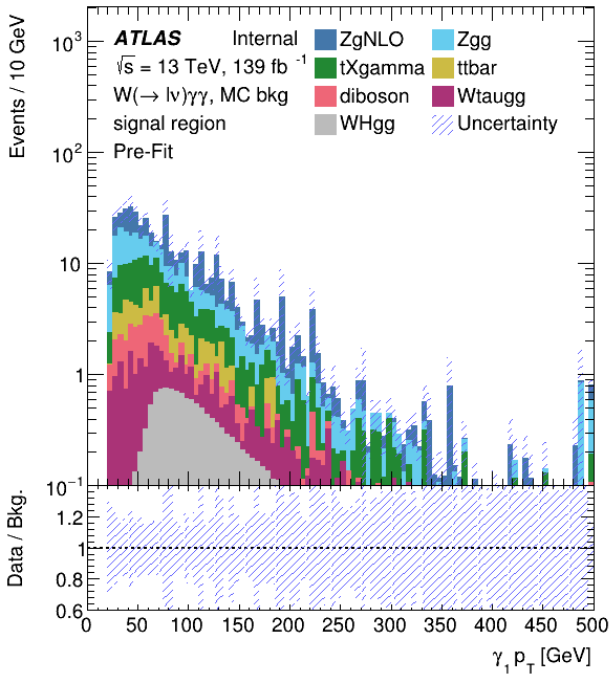

Figure 6.1: Distribution of leading photon p_{T} for the different simulated backgrounds in the Signal Region. Both systematic (Chapter 7) and statistical uncertainties are displayed.

Background processes	Estimated number of events in SR
$Z\gamma$	88.5 ± 2.1 (stat.)
$Z\gamma\gamma$	60.1 ± 1.1 (stat.)
$tX\gamma$	49.5 ± 0.8 (stat.)
$t\bar{t}$	14.6 ± 1.0 (stat.)
diboson	10.7 ± 0.3 (stat.)
$WH(\gamma\gamma)$	10.6 ± 0.1 (stat.)
$W(\tau\nu)\gamma\gamma$	6.5 ± 0.1 (stat.)

Table 6.2: Expected number of background events in the signal region from MC simulated processes. The statistical uncertainty on the estimated number of background events is also shown.

Truth matching

Background contributions coming from jets being misidentified as electrons/muons or photons are separately estimated. In order to avoid double-counting, this kind of contribution must be subtracted from the simulated background processes. This is done using truth level information in the MC: cuts are applied to discard simulated events with jet(s) misidentified as photons or leptons. The resulting MC background distributions are shown in Figure 6.1 and 6.2 and the number of events for each MC sample is summarised in Table 6.2. Note that the top quark and $Z\gamma$ background distributions are shown before final re-normalisation using scale factors computed with data.

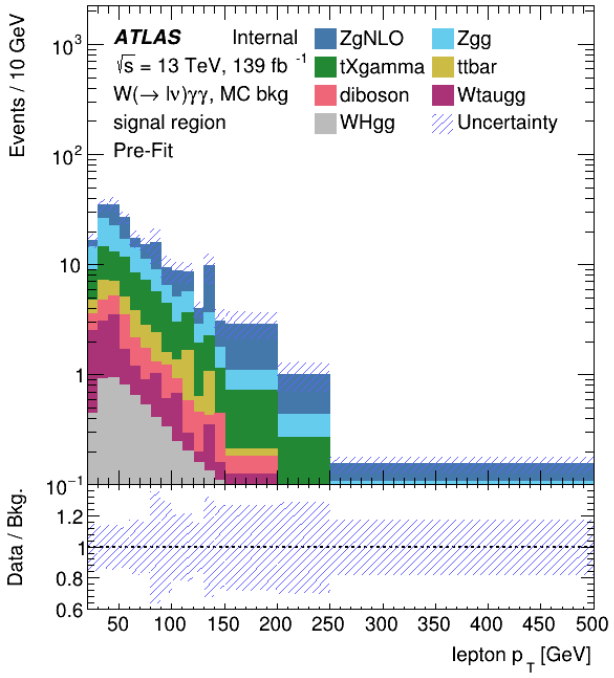

(a) Lepton (e/μ) transverse momentum

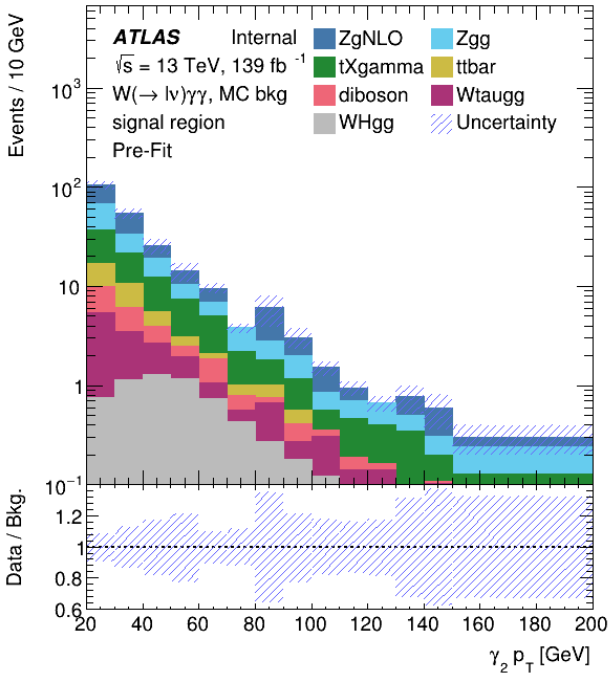

(b) Subleading photon transverse momentum

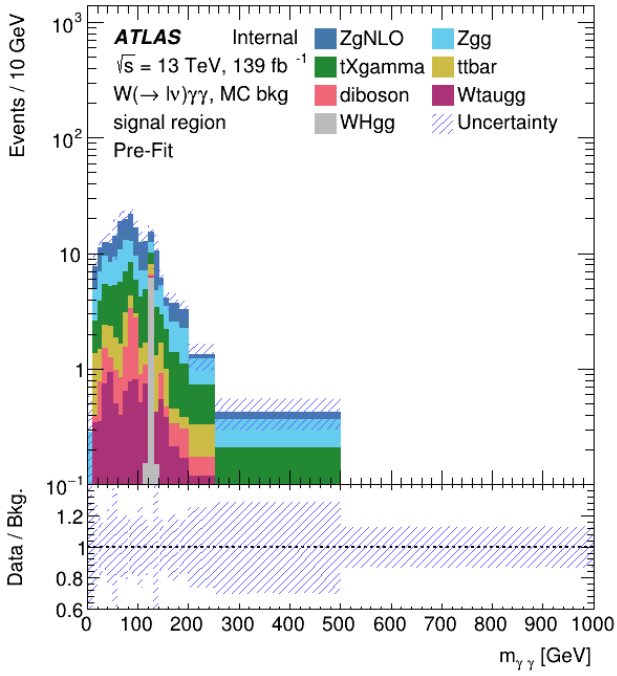

(c) Invariant diphoton mass

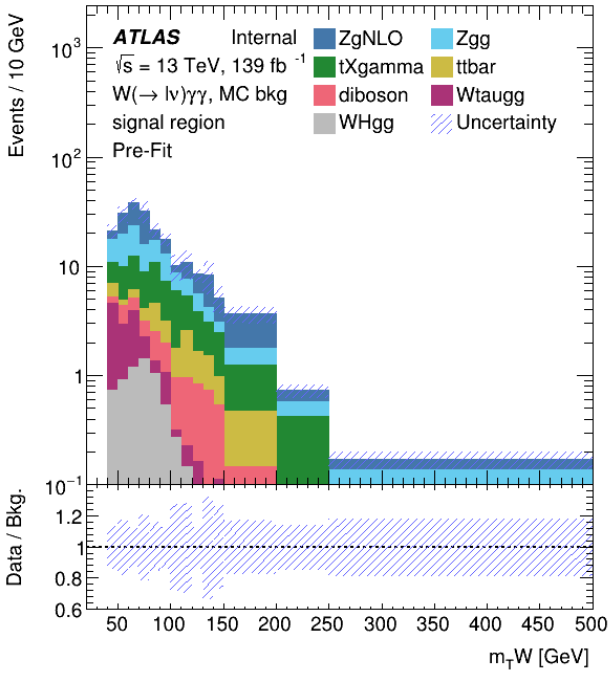

(d) W boson transverse mass

Figure 6.2: Distribution of different kinematic variables for the different simulated backgrounds in the signal region. Combined systematic (Chapter 7) and statistical uncertainties are displayed.

6.1.1 $Z\gamma$ normalisation

The $Z(\rightarrow e^+e^-)\gamma$ process constitutes an important background because one of the electrons coming from the Z leptonic decay can be misidentified as a photon. This lepton misidentification as a photon does not affect the muon channel. Although this fake background is better modelled than misidentified jets, its normalisation is corrected using data by computing a Scale Factor (SF). The SF computation is not fully finalised yet and only preliminary results are shown here.

Physics objects:	$Z\gamma$ control region LOW	$Z\gamma$ control region HIGH
Photon	2 signal photons	″
Lepton	1 signal electron	″
b-jets	0	0
$E_{\mathrm{T}}^{\mathrm{miss}}$	< 25 GeV	> 25 GeV
W boson	$m_T^W < 40$ GeV	$m_T^W > 40$ GeV
Inverted Z veto:	$p_T^{l\gamma\gamma} > 30$ GeV	″
	$m_{lgg} \in [81, 100]$ GeV	
	$m_{lg1} \in [81, 100]$ GeV	
	$m_{lg2} \in [81, 100]$ GeV	

Table 6.3: Control regions used to compute the $Z\gamma$ scale factor.

At the time of writing, the SF is computed in two control regions, both defined by inverting the Z veto cuts of the signal region, thereby corresponding to control regions with a particularly enhanced number of Z events. The two control regions are then defined by dividing them into a high control region with $m_T^W > 40$ GeV and $E_{\mathrm{T}}^{\mathrm{miss}} > 25$ GeV and a low control region where the m_T^W and $E_{\mathrm{T}}^{\mathrm{miss}}$ cuts are inverted (see Table 6.3). The high control region is used to compute the SF that will be used to normalize the $Z\gamma$ simulated distribution in the signal region. The low control region is used to compute the SF used to validate this method in a validation region VR2, which is later introduced in Section 6.4, see Table 6.7. In both cases, all other MC are subtracted from data in the $Z\gamma$ control re-

gions and the SF is computed as the ratio of remaining data over the $Z\gamma$ MC estimate.

The values of the scale factor derived from this method are shown in Figure 6.3. The scale factors are not constant as a function of the leading photon p_{T} and they are therefore binned. The error shown is statistical only. Such a high value for the scale factor is not expected and was not observed in the earlier development stages of the method and validation of the technique is ongoing.

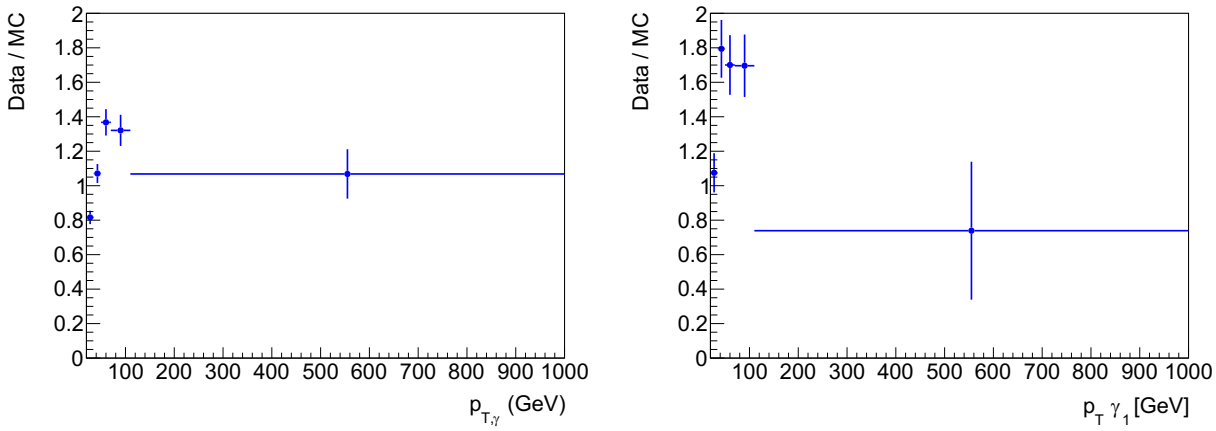

(a) $Z\gamma$ SF for signal region

(b) $Z\gamma$ SF for CR2 region

Figure 6.3: $Z\gamma$ scale factors computed in the High control region (left) and in the Low control region (right)

Validation and comments

The validation of the SF approach to normalize the yield of the $Z\gamma$ simulated background is carried out in the VR2 region by comparing the SF of the $Z\gamma$ low control region to the SF computed in the VR2 region. The SF is computed in VR2 by taking the ratio of data minus all MC excepted $Z\gamma$, divided by $Z\gamma$ MC. As shown in Figure 6.4, the scale factors do not agree within statistical uncertainty and show a systematic offset. The SF shown here have been computed with the MadGraph $Z\gamma$ samples. A second set of samples using the SHERPA generator have been tested as well but more discrepancies were observed. Due to this poor agreement, another method is being developed with the aim of deriving a

more robust estimate of the shape and yield of $Z\gamma$ events mimicking signal events through the mis-reconstruction of an electron as a photon.

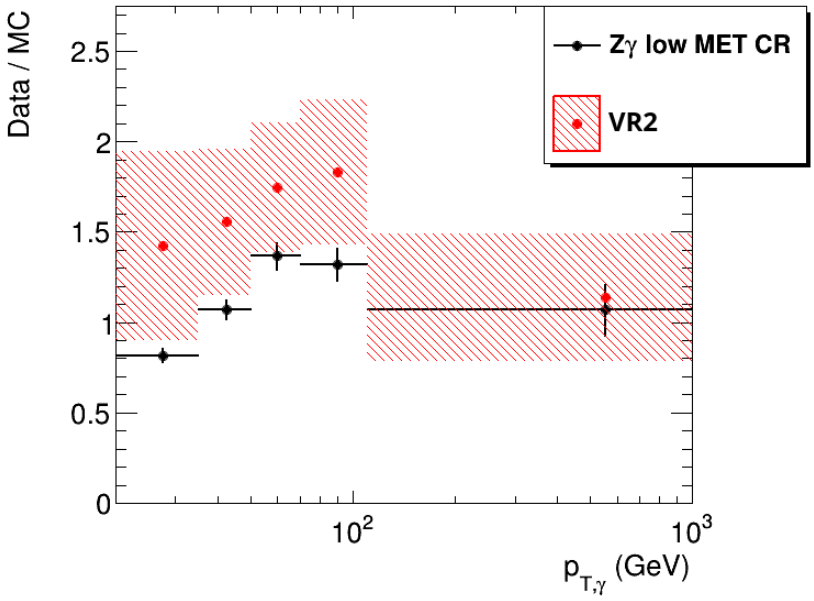

Figure 6.4: Validation of the SF in the VR2 validation region for the electron channel. In VR2 the SF is taken as the ratio of data minus all MC excepted $Z\gamma$, divided by $Z\gamma$ MC.

6.2 Fake photons from jets

The main background of this analysis comes from jets being misidentified as photons. These misidentified jets will be referred to as j-fake photon or j-fakes. Hadrons can be misidentified as photons when they deposit large amounts of energy in the electromagnetic calorimeters and display no or mismatched tracks in the trackers. This rare process can occur because on intrinsic fluctuations in the hadronic showers. In addition, neutral hadrons such as the π^0 and η can decay into real photons that are considered as background here [95]. Only a small fraction of jets lead to such misidentification problems but because of the abundance of jets in proton-proton collisions, they constitute a large background in this analysis.

The fraction of j-fake photons cannot be estimated using MC simulations as the jet showering in the electromagnetic calorimeter is not modelled well enough. In order to estimate the amount of j-fakes passing the nominal signal selection, a data-driven method is used: a 2D Template method described in Section 6.2.2. Background estimates obtained using this method were cross checked using another data-driven approach: a 2x2D sideband method detailed in Appendix D. Both methods rely on the difference in the isolation energy distribution between j-fake and prompt photons.

In this section, the general principle of the 2D Template fit method for one photon will be first introduced. Then the method will be extended to our two photon case.

6.2.1 Method description for one photon

The template fit method is a data-driven technique that uses the differences between signal and background in a given observable distribution to estimate the amount of background in the signal region. To differentiate between prompt photon and j-fakes, the photon calorimetric transverse isolation energy E_{iso} is used:

$$E_{\text{iso}} = E_T^{cone40} - 0.022 * p_T \tag{6.1}$$

where E_T^{cone40} is the energy deposited in the calorimeters in a radius of $\Delta R = 0.4$ around the photon (with $\Delta R = \sqrt{\Delta\eta^2 + \Delta\theta^2}$). The isolation energy of prompt photons is expected to be lower than for misidentified jets. Templates of the isolation energy distributions for j-fakes and for prompt photons are computed in control regions. The probability density functions (pdf) templates are then added and fitted to the signal region and the fraction of background events in the signal region is extracted from the fit. The implementation of the method requires the following three steps:

1. Finding control regions containing only (mostly) prompt or j-fake photons.

2. Finding and fitting appropriate functions to define prompt and j-fake photon pdf templates in these control regions.

3. Fitting the sum of the 2 probability density function templates to the data in the signal region to extract the estimated fraction of background events.

1. Control regions definition:

All control regions are defined by the nominal signal event selection (see Sec. 5.3.4) minus the photon isolation and identification (ID) cuts. The Tight photon isolation cut is not applied in order to use the full range of the isolation energy distribution to define the pdf templates. The ID cut is varied to select prompt or j-fake photons and the control regions are defined as follows:

- The prompt photon template is taken from simulated $W\gamma\gamma$ events since photon showers are generally modelled well enough. Photons are required to pass the Tight ID but no requirement is made on the photon isolation. The selected events must pass all the rest of the nominal signal selection. Photons falling into this control region are referred to as Tight photons (**T**)

- The j-fake photon template is taken from data in which the contribution from other backgrounds has been first subtracted using all background simulated processes. Photons are required to fail the Tight ID and pass the LoosePrime4 ID (defined in Appendix C.4) but no requirement is made on the photon isolation. The selected events must pass all the rest of the nominal signal selection. Photons falling into this control region are referred to as LoosePrime photons (**L′**).

Note that these control regions have been constructed to be orthogonal by design.

2. Template definition

Different types of mathematical functions were considered in order to achieve the best possible fit to the data. The two functions retained are the double crystal ball [96] and Bukin functions [97]. They are implemented using the RooFit framework [98]

- The Tight photons are fitted using a double sided crystal ball (CB) shape function. A crystal ball function is a Gaussian convoluted with a power law tail and is defined

as [96]:

$$f_{CB}(E) = \begin{cases} \exp\left(-\frac{(E-E_0)^2}{2\sigma^2}\right) & \text{, for } \frac{E-E_0}{\sigma} > -\alpha \\ \left(\frac{n}{|\alpha|}\right)^n \exp\left(-\frac{|\alpha|^2}{2}\right)\left(\frac{n}{|\alpha|} - |\alpha| - \frac{E-E_0}{\sigma}\right)^{-n} & \text{, for } \frac{E-E_0}{\sigma} \leqslant -\alpha \end{cases} \tag{6.2}$$

where E_0 is Gaussian mean, σ its width, α a cut-off parameter and n the power of the exponentially decaying tail. A double-sided CB is the addition of two CB functions sharing the same mean and width. The CB template describing the prompt photon isolation energy distribution is noted F_T.

- The LoosePrime photons are fitted with a Bukin function defined in ref [97] which is the convolution of a Gaussian with two exponential tails. This template describing the fake photon isolation energy distribution is noted $F_{L'}$

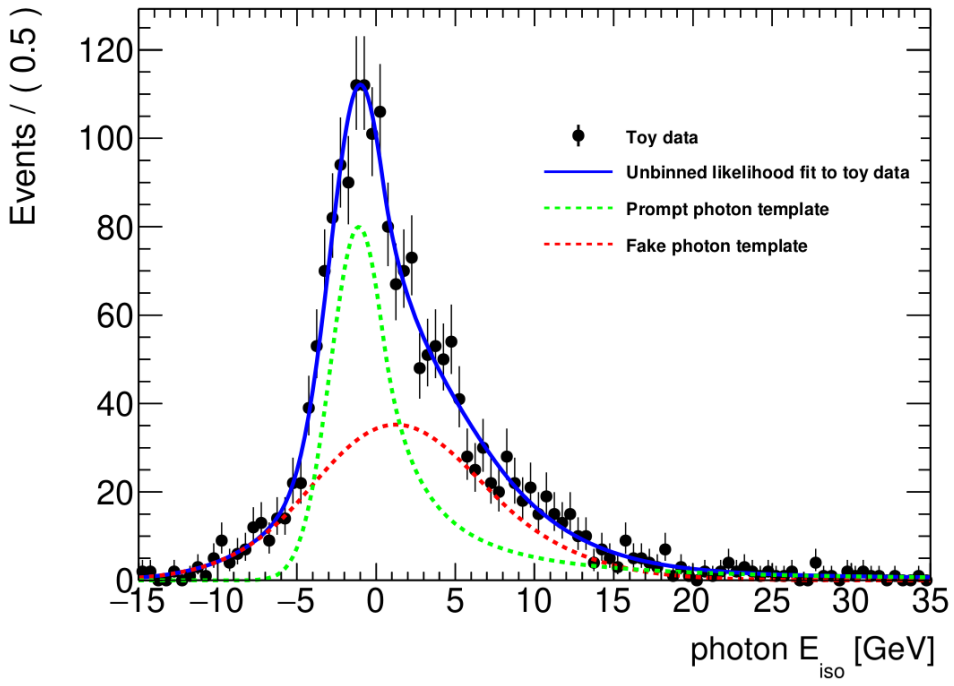

Figure 6.5: Toy example to illustrate the 2D fit method for one photon. The dashed red and green curves are the templates from control regions. They are then added and fitted to the signal region (toy) data. The blue curve is the final fit to data.

3. Fit to data

Once the pdf templates computed, their shape is fixed and they are added and fitted to signal region data (minus photon isolation). This is illustrated in Figure 6.5 and the result can be expressed as the sum of the pdfs (F) normalised by their respective yields (N):

$$N_{tot}F_{tot} = N_T F_T + N_{L'}F_{L'} \tag{6.3}$$

After the fit, the photon isolation cut must be applied to recover the exact signal region definition used in the analysis. The different pdf templates contribute differently above and below the photon isolation cut ($E_{\text{iso}} < 2.45$ GeV). To estimate the fraction of j-fakes and prompt photons in the signal region, the raw yields are corrected by computing the pdf integrals up to the isolation cut to scale them.

$$N_{SR} = N^{RAW} \times \frac{\text{Integral}_{\text{PDF}}}{\text{Integral}_{\text{totalfit}}} \tag{6.4}$$

6.2.2 2D template fit

Having two photons in the event final state of interest makes the template fit method more complex: leading and subleading photons display different isolation energy distributions (see Figure 6.6) and potential correlation between the two photons has to be taken into account. Two-dimensional pdf templates are therefore used.

The j-fake photon background is divided into three subcategories depending on which of the photon(s) is (are) fake. Adding the signal photons, four 2D pdf templates are needed:

- F_{TT}: Both photons are tight (**T**)
- $F_{TL'}$: The leading photon is tight (**T**) and the subleading photon is LoosePrime (**L'**)
- $F_{L'T}$: The leading photon is LoosePrime (**L'**) and the subleading photon is Tight (**T**)
- $F_{L'L'}$: Both photons are LoosePrime (**L'**)

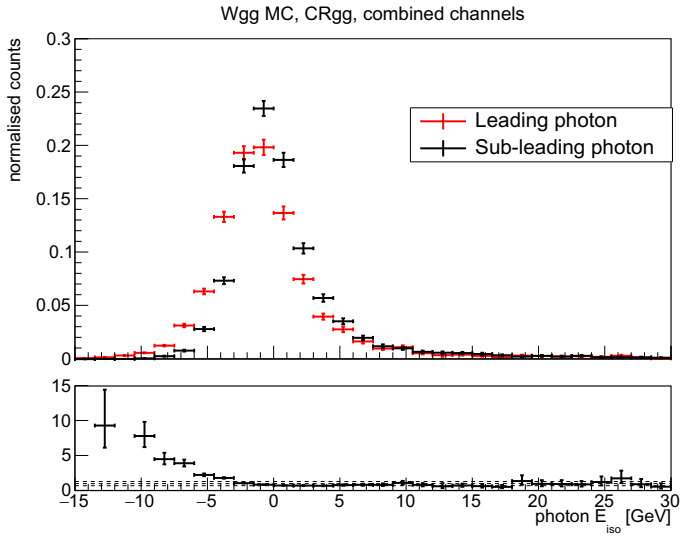

Figure 6.6: Comparison of the isolation energy of the leading and subleading photons obtained using simulated $W\gamma\gamma$ signal events falling in the **TT** control region. The bottom plot shows the ratio of the two distributions.

The background and signal content of the signal region can now be expressed as a function of the 2D templates (F) and the yields (N):

$$N_{tot}F_{tot} = N_{TT}F_{TT} + N_{TL'}F_{TL'} + N_{TL'}F_{TL'} + N_{L'L'}F_{L'L'} \tag{6.5}$$

Correlation between photons

The 2D distributions for **TT**, **TL'**, **L'T** and **L'L'** photons in MC photons obtained using signal $W\gamma\gamma$ simulated events are shown in Figure 6.7. The distributions correlations have been computed and are summarized in Table 6.4. For **TT**, **TL'** and **L'T** photons, the isolation energy correlation between the two photons is below 10%. It is therefore neglected when defining the corresponding 2D pdf templates. But for **L'L'** photons, the correlation is 46% and cannot be neglected.

2D template definition

For the three uncorrelated photon categories **TT**, **TL'** and **L'T**, the 2D templates F_{ij} are

	electron channel	muon channel	combined channels
TT	0.085	0.057	0.071
TL′	-0.016	-0.0063	-0.016
L′T	0.084	0.025	0.084
L′L′	0.512	0.427	0.463

Table 6.4: Correlation coefficients in the two-dimensional distribution of E_{iso} for leading and subleading photons measured in simulated events for electron, muon and combined channels.

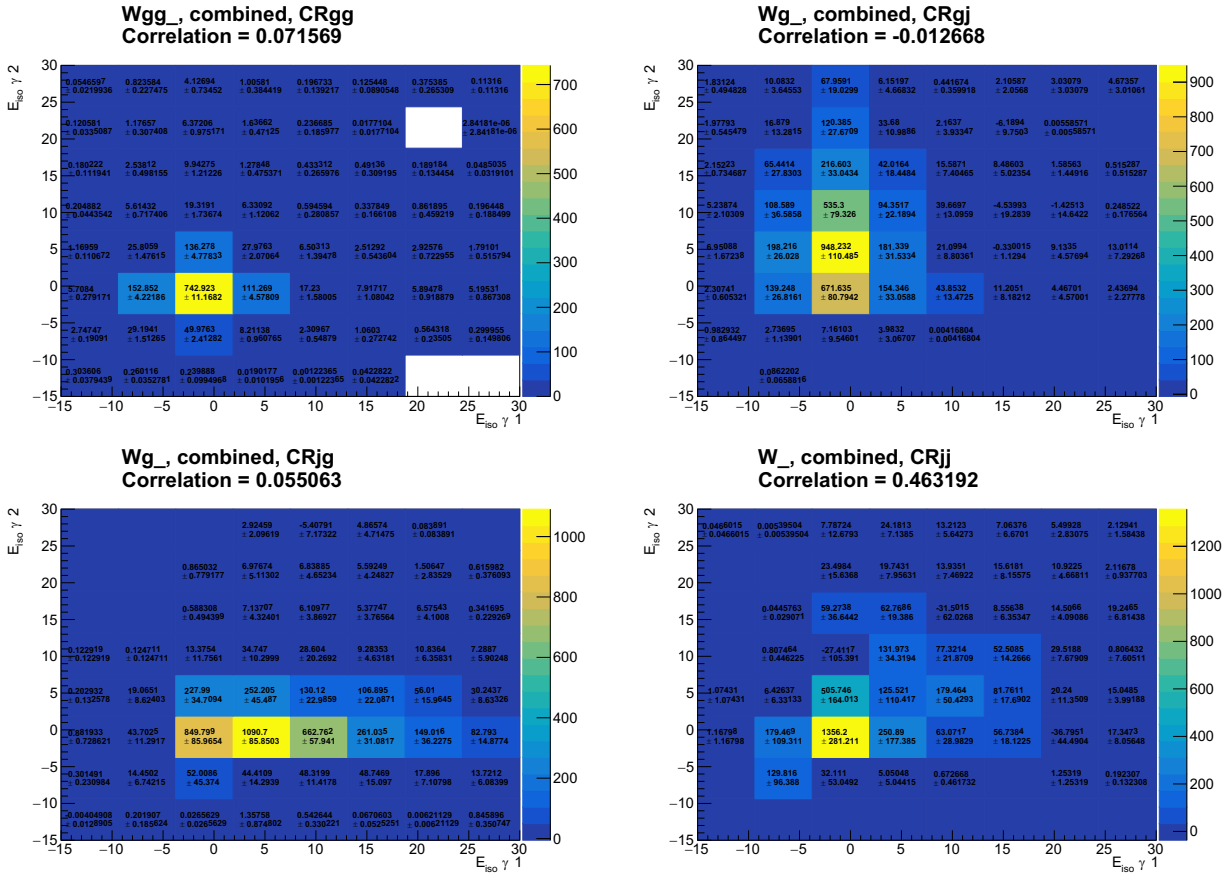

Figure 6.7: Two-dimensional distributions of the photons isolation energies for the leading and sub-leading photons. Top left: **TT** photons in $W\gamma\gamma$ simulated events, top right: **TL′** photons in $W\gamma$ simulated events, bottom left: **L′T** photons in $W\gamma$ simulated events, bottom right: **L′L′** photons in W+jets simulated events.

constructed from the product of the leading and subleading photon 1D templates:

$$F_{ij} = F_{1,i} \times F_{2,j} \tag{6.6}$$

where i, j correspond to the **T** or **L′** photon ID s and 1 (2) to the leading (subleading) photon. The **T** and **L′** 1D templates are computed as described in Section 6.2.2 for the leading and subleading photons: the **T** pdfs are a double-sided crystal ball shapes fitted to Tight photons in signal MC and the **L′** are Bukin functions fitted to LoosePrime photons in data. The 1D templates obtained are shown in Figure 6.8

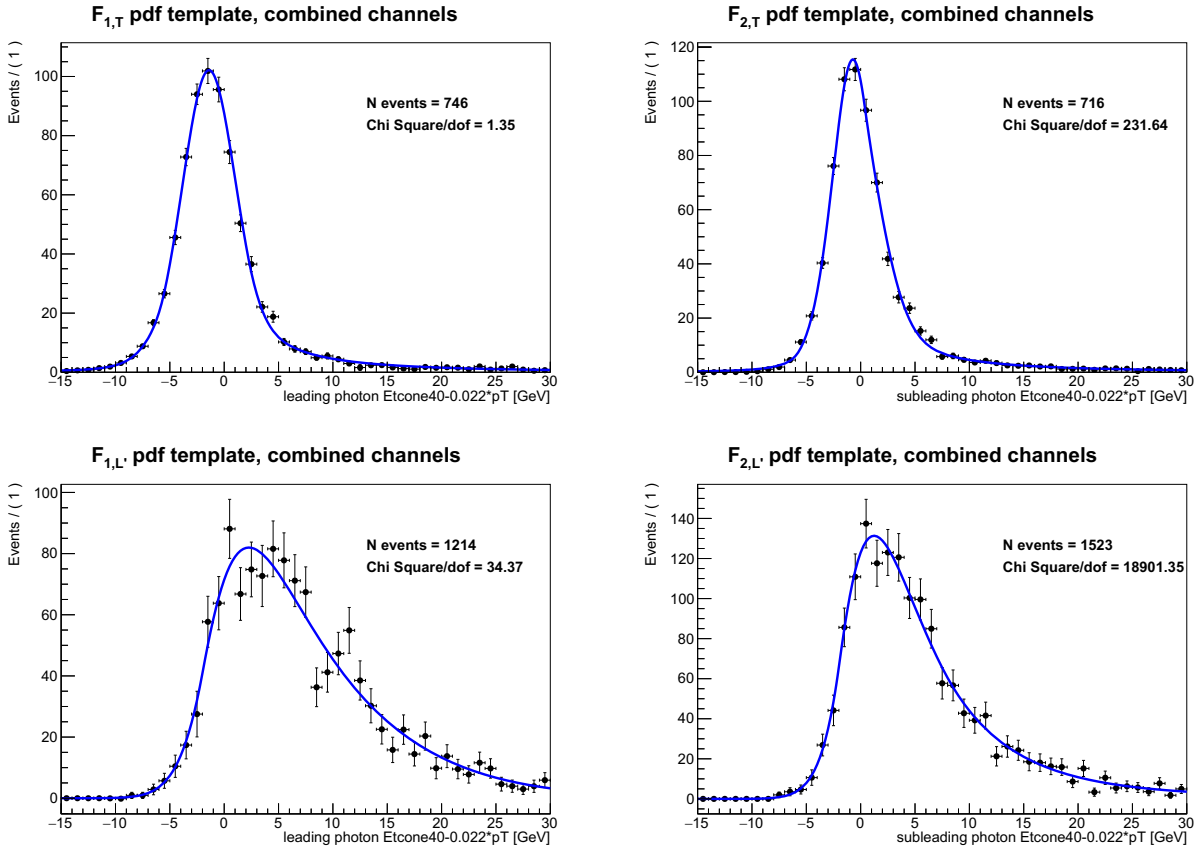

Figure 6.8: One-dimensional pdf templates overlaid over their respective control region data. Top: tight photons in signal simulated events, fitted using a double side crystal ball function. Bottom: jets faking photons in data control regions, fitted using a Bukin function.

Because of the correlation existing between leading and subleading photons, the $F_{L'L'}$ 2D pdf template is computed using a kernel density estimation [99] which is a non parametric method. The distribution is estimated by a superposition of Gaussian kernels, one for each data point, each contributing 1/N to the total integral of the pdf, and the technique

is implemented using the RooFit framework. The four 2D-templates obtained by the convolution of 1D templates and with the kernel method are shown of Figure 6.9 This allows to fully take into account the correlation in the 2D isolation energy distribution while obtaining a smooth pdf and compensating for the low statistics. Equation 6.5 now becomes:

$$N_{tot}F_{tot} = N_{TT}F_{1,T}F_{2,T} + N_{TL'}F_{1,T}F_{2,L'} + N_{L'T}F_{1,L'}F_{2,T} + N_{L'L'}F_{L'L'} \tag{6.7}$$

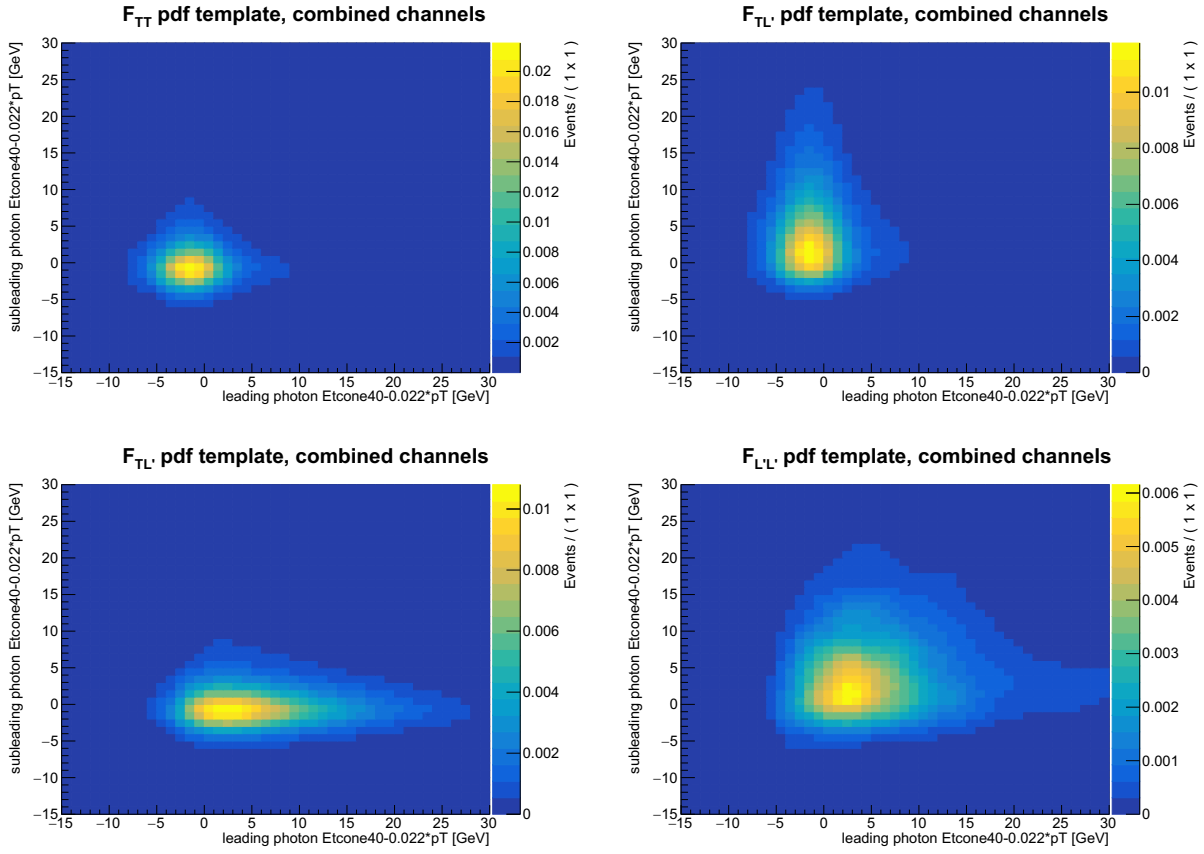

Figure 6.9: Two-dimensional templates: $F_{TT}, F_{TL'}, F_{L'T}$ are the convolution of 1D templates showed in Figure 6.8. The $F_{L'L'}$ template is computed using RooFit kernel function [99].

6.2.2.1 Signal leakage

The control regions used to extract the fake photon templates unavoidably contain some real photons that didn't pass the Tight photon identification cuts. The amount of real photons in these control regions is not negligible and will distort the fake photon templates. This signal leakage must be estimated and corrected for. The template pdf F'_L can be decomposed as the sum of the jet faking photons template F_j and of the real photon template F_γ as follows:

$$\begin{aligned} F_{L',i} &= \alpha_i F_{\gamma,i} + (1-\alpha_i) F_{j,i} \quad i \in 1,2 \\ F_{L'L'} &= (1-\alpha'_1-\alpha'_2-\alpha'_3) F_{jj} + \alpha'_1 F_{\gamma,1} F_{j,2} + \alpha'_2 F_{j,1} F_{\gamma,2} + \alpha'_3 F_{\gamma,1} F_{\gamma,2} \end{aligned} \tag{6.8}$$

The α parameters are the signal leakage coefficients: α_1 (α_2) are the fraction of real $\gamma\gamma$ events in the $L'T$ (TL') samples and the coefficients α'_1 (α'_2, α'_3) are the fraction of γj ($j\gamma, \gamma\gamma$) events in the $L'L'$. The leakage coefficients are computed using simulated event samples. The $W\gamma\gamma$ sample is used to compute α_1, α_2 and α'_3 and the $W\gamma$ sample is used to compute the α'_1 and α'_2 coefficients. Truth matching is applied to make sure to select true γj or $j\gamma$ events.

The leakage coefficients are defined as:

$$\begin{aligned} \alpha_1 &= \frac{N^{\mathbf{L'T}}_{\gamma\gamma,MC}}{N^{\mathbf{TT}}_{\gamma\gamma,MC}} \frac{N_{\gamma\gamma}}{N^{\mathbf{L'T}}} \\ \alpha_2 &= \frac{N^{\mathbf{TL'}}_{\gamma\gamma,MC}}{N^{\mathbf{TT}}_{\gamma\gamma,MC}} \frac{N_{\gamma\gamma}}{N^{\mathbf{TL'}}} \\ \alpha'_1 &= \frac{N^{\mathbf{L'L'}}_{\gamma j,MC}}{N^{\mathbf{TT}}_{\gamma j,MC}} \frac{N_{\gamma j}}{N^{\mathbf{L'L'}}} \\ \alpha'_2 &= \frac{N^{\mathbf{L'L'}}_{j\gamma,MC}}{N^{\mathbf{TT}}_{j\gamma,MC}} \frac{N_{j\gamma}}{N^{\mathbf{L'L'}}} \\ \alpha'_3 &= \frac{N^{\mathbf{L'L'}}_{\gamma\gamma,MC}}{N^{\mathbf{TT}}_{\gamma\gamma,MC}} \frac{N_{\gamma\gamma}}{N^{\mathbf{L'L'}}} \end{aligned} \tag{6.9}$$

where $N^{XX}_{ij,MC}$ is the number of simulated events with photons in the ij categories passing the XX IDs. The $N^{XX}_{\gamma\gamma,MC}$ counts are taken from the $W\gamma\gamma$ simulation, the $N^{XX}_{\gamma j,MC}$ and $N^{XX}_{j\gamma,MC}$

counts are taken from the $W\gamma$ simulated samples. Truth matching is applied on the MC: the reconstructed particle ID (Tight or LoosePrime photon) must match the particle type initially generated (photon or jet). Finally N^{XX} are the numbers of data events passing the XX IDs.

The yields obtained by the fit and defined in Equations 6.7 can be re-expressed as a function of the corrected yields defined in Equation 6.9 as:

$$\begin{aligned}
N_{TT} &= N_{\gamma\gamma} - \frac{\alpha'_3}{1-\alpha'_1-\alpha'_2-\alpha'_3}N_{jj} - \frac{\alpha_1}{1-\alpha_1}\left(N_{\gamma j} - \frac{\alpha'_1}{1-\alpha'_1-\alpha'_2-\alpha'_3}N_{jj}\right) \\
&- \frac{\alpha_2}{1-\alpha_2}\left(N_{j\gamma} - \frac{\alpha'_2}{1-\alpha'_1-\alpha'_2-\alpha'_3}N_{jj}\right) \\
N_{TL'} &= \frac{1}{1-\alpha_1}\left(N_{\gamma j} - \frac{\alpha'_1}{1-\alpha'_1-\alpha'_2-\alpha'_3}N_{jj}\right) \\
N_{L'T} &= \frac{1}{1-\alpha_2}\left(N_{j\gamma} - \frac{\alpha'_2}{1-\alpha'_1-\alpha'_2-\alpha'_3}N_{jj}\right) \\
N_{L'L'} &= \frac{1}{1-\alpha'_1-\alpha'_2-\alpha'_3}N_{jj}
\end{aligned} \tag{6.10}$$

To solve this system of equations, the leakage coefficients can be rewritten as $\beta_i = \frac{\alpha_i}{N_{jk}}$. The values of these leakage coefficient are given in AppendixC.

$$\begin{aligned}
\beta_1 &= \frac{N^{\mathbf{L'T}}_{\gamma\gamma,MC}}{N^{\mathbf{TT}}_{\gamma\gamma,MC}}\frac{1}{N^{\mathbf{L'T}}} \\
\beta_2 &= \frac{N^{\mathbf{TL'}}_{\gamma\gamma,MC}}{N^{\mathbf{TT}}_{\gamma\gamma,MC}}\frac{1}{N^{\mathbf{TL'}}} \\
\beta'_1 &= \frac{N^{\mathbf{L'L'}}_{\gamma j,MC}}{N^{\mathbf{TT}}_{\gamma j,MC}}\frac{1}{N^{\mathbf{L'L'}}} \\
\beta'_2 &= \frac{N^{\mathbf{L'L'}}_{j\gamma,MC}}{N^{\mathbf{TT}}_{j\gamma,MC}}\frac{1}{N^{\mathbf{L'L'}}} \\
\beta'_3 &= \frac{N^{\mathbf{L'L'}}_{\gamma\gamma,MC}}{N^{\mathbf{TT}}_{\gamma\gamma,MC}}\frac{1}{N^{\mathbf{L'L'}}}
\end{aligned} \tag{6.11}$$

and the corrected yields can then be expressed as:

$$\begin{aligned} N_{\gamma\gamma} &= \frac{N_{TT}}{1-\beta_1 N_{L'T}-\beta_2 N_{TL'}-\beta'_3 N_{L'L'}} \\ N_{\gamma j} &= \frac{N_{TL'}(1-\alpha_2(N_{\gamma\gamma}))}{1-\beta'_2 N_{L'L'}} \\ N_{j\gamma} &= \frac{N_{L'T}(1-\alpha_1(N_{\gamma\gamma}))}{1-\beta'_1 N_{L'L'}} \\ N_{jj} &= N_{L'L'}(1-\alpha'_1(N_{j\gamma})-\alpha'_2(N_{\gamma j})-\alpha'_3(N_{\gamma\gamma})) \end{aligned} \tag{6.12}$$

6.2.3 Final estimate

Total estimate

The yields obtained for the different fake photon backgrounds and signal are shown in Table 6.5. They are expressed both as a fraction and a number of events remaining in the signal region after all other sources of background have been subtracted, excepted the pile-up background. The numbers shown have been computed using the blinded dataset in the signal region (half of the available Run 2 data). Data and simulated events have been multiplied by a factor 2 to give an estimate of the total number of events expected.

The dominant fake photon background comes from events with a subleading fake photon, followed by events with a leading fake photon. Events where both photons are fake are rather rare (4%). The number of real $W\gamma\gamma$ events shown here is used as an input to compute the pile-up background described in Section 6.3. The estimated number of real $W\gamma\gamma$ signal events agrees within uncertainties with the sum of the $W\gamma\gamma$ estimate coming from signal MC simulation and pileup background estimate (both shown in Figure 8.3)). The corresponding results of the 2D likelihood fit are shown in Figure 6.10. The projection of the 2D templates on the leading and subleading photons isolation energies show a good agreement between the total fit with and the data.

Differential estimate

In order to compute the $W\gamma\gamma$ differential cross-section as a function of the leading photon p_T, the j-fake photon estimate must be expressed as a function of leading photon trans-

	fraction	Number of events
$N_{\gamma\gamma}$	0.57 ± 0.02	419.6 ± 16.4
$N_{\gamma j}$	0.24 ± 0.01	179.1 ± 6.6
$N_{j\gamma}$	0.14 ± 0.01	106.4 ± 5.3
N_{jj}	0.042 ± 0.001	31.3 ± 0.7

Table 6.5: Scaled yields of fake and signal photons in the signal region. These yields are computed using a fraction of the blinded data in the signal region. The error is statistical only.

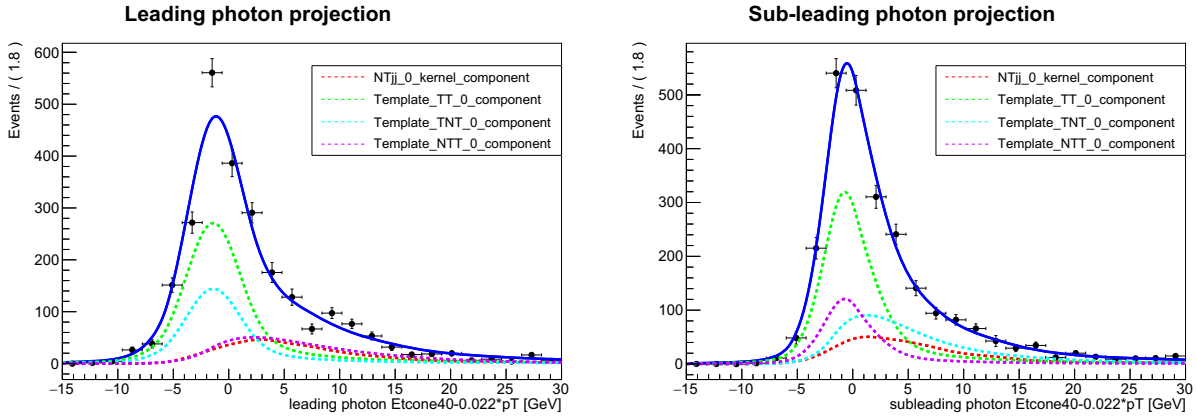

Figure 6.10: 2D Likelihood fit projection (solid blue) and the contributions of the three backgrounds and signal (dashed). Left: leading photon projection, right: subleading photon projection.

verse momentum ($p_T^{\gamma 1}$). However the statistics in the data control regions are too low to divide the dataset into more than three $p_T^{\gamma 1}$ bins and to compute the pdf templates for fake photons.

Three bins are insufficient to fully characterize the shape of the differential cross-section as function of leading photon p_{T} in order to derive meaningful constraints on aQGC in the future. Therefore, the differential estimate of the fake photon background is extrapolated from the $p_T^{\gamma 1}$ distributions in the control regions. The $p_T^{\gamma 1}$ is computed and normalised in each of the CRgg, CRgj, CRjg, CRjj and multiplied by the corresponding yields computed with the full dataset. The results are shown in Figure 6.11.

Detailed studies and the validation of this procedure are presented in Appendix C.1.

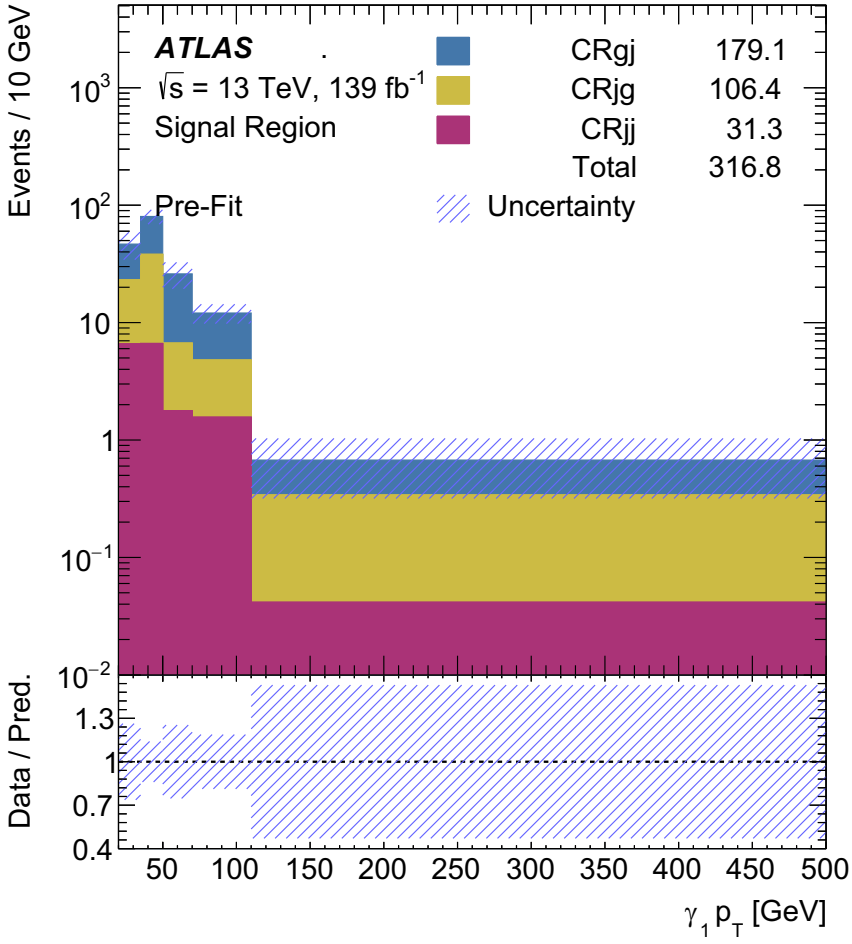

Figure 6.11: Fake photon yields estimate in the signal region as function of leading photon p_{T}.

6.3 Pile-up background

During one LHC bunch crossing, several proton-proton collisions happen. The hard scatter of interest is therefore overlaid with particles coming from other collisions. Most of these pile-up particles are removed at the reconstruction level using track and vertex information. But for photons, the event selection does not impose explicit requirements on the point of origin, as their direction is poorly measured. Hence events such

as $W\gamma + \gamma_{\text{pile-up}}$ can be confused with $W\gamma\gamma$ events. This small but non negligible background is referred to as the pile-up background. Note that out of time pile-up (events coming from different bunch crossings) is negligible.

Although this background could be estimated from simulations, the simulated samples used in this analysis yielded large uncertainties due to low statistics and high event weights. A data-driven method – developed for the recent ATLAS $Z\gamma$ measurement [100] – is used instead. It is adapted to the two photon case by applying the method separately to the leading and subleading photons. The variable used to differentiate pile-up from hard scatter photons is their longitudinal separation from the primary vertex $\Delta z = z_\gamma - z_{\text{vertex}}$.

The fraction of pile-up photons in the signal region is defined as:

$$f_{PU} = \frac{N_{PU,\gamma} + N_{PU,jet}}{N_{obs}} \tag{6.13}$$

where $N_{PU,\gamma}$ is the number of real pile-up photons, and N_{obs} the number of observed events in the signal region, with all other backgrounds removed. The background coming from pile-up jets misidentified as photons ($N_{PU,jet}$) has been shown to be negligible and only $N_{PU,\gamma}$ and N_{obs} need to be computed. These quantities are computed in a pile-up enriched region defined as the signal region plus a cut on the longitudinal parameter $|\Delta z| > 50$ mm. Additionally, only converted photons with at least one silicon track and a conversion radius of $r < 400$ mm are used. They are used since their longitudinal parameter resolution ($|\sigma_z| < 2$ mm) allows the accurate measurement of Δz.

The quantity $N_{PU,\gamma}$ is computed by subtracting the number of $W\gamma\gamma$ simulated events from the number of data events in the pile-up enriched region. Both distributions are shown in Figure 6.12 for leading and subleading photons. Finally N_{obs} must be scaled to match the control region. The expected z_{vertex} distribution is given by the LHC bunch shapes and it is well modelled by a Gaussian distribution with mean 0 and width 35.5 ± 0.2 mm [100]. The expected distribution for $\Delta z_{pile-up}$ is therefore the difference between two of these

Gaussians: another Gaussian of width $\sim \sigma = 50$ mm. The pile-up fraction expected in the region $\Delta z > 50$ mm corresponds therefore to 32% of pile-up photons.
The pile-up fraction can now be computed with:

$$f_{PU} = \frac{N^{|\Delta z|>50mm}_{data,\geq 1Sitrack} - N^{|\Delta z|>50mm}_{MC,\geq 1Sitrack}}{0.32 N_{obs}} \tag{6.14}$$

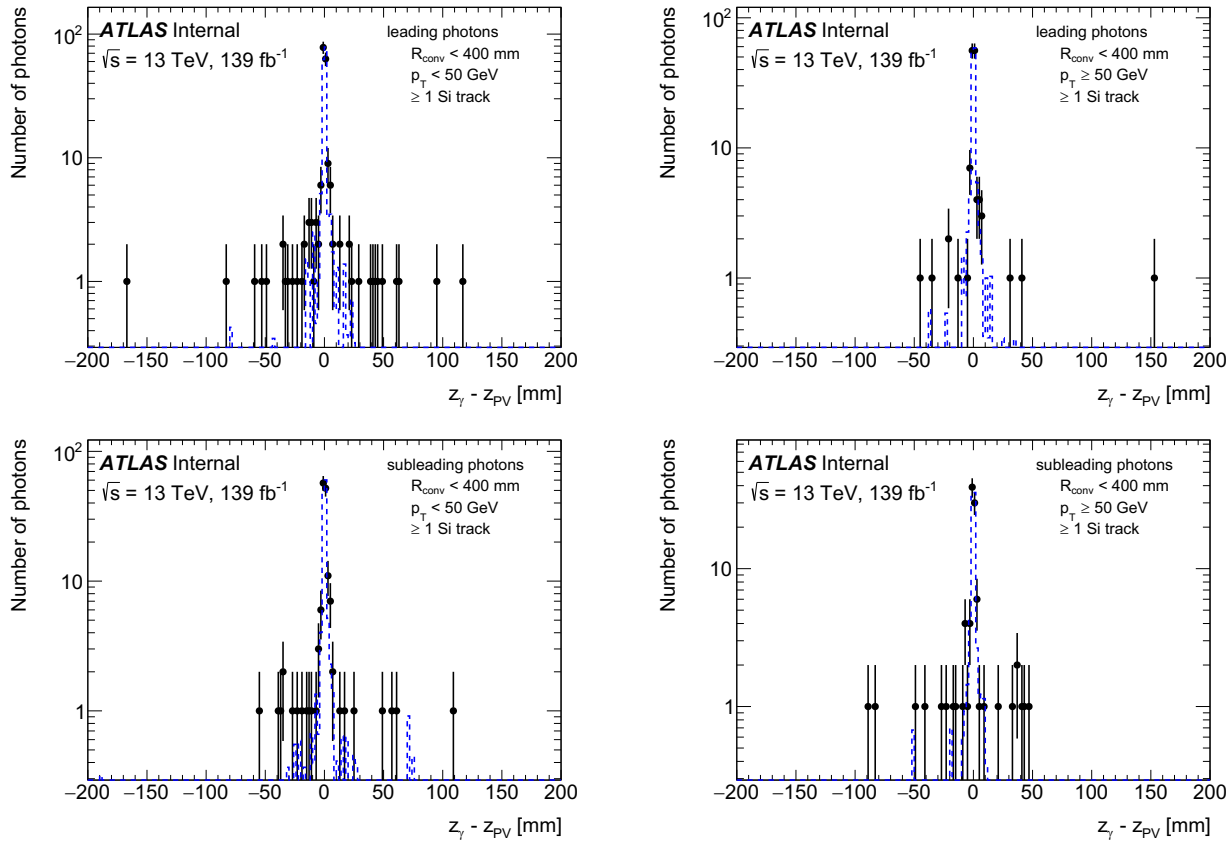

Figure 6.12: Longitudinal impact parameter for converted photons with at least one silicon track and $R_{conv} < 400$ mm, in data and signal simulation, for leading photons (top) and subleading photons (bottom), at low-p_{T} (left) and high-p_{T} (right). The simulations (dotted blue) are scaled such that the integral in the range $-2 < \Delta z < 2$ mm equals that of data. The fraction of photons from pile-up is calculated with photons with $|\Delta z| > 50$ mm

The results are shown in Table 6.6. The pile-up fraction was computed in two leading photons bins. Only one category of photons has a pile-up fraction that differs from zero in a statistically significant way: leading photons with $p_T < 50$ GeV. This shows that the

	$p_{\mathrm{T}} < 50$ GeV	$p_{\mathrm{T}} \geq 50$ GeV
Leading photon	0.10 ± 0.04	0.01 ± 0.02
Subleading photon	0.04 ± 0.05	0.02 ± 0.05

Table 6.6: Fraction of photons originating from pile-up interactions, split by leading/subleading and low/high-p_{T}. The fraction only significantly differs from zero for low-p_{T}, leading photons.

only process contributing significantly to the pile-up background is when a $W\gamma$ event overlaps with a high energy single photon from pile-up.
At this point, the pile-up single photon can be real or fake. The fake case is already taken into account in the fake photons background estimate as no requirements are made on the photon origin. To give a pile-up estimate for real photons only, the fractions of Table 6.6 have to be multiplied by the real photon purity for $p_{\mathrm{T}} < 50$ GeV. This fraction was calculated using an ABCD method (see method description in Appendix D) in single photon simulations and data events, and found to be 0.21 ± 0.01, with the uncertainty quoted representing the statistical uncertainty.

The final differential estimate of the pile-up background is shown in Figure 6.13. It was obtained by multiplying the initial pileup fraction and the photon purity with the number of signal events predicted by the 2D template fit method (Table 6.5). The error shown is statistical. The pile-up background is more important for low p_{T} photons which is expected as pile-up interactions have lower energy than the hard scatter. The total number of events for the pile-up background is 37.9 events. This result was cross-checked using simulation of the $W\gamma$ process and agrees within statistical uncertainties.

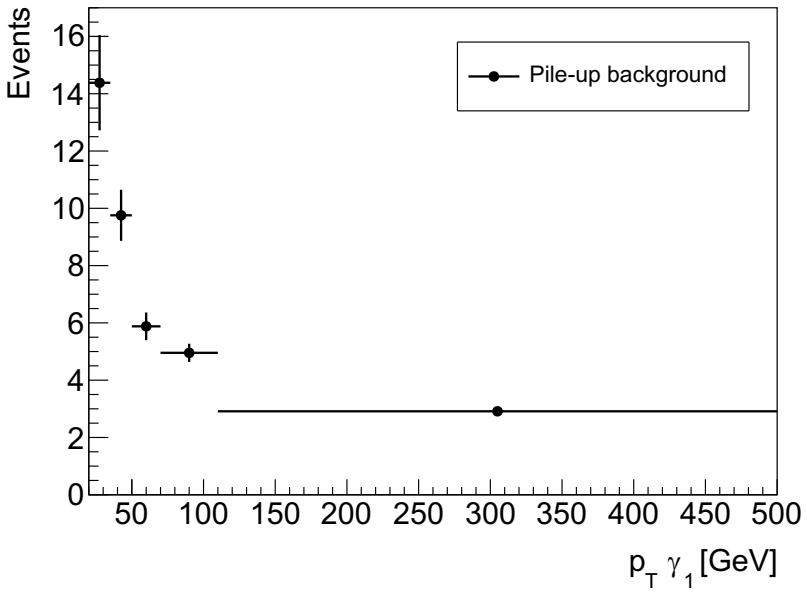

Figure 6.13: Differential estimate of the pile-up background in the signal region.

6.4 Fake leptons

The *fake* and *non-prompt* lepton backgrounds (commonly referred to as fake leptons here), correspond to events where either a jet, a lepton from heavy flavour decays, or a converted photon satisfies lepton identification criteria. Note that as previously mentioned, *lepton* refers here to only electrons and muons. These processes are poorly modelled as they depend strongly on the interaction of a particle with the detector materials and this background is therefore estimated from data using the *Fake Factor (FF)* method. The estimation is carried out using the Fake Background Tools developed by ATLAS [101].

6.4.1 Method description

The method relies on first measuring a *prompt efficiency* ϵ_r and a *fake efficiency* ϵ_f describing how likely real and fake leptons are to pass the signal lepton identification criteria. To compute these efficiencies, two sets of leptons are required: tight leptons and baseline leptons. Here tight leptons correspond to the signal leptons defined in Section 5.3.1.2 and

baseline leptons are defined by dropping the σ_{d0} and isolation cuts used to define tight leptons. All tight leptons therefore also pass the baseline selection and baseline leptons that do not pass the tight criteria are called loose leptons. The prompt and fake efficiencies are measured in data, in a control region orthogonal to the signal region.

The relations between the number of real/fake leptons in the tight and loose samples can be expressed as a function of the efficiencies:

$$\begin{pmatrix} N^T \\ N^L \end{pmatrix} = \begin{pmatrix} \epsilon_r & \epsilon_f \\ 1-\epsilon_r & 1-\epsilon_f \end{pmatrix} \begin{pmatrix} N_r^B \\ N_f^B \end{pmatrix} \tag{6.15}$$

where N^T and N^L are the numbers of tight and loose leptons, and N_r^B and N_f^B are the numbers of prompt and fake leptons in the baseline sample. To solve this equation using the Fake Factor (FF) method, both sides of eq. 6.15 are multiplied by a row vector:

$$\left(1, -\frac{\epsilon_f}{1-\epsilon_f}\right) \equiv (1, -F) \tag{6.16}$$

where F is called the fake factor. The equation to solve is now:

$$N^T - FN^L = \epsilon_r N_r^B + \epsilon_f N_f^B - F(1-\epsilon_r)N_r^B - \epsilon_f N_f^B \tag{6.17}$$

The number of fake leptons in the tight sample can be expressed as $N_f^T = N^T - N_r^T$. Note that also by definition: $N_r^T = \epsilon_r N_r^B$ and $N_r^L = (1-\epsilon_r)N_r^B$, which leads to the much simpler equation:

$$N_f^T = F(N^L - N_r^L) \tag{6.18}$$

To compute the number of fake leptons in the tight regions, the fake factor F will first have to be determined from a control region. Note that it can be computed for the full dataset but also bin by bin to obtain a differential estimate. The number of loose leptons N^L are measured in data and the number of real loose leptons N_r^L is estimated from truth matched MC simulations as prompt leptons are well modelled.

Poisson likelihood extension

Statistical variations affecting the computation of the number of fake lepton events passing signal selection N_f^T can be mitigated with a Poisson likelihood extension of the fake factor method. In this method, the computed values of N^L and N_r^L are treated as the observed number of events n of a Poisson distribution $P(\mu_i, n)$ with μ_i the expected number of events. The likelihood function is defined as the product of Poisson distributions varying the value $\mu_{1,i} = N_{p_i}^L$ or $\mu_{2,i} = N_{r,p_i}^L$:

$$L = \prod_i P_1(N_{p_i}^L, N^L) P_2(N_{r,p_i}^T, N_r^T) \tag{6.19}$$

The inverse log likelihood is then minimised while requiring that $N_{f,p_i}^T = F(N_{p_i}^L - N_{r,p_i}^T)$ stays positive. The Maximum Likelihood Estimate (MLE) $\hat{N}_{p_i}^L$ and $\hat{N}_{r,p_i}^T$ are used to compute the final estimate of the number of fake lepton events N_f^T.

This method is especially useful in cases of low statistics as it guaranties a positive estimate of N_f^T and gives a more accurate estimation of the uncertainty.

6.4.2 Efficiency computation

To compute the fake efficiency F, a control region (CR) similar to the signal region (SR) but enriched in fake leptons is defined. This is done with a *tag-and-probe* method [102]: the CR events are selected when they are compatible with a well-known physics process, for instance a Z boson decay, that produces two objects of the same type.

The CR is defined by selecting events with two same-flavour opposite sign baseline leptons of invariant mass within $\pm 10\%$ of the Z boson mass, and one opposite-flavour baseline lepton. Events with additional baseline leptons are vetoed. A b-jet veto is applied to be consistent with the SR. To reduce contributions from WZ events, cuts are applied on missing transverse energy and on the W transverse mass: $m_{T,W} < 40$ GeV and $E_{\mathrm{T}}^{\mathrm{miss}} < 40$ GeV. Finally, truth matched diboson simulations are subtracted from data to account for the remaining contribution from real WZ events.

The same-flavour opposite sign leptons act as tags. They have to pass the tight lepton selection and at least one of them has to trigger the lowest unprescaled single lepton trigger. The opposite-flavour third lepton acts as the probe and is used to measure the fake efficiency.

$$\epsilon_f = \frac{N_T}{N_B} \tag{6.20}$$

The results are binned in lepton p_T and η and shown in Figure 6.14. For electrons, the fake efficiency varies from 0.6 at high p_{T} and η down to about 0.1 at low p_{T} and η. For muons, the efficiency varies from 0.4 to 0.1. These lower values are expected as muon identification is expected to be more efficient thanks to the muon spectrometers (Section 3.2.3).

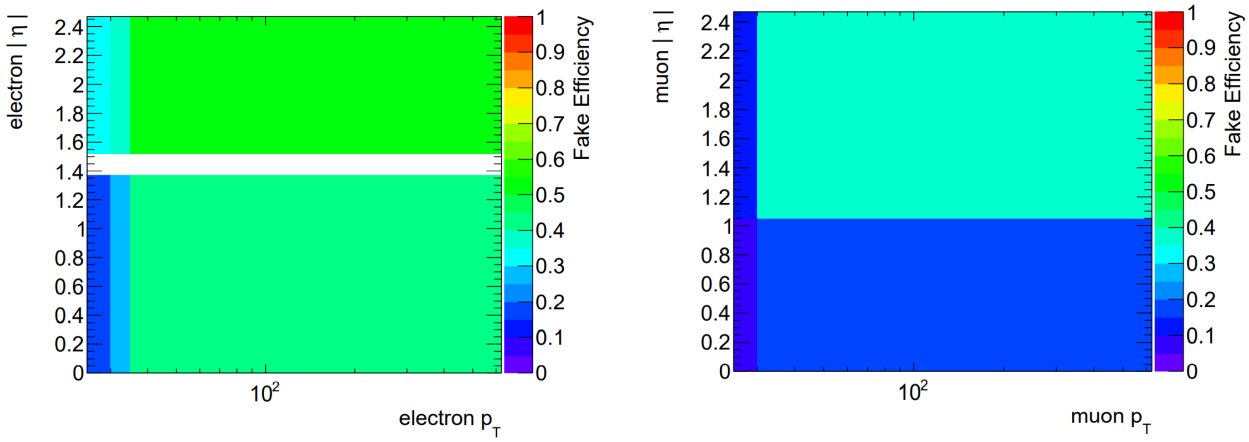

Figure 6.14: Fake lepton efficiency estimates computed in a data control region for electrons (left) and muons (right). The region of the calorimeter with limited sensitivity is excluded for electrons.

6.4.3 Results

The total estimated number of events from the fake lepton backgrounds is of $N_e^{fake} = 27^{+7}_{-6}$ for the electron channel and $N_\mu^{fake} = 16^{+3}_{-3}$ for the muon channel. Results are consistent with the estimate derived from truth-matched simulations for a one bin estimate ($N_e^{fake,MC} = 34 \pm 3$ and $N_\mu^{fake,MC} = 23 \pm 4$). The discrepancy between the number of estimated fake muons and electrons is expected: thanks to the Muon Spectrometer (MS), muon reconstruction has lower fake rate and less jets are misidentified as muons.

The differential distributions of the fake lepton backgrounds are shown in Figure 6.15. The corresponding uncertainty is statistical only.

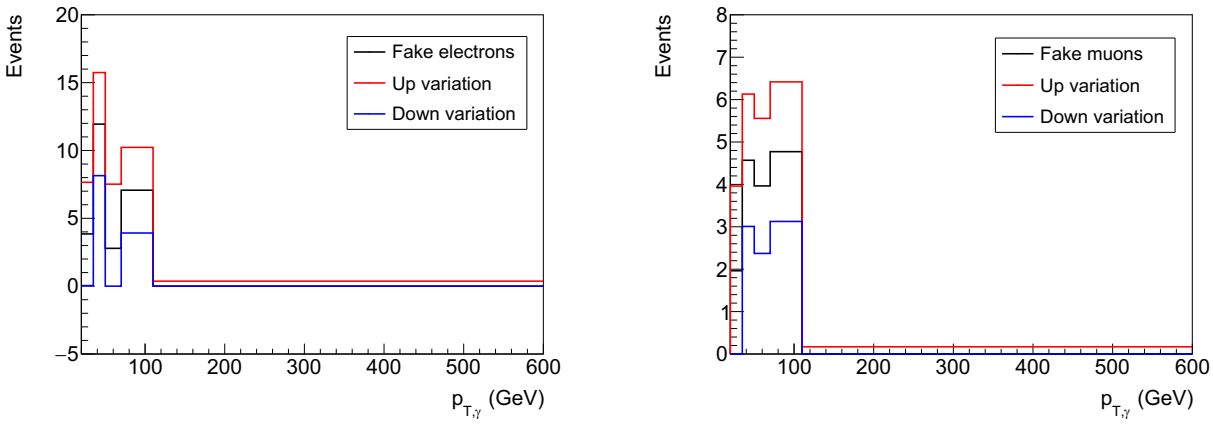

Figure 6.15: Differential distribution of the fake electron background (left) and fake muon background (right).

Physics objects:	VR2	Signal selection
Photon	2 signal photons	″
Lepton	1 signal lepton	″
$E_{\mathrm{T}}^{\mathrm{miss}}$	< 25 GeV	> 25 GeV
b-jets	0	″
W boson	$m_T^W < 40$ GeV	$m_T^W > 40$
Z veto	applied	″
Overlap removal	applied	″

Table 6.7: Definition of the VR2 validation region and comparison with the signal region definition.

Result validation

The fake lepton estimate was validated in a dedicated validation region *VR2* similar but orthogonal to the signal region. It is defined by inverting the signal region $E_{\mathrm{T}}^{\mathrm{miss}}$ and m_T^W cuts, and by loosening the lepton selection from tight to baseline. The full region definition is given in Table 6.7.

The sum of truth-matched simulated backgrounds and fake lepton estimate is compared with data in VR2. Work is still on going for the validation and preliminary results are shown in Table 6.8.

- In the electron channel, good agreement is observed between data and the sum of the data-driven fake lepton background estimate plus truth-matched background simulations for all other backgrounds. Note that however, the simulated backgrounds include here the $Z\gamma$ simulated events scaled by the scale factor described in Section 6.1.1, a background estimate that will be further refined in the coming weeks.
- In the muon channel work is in progress: the validation region is expected to have a large signal content and looking at the data would violate ATLAS blinding policy. Modifications to the VR2 region definition are being studied for the muon channel.

Electron Channel	
Truth MC	286 ± 20
Fakes Estimate	37^{+7}_{-6}
Data	322 ± 18

Muon Channel	
Truth MC	80 ± 5
Fakes Estimate	18^{+3}_{-2}
Data	Work in progress

Table 6.8: Preliminary validation of the fake lepton background estimate in the VR2 validation region.

Chapter 7

Systematic uncertainties

Systematic uncertainties are measurement errors that affect data or simulations and that are not due to statistical fluctuations [103]. They are separated into three categories in this thesis: uncertainties on data-driven backgrounds (Section 7.1), experimental uncertainties (Section 7.2) and theoretical uncertainties affecting the MC simulations (Section 7.3). This chapter describes which uncertainties are taken into account and how their values are estimated. The impact of all uncertainties combined on the final measurement is described in Chapter 8.

An overview of the main uncertainties is shown in Figure 7.1. The differential cross-section estimate main uncertainty comes from the data-driven j-fake photon background estimation.

7.1 Data-driven backgrounds uncertainties

7.1.1 j-fake photon

Due to the complex nature of the j-fake photon background estimation method, the uncertainties are split into two categories. First, uncertainties on the global yield, obtained by using the full unbinned datasets are computed. The statistical uncertainty coming from the limited statistics in all control regions, is propagated through all of the method

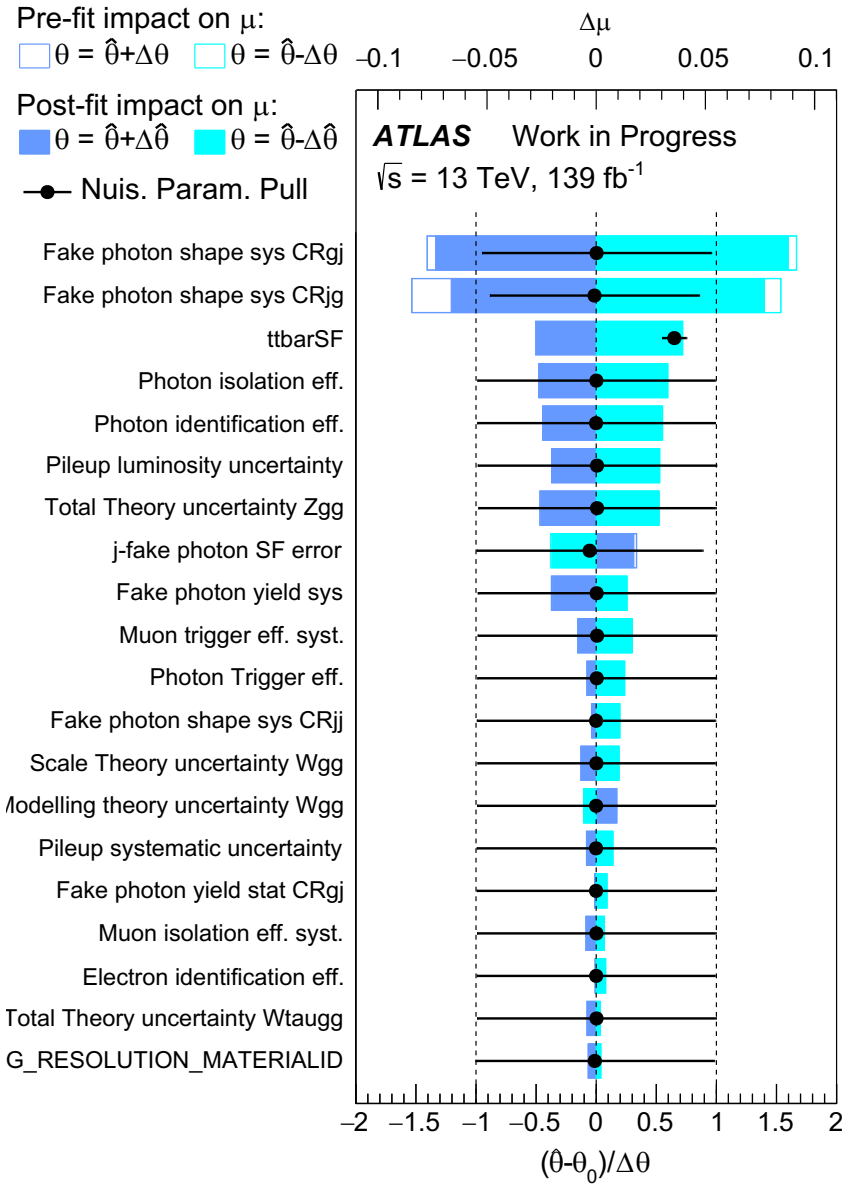

Figure 7.1: Overview of the systematic uncertainties with the highest impact on the final differential cross-section. The parameter $\hat{\theta}$ is the Maximum Likelihood Estimate of the corresponding uncertainty and θ_0 its initial value (see Chapter 8).

computational steps. The uncertainties on the extrapolation method, used to get the differential distributions of the j-fake photon background, are computed separately.

j-fake photon yield statistical uncertainty:

The statistical uncertainty on the j-fake photon background yield takes into account the limited data statistics in the different control regions: CRgg, CRgj, CRjg and CRjj. This

	Statistical uncertainty as a percentage	Statistical uncertainty as a number of events
$N_{\gamma j}$	2 %	12.8
$N_{j\gamma}$	1 %	7.9
N_{jj}	0.1%	0.2

Table 7.1: Statistical error on j-fake photons yields in the signal region.

statistical uncertainty is propagated through the 2D template method to obtain the final uncertainty estimate on the three event yields $N_{\gamma j},\ N_{j\gamma},\ N_{jj}$. Error propagation is carried out with the RooFit framework [98] using Gaussian constraints: when the templates are initially computed, each function's parameters are obtained with a central value $\mu_{\theta i}$ and an error $\sigma_{\theta i}$. When the 2D template fit is performed, each of the parameters are modelled by a Gaussian distribution of mean $\mu_{\theta i}$ and an error $\sigma_{\theta i}$ so that the fluctuation of each parameter is constrained. Standard error propagation is used when correcting the yields for signal leakage (Equation 6.12). The statistical error on the leakage coefficients is taken into account as well. This uncertainty is displayed in Table 7.1 and used as an overall systematic uncertainty for each of the fake photon sub-backgrounds γj, $j\gamma$ and jj.

j-fake photon yield systematic uncertainty:

The systematic error on the yield takes into account the imperfections in the method: the small correlation between isolation and photon ID, and the dependence on the choice of control regions. Alternate LoosePrime ID definition are used to define the alternate control regions and the j-fake photon yields are computed for each of the ID variations: LoosePrime2, LoosePrime3, LoosePrime4a and LoosePrime5 (defined in Appendix C.4). The difference between the nominal yields and the alternative LoosePrime yields is shown in Table 7.2. The largest variations for $W\gamma\gamma$ (LoosePrime2 and LoosePrime5) are taken as the overall systematic affecting the sum of all three fake photon sub-backgrounds γj, $j\gamma$ and jj. This approach has been chosen over using variations on individual backgrounds as systematic variations are correlated between sub-backgrounds.

j-fake photon background shape uncertainties:

Two uncertainties are defined for the extrapolation method. First the limited data statis-

	LoosePrime2	LoosePrime3	LoosePrime4a	LoosePrime5
$W_{\gamma j}$	-4.92%	-5.12%	-3.60%	1.54%
$W_{j\gamma}$	-2.17%	-0.80%	-0.71%	0.48%
W_{jj}	1.18%	1.47%	1.69%	0.56%

Table 7.2: Difference between the yields of different LoosePrime ID working points and the nominal ID: LoosePrime4.

tics in the control regions used for shape extrapolation is taken into account, defining a statistical uncertainty. It is defined bin by bin. Then, since the template method can be computed in a maximum of three $p_T^{\gamma 1}$ bins, the difference between the binned yields obtained by a binned likelihood fit and by a 3-bin extrapolation is used to define the uncertainty. This uncertainty, originally defined in three $p_T^{\gamma 1}$ bins is then smoothed to 5 bin (weighted average between bins). It is computed for the three j-fake sub-backgrounds individually as their shapes are different. The resulting variations are shown in Figure 7.2.

7.1.2 Other data-driven backgrounds

The two other data-driven backgrounds estimates in this analysis are the pile-up background (Section 6.3) and the fake leptons from jets background (Section 6.4). Both methods have statistically dominated uncertainties and beyond propagating this statistical uncertainty through the estimate of the yields, no further systematic uncertainties are taken into account.

For the fake lepton background, the potential effect of experimental uncertainties was studied, following the method described in Section 7.2. The ranking of uncertainties shown in Figure 7.3 clearly shows the dominance of the statistical uncertainty on that background component. This justify the decision of only taking into account statistical uncertainty in the fake lepton background estimate, potential effect from other experimental uncertainties are taken as negligible.

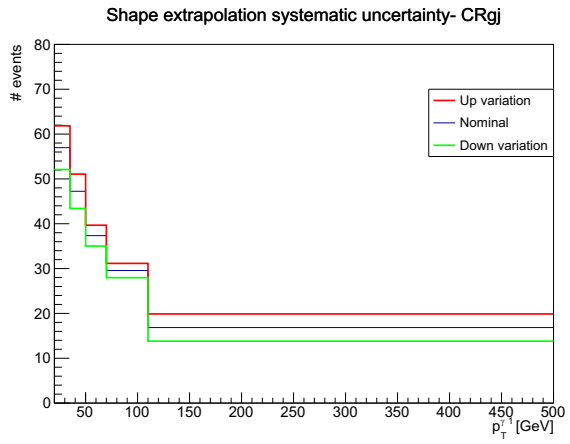

(a) Uncertainty for γj sub-background

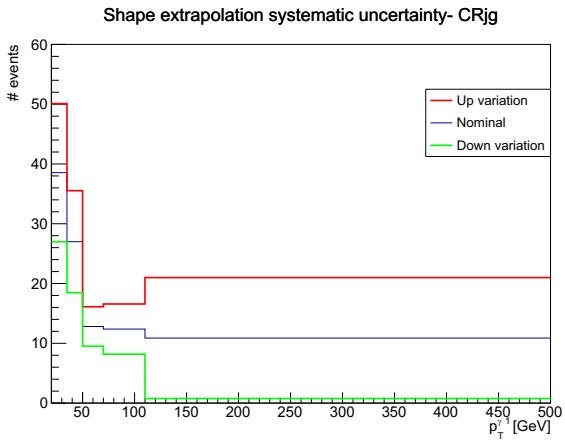

(b) Uncertainty for $j\gamma$ sub-background

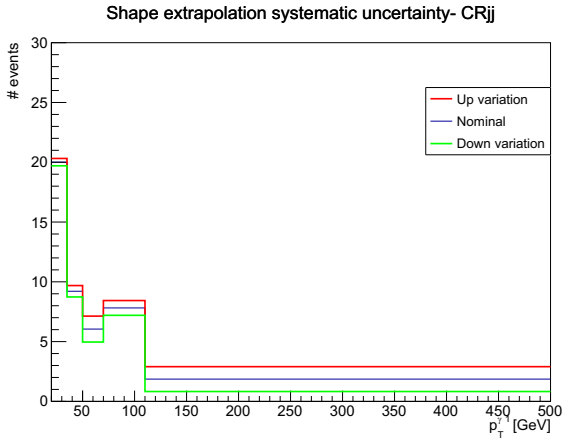

(c) Uncertainty for jj sub-background

Figure 7.2: Shape systematic uncertainty for the three j-fake photon sub-backgrounds

7.2 Experimental uncertainties

Experimental uncertainties refer here to a long list of uncertainties including badly known detector acceptances, resolutions, efficiencies, and calibrations. Their computation is harmonised within the ATLAS collaboration to ensure the best results and consistency between analyses. The latest recommendations made by the ATLAS Combined Performance group (CP) were followed in this study. This section gives an overview of the procedures used to estimate these various uncertainties. The detailed list of all uncertainties considered is given in Appendix E.

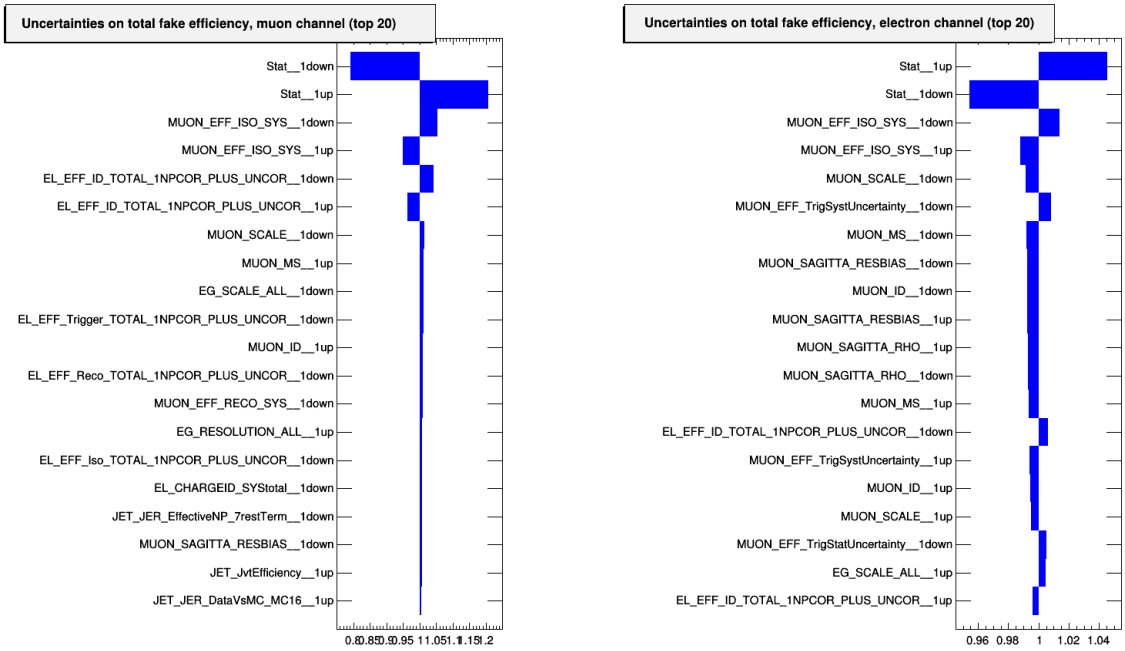

Figure 7.3: Uncertainties on the total fake muon (left) and fake electron (right) background estimate. Statistical uncertainty clearly dominates other sources of uncertainty. Details on the experimental uncertainties shown here are given in Appendix E.

Photon identification efficiency

The efficiency of the selection cuts on certain variables differ between data and simulations. The simulated events are therefore corrected using *scale factors* so that they closely resemble data and the uncertainty on these scale factors must be included as nuisance parameters. The scale factors for the Tight photon identification variable has been measured by the ATLAS collaboration using three different methods [104]. Each method comes with its own estimate of uncertainty, covering effects such as mismodeling in the simulation used, or uncertainties of the methods themselves computed by varying fit ranges or selection criteria. The total uncertainty on the combined ID scale factors ranges between 7% at low photon transverse energy to 0.5% at high transverse energy for unconverted photons, and between 12%-1% for converted photons.

Photon & electron isolation efficiency

Isolation energy quantifies the activity recorded in the vicinity of a photon or electron. Its correct computation requires the calibration of calorimeter energy, the estimation of energy leakage coming from the particle of interest (e/γ) and from pile-up. The scale factor for electron isolation energy is small: the overall difference between data and simulation is of 1-5% The corresponding uncertainties on that scale factor range from about 5% at $E_T = 7$ GeV to 0.5% towards high energies. For photons, the isolation efficiency uncertainty is of 1% in the $[25, 100]$ GeV range and goes up to 1-2% at higher energies.

Electron/photon energy scale and resolution

The simulation of electron/photon (EG) calorimeter energy deposits shows some differences with what is observed in data. This difference in scale and resolution is corrected for in simulation and measured using $Z \to ee$ decays [104].

The uncertainty on the electron and photon energy scale calibration consists of 64 independent nuisance parameters described in reference [105]. They account for calibration uncertainties coming from the various steps used to compute the energy scale, including calibration errors linked to the method used to extract the electron energy scale from $Z \to ee$ decays, uncertainties on scintillator and electronics calibrations, internal calorimeter geometry or material effects.

The uncertainties on the electron/photon energy resolution are described by 9 independent nuisance parameters. They quantify uncertainty on the resolution coming from causes such as the resolution difference between data and simulated samples measured in $Z \to ee$ events, test-beam analysis of EM calorimeter modules or material effects.

Integrated luminosity

The integrated luminosity is computed by combining the measurements of several detectors as described in Section 3.3. The total uncertainty is of 1.7% for the full Run 2 [57]. The

largest component comes from the van der Meer scans calibration transfer to the physics regime (1.3 %), followed by uncertainties on the long-term stability (0.6 %).

Trigger efficiencies

The ratio between the measured trigger efficiency in simulated and real data is used to correct simulations. Two methods can be used to compute the correction scale factor: a *tag and probe* approach or a *bootstrap* method [61]. The uncertainty on that correction factor will depend on the trigger and includes statistical uncertainties on the dataset used and uncertainties on the computation method. Generally, these uncertainties are below 1% for muons [106], of 0.1% for electrons [107], and of 0.5% for di-photons triggers.

7.3 Theoretical uncertainties

The MC simulations used to model the backgrounds and the signal processes have limited accuracy. That is due to the several approximations made during the generation of events which fall into three categories:

- The uncertainty coming from missing higher order terms in the cross-section computation is accounted for by varying the renormalization and factorization scales by a factor of two (scale variation).
- Several sets of parton density function (PDF) are compared to account for the experimental and theoretical uncertainties on the PDF sets used (PDF variation).
- The error coming from the strong coupling constant value α_S is computed by varying the value of α_S used (alphaS variations).

Theoretical uncertainties have been computed for all simulated samples using a dedicated library developed by the ATLAS Physics Modeling Group (PMG) [108], which follows the PDF4LHC recommendations [109] for systematic uncertainties combination.

The different variations for all simulated samples are shown in Figure 7.5. The uncertainty on the simulated $W\gamma\gamma$ and $WH(\rightarrow \gamma\gamma)$ event yields is dominated by the scale variation.

For estimating the total theoretical uncertainty on the $W\gamma\gamma$ signal yields, the scale, PDF and alphaS variations are taken into account separately.

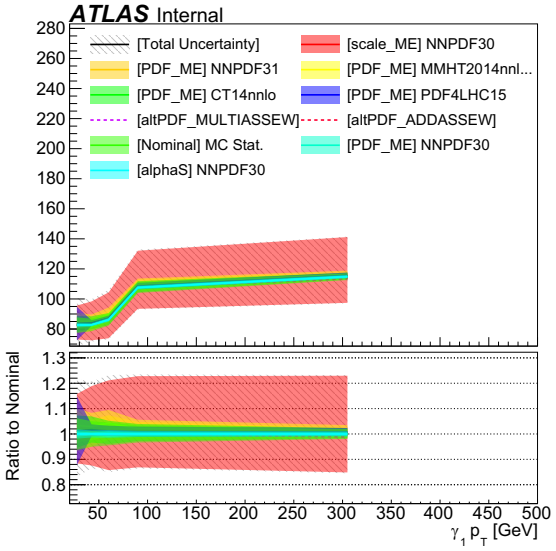

(a)

Figure 7.4: Theoretical uncertainties on the simulated signal process $W\gamma\gamma$ simulated with SHERPA.

For the $W(\rightarrow \tau\nu)\gamma\gamma$ simulated sample, the PDF and scale variations are of similar magnitude and since the p_T dependence of these uncertainties was negligible, an overall systematic is used for that background process. The different uncertainties are combined and the total theoretical uncertainty of $+26.8\%$ -17.4% is used on the $W(\rightarrow \tau\nu)\gamma\gamma$ sample. The diboson sample is treated in the same way and the overall total theoretical uncertainty on the simulated diboson yields is of $\pm 9.2\%$

The uncertainty on the simulated $Z\gamma$ and $Z\gamma\gamma$ samples is dominated by the scale uncertainty and show a p_T dependence. The different uncertainties are combined into a total theoretical uncertainty and the shape is taken into account for more precision. The uncertainty on the predicted event yields varies from $+[50-35]\%$ $-[40-35]\%$ for $Z\gamma$ and $+[30-20]\%$ to $-[25-15]\%$ for the $Z\gamma\gamma$ sample. Finally, the theoretical uncertainties on the$t\bar{t}$, $tt\gamma$ and $tW\gamma$ events yields are dominated be a scale uncertainty as well of 20%. These backgrounds are normalized using a control region. To avoid double counting this

theoretical uncertainty and the uncertainty on the cross-section, no theory uncertainty is applied.

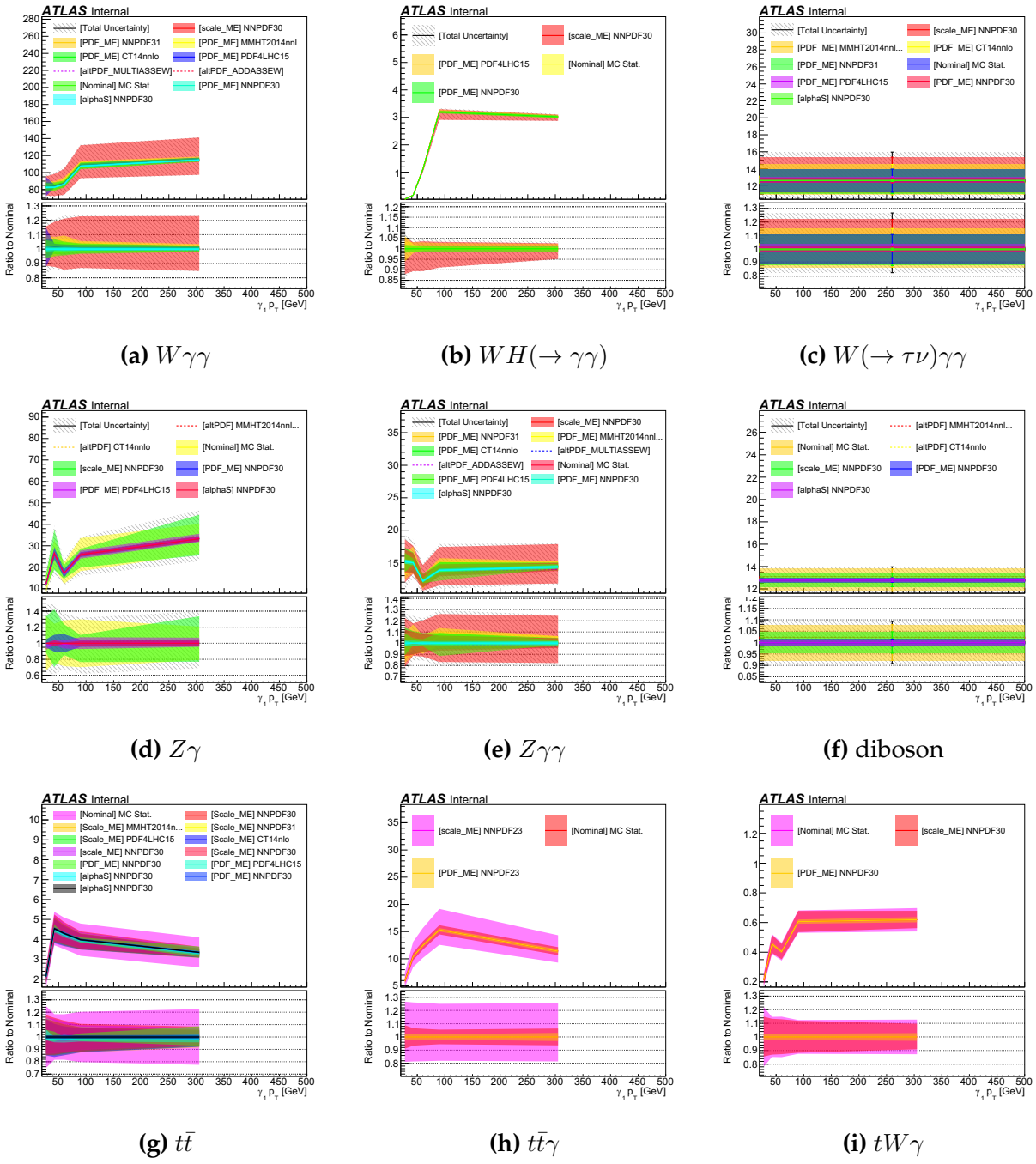

(a) $W\gamma\gamma$ **(b)** $WH(\to \gamma\gamma)$ **(c)** $W(\to \tau\nu)\gamma\gamma$

(d) $Z\gamma$ **(e)** $Z\gamma\gamma$ **(f)** diboson

(g) $t\bar{t}$ **(h)** $t\bar{t}\gamma$ **(i)** $tW\gamma$

Figure 7.5: Theoretical uncertainties on the simulated backgrounds and on the SHERPA $W\gamma\gamma$ signal sample (top left).

Signal modelling uncertainty

The uncertainty on shower modelling for the simulated signal sample is estimated by comparing the MadGraph and signal samples. It is taken as the difference between the two simulated samples and varies from 1% to 10% depending on the leading photon p_{T}. The full SHERPA/Madgraph comparison plots are available in Appendix E.2

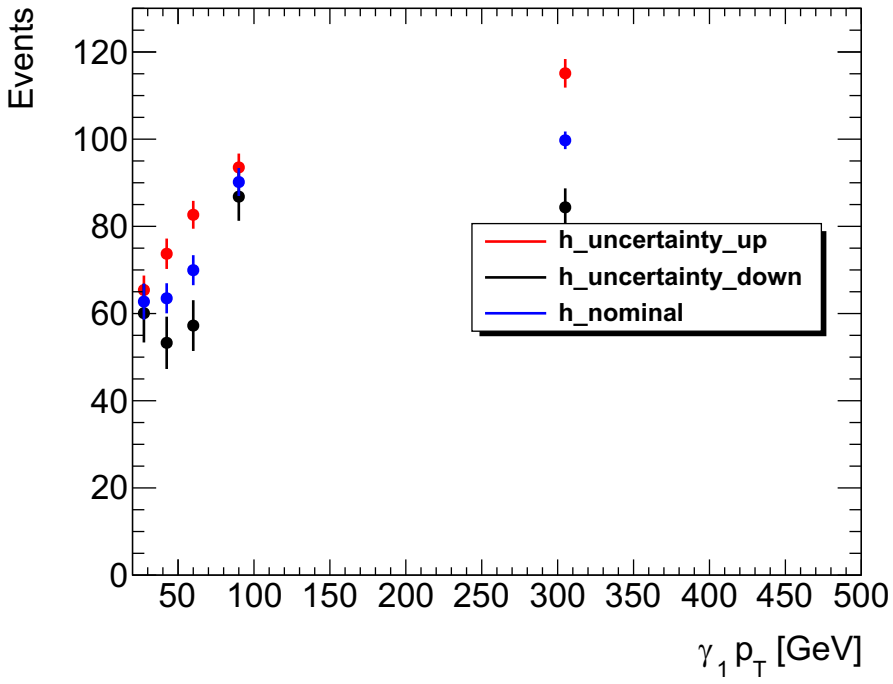

Figure 7.6: Uncertainty in the photon shower modelling derived from a comparison between MadGraph and SHERPA simulated $W\gamma\gamma$ signal events.

Chapter 8

Results

At this point in the analysis, the event yield from different sources of background has been estimated, as well as an uncertainty on these yields. The statistical significance of the number of expected $W\gamma\gamma$ signal events, and the corresponding measurement of the process cross-section, can be calculated. The statistical methods used to extract the signal are first presented in Section 8.1. Then the results of the likelihood fit used to compute the expected statistical significance of the measurement are presented in Section 8.2.

8.1 Statistical method

The statistical methods used to extract the signal and evaluate its significance are introduced in this section. More details on the statistical methods used can be found in references [102] and [103]. The statistical procedures described here are implemented using the TRExFitter framework [110] which is itself based on the HistFactory tool [111].

8.1.1 Signal strength extraction

The signal strength μ is extracted from data using a binned extended likelihood. The likelihood is defined here as the product of Poisson probability distributions ($P(n|\nu) = \frac{\nu^n}{n!}e^{-\nu}$) to observe n_i events in bin i while $\nu = \mu S_i + B_i$ events are expected, with S_i the number of expected signal events and B_i the number of expected background events.

The expected number of events per bin is obtained from the combination of simulated and data-driven estimates.

$$L_{\text{Poisson}}(\mu, \boldsymbol{\alpha}, \boldsymbol{\gamma}, \boldsymbol{\tau}) = \prod_{i \in n_{bim}} P(n_i |\, \mu S_i(\boldsymbol{\alpha}) + B_i(\boldsymbol{\alpha}, \boldsymbol{\gamma}, \boldsymbol{\tau})) \tag{8.1}$$

This likelihood function depends on the signal strength μ which is our Parameter Of Interest (POI) and on Nuisance Parameters (NPs) noted $\boldsymbol{\alpha} = \{\alpha_1, ..., \alpha_n\}, \boldsymbol{\gamma} = \{\gamma, ..., \gamma_m\}, \boldsymbol{\tau} = \{\tau, ..., \tau_p\}$. The signal strength μ corresponds to the signal rate scaled with respect to the Standard Model predicted value: $\mu = \frac{\sigma}{\sigma_{SM}}$. A background only model corresponds to $\mu = 0$ and $\mu = 1$ corresponds to the Standard Model signal. The NPs $\boldsymbol{\alpha}$ represent the modelling and experimental uncertainties, they affect both the signal and background estimates and have been introduced in Section 7. The statistical uncertainties due to the limited size of simulated samples are noted as $\boldsymbol{\gamma}$. Finally the background normalisations parameters $\boldsymbol{\tau}$ will be treated separately as they will be allowed to float in the fit. They are used to rescale some of the background components ($t\bar{t}$ and $tX\gamma$ in this analysis).

Nuisance parameters should be accounted for even though they are not of direct interest. This is done by adding the appropriate *constraint terms* to the likelihood. The NPs $\boldsymbol{\alpha}$ have been estimated via auxiliary measurements but only their central value was obtained. Not knowing their exact distribution, they are approximated with a Gaussian term of mean 0 and variance 1 [103].

$$L_{\text{constrain}}(\boldsymbol{\alpha}) = \prod_{i=1}^{n} G(\alpha_i |\, 0, 1) = \prod_{i=1}^{n} \frac{1}{\sqrt{2\pi}} e^{-\frac{\alpha_i^2}{2}} \tag{8.2}$$

When multiplying the initial likelihood by this constraint term, the likelihood is penalised by a factor that grows smaller as α diverges from its best fit value. Note that some uncertainties, for instance the photon identification efficiency uncertainty, can be correlated across the various types of background. Their effect is estimated over the sum of backgrounds. Other NPs such as the theoretical modelling uncertainties are process depen-

dent and estimated individually for each simulated sample.

The statistical uncertainties $\boldsymbol{\gamma}$ are accounted for in the likelihood by including one γ NP for each bin. They represent the statistical uncertainty on the sum of all backgrounds in that bin. This time, the NP is modelled by a Poisson distribution $P(b_i|\ \gamma_i b_i)$. Since the expected number of events can be non-integer[1] , the usual factorial is replaced by the Gamma function.

$$\begin{aligned} L_{\text{stat}}(\boldsymbol{\gamma}) &= \prod_{i=0}^{bmax} P(b_i|\ \gamma_i b_i) = \prod_{i=0}^{bmax} \frac{(\gamma_i b_i)^{b_i} e^{-\gamma_i b_i}}{\Gamma(b_i+1)} \\ \text{with}: \quad \Gamma(x) &= \int t^{x-1} e^{-t} dt \end{aligned} \tag{8.3}$$

The final expression for the likelihood function used is therefore:

$$L(\mu, \boldsymbol{\alpha}, \boldsymbol{\gamma}, \boldsymbol{\tau}) = \prod_{i=0}^{bmax} P(n_i|\ \mu S_i(\boldsymbol{\alpha}, \boldsymbol{\gamma}) + B_i(\boldsymbol{\alpha}, \boldsymbol{\gamma}, \boldsymbol{\tau})) \prod_{i=1}^{n} G(\alpha_i|\ 0, 1) \prod_{i=0}^{bmax} P(b_i|\ \gamma_i b_i) \tag{8.4}$$

To simplify the notation, NPs are collectively referred to as $\boldsymbol{\theta} = \{\boldsymbol{\alpha}, \boldsymbol{\gamma}, \boldsymbol{\tau}\}$ in the remaining of this section and the likelihood function of Equation 8.4 is then referred to as $L(\mu, \boldsymbol{\theta})$.

To estimate the value of μ from the observed data, a MLE is used. The estimates, noted $\hat{\mu}$ and $\hat{\boldsymbol{\theta}}$ are obtained by finding the global maximum of the likelihood function, or in practice, the global minimum of the negative log-likelihood that is, when :

$$-\frac{\partial \ln(L(\mu, \boldsymbol{\theta})}{\partial \theta_j} = 0, \text{ and } \quad -\frac{\partial \ln(L(\mu, \boldsymbol{\theta})}{\partial \mu} = 0 \tag{8.5}$$

This minimization step is carried out using the standard MINUIT tool [112]. Note that this fitting procedure is first carried out in a dedicated control region in order to define the $t\bar{t}$ and $tX\gamma$ backgrounds scaling coefficients (see Section 8.2.1).

[1] Neither the data-driven techniques nor the simulated samples, which use event weights, yield integers as expected number of background events.

8.1.2 Significance estimation

The aim of this analysis is also to determine if the observed data is compatible with the SM. This is inferred using an hypothesis test. Two hypotheses are compared: H_0 the null hypothesis corresponding to the data coming from background processes only ($\mu = 0$) and H_1 the alternative hypothesis corresponding to the data coming from background + SM signal ($\mu = 1$). To differentiate between these two hypotheses, a profile likelihood ratio is used as test-statistic: [2]

$$q_\mu(x) = -2 \ln \frac{L(x, H_0)}{L(x, H_1)} \tag{8.6}$$

From this quantity, the p-value and significance levels can be defined. The p-value quantifies the probability to observe as many events as were found in data (or more), assuming the null hypothesis to be true.
It is defined as:

$$p_0 = \int_{x_{obs}}^{\infty} q_\mu(x|H_0)dx \tag{8.7}$$

The significance level Z or *observed significance* is often preferred in physics and expresses the p-value in units of sigma (σ). It is defined such that a Gaussian distributed variable found Z standard deviations above its mean has an upper-tail probability equal to p:

$$Z = \Phi^{-1}(1 - p_0) \tag{8.8}$$

where Φ^{-1} is the quantile (inverse of the cumulative distribution) of the standard Gaussian. A 5 σ statistical significance corresponds to a p-value of $p = 2.87 \times 10^{-7}$.

Finally, it is interesting to compute the *expected significance* of an analysis, which corresponds to its expected ability to separate the two hypotheses. It is defined as the significance associated with the median number of expected events under the H_1 hypothesis. It is computed by generating pseudo-data corresponding to the expected numbers of events

[2] A test statistic $t(x)$ is a variable constructed from data, used to test certain hypothesis and determine their level of agreement with observation. They have their own probability density function (probability density function (pdf) $g(t|H)$ and should yield a clear separation of the distributions of $g(t|H_1)$ and $g(t|H_0)$.

obtained from simulations and data-driven estimates for H_0 and H_1 hypotheses. Single-sided significance is used here and it is represented graphically in Figure 8.1

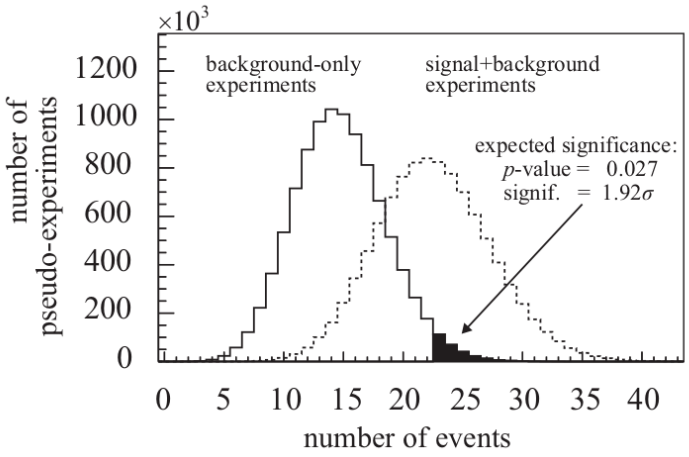

Figure 8.1: Example of probability distribution functions of the number of events for the H_0 (solid line) and H_1 (dashed line) hypotheses. The expected significance corresponds to the integral of the shaded pdf [103].

8.2 Likelihood fit results

To avoid any human bias in the methods developed, the analysis is first *blinded*: the data in the signal region is not looked at before finishing the analysis and only expected significance is computed. However, data in control regions orthogonal to the signal region can be used. The global likelihood fit is therefore performed in control regions, validated in validation regions. *Unblinding* the analysis can only be carried out once all aspects of the analysis have been finalised and with the official approval of the ATLAS collaboration. At the time of this thesis, the $W\gamma\gamma$ analysis is still blinded.

The global likelihood fit is carried out also in order to normalise the $t\bar{t}$ and $tX\gamma$ backgrounds (Section 8.2.1) and to constrain the NP using a control region (Section 8.2.2). The computation of the expected analysis significance also uses the expected yields from the $W\gamma\gamma$ simulated samples (8.2.3).

8.2.1 Top quark background normalisation

In addition to the signal strength μ, the signal and background models contain one NP which value is not known a priori and must be fitted to the data: the normalisation factor of the top quark background. This background includes the $t\bar{t}$, $tW\gamma$ & $t\bar{t}\gamma$ processes. Because of the uncertainty on these processes cross-sections, the MC samples are normalised in a b-jet enriched control region "VR1high" and the normalisation is then validated in the validation region "VR1low". These two regions are defined as follow:

- **VR1high** is defined as the signal region with the b-jet veto cut inverted: $n_{\mathrm{b-jets}} > 0$
- **VR1low** is defined as the signal region with the b-jet veto, $E_{\mathrm{T}}^{\mathrm{miss}}$ and M_{TW} cuts inverted: $n_{\mathrm{b-jets}} > 0$ and $E_{\mathrm{T}}^{\mathrm{miss}} < 25$ GeV and $M_{TW} < 40$ GeV

The fit performed to extract the top background normalisation factor using the TRExFitter framework [110]. All other backgrounds in the control and validation regions are estimated from simulated events since the amount of statistics in real data is too low to use the data-driven methods described in Chapter 6. For this fit, the pile-up background is estimated from the $W\gamma$ simulated samples and the background from jets misidentified as leptons, estimated from the $\gamma\gamma$ simulated samples. The jet faking photon background is estimated using truth matched $W\gamma$ and Wjets simulated samples, scaled by a scale factor of 1 ± 0.37 computed in the signal region (details in Appendix C.2). The result of the fit in the control and validation regions is shown in Figure 8.2. The normalization factor obtained by the fit is:

$$SF_{\mathrm{top}} = 0.65 \pm 0.10 \tag{8.9}$$

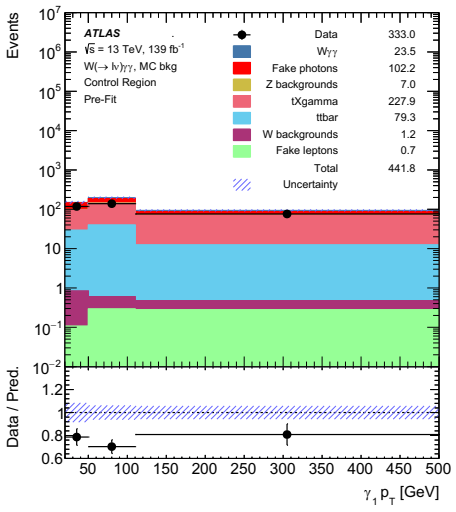

(a) Control region VR1high pre-fit

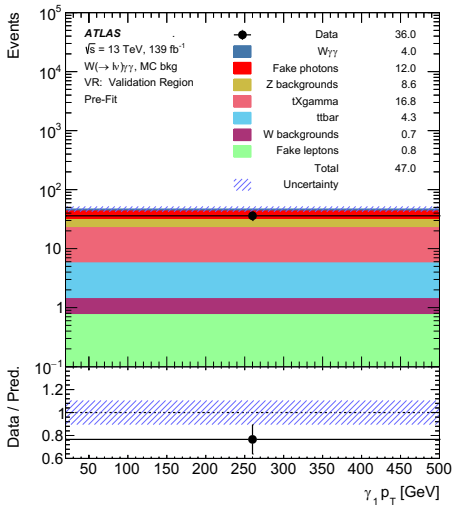

(b) Validation region VR1low pre-fit

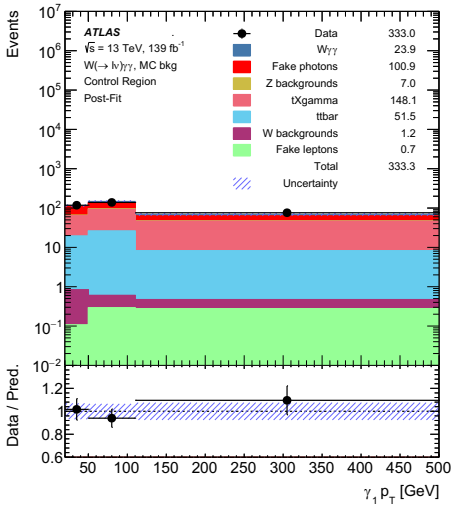

(c) Control region VR1high post-fit

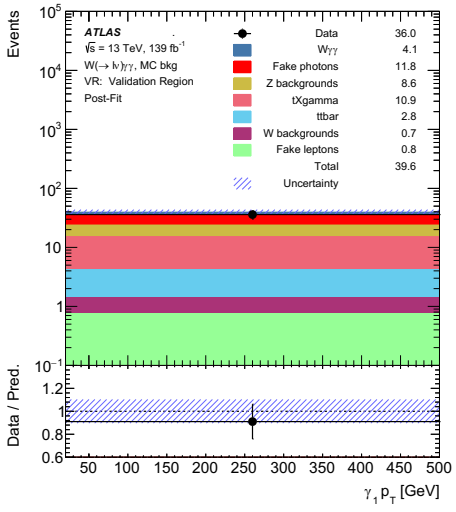

(d) Validation region VR1low post-fit

Figure 8.2: Distributions in the top quark control and validation regions before and after performing the fit to extract an overal normalization scale factor SF_{top} for the top quark background.

8.2.2 Nuisance parameters

Nuisance parameters play a fundamental role in the fit that is carried out in the VR1high control region. To visualise the information of the fit results and spot potential problems, the *pull* of the various NPs are displayed. Pulls quantify the difference between the NP

expected value and its fitted value and are defined as:

$$\text{pull}(\theta) = \frac{\hat{\theta} - \theta_0}{\hat{\sigma}_\theta} \tag{8.10}$$

where $\hat{\theta}$ is the NP central value obtained from the maximum likelihood fit and θ_0 is the input value. Ideally a pull should be close to zero and have an uncertainty of ± 1. A non-zero pull or smaller uncertainty means the NP are constrained by the likelihood fit and potentially implies a problem in the modelling of the various processes considered. Here all the the NP pulls are within the expected range. The list of all pulls is shown in Appendix E.

It is also interesting to measure the *impact* $\Delta\mu$ of the various NPs. It corresponds to the shift in signal strength between the nominal fit and the case where θ is fixed to a $\theta_0 \pm \sigma_\theta$ value:

$$\Delta\mu^{\pm}(\theta) = \hat{\hat{\mu}}_{\theta_0 \pm \sigma_\theta} - \hat{\mu} \tag{8.11}$$

with $\hat{\hat{\mu}}_{\theta_0 \pm \sigma_\theta}$ is the conditional MLE computed for θ fixed but with all other NP allowed to vary. The impact of the various systematic groups are shown in Table 8.1 for the differential estimate, and in Table 8.2 for the total cross-section. For the differential cross-section, the dominant systematic uncertainty is due to the fake photon background estimation and more precisely to the shape extrapolation procedure used to obtain the binned estimate. For the total cross-section, this uncertainty is not present and the biggest impact on the expected significance comes from the combined effect of photon uncertainties on identification, isolation, reconstruction and trigger efficiencies.

8.2.3 Expected significance

The expected distributions for the signal and backgrounds are shown of Figure 8.3. Backgrounds have been grouped into families:

Differential cross-section	
Source of uncertainty	Impact [%]
Fake photons	12.10
Statistical uncertainty	5.29
Photon eff.	4.82
Theory	3.59
Luminosity	2.69
NormFactors	2.24
Muon	1.41
Egamma res. & scale	0.87
Electron eff.	0.54
Pile-up	0.35
Jets	0.27
Total uncertainty	13.96

Table 8.1: Impact of the different systematics groups for the differential estimate. The efficiency groups include uncertainties on ID, isolation, reconstruction and trigger efficiencies for each particle type.

Total cross-section	
Source of uncertainty	Impact [%]
Photon eff.	5.24
Fake photons	3.78
Theory	3.61
Statistical uncertainty	2.96
Luminosity	2.80
ZgSF	2.23
Muon	1.41
Egamma res. & scale	1.07
Pile-up	0.82
Electron eff.	0.55
NormFactors	0.45
Jets	0.21
Total uncertainty	9.13

Table 8.2: Impact of the different systematics groups for the total cross-section.

- Fake photons include the three subcategories of jets faking photons and leptons faking photons.
- Z Backgrounds include the $Z\gamma$ and $Z\gamma\gamma$.
- Top backgrounds refer to $t\bar{t}$, $tW\gamma$ and $t\bar{t}\gamma$.
- Fake leptons are jets misidentified as electrons or muons.
- W Backgrounds regroup the $W(\tau\nu)\gamma\gamma$, $WH(\gamma\gamma)$ and diboson (ZZ, ZW, WW) backgrounds.

The dominant background come from the jets faking photons followed by the Z background. The uncertainty shown is the total uncertainty on the sum of all background sources. It varies from 10% to 20% depending on the p_{T} bin.

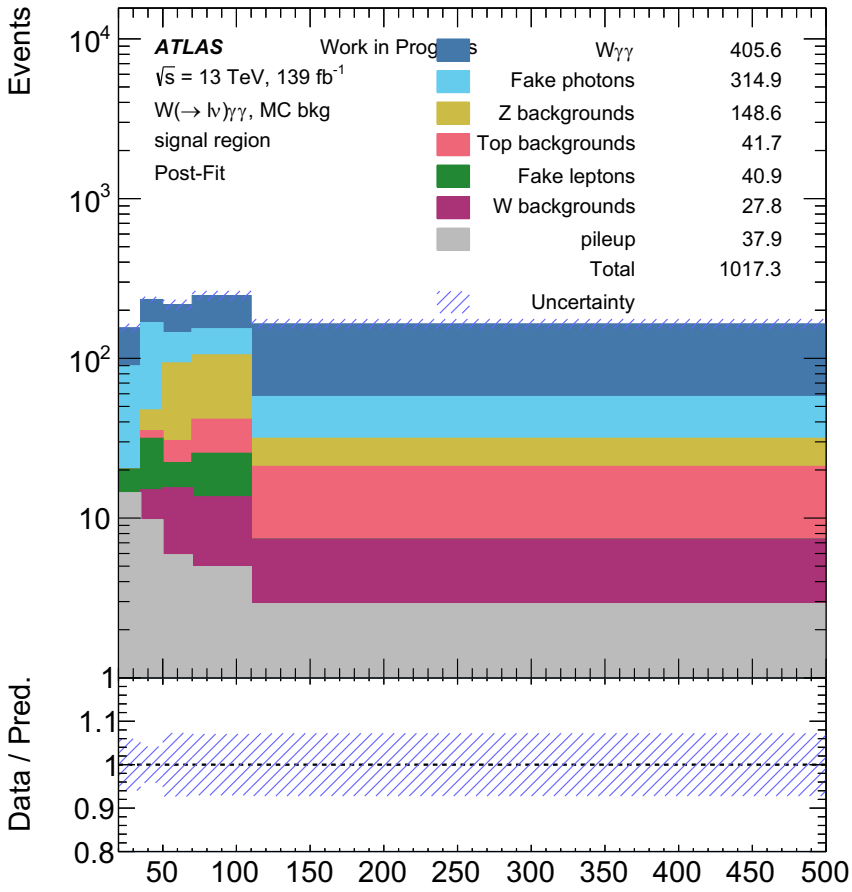

Figure 8.3: Backgrounds and expected signal in the signal region after the likelihood fit.

Finally, using the top quark background scale factor SF_{top}, the expected significance can then be computed both for a differential estimate and for a one bin estimate. Measuring the differential cross-section is especially interesting to constrain potential aQGC in the future, but it also increases the statistical uncertainty and significant systematic uncertainties are added by the extrapolation method used to obtain the differential estimate of the fake photon background. The expected significance measured is:

$$1 \text{ bin} : 7.8\ \sigma \tag{8.12}$$

$$5 \text{ bin} : 5.1\ \sigma \tag{8.13}$$

Chapter 9

Summary and Outlook

The measurement of the $pp \to W\gamma\gamma$ process was presented in this thesis. At the time of writing, the data is still blinded and the expected statistical significance of the total cross-section measurement is of 7.8 σ and of 5.1 σ for the differential cross-section measurement. The main background for this measurement comes from jets misidentified as photons which has been estimated from data using a 2D Template fit method. The other backgrounds are estimated with a combination of data-driven techniques and simulations. For the differential cross-section measurement, the main uncertainty comes from the fake photon background estimate. More data would be required to get a reliable background estimate with a binned 2D-template method.

A few aspects of the analysis are still being investigated. The background coming from electrons misidentified as photons is still being further studied and the corresponding systematic uncertainties have to be evaluated. The finalisation of that background estimate will in turn allow for a more accurate validation of the fake lepton from jets background. No major changes to the cross-section measurement and to its statistical significance are expected as a consequence of that background estimate update. That is because the $Z\gamma$ SF only requires tuning, which will neither change drastically the total number of background events estimated nor the total uncertainty on the cross-section measurement.

Once all background estimations are finalised, the total and differential cross-section measurements will have to be *unfolded*. Unfolding consists in determining the true cross-section at the theoretical level from the measured cross-section. It requires computing the ATLAS detector's efficiency and acceptance corresponding to the selection criteria used for the $W\gamma\gamma$ measurement. The unfolding procedure is currently work in progress. Once the unfolding procedure is finalised, approval from the ATLAS collaboration will be granted to *unblind* the data and the $W\gamma\gamma$ cross-section will be measured. The first observation of the process is expected considering the estimation of the expect statistical significance.

On a longer timescale, the cross-section measurement for the $W\gamma\gamma$ process will be included in global EFT fits. Its sensitivity to dimension-8 operators describing anomalous Quartic Gauge Coupling (aQGC) make it a valuable probe to constrain potential new physics phenomena. Finally, the upcoming LHC Run 3 promises to double the combined integrated luminosity recorded during the LHC Run 1 and Run 2. This increase in statistics will yield a significant improvement in the precision of the $W\gamma\gamma$ differential measurement, especially by allowing a binned 2D Template fit estimation of the fake photon background and reducing the corresponding systematic uncertainty associated to that background. This in turn will provide more stringent constraints on possible anomalous quartic gauge couplings that would indicate the existence of new physical phenomena.

Bibliography

[1] ATLAS collaboration, "Observation of a new particle in the search for the Standard Model Higgs boson with the ATLAS detector at the LHC," *Physics Letters B*, vol. 716, no. 1, pp. 1–29, 2012. 10.1016/j.physletb.2012.08.020.

[2] CMS collaboration, "Observation of a new boson at a mass of 125 GeV with the CMS experiment at the LHC," *Physics Letters B*, vol. 716, no. 1, pp. 30–61, 2012. 10.1016/j.physletb.2012.08.021.

[3] ATLAS Collaboration, "Evidence of $W\gamma\gamma$ production in pp collisions at $\sqrt{s}$ = 8 TeV and limits on anomalous Quartic Gauge Couplings with the ATLAS Detector," *Phys. Rev. Lett.*, vol. 115, p. 031802, 2015. 10.1103/PhysRevLett.115.031802.

[4] CMS Collaboration, "Measurements of the $\mathrm{pp} \to \mathrm{W}^{\pm}\gamma\gamma$ and $\mathrm{pp} \to \mathrm{Z}\gamma\gamma$ cross sections and limits on anomalous quartic gauge couplings at $\sqrt{s}$ = 13 TeV," Tech. Rep. CMS-PAS-SMP-19-013, CERN, Geneva, 2021. cds.cern.ch/record/2756372.

[5] Wikimedia Commons, "Standard Model of Elementary Particle," 2019. (Image) accessed on 23-July-2021 Standard_Model_of_Elementary_Particles.svg.

[6] I. C. Brock, K. Büsser and T. Schörner-Sadenius, *Physics at the Terascale*. John Wiley and Sons, Ltd. 10.1002/9783527634965.ch13.

[7] C. Burgess and G. Moore, *The Standard Model: A Primer*. Cambridge University Press, 2006. 10.1017/CBO9780511819698.

[8] R. P. Feynman, "Mathematical formulation of the quantum theory of electromagnetic interaction," *Phys. Rev.*, vol. 80, pp. 440–457, Nov 1950. 10.1103/PhysRev.80.440.

[9] F. Englert and R. Brout, "Broken symmetry and the mass of gauge vector mesons," *Phys. Rev. Lett.*, vol. 13, pp. 321–323, Aug 1964. 10.1103/PhysRevLett.13.321.

[10] P. W. Higgs, "Broken symmetries, massless particles and gauge fields," *Physics Letters*, vol. 12, no. 2, pp. 132–133, 1964. 10.1016/0031-9163(64)91136-9.

[11] J. Ellis, "Higgs Physics," Tech. Rep. CERN-PH-TH-2013-315, Dec 2013. (Image) 10.5170/CERN-2015-004.117.

[12] T. Asselmeyer-Maluga, *At the frontier of spacetime*. Springer, 2016.

[13] Particle Data Group, "Review of Particle Physics: 26. Dark Matter," *Phys. Rev. D*, vol. 98, 2018. 10.1093/ptep/ptaa104.

[14] F. L. Wilson, "Fermi's theory of beta decay," *American Journal of Physics*, vol. 36, 1968. 10.1119/1.1974382.

[15] O. J. P. Éboli and M. C. Gonzalez-Garcia, "Classifying the bosonic quartic couplings," *Phys. Rev. D*, vol. 93, no. 9, p. 093013, 2016. 10.1103/PhysRevD.93.093013.

[16] ATLAS Collaboration, "Measurements of $W\gamma$ and $Z\gamma$ production in pp collisions at $\sqrt{s}$ = 7 TeV with the ATLAS detector at the LHC," *Phys. Rev. D*, vol. 87, p. 112003, 2013. 10.1103/PhysRevD.87.112003.

[17] ATLAS Collaboration, "Measurement of W^+W^- production in pp collisions at $\sqrt{s}$ = 7 TeV with the ATLAS detector and limits on anomalous WWZ and $WW\gamma$ couplings," *Phys. Rev. D*, vol. 87, p. 112001, 2013. 10.1103/PhysRevD.87.112001.

[18] CMS Collaboration, "Measurement of Wγ production cross section in proton-proton collisions at $\sqrt{s}$ = 13 TeV and constraints on effective field theory coefficients," *Phys. Rev. Lett.*, vol. 126, p. 252002, Jun 2021. 10.1103/PhysRevLett.126.252002.

[19] P. Achard *et al.*, "Study of the $W^+W^-\gamma$ process and limits on anomalous quartic gauge boson couplings at LEP," *Physics Letters B*, vol. 527, p. 29–38, Feb 2002. 10.1016/S0370-2693(02)01167-X.

[20] G. Abbiendi *et al.*, "A study of $W^+W^-\gamma$ events at LEP," *Physics Letters B*, vol. 580, p. 17–36, Jan 2004. 10.1016/j.physletb.2003.10.063.

[21] CMS collaboration, "Observation of the production of three massive gauge bosons at $\sqrt{s}$ = 13 TeV," *Physical Review Letters*, vol. 125, Oct 2020. 10.1103/PhysRevLett.125.151802.

[22] ATLAS Collaboration, "Observation of WWW production in pp collisions at $\sqrt{s}$= 13 TeV with the ATLAS detector," Tech. Rep. ATLAS-CONF-2021-039, CERN, Aug 2021. cds.cern.ch/record/2779173.

[23] ATLAS Collaboration, "Study of $WW\gamma$ and $WZ\gamma$ production in pp collisions at $\sqrt{s}$ = 8 TeV and search for anomalous quartic gauge couplings with the ATLAS experiment," *Eur. Phys. J. C*, vol. 77, p. 646, 2017. 10.1140/epjc/s10052-017-5180-3.

[24] ATLAS Collaboration, "Observation of photon-induced W^+W^- production in pp collisions at $\sqrt{s}$ = 13 TeV using the ATLAS detector," *Phys. Lett. B*, vol. 816, p. 136190, 2021. 10.1016/j.physletb.2021.136190.

[25] ATLAS Collaboration, "Observation of electroweak production of two jets and a Z-boson pair with the ATLAS detector at the LHC," Tech. Rep. CERN-EP-2020-016, Apr 2020. arXiv 2004.10612.

[26] ATLAS Collaboration, "Observation of electroweak production of a same-sign W boson pair in association with two jets in pp collisions at $\sqrt{s}$ = 13 TeV with the ATLAS detector," *Phys. Rev. Lett.*, vol. 123, no. 16, p. 161801, 2019. 10.1103/PhysRevLett.123.161801.

[27] ATLAS Collaboration, "Evidence of W$\gamma\gamma$ Production in pp Collisions at $\sqrt{s}$ = 8 TeV and Limits on Anomalous Quartic Gauge Couplings with the ATLAS Detector," *Phys. Rev. Lett.*, vol. 115, no. 3, p. 031802, 2015. 10.1103/PhysRevLett.115.031802.

[28] CMS collaboration, "Measurements of the $pp \to W\gamma\gamma$ and $pp \to Z\gamma\gamma$ cross sections and limits on anomalous quartic gauge couplings at $\sqrt{s}$ = 8 TeV," *Journal of High Energy Physics*, vol. 72, no. 10, p. 031802, 2017. 10.1007/JHEP10(2017)072.

[29] L. Evans and P. Bryant, "LHC machine," *Journal of Instrumentation*, vol. 3, no. 08, p. S08001, 2008. 10.1088/1748-0221/3/08/s08001.

[30] ATLAS Collaboration, "The ATLAS experiment at the CERN large hadron collider," *Journal of Instrumentation*, vol. 3, no. 08, p. S08003, 2008. 10.1088/1748-0221/3/08/s08003.

[31] ALICE Collaboration, "The ALICE experiment at the CERN LHC," *Journal of Instrumentation (JINST)*, vol. 3, p. S08002, 2008. 10.1088/1748-0221/3/08/S08002.

[32] CMS Collaboration, "The CMS Experiment at the CERN LHC," *Journal of Instrumentation (JINST)*, vol. 3, p. S08004, 2008. 10.1088/1748-0221/3/08/S08004.

[33] LHCb Collaboration, "The LHCb Detector at the LHC," *Journal of Instrumentation (JINST)*, vol. 3, p. S08005, 2008. 10.1088/1748-0221/3/08/S08005.

[34] C. Lefèvre, "The CERN accelerator complex. Complexe des accélérateurs du CERN." (Image) cds.cern.ch/record/1260465, Dec 2008.

[35] "Radiofrequency cavities," Sep 2012. (Image) cds.cern.ch/record/1997424.

[36] M. Rayner, "Final stretch for LHC upgrades," *CERN Courier*, Dec 2020. https://cerncourier.com/a/final-stretch-for-lhc-upgrades/.

[37] European Strategy Group, "2020 Update of the European strategy for particle physics," Tech. Rep. CERN-ESU-015, Geneva, 2020. cds.cern.ch/record/2721370.

[38] *ATLAS inner detector: Technical Design Report, 1*. Technical design report. ATLAS, Geneva: CERN, 1997. cds.cern.ch/record/331063.

[39] S. Haywood *et al.*, *ATLAS inner detector: Technical Design Report, 2*. Technical design report. ATLAS, Geneva: CERN, 1997. cds.cern.ch/record/331064.

[40] ATLAS Collaboration, "Studies of the performance of the ATLAS detector using cosmic-ray muons," *Eur. Phys. J. C*, vol. 71, p. 1593, 2011. 10.1140/epjc/s10052-011-1593-6.

[41] ATLAS Collaboration, *ATLAS: a 25-year insider story of the LHC experiment*. Advanced series on directions in high energy physics, Singapore: World Scientific, 2019. cds.cern.ch/record/2636577.

[42] ATLAS Collaboration, "ATLAS pixel detector electronics and sensors," *Journal of Instrumentation*, vol. 3, pp. P07007–P07007, Jul 2008. 10.1088/1748-0221/3/07/p07007.

[43] A. Vogel, "ATLAS Transition Radiation Tracker (TRT): straw tube gaseous detectors at high rates," Tech. Rep. ATL-INDET-PROC-2013-005, CERN, Geneva, Apr 2013. cds.cern.ch/record/1537991.

[44] M. Capeans *et al.*, *ATLAS Insertable B-Layer Technical Design Report*. Sep 2010. cds.cern.ch/record/1291633.

[45] A. La Rosa, "The ATLAS insertable B-Layer: from construction to operation," Tech. Rep. ATL-INDET-PROC-2013-005, 2016. arXiv:1610.01994.

[46] Particle Data Group, "Review of particle physics," *Progress of Theoretical and Experimental Physics*, vol. 2020, no. 8, 2020. 10.1093/ptep/ptaa104.

[47] ATLAS Collaboration, *ATLAS liquid-argon calorimeter: Technical Design Report*. Geneva: CERN, 1996. cds.cern.ch/record/331061.

[48] ATLAS Collaboration, "Electron and photon energy calibration with the ATLAS detector using 2015–2016 LHC proton-proton collision data," *Journal of Instrumentation*, vol. 14, no. 03, p. P03017–P03017, 2019. 10.1088/1748-0221/14/03/P03017.

[49] ATLAS Collaboration, *ATLAS tile calorimeter: Technical design report*. No. CERN-LHCC-96-42, Dec 1996. cds.cern.ch/record/331062.

[50] ATLAS Collaboration, "Testbeam studies of production modules of the ATLAS Tile Calorimeter," *Nucl. Instrum. Methods Phys. Res., A*, vol. 606, no. 3, pp. 362–394, 2009. 10.1016/j.nima.2009.04.009.

[51] A. Artamonov *et al.*, "The ATLAS forward calorimeter," *Journal of Instrumentation*, vol. 3, no. 02, pp. P02010–P02010, 2008. 10.1088/1748-0221/3/02/p02010.

[52] ATLAS Collaboration, *ATLAS muon spectrometer: Technical Design Report*. Geneva: CERN, 1997. cds.cern.ch/record/331068.

[53] N. P. Hessey, "The precision drift chambers for the ATLAS muon spectrometer," *Nucl. Instrum. Methods Phys. Res., A*, vol. 419, no. 2-3, pp. 326–30, 1998. 10.1016/S0168-9002(98)00867-5.

[54] T. Argyropoulos *et al.*, "Cathode strip chambers in ATLAS: Installation, commissioning and in situ performance," IEEE Nuclear Science Symposium Conference Record, pp. 2819–2824, Dec. 2008. 10.1109/NSSMIC.2008.4774958.

[55] R. Santonico and R. Cardarelli, "Development of resistive plate counters," *Nucl. Instrum. Methods Phys. Res.*, vol. 187, no. 2, pp. 377–380, 1981. 10.1016/0029-554X(81)90363-3.

[56] K. Nagai, "Thin gap chambers in ATLAS," *Nucl. Instrum. Methods Phys. Res., A*, vol. 384, no. 1, pp. 219–221, 1996. 10.1016/S0168-9002(96)01065-0.

[57] ATLAS Collaboration, "Luminosity determination in pp collisions at $\sqrt{s}$ = 13 TeV using the ATLAS detector at the LHC," Tech. Rep. ATLAS-CONF-2019-021, CERN, Geneva, Jun 2019. cds.cern.ch/record/2677054.

[58] G. Avoni *et al.*, "The new LUCID-2 detector for luminosity measurement and monitoring in ATLAS," *Journal of Instrumentation*, vol. 13, pp. P07017–P07017, Jul 2018. 10.1088/1748-0221/13/07/p07017.

[59] V. Cindro *et al.*, "The ATLAS beam conditions monitor," *Journal of Instrumentation*, vol. 3, pp. P02004–P02004, Feb 2008. 10.1088/1748-0221/3/02/p02004.

[60] S. van der Meer, "Calibration of the effective beam height in the ISR," Tech. Rep. CERN-ISR-PO-68-31, ISR-PO-68-31, CERN, Geneva, 1968. cds.cern.ch/record/296752.

[61] ATLAS Collaboration, "Performance of the ATLAS Trigger System in 2015," *Eur. Phys. J. C*, vol. 77, p. 317. 76 p, Nov 2016. 10.1140/epjc/s10052-017-4852-3.

[62] A. Ruiz Martinez on behalf of the ATLAS Collaboration, "The Run 2 ATLAS trigger system," *Journal of Physics: Conference Series*, vol. 762, p. 012003, Oct 2016. 10.1088/1742-6596/762/1/012003.

[63] J. Pequenao and P. Schaffner, "How ATLAS detects particles: diagram of particle paths in the detector," Tech. Rep. CERN-EX-1301009, Jan 2013. cds.cern.ch/record/1505342.

[64] ATLAS Collaboration, "Performance of the ATLAS track reconstruction algorithms in dense environments in LHC Run 2," *Eur. Phys. J. C*, vol. 77, p. 673, 2017. 10.1140/epjc/s10052-017-5225-7.

[65] R. E. Kalman, "A new approach to linear filtering and prediction problems," *Journal of Basic Engineering*, vol. 82.1, p. 35, 1960. 10.1115/1.3662552.

[66] ATLAS Collaboration, "Vertex reconstruction performance of the ATLAS detector at $\sqrt{s}$ = 13 TeV," Tech. Rep. ATL-PHYS-PUB-2015-026, 2015. cds.cern.ch/record/2037717.

[67] ATLAS collaboration, "Reconstruction of primary vertices at the ATLAS experiment in Run 1 proton–proton collisions at the LHC," *Eur. Phys. J. C*, vol. 77, May 2017. 10.1140/epjc/s10052-017-4887-5.

[68] W. Lampl *et al.*, "Calorimeter clustering algorithms: Description and performance," Tech. Rep. ATL-COM-LARG-2008-003, CERN, Geneva, Apr 2008. cds.cern.ch/record/1099735.

[69] ATLAS collaboration, "Topological cell clustering in the ATLAS calorimeters and its performance in LHC Run 1," *Eur. Phys. J. C*, vol. 77, Jul 2017. 10.1140/epjc/s10052-017-5004-5.

[70] ATLAS collaboration, "Electron and photon energy calibration with the ATLAS detector using 2015-2016 LHC proton-proton collision data," *Journal of Instrumentation (JINST)*, vol. 14, p. P03017. 61 p, Dec 2018. 10.1088/1748-0221/14/03/P03017.

[71] ATLAS collaboration, "Electron reconstruction and identification in the ATLAS experiment using the 2015 and 2016 LHC proton–proton collision data at $\sqrt{s}$ = 13 TeV," *Eur. Phys. J. C*, vol. 79, no. 639, 2015. 0.1140/epjc/s10052-019-7140-6.

[72] ATLAS collaboration, "Measurement of the photon identification efficiencies with the ATLAS detector using LHC Run 2 data collected in 2015 and 2016," *Eur. Phys. J. C*, vol. 79, p. 205. 55 p, Oct 2018. 10.1140/epjc/s10052-019-6650-6.

[73] R. Frühwirth, "A gaussian-mixture approximation of the bethe–heitler model of electron energy loss by bremsstrahlung," *Computer Physics Communications*, vol. 154, no. 2, pp. 131–142, 2003. 10.1016/S0010-4655(03)00292-3.

[74] ATLAS collaboration, "Muon reconstruction performance of the ATLAS detector in proton–proton collision data at $\sqrt{s}$ = 13 TeV," *Eur. Phys. J. C*, vol. 76, p. 292, May 2016. 10.1140/epjc/s10052-016-4120-y.

[75] M. Cacciari, G. P. Salam and G. Soyez, "The anti-kt jet clustering algorithm," *Journal of High Energy Physics*, vol. 2008, pp. 063–063, Apr 2008. 10.1088/1126-6708/2008/04/063.

[76] ATLAS collaboration, "Jet reconstruction and performance using particle flow with the ATLAS detector," *Eur. Phys. J. C*, vol. 77, Jul 2017. 10.1140/epjc/s10052-017-5031-2.

[77] M. Cacciari and G. P. Salam, "Pileup subtraction using jet areas," *Physics Letters B*, vol. 659, no. 1, pp. 119–126, 2008. 10.1016/j.physletb.2007.09.077.

[78] ATLAS collaboration, "ATLAS b-jet identification performance and efficiency measurement with $t\bar{t}$ events in pp collisions at $\sqrt{s}$ = 13 TeV," *Eur. Phys. J. C*, vol. 79, Nov 2019. 10.1140/epjc/s10052-019-7450-8.

[79] ATLAS Collaboration, "Optimisation and performance studies of the ATLAS b-tagging algorithms for the 2017-18 LHC run," Tech. Rep. ATL-PHYS-PUB-2017-013, CERN, Geneva, Jul 2017. cds.cern.ch/record/2273281.

[80] ATLAS Collaboration, "Secondary vertex finding for jet flavour identification with the ATLAS detector," Tech. Rep. ATL-PHYS-PUB-2017-011, CERN, Geneva, Jun 2017. cds.cern.ch/record/2270366.

[81] ATLAS Collaboration, "Topological b-hadron decay reconstruction and identification of b-jets with the JetFitter package in the ATLAS experiment at the LHC," Tech. Rep. ATL-PHYS-PUB-2018-025, CERN, Oct 2018. cds.cern.ch/record/2645405.

[82] ATLAS collaboration, "Performance of missing transverse momentum reconstruction with the ATLAS detector using proton–proton collisions at $\sqrt{s}$ = 13 TeV," *Eur. Phys. J. C*, vol. 78, Nov 2018. 10.1140/epjc/s10052-018-6288-9.

[83] ATLAS collaboration, "ATLAS data quality operations and performance for 2015–2018 data-taking," *Journal of Instrumentation (JINST)*, vol. 15, pp. P04003–P04003, apr 2020. 10.1088/1748-0221/15/04/p04003.

[84] A. Buckley *et al.*, "General-purpose event generators for LHC physics," *Physics Reports*, vol. 504, p. 145–233, Jul 2011. 10.1016/j.physrep.2011.03.005.

[85] S. Agostinelli *et al.*, "Geant4 – a simulation toolkit," *Nucl. Instrum. Methods Phys. Res., A*, vol. 506, no. 3, pp. 250–303, 2003. 10.1016/S0168-9002(03)01368-8.

[86] E. Bothmann *et al.*, "Event generation with Sherpa 2.2," *SciPost Physics*, vol. 7, Sep 2019. 10.21468/SciPostPhys.7.3.034.

[87] J. Alwall *et al.*, "The automated computation of tree-level and next-to-leading order differential cross sections, and their matching to parton shower simulations," *Journal of High Energy Physics*, vol. 2014, Jul 2014. 10.1007/JHEP07(2014)079.

[88] R. Frederix *et al.*, "The automation of next-to-leading order electroweak calculations," *JHEP*, vol. 07, p. 185, 2018. 10.1007/JHEP07(2018)185.

[89] ATLAS collaboration, "Jet energy scale measurements and their systematic uncertainties in proton-proton collisions at $\sqrt{s}$ = 13 TeV with the ATLAS detector," *Physical Review D*, vol. 96, Oct 2017. 10.1103/PhysRevD.96.072002.

[90] ATLAS collaboration, "Tagging and suppression of pileup jets with the ATLAS detector," Tech. Rep. ATLAS-CONF-2014-018, CERN, May 2014. cds.cern.ch/record/1700870.

[91] ATLAS Collaboration, "Performance of missing transverse momentum reconstruction with the ATLAS detector in the first proton–proton collisions at $\sqrt{s}$ = 13 TeV." ATL-PHYS-PUB-2015-027, 2015. cds.cern.ch/record/2037904.

[92] ATLAS collaboration, "Met utility tool." `https://gitlab.cern.ch/atlas/athena/tree/21.2/Reconstruction/MET/METUtilities`.

[93] D. Adams *et al.*, "Recommendations of the physics objects and analysis harmonisation study groups," Tech. Rep. ATL-PHYS-INT-2014-018, CERN, Jul 2014. cds.cern.ch/record/1743654.

[94] ATLAS collaboration, "Overlap removal tool." `https://gitlab.cern.ch/atlas/athena/tree/21.2/PhysicsAnalysis/AnalysisCommon/AssociationUtils`. version 21.2, 2021-06-21.

[95] N. Proklova *et al.*, "Measurements of Photon efficiencies in pp collision data collected in 2015, 2016 and 2017 at $\sqrt{s}$ = 13 TeV with the ATLAS detector," Tech. Rep. ATL-COM-PHYS-2018-1604, CERN, Geneva, Nov 2018. cds.cern.ch/record/2647979.

[96] S. Das, "A simple alternative to the crystal ball function." arXiv:1603.08591, 2016.

[97] A. D. Bukin, "Fitting function for asymmetric peaks." arXiv:0711.4449, 2007.

[98] W. Verkerke and D. P. Kirkby, "The RooFit toolkit for data modeling," *eConf*, vol. C0303241, p. MOLT007, 2003. arXiv:physics/0306116.

[99] K. Cranmer, "Kernel estimation in high-energy physics," *Computer Physics Communications*, vol. 136, p. 198–207, May 2001. 10.1016/S0010-4655(00)00243-5.

[100] ATLAS Collaboration, "Measurement of the $Z(\to l^+l^-)\gamma$ production cross-section in pp collisions at $\sqrt{s}$ = 13 TeV with the ATLAS detector," *Journal of High Energy Physics*, vol. 2020, Mar 2020. 10.1007/JHEP03(2020)054.

[101] F. Cardillo *et al.*, "Tools for estimating fake/non-prompt lepton backgrounds in ATLAS," Tech. Rep. ATL-COM-PHYS-2019-1071, CERN, Geneva, 2021. cds.cern.ch/record/2686919.

[102] O. Behnke *et al.*, *Data Analysis in High Energy Physics A Practical Guide to Statistical Methods*. Jun 2013.

[103] K. Cranmer, *Practical statistics for the LHC*. No. CERN-2014-003, 2015. arXiv:1503.07622.

[104] ATLAS collaboration, "Electron and photon performance measurements with the ATLAS detector using the 2015-2017 LHC proton-proton collision data," *Journal of Instrumentation (JINST)*, vol. 14, p. P12006. 70 p, Aug 2019. 10.1088/1748-0221/14/12/P12006.

[105] T. Guillemin *et al.*, "Energy scale and resolution systematics: summary and correlations," Tech. Rep. ATL-COM-PHYS-2017-754, CERN, Geneva, Jun 2017. cds.cern.ch/record/2268796.

[106] ATLAS collaboration, "Performance of the ATLAS muon triggers in Run 2," *Journal of Instrumentation (JINST)*, vol. 15, pp. P09015–P09015, Sep 2020. 10.1088/1748-0221/15/09/p09015.

[107] ATLAS collaboration, "Performance of electron and photon triggers in ATLAS during LHC Run 2," *Eur. Phys. J. C*, vol. 80, no. 47, 2020. 10.1140/epjc/s10052-019-7500-2.

[108] ATLAS Physics Modeling Group, "PMG Systematics Tool." https://twiki.cern.ch/twiki/bin/viewauth/AtlasProtected/PMGSystematicsTool. 2021-04-01.

[109] J. Butterworth *et al.*, "PDF4LHC recommendations for LHC Run 2," *Journal of Physics G: Nuclear and Particle Physics*, vol. 43, p. 023001, Jan 2016. 10.1088/0954-3899/43/2/023001.

[110] M. Pinamonti *et al.*, "TRExFitter framework." https://gitlab.cern.ch/TRExStats/TRExFitter/-/tree/master, 2021. version 00-04-10.

[111] K. Cranmer *et al.*, "HistFactory: A tool for creating statistical models for use with RooFit and RooStats," Tech. Rep. CERN-OPEN-2012-016, New York U., Jan 2012. cds.cern.ch/record/1456844.

[112] F. James and M. Roos, "Minuit: a system for function minimization and analysis of the parameter errors and correlations," *Comput. Phys. Commun.*, vol. 10, pp. 343–367, 1975. 10.1016/0010-4655(75)90039-9.

[113] H. Abreu *et al.*, "Measurement of isolated di-photon cross section in pp collision at $\sqrt{s}$ = 7 TeV with the ATLAS detector," Tech. Rep. ATL-COM-PHYS-2011-301, CERN, Geneva, Mar 2011. cds.cern.ch/record/1337015.

[114] P. Bell *et al.*, "Measurement of $W\gamma\gamma$ production in proton-proton collisions at $\sqrt{s}$ = 8 TeV with the ATLAS detector," Tech. Rep. ATL-COM-PHYS-2013-910, CERN, Geneva, Jul 2013. cds.cern.ch/record/1560073.

Acronyms

aQGC	anomalous Quartic Gauge Coupling 120
BSM	Beyond Standard Model 1
CMOS	Complementary Metal-Oxide Semiconductor
CR	control region 55
CSC	Cathode strip chamber 33
DM	Dark Matter 1
EFT	Effective Field Theory 5
EM	electomagnetic 29
EWSB	Electroweak Symmetry Breaking 7
FCAL	Forward Calorimeter 29
FF	Fake Factor 91
FSR	Final State Radiation 2
GSF	Gaussian Sum Filter 45
HEC	Hadronic End-cap Calorimeter 29
HL-LHC	High Luminosity LHC 23
HLT	High Level Trigger 37
IBL	Inner b-Layer 29
ID	Inner Detector 24
ISR	Initial State Radiation 2

JVT Jet Vertex Tagger 62

L1 Level 1 trigger 37

LAr liquid argon 30

LEP Large Electron Positron collider 23

LHC Large Hadron Collider iii

MC Monte Carlo iii

MDT Monitored Drift Tube 33

MIP Minimum Ionizing Particle 32

MLE Maximum Likelihood Estimate 93

MS Muon Spectrometer 25

NP Nuisance Parameter 110

NSW New Small Wheel viii

pdf probability density function 112

PMT Photomultiplier Tube 31

POI Parameter Of Interest 110

PS Proton Synchrotron 21

PV Primary Vertex 43

QCD Quantum Chromodynamics 7

QED Quantum Electrodynamics 7

QGC Quartic Gauge Coupling 1

RF radio frequency 20

RoI Regions of Interest 38

RPC Resistive Plate Chamber 34

SCT Semi-Conductor Tracker 28

SF Scale Factor 72

SM Standard Model 1

SPS Super Proton Synchrotron 21

SR signal region 54

sTGC small-Strip Thin Gap Chamber viii

TGC Thin Gap Chambers 34

TRT Transition Radiation Tracker 27

Appendix A

Trigger List

Here is the detailed list of the trigger selection criteria used for this analysis. Note that for the elctron channel control regions, several single electron triggers are combined as they are seeded from different L1 triggers.

Signal region

- Muon:
  - 2015-2018: HLT_2g10_loose_mu20
- Electron:
  - 2015: HLT_e20_lhmedium_2g10_loose
  - 2016: HLT_e20_lhmedium_nod0_2g10_loose
  - 2017-2018: HLT_e24_lhmedium_nod0_2g12_loose

Control region

- Muon:
  - 2015: HLT_mu20_iloose_L1MU15
  - 2016-2018: muon:HLT_mu26_ivarmedium
- Electron:
  - 2015:HLT_e24_lhmedium_L1EM20VH, e60_lhmedium, e120_lhloose
  - 2016-2018: HLT_e26_lhtight_nod0_ivarloose, e60_lhmedium_nod0, e140_lhloose_nod0

Appendix B

MC sample list

Sample	Generator	Cross-section in [nb]
Wgg NLO		
$pp \to W(\to e\nu)\gamma\gamma$	SHERPA 2.2.10	$2.01\ 10^{-3}$
$pp \to W(\to \mu\nu)\gamma\gamma$	SHERPA 2.2.10	$2.01\ 10^{-3}$
$pp \to W(\to \tau\nu)\gamma\gamma$	SHERPA 2.2.10	$2.01\ 10^{-3}$
$pp \to W(\to e\nu)\gamma\gamma, \quad m_{\gamma\gamma} \in [0, 80]$ GeV	MADGRAPH5_aMC@NLO	$1.49\ 10^{-4}$
$pp \to W(\to e\nu)\gamma\gamma, \quad m_{\gamma\gamma} > 80$ GeV	MADGRAPH5_aMC@NLO	$7.15\ 10^{-5}$
$pp \to W(\to \mu\nu)\gamma\gamma, \quad m_{\gamma\gamma} \in [0, 80]$ GeV	MADGRAPH5_aMC@NLO	$1.49\ 10^{-4}$
$pp \to W(\to \mu\nu)\gamma\gamma, \quad m_{\gamma\gamma} > 80$ GeV	MADGRAPH5_aMC@NLO	$7.15\ 10^{-5}$
Wgg LO		
$pp \to W(\to e\nu)\gamma\gamma, \quad p_T^{\gamma 2} \in [9, 17]$ GeV	SHERPA 2.2.2	$4.40\ 10^{-4}$
$pp \to W(\to e\nu)\gamma\gamma, \quad p_T^{\gamma 2} > 17$ GeV, $m_{\gamma\gamma} \in [0, 80]$ GeV	SHERPA 2.2.2	$7.15\ 10^{-5}$
$pp \to W(\to e\nu)\gamma\gamma, \quad p_T^{\gamma 2} > 17$ GeV, $m_{\gamma\gamma} > 80$ GeV	SHERPA 2.2.2	$3.79\ 10^{-5}$
$pp \to W(\to \mu\nu)\gamma\gamma, \quad p_T^{\gamma 2} \in [9, 17]$ GeV	SHERPA 2.2.2	$4.40\ 10^{-4}$
$pp \to W(\to \mu\nu)\gamma\gamma, \quad p_T^{\gamma 2} > 17$ GeV, $m_{\gamma\gamma} \in [0, 80]$ GeV	SHERPA 2.2.2	$7.15\ 10^{-5}$
$pp \to W(\to \mu\nu)\gamma\gamma, \quad p_T^{\gamma 2} > 17$ GeV, $m_{\gamma\gamma} > 80$ GeV	SHERPA 2.2.2	$3.79\ 10^{-5}$
WHgg		
$pp \to W(\to e\nu)H(\to \gamma\gamma)$	Powheg & Pythia8	$5.40\ 10^{-4}$
$pp \to W(\to \mu\nu)H(\to \gamma\gamma)$	Powheg & Pythia8	$8.62\ 10^{-4}$
Zgg NLO		

$pp \to Z(\to e^+e^-)\gamma\gamma$	SHERPA 2.2.10	$1.32\ 10^{-3}$
$pp \to Z(\to mu^+mu^-)\gamma\gamma$	SHERPA 2.2.10	$1.32\ 10^{-3}$
$pp \to Z(\to \tau^+\tau^-)\gamma\gamma$	SHERPA 2.2.10	$1.32\ 10^{-3}$
$pp \to Z(\to \nu\bar{\nu})\gamma\gamma$	SHERPA 2.2.10	$2.37\ 10^{-3}$
Wg NLO		
$pp \to W(\to e\nu)\gamma$	SHERPA 2.2.10	0.356
$pp \to W(\to \mu\nu)\gamma$	SHERPA 2.2.10	0.356
$pp \to W(\to \tau\nu)\gamma$	SHERPA 2.2.10	0.356
Zg NLO		
$pp \to Z(\to e^+e^-)\gamma$	SHERPA 2.2.10	$9.87\ 10^{-2}$
$pp \to Z(\to \mu^+\mu^-)\gamma$	SHERPA 2.2.10	$9.87\ 10^{-2}$
$pp \to Z(\to \tau^+\tau^-)\gamma$	SHERPA 2.2.10	$9.87\ 10^{-2}$
$pp \to Z(\to e^+e^-)\gamma$ HT0_125	MADGRAPH5_aMC@NLO	$2.09\ 10^{-2}$
$pp \to Z(\to e^+e^-)\gamma$ HTGT125_MjjLT150	MADGRAPH5_aMC@NLO	$1.02\ 10^{-2}$
$pp \to Z(\to e^+e^-)\gamma$ HTGT125_MjjLT500	MADGRAPH5_aMC@NLO	$1.02\ 10^{-2}$
$pp \to Z(\to e^+e^-)\gamma$ HTGT125_MjjGT150	MADGRAPH5_aMC@NLO	$1.02\ 10^{-2}$
ttbar		
$pp \to t\bar{t}$, dileptonic, lepton+jets channels	Powheg & Pythia8	0.397
$pp \to t\bar{t}$, fully hadronic channels	Powheg & Pythia8	0.333
tXgamma		
$pp \to t\bar{t}\gamma$, dileptonic, lepton+jets channels	MadGraph & Pythia8	$4.62\ 10^{-3}$
$pp \to tW\gamma$, GamFromDec	MadGraph & Pythia8	$2.88\ 10^{-4}$
$pp \to tW\gamma$,	MadGraph & Pythia8	$1.23\ 10^{-4}$
Diboson		
$pp \to ll\nu\nu$	SHERPA 2.2.2	$1.25\ 10^{-2}$
$pp \to lll\nu$	SHERPA 2.2.2	$4.57\ 10^{-3}$
$pp \to llll$	SHERPA 2.2.2	$1.25\ 10^{-3}$
Diphoton		
$pp \to \gamma\gamma$, $m_{\gamma\gamma} < 50$ GeV	SHERPA 2.2.4	$9.35\ 10^{-2}$
$pp \to \gamma\gamma$, $m_{\gamma\gamma} \in [50, 90]$ GeV	SHERPA 2.2.4	0.139
$pp \to \gamma\gamma$, $m_{\gamma\gamma} \in [90, 175]$ GeV	SHERPA 2.2.4	$5.18\ 10^{-2}$
$pp \to \gamma\gamma$, $m_{\gamma\gamma} \in [175, 2000]$ GeV	SHERPA 2.2.4	$1.10\ 10^{-2}$

$pp \to \gamma\gamma, \quad m_{\gamma\gamma} > 2000$ GeV	SHERPA 2.2.4	$7.03\ 10^{-7}$
W-jets		
$pp \to W(\to e\nu) + \text{jets}$, b filter	SHERPA 2.2.10	0.186
$pp \to W(\to e\nu) + \text{jets}$, b veto, c filter	SHERPA 2.2.10	2.91
$pp \to W(\to e\nu) + \text{jets}$, c & b veto	SHERPA 2.2.10	17.0
$pp \to W(\to \mu\nu) + \text{jets}$, b filter	SHERPA 2.2.10	0.182
$pp \to W(\to \mu\nu) + \text{jets}$, b veto, c filter	SHERPA 2.2.10	2.90
$pp \to W(\to \mu\nu) + \text{jets}$, c & b veto	SHERPA 2.2.10	17.0
$pp \to W(\to \tau\nu) + \text{jets}$, b filter	SHERPA 2.2.10	0.185
$pp \to W(\to \tau\nu) + \text{jets}$, b veto, c filter	SHERPA 2.2.10	2.89
$pp \to W(\to \tau\nu) + \text{jets}$, c & b veto	SHERPA 2.2.10	17.0
Z-jets		
$pp \to Z(ee) + \text{jets}$, b filter	SHERPA 2.2.10	$5.09\ 10^{-2}$
$pp \to Z(ee) + \text{jets}$, b veto, c filter	SHERPA 2.2.10	0.267
$pp \to Z(ee) + \text{jets}$, c & b veto	SHERPA 2.2.10	1.79
$pp \to Z(\mu\mu) + \text{jets}$, b filter	SHERPA 2.2.10	$4.98\ 10^{-2}$
$pp \to Z(\mu\mu) + \text{jets}$, b veto, c filter	SHERPA 2.2.10	0.267
$pp \to Z(\mu\mu) + \text{jets}$, c & b veto	SHERPA 2.2.10	1.79
$pp \to Z(\tau\tau) + \text{jets}$, b filter	SHERPA 2.2.10	$6.14\ 10^{-3}$
$pp \to Z(\tau\tau) + \text{jets}$, b veto, c filter	SHERPA 2.2.10	$3.23\ 10^{-2}$
$pp \to Z(\tau\tau) + \text{jets}$, c & b veto	SHERPA 2.2.10	0.223

Table B.1: MC sample list

Appendix C

Fake photons - 2D template additional studies

C.1 Differential estimate

The differential estimate of the jets faking photons is obtained by taking the appropriate distribution shape in the control regions and scale it by the right yield using the result of the template fit, computed with the full dataset. To validate the this extrapolation method, cross checks have been carried out and it was observed that:

- The $p_T^{\gamma 1}$ distributions in the control regions agree with the truth matched MC samples. The comparison was made between: CRgj and the truth matched $W\gamma^{\gamma j}$sample, CRjg and the truth matched $W\gamma^{j\gamma}$ sample, and CRjj and the truth matched W+jets^{jj} sample (see Fig C.1)

- The $W\gamma$ and W+jets MC simulations are not used directly to extract the $p_T^{\gamma 1}$ shape as their statistics are quite low once truth matching is applied. The $p_T^{\gamma 1}$ shape is therefore taken form the different data control regions adding the photon tight isolation requirement on both photons. Adding the tight isolation ensures that the $p_T^{\gamma 1}$ distributions from CR correspond well to the distribution of the corresponding backgrounds in the signal region.

- The CR extrapolation agrees we a binned template estimation within statistical uncertainties in the 3 bin case: The template fit was computed in each $p_T^{\gamma 1}$ bin and the results are shown in Figure C.2. Note that the statistical error on the binned template is slightly higher in the binned template than with the CR extrapolation and a binned template could not be reliably computed for more than 3 bins because of the limited statistics.

- The difference between the binned template and CR extrapolation (Figure C.2 is taken as a systematic uncertainty on the final result.

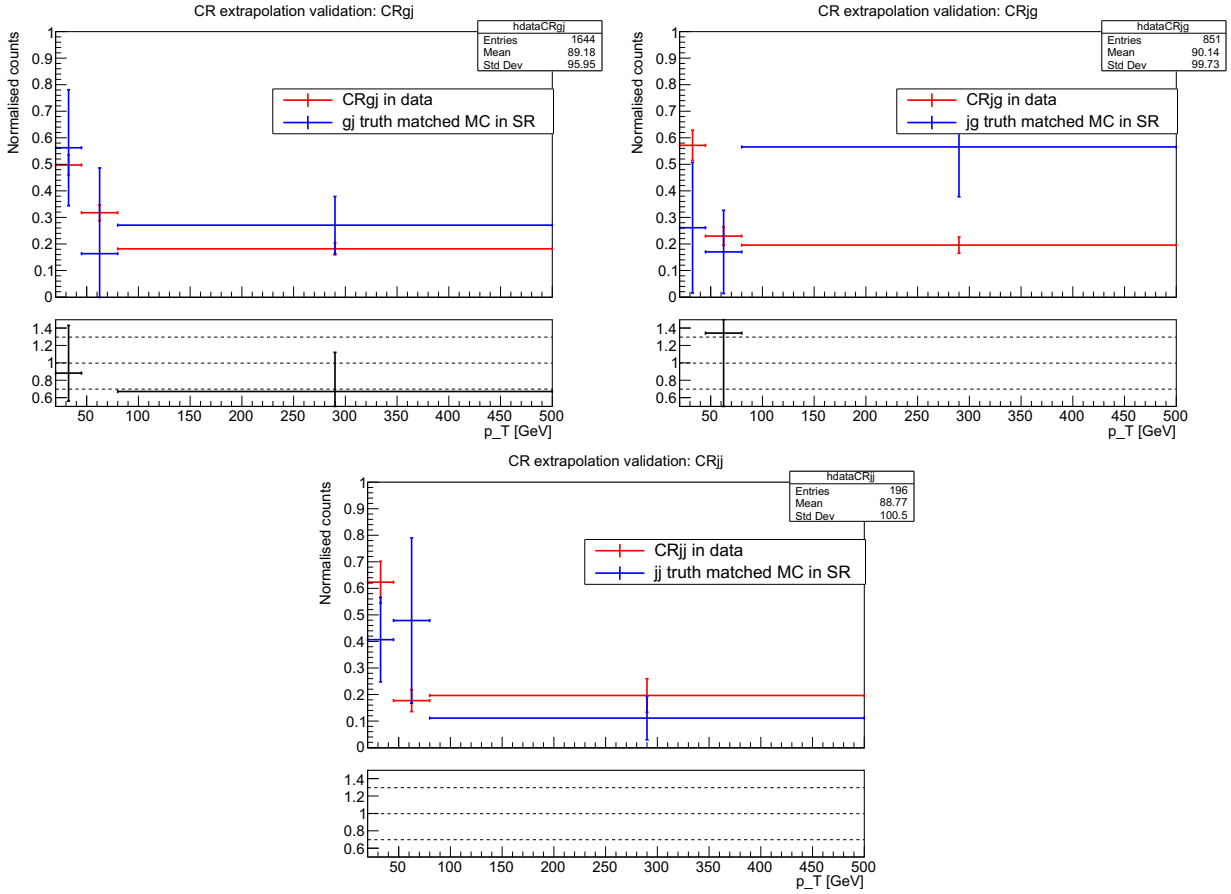

Figure C.1: Comparison of the $p_T^{\gamma 1}$ distributions in the different data control regions and the corresponding truth matched MC simulations in the signal region. The good agreement shows that the data CR distributions are a good estimate of the j-fake background distribution in the signal region

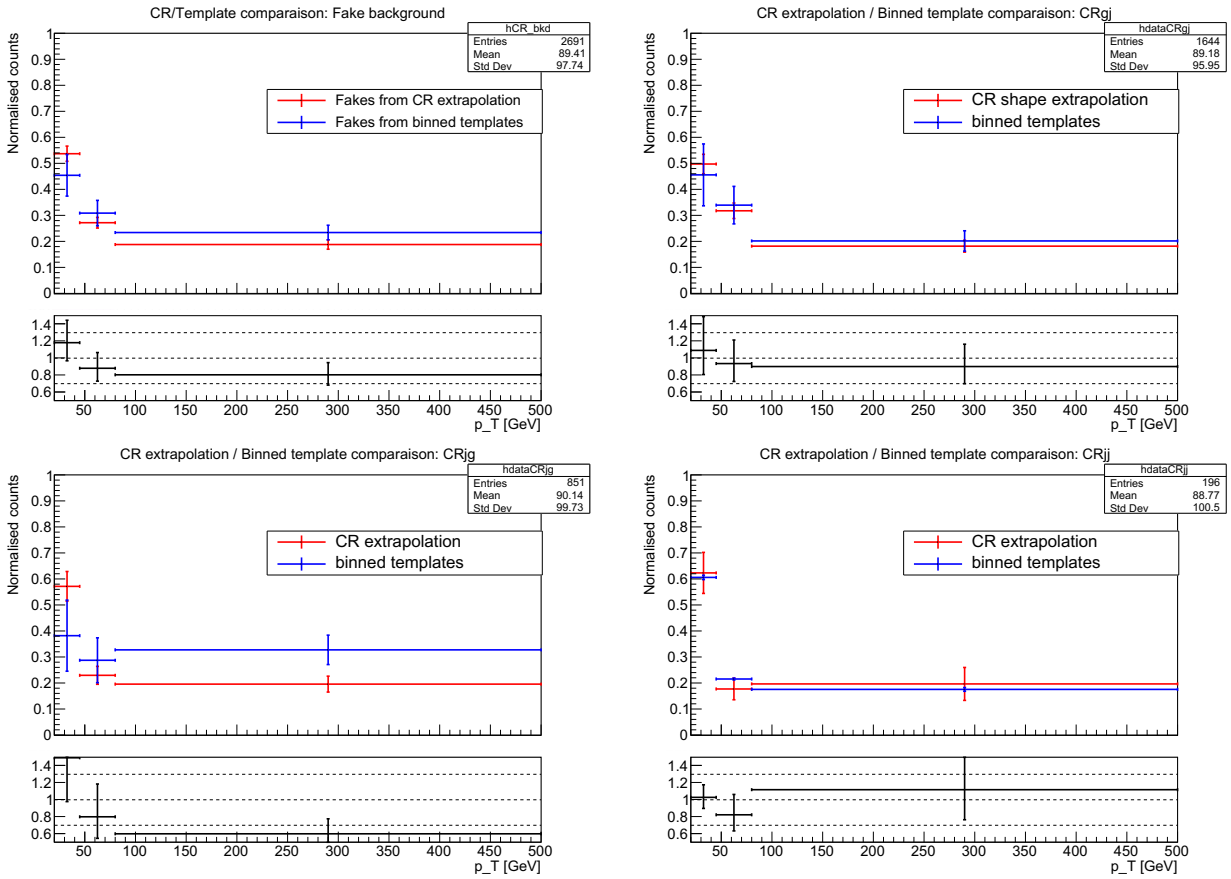

Figure C.2: Comparison of the $p_T^{\gamma 1}$ shape obtained with CR extrapolation (red) and binned templates (blue) for the different j-fake photon backgrounds and their sum.

C.2 J-Fake photon estimate in VR1

The fake photon background must be estimated in the control regions used to normalise the $t\bar{t}$ background. Unfortunately, the 2D template fit cannot be applied in the $t\bar{t}$ control and validation regions "VR1high" and "VR1low" as the stats are too low and the fits do not converge. In these two regions, jets faking photons are estimated using MC scaled with the appropriate scale factor. The scale factor $SF_{\text{j-fake}}$ is computed in the signal region by using the data-driven fake estimate and truth matched MC. This is possible since it has been shown that the control regions VR1high and VR1low have a fake photon fraction similar to the Signal Region fraction as shown in Figure C.3.

$$SF_{\text{j-fake}} = \frac{N^{SR}_{\text{fakes,MC}}}{N^{SR}_{\text{fakes, datadriven}}} = 1.388 \pm 0.368 \tag{C.1}$$

Where the error is statistical only. Since the scale factor agrees with 1 within uncertainties, the value used is 1 ± 0.37. Figure C.3 shows that the fake photon fraction is similar in the Signal Region and control regions VR1high and VR1low.

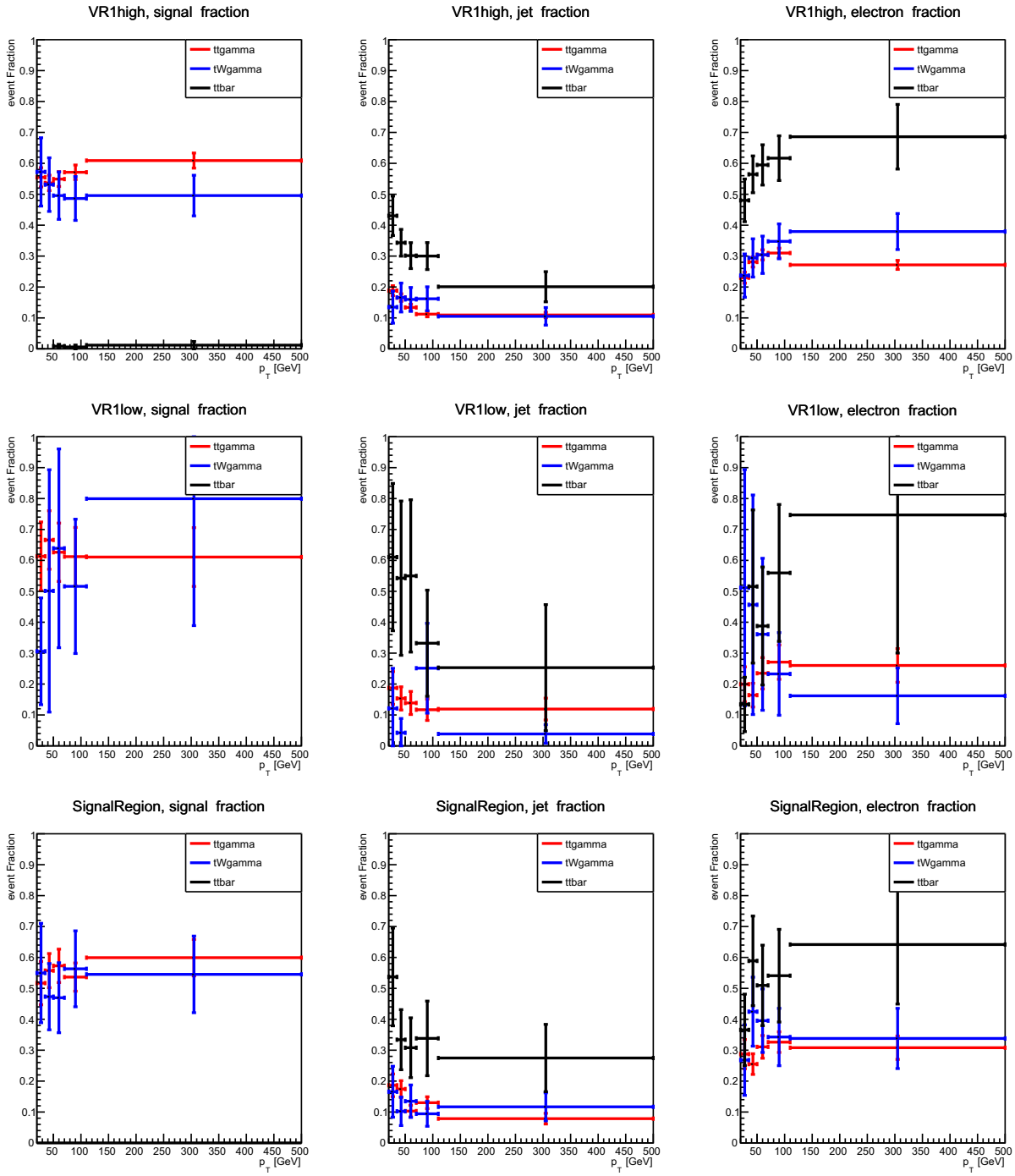

Figure C.3: Comparison of true photon type in the ttγ (red), tWγ (blue) and $t\bar{t}$ (black) samples. Top: Control region, middle : Validation region, bottom: Signal region. These plots show that the ttγ (red) and tWγ distributions are in agreement and the photon truth content is the same in the 3 regions for a given sample.

C.3 Cross-check: systematic propagation for 2D fit

As shown in Chapter 7, the leading experimental uncertainties are the uncertainties on the photon isolation efficiency and the photon identification efficiency. Since the 2D template fit method relies both on the photon isolation and identification variable, a cross check was carried out to see if the these uncertainties had to be propagated through the fit. The 2D template fit estimate was run again using the up and down variations on photon identification and isolation efficiency. The results are shown in Table C.1: the variation on the yields is typically smaller than 1% and much below the statistical uncertainty on the fit's results. It was therefore decided not to propagate any uncertainties through the 2D template fit.

	Nominal (%)	iso up (%)	iso down (%)	ID up (%)	ID down (%)
$N_{\gamma\gamma}$	69.90 ± 11.94	69.92 ± 11.77	69.89 ± 12.08	69.95 ± 11.746	69.86 ± 12.12
$N_{\gamma j}$	12.06 ± 5.86	11.99 ± 5.87	12.15 ± 5.94	11.98 ± 5.87	12.17 ± 5.91
$N_{j\gamma}$	15.27 ± 6.45	15.32 ± 6.24	15.20 ± 6.51	15.31 ± 6.25	15.22 ± 6.56
N_{jj}	2.74 ± 0.20	2.75 ± 0.20	2.73 ± 0.20	2.75 ± 0.20	2.73 ± 0.20

Table C.1: Fake photon yields obtained for the up and down variations of the photon identification and isolation efficiency.

C.4 Photon ID

The photon ID is computed using by imposing cuts on a combination of strip variables and calorimeter variables defined as follows:

Calorimeter variables:

- R_{had}: ratio of E_T deposited in the first layer of the EM calorimeter compared to the enegery in the first layer of the hadronic calorimeter.
- R_η: In the middle layer of the EM calorimeter: energy ratio in the $3 \times 7(\eta \times \phi)cells$ to the 7×7 cells cluster.

- R_ϕ: In the middle layer of the EM calorimeter: energy ratio in the $3 \times 3(\eta \times \phi)cells$ to the 7×3 cells cluster.
- w_2: Lateral width on the shower (EM middle layer)

Strip variable:

- w_{s3}: the shower width for three strips around maximum strip, using the energy weighted sum over the total energy contained in the three strips.
- w_{stot} : the total lateral shower width determined with the energy weighted sum over cells in a window corresponding to the cluster size.
- F_{side}: the fraction of energy outside a core of 3 central strips, but within 7 strips.
- ΔE: the difference between the energy of the strip with the second largest energy deposited and the energy of the strip with the smallest energy deposit between the two leading strips.
- E_{ratio} : the ratio of the energy difference between the largest and second largest energy deposits over the sum of these energies.

The LoosePrime ID working points are defined by allowing some of the strip variables to fail as detailed in Table C.2. The nominal Loose prime working point used for the j-fake estimation is LoosePrime4, the other LoosePrime IDs are used for systematics estimation.

	Tight	LoosePrime2	LoosePrime3	LoosePrime4a	LoosePrime4	LoosePrime5
R_{had}	✓	✓	✓	✓	✓	✓
R_{η}	✓	✓	✓	✓	✓	✓
R_{ϕ}	✓	✓	✓	✓	✓	✓
w_2	✓	✓	✓	✓	✓	✓
w_{s3}	✓	×	×	×	×	×
w_{stot}	✓	✓	✓	✓	✓	×
F_{side}	✓	×	×	×	×	×
ΔE	✓	✓	×	✓	×	×
E_{ratio}	✓	✓	✓	×	×	×

Table C.2: Summary of the different photon ID definitions. The variable cuts marked with ✓must be passed while the ones marked with × can be failed. At least one of the strip variables marked with × must be failed for each LoosePrime working point.

Appendix D

Fake Photons - 2x2D sideband method

The 2x2D sideband method is a cut and count data-driven method used as a cross check to validate the 2D template fit method (Sec. 6.2). It is used to estimate the background coming from jets misidentified as photons. The method was first used by the 2011 diphoton cross-section measurement [113] and by the Run 1 $W\gamma\gamma$ analysis [114].

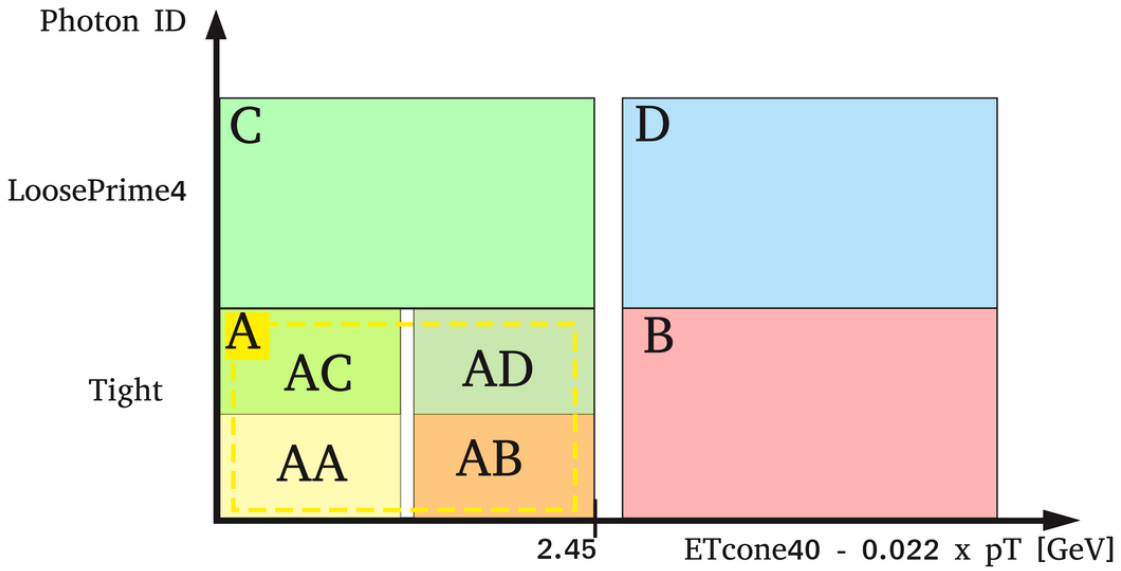

Figure D.1: The eight regions used for the 2x2D sideband method. Region AA is the signal region. The gap between regions is 3 GeV wide.

D.1 Method description

The number of j-fake photons in the signal region – where photons are isolated (**I**) and pass the photon Tight ID selection (**T**) – is extrapolated from the background in control regions located in the sidebands of identification and isolation variables. Events used in the 2x2D sideband method are data events passing the signal selection excepted for the photon isolation cut and the ID selection. The ID selection is relaxed from Tight to include both Tight (T) and LoosePrime4 (**L**) ID photons. The other backgrounds are estimated from MC and subtracted from data before using the 2x2D sideband method.
The number of events passing the signal selection N_{tot}^{TITI} can be decomposed depending on the true nature of the reconstructed photons (either γ: real photons or j: jets).

$$N_{tot}^{TITI} = N_{\gamma\gamma}^{TITI} + N_{\gamma j}^{TITI} + N_{j\gamma}^{TITI} + N_{jj}^{TITI} \tag{D.1}$$

Where $N_{\gamma\gamma}^{TITI}$ is the number of signal events to estimate and ^{TI} refers to a given photon passing the Tight ID and isolation cuts. Here the two photon candidates are studied one after the other. The method is first applied to the leading photon and no requirements are made about the subleading photon. Then the method is applied to the subleading photon and the leading photon is required to be of Tight ID and isolated.

D.2 Leading photon

For each photon, three control regions (CR) are defined and used to estimate the background in the signal region (SR) (see figure D.1). The regions are defined as follows:

A: Signal region: the leading photon is isolated ($E_{iso} < 2.45$ GeV) and ID Tight

B: The leading photon is not isolated ($E_{iso} > 5.45+$ GeV) and ID Tight

C: The leading photon is isolated ($E_{iso} < 2.45$ GeV) and the ID is LoosePrime4 & fails Tight

D: The leading photon is not isolated ($E_{iso} > 5.45+$ GeV) and the ID is LoosePrime4 & fails Tight

Note that an energy gap between of 3 GeV is implemented between regions A & B and C & D in order to reduce signal leakage. The four regions will each contain signal events (sig) and background events (bkg). The signal is expected to dominate in the signal region A and the background should be dominant in the control regions B, C and D. The number of events in each region can be re-written as the sum of signal and background events:

$$N_A = N_A^{sig} + N_A^{bkg} \tag{D.2}$$

$$N_B = N_B^{sig} + N_B^{bkg} \tag{D.3}$$

$$N_C = N_C^{sig} + N_C^{bkg} \tag{D.4}$$

$$N_D = N_D^{sig} + N_D^{bkg} \tag{D.5}$$

If the number of signal events in regions B, C, D (signal leakage) was negligible and if there was no correlation between the photon ID and isolation variables, the number of signal events in region A would simply be:

$$N_A^{bkg} = \frac{N_B^{bkg} N_C^{bkg}}{N_D^{bkg}} = \frac{N_B N_C}{N_D} \tag{D.6}$$

$$N_A^{sig} = N_A - N_A^{bkg} = N_A - \frac{N_B . N_C}{N_D} \tag{D.7}$$

In reality the signal leakage is not negligible and it must be computed and taken into account. The different leakage coefficients are defined as:

$$c_i = \frac{N_i^{sig}}{N_A^{sig}} \tag{D.8}$$

Where $i = B, C, D$. The leakage coefficients are computed using truth-matched MC events from the $W\gamma\gamma$ sample. The number of background events in the different control regions can be re-written as:

$$N_i^{bkg} = N_i - c_i N_A^{sig} \tag{D.9}$$

The correlation between the photon ID and isolation is also non-zero and must be taken into account. The correlation factor R is defined as:

$$R = \frac{N_A N_D}{N_B N_D} \tag{D.10}$$

For leading the leading photon, it is computed from the W+jet MC sample. Since this sample contains few diphoton events, the event selection was relaxed to require only one photon. Taking into account the signal leakage and correlation, the expression for the number of signal events in the region A becomes:

$$N_A^{sig} = N_A - R\left[(N_B - c_B N_A^{sig})\frac{N_C - c_C N_A^{sig}}{N_D - c_D N_A^{sig}}\right] \tag{D.11}$$

This equation can be solved and we get (the second solution is unphysical):

$$N_A^{sig} = \frac{-b + \sqrt{b^2 - 4ac}}{2a} \tag{D.12}$$

$$a = C_B c_C R - c_D \tag{D.13}$$

$$b = N_D + c_D N_A - R(c_C N_B + c_B N_C) \tag{D.14}$$

$$c = R N_B N_C - N_A N_D \tag{D.15}$$

D.3 Subleading photon

The same method is then applied to the subleading photon candidates. The events used pass the selection described for the leading photon section + the additional requirement that the leading photon must fall in region A. The regions for the subleading photon are defined as follows:

AA: Signal region: leading photon is in region A, the subleading photon is isolated ($E_{iso} < 2.45$ GeV) and ID Tight

AB: The leading photon is in region A, the subleading photon is not isolated ($E_{iso} > 5.45+$ GeV) and ID Tight

AC: The leading photon is in region A, the subleading photon is isolated ($E_{iso} < 2.45$ GeV) and the ID is LoosePrime4 & fails Tight

AD: The leading photon is in region A, the subleading photon is not isolated ($E_{iso} > 5.45+$ GeV) and the ID is LoosePrime4 & fails Tight

The equation for the number of signal events in the signal region is as follows and can be solved in the exact same way as Equation D.11.

$$N_{AA}^{sig} = N_{AA} - R_2 \left[(N_{AB} - c_{B2} N_{AA}^{sig}) \frac{N_{AC} - c_{C2} N_{AA}^{sig}}{N_{AD} - c_{D2} N_{AA}^{sig}} \right] \tag{D.16}$$

Where the leakage coefficients c_{i2} and the correlation coefficient R_2 are defined as follows:

$$c_{i2} = \frac{N_{Ai}^{sig}}{N_{AA}^{sig}} \tag{D.17}$$

$$R_2 = \frac{N_{AA} N_{AD}}{N_{AB} N_{AD}} \tag{D.18}$$

Where $i = B, C, D$. The leakage coefficients are computed using the same truth-matched $W\gamma\gamma$ MC sample but the correlation coefficient is computed from the inclusive $W\gamma$ sample.

D.4 Yield extraction

The number of signal events N_A^{sig} and N_{AA}^{sig} obtained from equations D.11 and D.16 are linked to the yields as follows:

$$N_A^{sig} = N_{\gamma\gamma}^{TI} + N_{\gamma j}^{TI} \tag{D.19}$$

$$N_A^{bkg} = N_{j\gamma}^{TI} + N_{jj}^{TI} \tag{D.20}$$

$$N_{AA}^{sig} = N_{\gamma\gamma}^{TITI} + N_{j\gamma}^{TITI} \tag{D.21}$$

$$N_{AA}^{bkg} = N_{\gamma j}^{TITI} + N_{jj}^{TITI} \tag{D.22}$$

$$\tag{D.23}$$

Where N_{xx}^{TI} are the yields for the true xx type to have the leading photon being Tight and Isolated and N_{xx}^{TITI} are the yields for the true xx type to have both the leading and subleading photon being Tight and Isolated .

Efficiencies:

The efficiency ϵ of our selection is the probability of having the (real) leading photon passing the signal selection. It is given by:

$$\epsilon = \frac{N_A^{sig}}{N_A^{sig} + N_B^{sig} + N_C^{sig} + N_D^{sig}} = \frac{1}{1 + c_B + c_C + c_D} \tag{D.24}$$

Similaraly, the efficiency ϵ_2 for the subleading photon is given by:

$$\epsilon_2 = \frac{N_{AA}^{sig}}{N_{AA}^{sig} + N_{AB}^{sig} + N_{AC}^{sig} + N_{AD}^{sig}} = \frac{1}{1 + c_{B2} + c_{C2} + c_{D2}} \tag{D.25}$$

Fake rate:

The probability of a leading jet passing our selection and faking a photon is the fake rate f given by:

$$f = \frac{N_A^{bkg}}{N_{tot}^{bkg}} = \frac{N_A - N_A^{sig}}{N_{tot} - N_{tot}^{sig}} = \frac{N_A - N_A^{sig}}{N_A + N_B + N_C + N_D - \frac{1}{\epsilon} N_A^{sig}} \tag{D.26}$$

For the subleading jet, the fake rate f_2 is:

$$f = \frac{N_{AA}^{bkg}}{N_A^{bkg}} = \frac{N_{AA} - N_{AA}^{sig}}{N_A - \frac{1}{\epsilon_2} N_{AA}^{sig}} \tag{D.27}$$

Now equations D.19 can be re-expressed using the efficiencies and fake rates as:

$$N_A^{sig} = \frac{1}{\epsilon_2} W_{\gamma\gamma}^{TITI} + \frac{1}{f_2} W_{\gamma j}^{TITI} \tag{D.28}$$

$$N_A^{bkg} = N_A - N_A^{sig} = \frac{1}{\epsilon_2} W_{j\gamma}^{TITI} + \frac{1}{f_2} W_{jj}^{TITI} \tag{D.29}$$

$$N_{AA}^{sig} = W_{\gamma\gamma}^{TITI} + W_{j\gamma}^{TITI} \tag{D.30}$$

$$N_{AA}^{bkg} = N_{AA} - N_{AA}^{sig} = W_{\gamma j}^{TITI} + W_{jj}^{TITI} \tag{D.31}$$

To solve this system of equations and compute the yields, an additionnal constraint is needed as N_A^{sig} depends on the fake rate. The chosen parameter is the fraction of $j\gamma$ events over the number of $j\gamma + \gamma j$ events:

$$\alpha = \frac{W_{j\gamma}^{TITI}}{W_{j\gamma}^{TITI} + W_{\gamma j}^{TITI}} \tag{D.32}$$

The parameter α is measured in W_γ+jets MC using truth matching. The system of equations D.28 can now be solved as follows:

$$W_{\gamma\gamma}^{TITI} = \frac{\epsilon_2(\alpha f_2 N_A^{sig} + (\alpha-1)N_{AA}^{sig})}{(\alpha-1)\epsilon_2 + \alpha f_2} \tag{D.33}$$

$$W_{\gamma j}^{TITI} = \frac{(\alpha-1) f_2(\epsilon_2 N_A^{sig} - N_{AA}^{sig})}{(\alpha-1)\epsilon_2 + \alpha f_2} \tag{D.34}$$

$$W_{j\gamma}^{TITI} = \frac{\alpha f_2(N_{AA}^{sig} - \epsilon_2 N_A^{sig})}{(\alpha-1)\epsilon_2 + \alpha f_2} \tag{D.35}$$

$$W_{jj}^{TITI} = \frac{f_2(\alpha\epsilon_2 f_2 N_A + (\alpha-1)\epsilon_2^2(N_A - N_A^{sig}) - \alpha f_2 N_{AA}^{sig})}{\epsilon_2((\alpha-1)\epsilon_2 + \alpha f_2)} \tag{D.36}$$

D.5 Results

Results presented here are computed are in good agreement with the 2D template fit estimate of the fake photons fron jets. The errors are statistical only.

c_B	0.146 ± 0.024
c_C	0.044 ± 0.013
c_D	0.011 ± 0.006
c_{B2}	0.173 ± 0.032
c_{C2}	0.087 ± 0.022
c_{D2}	0.020 ± 0.010
R	1.103 ± 0.461
R_2	1.225 ± 0.301
α	0.52 ± 0.05

Table D.1: Signal leakage parameters (c_i), correlation coefficients R and R_2 and fraction of $\gamma j/j\gamma$ events α. The errors are statistical only.

	Number of events	percentage
$N_{\gamma\gamma}$	$269.2^{+95.8}_{-94.2}$	$67.7\%^{+24.1\%}_{-23.7\%}$
$N_{\gamma\gamma}$	$55.4^{+45.6}_{-44.4}$	$13.9\%^{+11.5\%}_{-11.2\%}$
$N_{\gamma\gamma}$	$59.9^{+47.1}_{-48.9}$	$15.1\%^{+11.8\%}_{-12.3\%}$
$N_{\gamma\gamma}$	$13.2^{+11.3}_{-15.7}$	$3.3\%^{+2.8\%}_{-3.9\%}$

Table D.2: Fake photon and signal yields expected in the signal region. The errors are statistical only. The agreement with the Template method is very good.

D.6 Statistical uncertainty computation

The uncertainty on the yields presented in table D.2 have been computed using toy simulations. Random generators were used to generate the number of events N_i falling into the 8 control regions A to D and AA to AD for data, $W\gamma\gamma$, $W\gamma$ and W+jets MC. The N_i distributions where approxmated by a gaussian and for each sample, the gaussian parameters are taken to be the observed N_i as mean and the statistical error as width. For each set of N_i generated, the yields and intermediate coefficients are computed. The final yields distributions hence obtained are used to estimate the statistical error: error on the yield is taken as the width at half maximum of the distributions. Note that:

- The analytically computed yields agree very well with the maximum of the toy distributions.
- The distributions beeing asymetric, the upper and lower errors are computed separately.

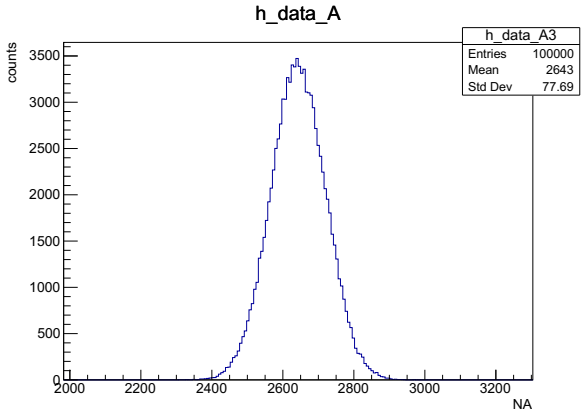

(a) Generated number of events N_A

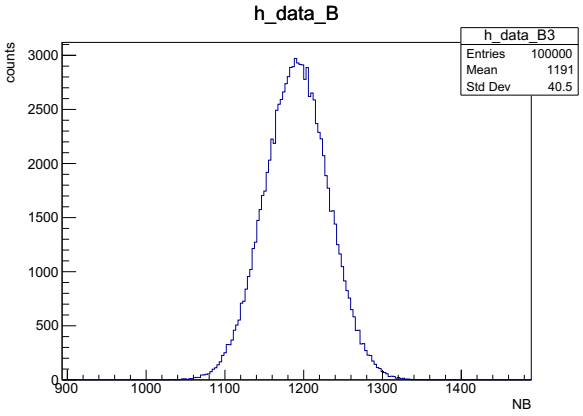

(b) Generated number of events N_B

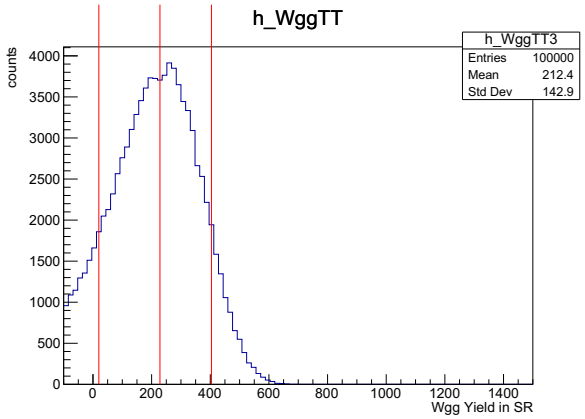

(c) Number of signal events $N_{\gamma\gamma}^{TITI}$

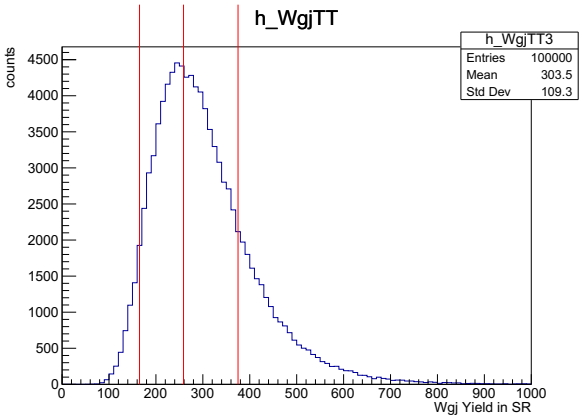

(d) Number of γj background events $N_{\gamma j}^{TITI}$

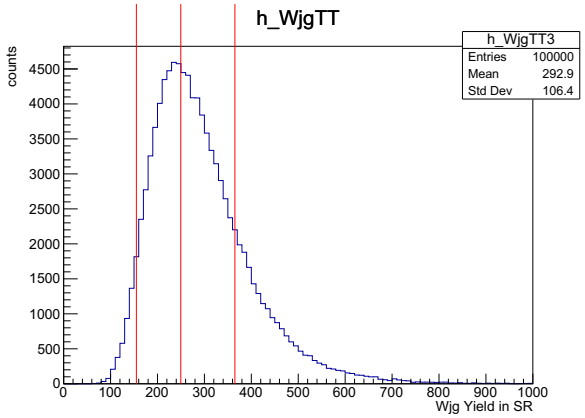

(e) Number of $j\gamma$ background events $N_{j\gamma}^{TITI}$

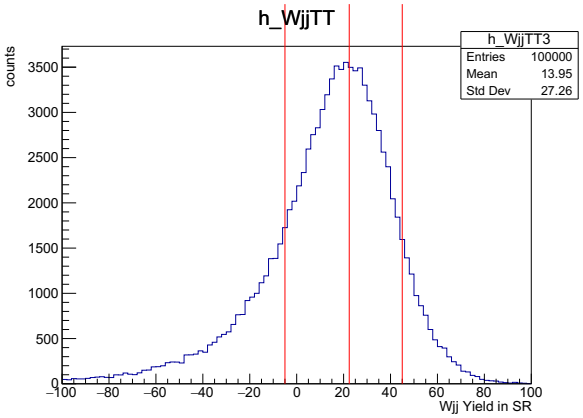

(f) Number of jj background events N_{jj}^{TITI}

Figure D.2: Toy distributions used to estimate the statistical uncertainty on the final 2x2D sideband yields. The central vertical lines mark the analytical values computed from observation, the external lines mark the width at half maximum.

Appendix E

Systematic uncertainties

The relative values of all the instrumental and theoretical uncertainties are given in Figures E.2 to E.7 for the signal region, control region VR1high and validation region VR1low. Figure E.1 shows the pull of the main systematics.

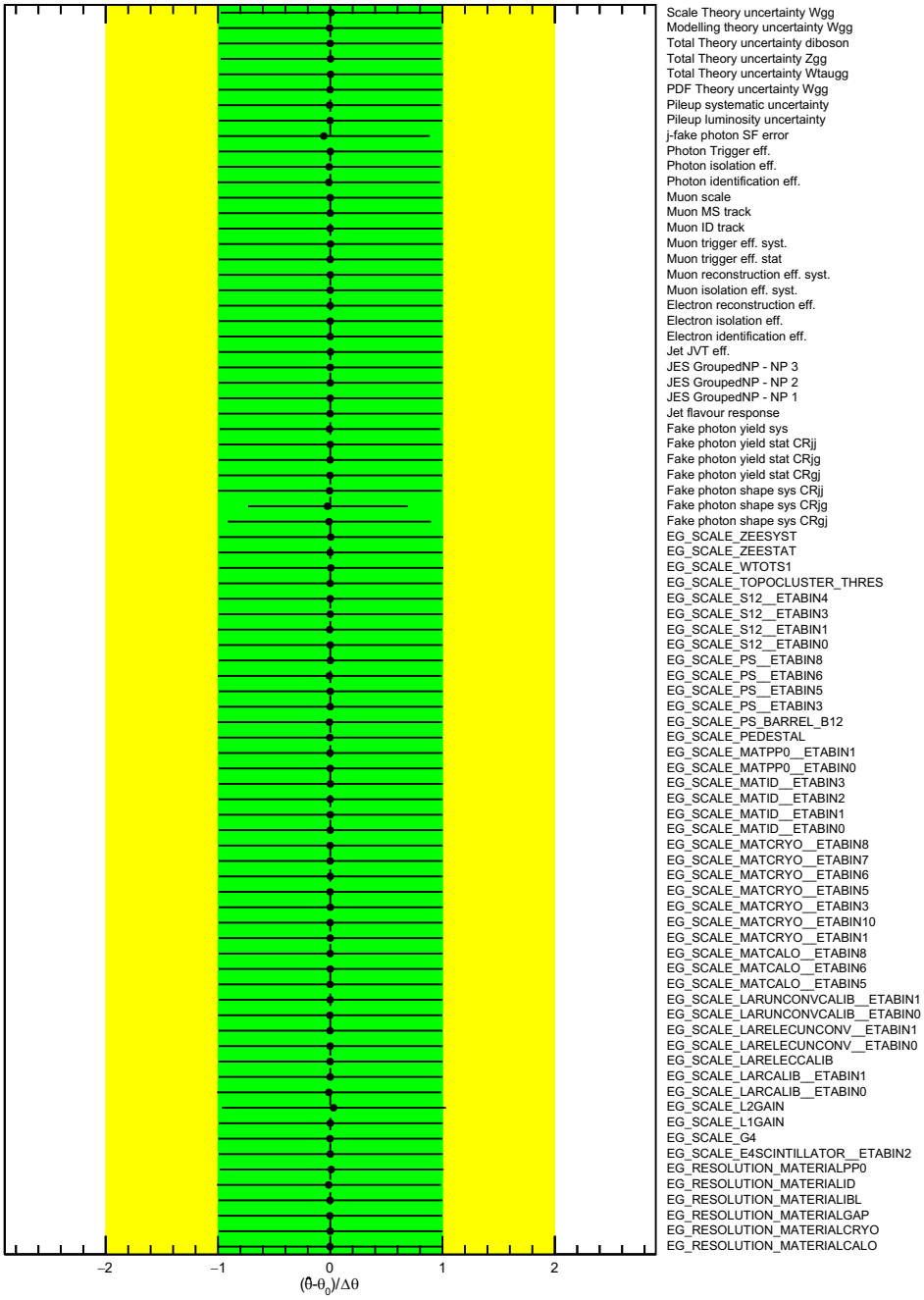

Figure E.1: No significant pull from any of the systematics has been observed.

	$CR_{\ell\bar{\ell}}$	$CR_{\ell\bar{\ell}}$	$CR_{\ell\bar{\ell}}$	$W\gamma\gamma$	$Z\gamma$	$Z\gamma\gamma$	$tX\gamma$	$t\bar{t}$	Fake electrons	Fake muons	diboson	$W(\tau\nu)\gamma\gamma$	$WH\gamma\gamma$	pileup
Fake photon yield stat CRej	0.021 / -0.021	0 / 0		0 / 0	0 / 0	0 / 0	0 / 0	0 / 0	0 / 0	0 / 0	0 / 0	0 / 0	0 / 0	0 / 0
Fake photon yield sys	0.059 / -0.026	0.059 / -0.026	0.059 / -0.026	0 / 0	0 / 0	0 / 0	0 / 0	0 / 0	0 / 0	0 / 0	0 / 0	0 / 0	0 / 0	0 / 0
Fake photon shape sys CRej	0.145 / -0.145	0 / 0	0 / 0	0 / 0	0 / 0	0 / 0	0 / 0	0 / 0	0 / 0	0 / 0	0 / 0	0 / 0	0 / 0	0 / 0
shape_FakePhotonShapeStat_ej_SignalRegion_bin_0	0 / 0	0 / 0	0 / 0	0 / 0	0 / 0	0 / 0	0 / 0	0 / 0	0 / 0	0 / 0	0 / 0	0 / 0	0 / 0	0 / 0
shape_FakePhotonShapeStat_ej_SignalRegion_bin_1	0 / 0	0 / 0	0 / 0	0 / 0	0 / 0	0 / 0	0 / 0	0 / 0	0 / 0	0 / 0	0 / 0	0 / 0	0 / 0	0 / 0
shape_FakePhotonShapeStat_ej_SignalRegion_bin_2	0 / 0	0 / 0	0 / 0	0 / 0	0 / 0	0 / 0	0 / 0	0 / 0	0 / 0	0 / 0	0 / 0	0 / 0	0 / 0	0 / 0
shape_FakePhotonShapeStat_ej_SignalRegion_bin_3	0 / 0	0 / 0	0 / 0	0 / 0	0 / 0	0 / 0	0 / 0	0 / 0	0 / 0	0 / 0	0 / 0	0 / 0	0 / 0	0 / 0
shape_FakePhotonShapeStat_ej_SignalRegion_bin_4	0 / 0	0 / 0	0 / 0	0 / 0	0 / 0	0 / 0	0 / 0	0 / 0	0 / 0	0 / 0	0 / 0	0 / 0	0 / 0	0 / 0
Fake photon yield stat CRjg	0 / 0	0.013 / -0.013	0 / 0	0 / 0	0 / 0	0 / 0	0 / 0	0 / 0	0 / 0	0 / 0	0 / 0	0 / 0	0 / 0	0 / 0
Fake photon shape sys CRjg	0 / 0	0.475 / -0.45	0 / 0	0 / 0	0 / 0	0 / 0	0 / 0	0 / 0	0 / 0	0 / 0	0 / 0	0 / 0	0 / 0	0 / 0
shape_FakePhotonShapeStat_jg_SignalRegion_bin_0	0 / 0	0 / 0	0 / 0	0 / 0	0 / 0	0 / 0	0 / 0	0 / 0	0 / 0	0 / 0	0 / 0	0 / 0	0 / 0	0 / 0
shape_FakePhotonShapeStat_jg_SignalRegion_bin_1	0 / 0	0 / 0	0 / 0	0 / 0	0 / 0	0 / 0	0 / 0	0 / 0	0 / 0	0 / 0	0 / 0	0 / 0	0 / 0	0 / 0
shape_FakePhotonShapeStat_jg_SignalRegion_bin_2	0 / 0	0 / 0	0 / 0	0 / 0	0 / 0	0 / 0	0 / 0	0 / 0	0 / 0	0 / 0	0 / 0	0 / 0	0 / 0	0 / 0
shape_FakePhotonShapeStat_jg_SignalRegion_bin_3	0 / 0	0 / 0	0 / 0	0 / 0	0 / 0	0 / 0	0 / 0	0 / 0	0 / 0	0 / 0	0 / 0	0 / 0	0 / 0	0 / 0
shape_FakePhotonShapeStat_jg_SignalRegion_bin_4	0 / 0	0 / 0	0 / 0	0 / 0	0 / 0	0 / 0	0 / 0	0 / 0	0 / 0	0 / 0	0 / 0	0 / 0	0 / 0	0 / 0
Fake photon yield stat CRjj	0 / 0	0 / 0	0.001 / -0.001	0 / 0	0 / 0	0 / 0	0 / 0	0 / 0	0 / 0	0 / 0	0 / 0	0 / 0	0 / 0	0 / 0
Fake photon shape sys CRjj	0 / 0	0 / 0	0.169 / -0.169	0 / 0	0 / 0	0 / 0	0 / 0	0 / 0	0 / 0	0 / 0	0 / 0	0 / 0	0 / 0	0 / 0
shape_FakePhotonShapeStat_jj_SignalRegion_bin_0	0 / 0	0 / 0	0 / 0	0 / 0	0 / 0	0 / 0	0 / 0	0 / 0	0 / 0	0 / 0	0 / 0	0 / 0	0 / 0	0 / 0
shape_FakePhotonShapeStat_jj_SignalRegion_bin_1	0 / 0	0 / 0	0 / 0	0 / 0	0 / 0	0 / 0	0 / 0	0 / 0	0 / 0	0 / 0	0 / 0	0 / 0	0 / 0	0 / 0
shape_FakePhotonShapeStat_jj_SignalRegion_bin_2	0 / 0	0 / 0	0 / 0	0 / 0	0 / 0	0 / 0	0 / 0	0 / 0	0 / 0	0 / 0	0 / 0	0 / 0	0 / 0	0 / 0
shape_FakePhotonShapeStat_jj_SignalRegion_bin_3	0 / 0	0 / 0	0 / 0	0 / 0	0 / 0	0 / 0	0 / 0	0 / 0	0 / 0	0 / 0	0 / 0	0 / 0	0 / 0	0 / 0
shape_FakePhotonShapeStat_jj_SignalRegion_bin_4	0 / 0	0 / 0	0 / 0	0 / 0	0 / 0	0 / 0	0 / 0	0 / 0	0 / 0	0 / 0	0 / 0	0 / 0	0 / 0	0 / 0
Luminosity	0 / 0	0 / 0	0 / 0	0.017 / -0.017	0.017 / -0.017	0.017 / -0.017	0.017 / -0.017	0.017 / -0.017	0 / 0	0 / 0	0.017 / -0.017	0.017 / -0.017	0.017 / -0.017	0 / 0
PDF Theory uncertainty Wgg	0 / 0	0 / 0	0 / 0	1.97e-08 / 1.97e-08	0 / 0	0 / 0	0 / 0	0 / 0	0 / 0	0 / 0	0 / 0	0 / 0	0 / 0	0 / 0
Scale Theory uncertainty Wgg	0 / 0	0 / 0	0 / 0	1.97e-08 / 1.97e-08	0 / 0	0 / 0	0 / 0	0 / 0	0 / 0	0 / 0	0 / 0	0 / 0	0 / 0	0 / 0
α_S Theory uncertainty Wgg	0 / 0	0 / 0	0 / 0	1.97e-08 / 1.97e-08	0 / 0	0 / 0	0 / 0	0 / 0	0 / 0	0 / 0	0 / 0	0 / 0	0 / 0	0 / 0
Modelling theory uncertainty Wgg	0 / 0	0 / 0	0 / 0	-5.68e-08 / 5.68e-08	0 / 0	0 / 0	0 / 0	0 / 0	0 / 0	0 / 0	0 / 0	0 / 0	0 / 0	0 / 0
Electron identification eff.	0 / 0	0 / 0	0 / 0	0.0039 / -0.0039	0.00625 / -0.00625	0 / 0	0 / 0	0 / 0	0 / 0	0 / 0	0 / 0	0 / 0	0 / 0	0 / 0
Electron isolation eff.	0 / 0	0 / 0	0 / 0	0.000595 / -0.000595	0.00105 / -0.00105	0 / 0	0 / 0	0 / 0	0 / 0	0 / 0	0 / 0	0 / 0	0 / 0	0 / 0
Electron reconstruction eff.	0 / 0	0 / 0	0 / 0	0.000743 / -0.000743	0.00119 / -0.00119	0 / 0	0 / 0	0 / 0	0 / 0	0 / 0	0 / 0	0 / 0	0 / 0	0 / 0
Electron Trigger eff.	0 / 0	0 / 0	0 / 0	1.97e-08 / 1.97e-08	5.21e-09 / 5.21e-09	0 / 0	0 / 0	0 / 0	0 / 0	0 / 0	0 / 0	0 / 0	0 / 0	0 / 0
Photon identification eff.	0 / 0	0 / 0	0 / 0	0.0248 / -0.0248	0.0257 / -0.0257	0.0277 / -0.0277	0.0247 / -0.0247	0.0274 / -0.0274	0 / 0	0 / 0	0.0262 / -0.0262	0.0234 / -0.0234	0.0173 / -0.0173	0 / 0
Photon isolation eff.	0 / 0	0 / 0	0 / 0	0.0247 / -0.0247	0.0292 / -0.0292	0.0262 / -0.0262	0.0263 / -0.0263	0.0284 / -0.0284	0 / 0	0 / 0	0.0274 / -0.0274	0.0238 / -0.0238	0.0203 / -0.0203	0 / 0
Photon Trigger eff.	0 / 0	0 / 0	0 / 0	0.00635 / -0.00635	0.000737 / -0.000737	0.0066 / -0.0066	0.00663 / -0.00663	0.00599 / -0.00599	0 / 0	0 / 0	0.00588 / -0.00588	0.00586 / -0.00586	0.00771 / -0.00771	0 / 0
Muon isolation eff. stat	0 / 0	0 / 0	0 / 0	0.000568 / -0.000568	2.74e-05 / -2.74e-05	0.000522 / -0.000522	0.000564 / -0.000564	0.000612 / -0.000612	0 / 0	0 / 0	0.000367 / -0.000368	0.000334 / -0.000334	0.000591 / -0.000591	0 / 0
Muon isolation eff. syst.	0 / 0	0 / 0	0 / 0	0.00365 / -0.00365	0.00359 / -0.00359	0.00359 / -0.00359	0.00301 / -0.00301	0.00335 / -0.00335	0 / 0	0 / 0	0.00322 / -0.00322	0.0051 / -0.0051	0.00301 / -0.00301	0 / 0
Muon reconstruction eff. stat	0 / 0	0 / 0	0 / 0	0.00023 / -0.00023	2.22e-05 / -2.21e-05	0.000248 / -0.000248	0.000235 / -0.000235	0.000191 / -0.000191	0 / 0	0 / 0	0.000144 / -0.000144	0.000182 / -0.000182	0.000234 / -0.000234	0 / 0
Muon reconstruction eff. low-pT stat.	0 / 0	0 / 0	0 / 0	1.97e-08 / 1.97e-08	5.21e-09 / 5.21e-09	-1.19e-10 / -1.19e-10	2.91e-08 / 2.91e-08	-2.07e-08 / -2.07e-08	0 / 0	0 / 0	-1.62e-08 / -1.62e-08	-3.87e-08 / -3.87e-08	9.49e-09 / 9.49e-09	0 / 0
Muon reconstruction eff. syst.	0 / 0	0 / 0	0 / 0	0.00097 / -0.00097	8.06e-05 / -8.06e-05	0.0012 / -0.0012	0.00095 / -0.00095	0.000859 / -0.000859	0 / 0	0 / 0	0.000711 / -0.000711	0.000667 / -0.000667	0.000983 / -0.000983	0 / 0
Muon reconstruction eff. low-pT syst.	0 / 0	0 / 0	0 / 0	1.97e-08 / 1.97e-08	5.21e-09 / 5.21e-09	1.19e-10 / 1.19e-10	2.91e-08 / 2.91e-08	2.07e-08 / 2.07e-08	0 / 0	0 / 0	-1.62e-08 / -1.62e-08	-3.87e-08 / -3.87e-08	9.49e-09 / 9.49e-09	0 / 0
Muon TTVA eff. stat	0 / 0	0 / 0	0 / 0	0.000135 / -0.000135	1.04e-05 / -1.04e-05	0.000135 / -0.000135	0.000137 / -0.000137	0.000128 / -0.000128	0 / 0	0 / 0	8.44e-05 / -8.44e-05	8.83e-05 / -8.84e-05	0.000143 / -0.000143	0 / 0
Muon TTVA eff. syst.	0 / 0	0 / 0	0 / 0	0.000175 / -0.000175	8.28e-06 / -8.27e-06	0.000172 / -0.000172	0.000171 / -0.000171	0.000176 / -0.000176	0 / 0	0 / 0	0.000101 / -0.000101	5.83e-05 / -5.83e-05	0.000177 / -0.000177	0 / 0
Muon trigger eff. stat	0 / 0	0 / 0	0 / 0	0.00157 / -0.00157	0.000125 / -0.000125	0.0015 / -0.0015	0.00152 / -0.00152	0.0015 / -0.0015	0 / 0	0 / 0	0.00099 / -0.00099	0.00165 / -0.00165	0.00156 / -0.00156	0 / 0
Muon trigger eff. syst.	0 / 0	0 / 0	0 / 0	0.0107 / -0.0107	0.000701 / -0.000701	0.00963 / -0.00963	0.0117 / -0.0117	0.0107 / -0.0107	0 / 0	0 / 0	0.00634 / -0.00634	0.00928 / -0.00928	0.0109 / -0.0109	0 / 0
Jet JVT eff.	0 / 0	0 / 0	0 / 0	-0.000478 / 0.000478	0.00034 / -0.00034	-0.00724 / 0.00724	-0.00191 / 0.00191	-0.00199 / 0.00199	0 / 0	0 / 0	-0.00172 / 0.00172	0.0016 / -0.0016	-0.000303 / 0.000303	0 / 0
Flavour Tagging eff. B0	0 / 0	0 / 0	0 / 0	1.97e-08 / 1.97e-08	5.21e-09 / 5.21e-09	-1.19e-10 / -1.19e-10	2.91e-08 / 2.91e-08	-2.07e-08 / -2.07e-08	0 / 0	0 / 0	-1.62e-08 / -1.62e-08	-3.87e-08 / -3.87e-08	9.49e-09 / 9.49e-09	0 / 0
Flavour Tagging eff. B1	0 / 0	0 / 0	0 / 0	1.97e-08 / 1.97e-08	5.21e-09 / 5.21e-09	-1.19e-10 / -1.19e-10	2.91e-08 / 2.91e-08	-2.07e-08 / -2.07e-08	0 / 0	0 / 0	-1.62e-08 / -1.62e-08	-3.87e-08 / -3.87e-08	9.49e-09 / 9.49e-09	0 / 0
Flavour Tagging eff. B2	0 / 0	0 / 0	0 / 0	1.97e-08 / 1.97e-08	5.21e-09 / 5.21e-09	-1.19e-10 / -1.19e-10	2.91e-08 / 2.91e-08	-2.07e-08 / -2.07e-08	0 / 0	0 / 0	-1.62e-08 / -1.62e-08	-3.87e-08 / -3.87e-08	9.49e-09 / 9.49e-09	0 / 0
Flavour Tagging eff. B3	0 / 0	0 / 0	0 / 0	1.97e-08 / 1.97e-08	5.21e-09 / 5.21e-09	-1.19e-10 / -1.19e-10	2.91e-08 / 2.91e-08	-2.07e-08 / -2.07e-08	0 / 0	0 / 0	-1.62e-08 / -1.62e-08	-3.87e-08 / -3.87e-08	9.49e-09 / 9.49e-09	0 / 0
Flavour Tagging eff. B4	0 / 0	0 / 0	0 / 0	1.97e-08 / 1.97e-08	5.21e-09 / 5.21e-09	-1.19e-10 / -1.19e-10	2.91e-08 / 2.91e-08	-2.07e-08 / -2.07e-08	0 / 0	0 / 0	-1.62e-08 / -1.62e-08	-3.87e-08 / -3.87e-08	9.49e-09 / 9.49e-09	0 / 0
Flavour Tagging eff. B5	0 / 0	0 / 0	0 / 0	1.97e-08 / 1.97e-08	5.21e-09 / 5.21e-09	-1.19e-10 / -1.19e-10	2.91e-08 / 2.91e-08	-2.07e-08 / -2.07e-08	0 / 0	0 / 0	-1.62e-08 / -1.62e-08	-3.87e-08 / -3.87e-08	9.49e-09 / 9.49e-09	0 / 0
Flavour Tagging eff. B6	0 / 0	0 / 0	0 / 0	1.97e-08 / 1.97e-08	5.21e-09 / 5.21e-09	-1.19e-10 / -1.19e-10	2.91e-08 / 2.91e-08	-2.07e-08 / -2.07e-08	0 / 0	0 / 0	-1.62e-08 / -1.62e-08	-3.87e-08 / -3.87e-08	9.49e-09 / 9.49e-09	0 / 0
Flavour Tagging eff. B7	0 / 0	0 / 0	0 / 0	1.97e-08 / 1.97e-08	5.21e-09 / 5.21e-09	-1.19e-10 / -1.19e-10	2.91e-08 / 2.91e-08	-2.07e-08 / -2.07e-08	0 / 0	0 / 0	-1.62e-08 / -1.62e-08	-3.87e-08 / -3.87e-08	9.49e-09 / 9.49e-09	0 / 0
Flavour Tagging eff. B8	0 / 0	0 / 0	0 / 0	1.97e-08 / 1.97e-08	5.21e-09 / 5.21e-09	-1.19e-10 / -1.19e-10	2.91e-08 / 2.91e-08	-2.07e-08 / -2.07e-08	0 / 0	0 / 0	-1.62e-08 / -1.62e-08	-3.87e-08 / -3.87e-08	9.49e-09 / 9.49e-09	0 / 0
Flavour Tagging eff. C0	0 / 0	0 / 0	0 / 0	1.97e-08 / 1.97e-08	5.21e-09 / 5.21e-09	-1.19e-10 / -1.19e-10	2.91e-08 / 2.91e-08	-2.07e-08 / -2.07e-08	0 / 0	0 / 0	-1.62e-08 / -1.62e-08	-3.87e-08 / -3.87e-08	9.49e-09 / 9.49e-09	0 / 0
Flavour Tagging eff. C1	0 / 0	0 / 0	0 / 0	1.97e-08 / 1.97e-08	5.21e-09 / 5.21e-09	-1.19e-10 / -1.19e-10	2.91e-08 / 2.91e-08	-2.07e-08 / -2.07e-08	0 / 0	0 / 0	-1.62e-08 / -1.62e-08	-3.87e-08 / -3.87e-08	9.49e-09 / 9.49e-09	0 / 0
Flavour Tagging eff. C2	0 / 0	0 / 0	0 / 0	1.97e-08 / 1.97e-08	5.21e-09 / 5.21e-09	-1.19e-10 / -1.19e-10	2.91e-08 / 2.91e-08	-2.07e-08 / -2.07e-08	0 / 0	0 / 0	-1.62e-08 / -1.62e-08	-3.87e-08 / -3.87e-08	9.49e-09 / 9.49e-09	0 / 0
Flavour Tagging eff. C3	0 / 0	0 / 0	0 / 0	1.97e-08 / 1.97e-08	5.21e-09 / 5.21e-09	-1.19e-10 / -1.19e-10	2.91e-08 / 2.91e-08	-2.07e-08 / -2.07e-08	0 / 0	0 / 0	-1.62e-08 / -1.62e-08	-3.87e-08 / -3.87e-08	9.49e-09 / 9.49e-09	0 / 0
Flavour Tagging eff. Light0	0 / 0	0 / 0	0 / 0	1.97e-08 / 1.97e-08	5.21e-09 / 5.21e-09	-1.19e-10 / -1.19e-10	2.91e-08 / 2.91e-08	-2.07e-08 / -2.07e-08	0 / 0	0 / 0	-1.62e-08 / -1.62e-08	-3.87e-08 / -3.87e-08	9.49e-09 / 9.49e-09	0 / 0
Flavour Tagging eff. Light1	0 / 0	0 / 0	0 / 0	1.97e-08 / 1.97e-08	5.21e-09 / 5.21e-09	-1.19e-10 / -1.19e-10	2.91e-08 / 2.91e-08	-2.07e-08 / -2.07e-08	0 / 0	0 / 0	-1.62e-08 / -1.62e-08	-3.87e-08 / -3.87e-08	9.49e-09 / 9.49e-09	0 / 0
Flavour Tagging eff. Light2	0 / 0	0 / 0	0 / 0	1.97e-08 / 1.97e-08	5.21e-09 / 5.21e-09	-1.19e-10 / -1.19e-10	2.91e-08 / 2.91e-08	-2.07e-08 / -2.07e-08	0 / 0	0 / 0	-1.62e-08 / -1.62e-08	-3.87e-08 / -3.87e-08	9.49e-09 / 9.49e-09	0 / 0
Flavour Tagging eff. Light3	0 / 0	0 / 0	0 / 0	1.97e-08 / 1.97e-08	5.21e-09 / 5.21e-09	-1.19e-10 / -1.19e-10	2.91e-08 / 2.91e-08	-2.07e-08 / -2.07e-08	0 / 0	0 / 0	-1.62e-08 / -1.62e-08	-3.87e-08 / -3.87e-08	9.49e-09 / 9.49e-09	0 / 0
Flavour Tagging eff. extrapolation	0 / 0	0 / 0	0 / 0	1.97e-08 / 1.97e-08	5.21e-09 / 5.21e-09	-1.19e-10 / -1.19e-10	2.91e-08 / 2.91e-08	-2.07e-08 / -2.07e-08	0 / 0	0 / 0	-1.62e-08 / -1.62e-08	-3.87e-08 / -3.87e-08	9.49e-09 / 9.49e-09	0 / 0
Flavour Tagging eff. extrapolation from charm	0 / 0	0 / 0	0 / 0	1.97e-08 / 1.97e-08	5.21e-09 / 5.21e-09	-1.19e-10 / -1.19e-10	2.91e-08 / 2.91e-08	-2.07e-08 / -2.07e-08	0 / 0	0 / 0	-1.62e-08 / -1.62e-08	-3.87e-08 / -3.87e-08	9.49e-09 / 9.49e-09	0 / 0
EG_RESOLUTION_AF2	0 / 0	0 / 0	0 / 0	1.97e-08 / 1.97e-08	5.21e-09 / 5.21e-09	-1.19e-10 / -1.19e-10	2.91e-08 / 2.91e-08	-2.07e-08 / -2.07e-08	0 / 0	0 / 0	-1.62e-08 / -1.62e-08	-3.87e-08 / -3.87e-08	9.49e-09 / 9.49e-09	0 / 0
EG_RESOLUTION_MATERIALCALO	0 / 0	0 / 0	0 / 0	-0.000171 / 0.000172	2.43e-05 / -2.43e-05	0.00146 / -0.00146	-1.31e-05 / 1.3e-05	-2.07e-08 / -2.07e-08	0 / 0	0 / 0	0.00423 / -0.00422	4.48e-06 / -4.48e-06	-2.35e-05 / 2.35e-05	0 / 0
EG_RESOLUTION_MATERIALCRYO	0 / 0	0 / 0	0 / 0	0.000415 / -0.000415	0.000205 / -0.000205	0.000955 / -0.000955	-0.000393 / 0.000393	6.8e-05 / -6.8e-05	0 / 0	0 / 0	0.00929 / -0.00929	0.00763 / -0.00763	-5.41e-05 / 5.4e-05	0 / 0
EG_RESOLUTION_MATERIALGAP	0 / 0	0 / 0	0 / 0	0.000616 / -0.000616	-0.00369 / 0.00369	-1.7e-05 / 1.7e-05	-0.00279 / 0.00279	-2.07e-08 / -2.07e-08	0 / 0	0 / 0	0.00454 / -0.00454	0.00459 / -0.00459	8.88e-05 / -8.08e-05	0 / 0
EG_RESOLUTION_MATERIALIBL	0 / 0	0 / 0	0 / 0	0.00115 / -0.00115	0.000181 / -0.000181	0.00967 / -0.00967	-0.000441 / 0.000441	0.0127 / -0.0127	0 / 0	0 / 0	0.00415 / -0.00415	0.00421 / -0.00421	-5.93e-05 / 6.92e-05	0 / 0
EG_RESOLUTION_MATERIALID	0 / 0	0 / 0	0 / 0	0.00147 / -0.00147	0.01 / -0.01	0.00523 / -0.00523	-0.00142 / 0.00142	0.00128 / -0.00128	0 / 0	0 / 0	0.0163 / -0.0163	0.011 / -0.011	-2.7e-05 / 3.67e-05	0 / 0
EG_RESOLUTION_MATERIALPP0	0 / 0	0 / 0	0 / 0	0.0019 / -0.0019	0.00969 / -0.00868	0.000429 / 0.000429	-0.00237 / 0.00237	9.18e-05 / -9.19e-05	0 / 0	0 / 0	0.0073 / -0.0073	0.00447 / -0.00447	0.000127 / -0.000127	0 / 0
EG_SCALE_AF2	0 / 0	0 / 0	0 / 0	1.97e-08 / 1.97e-08	5.21e-09 / 5.21e-09	-1.19e-10 / -1.19e-10	2.91e-08 / 2.91e-08	-2.07e-08 / -2.07e-08	0 / 0	0 / 0	-1.62e-08 / -1.62e-08	-3.87e-08 / -3.87e-08	9.49e-09 / 9.49e-09	0 / 0
EG_SCALE_E4SCINTILLATOR__ETABIN0	0 / 0	0 / 0	0 / 0	1.97e-08 / 1.97e-08	5.21e-09 / 5.21e-09	-1.19e-10 / -1.19e-10	2.91e-08 / 2.91e-08	-2.07e-08 / -2.07e-08	0 / 0	0 / 0	-1.62e-08 / -1.62e-08	-3.87e-08 / -3.87e-08	9.49e-09 / 9.49e-09	0 / 0
EG_SCALE_E4SCINTILLATOR__ETABIN1	0 / 0	0 / 0	0 / 0	-2.93e-05 / 2.93e-05	0.000135 / -0.000135	-2.69e-05 / 2.69e-05	2.91e-08 / 2.91e-08	-2.07e-08 / -2.07e-08	0 / 0	0 / 0	-1.62e-08 / -1.62e-08	-3.87e-08 / -3.87e-08	3.05e-07 / -3.6e-07	0 / 0
EG_SCALE_E4SCINTILLATOR__ETABIN2	0 / 0	0 / 0	0 / 0	-3.7e-05 / 3.7e-05	5.21e-09 / 5.21e-09	-0.000125 / 0.000125	-6.8e-05 / 6.8e-05	-2.07e-08 / -2.07e-08	0 / 0	0 / 0	-8.48e-06 / 8.45e-06	-1.9e-06 / 1.91e-06	-4.27e-05 / 4.97e-05	0 / 0
EG_SCALE_G4	0 / 0	0 / 0	0 / 0	6.23e-05 / -6.23e-05	5.21e-09 / 5.21e-09	0.000873 / -0.000873	2.17e-05 / -2.17e-05	2.07e-08 / -2.07e-08	0 / 0	0 / 0	0.000119 / -0.000119	-0.00323 / 0.00323	3.93e-05 / -3.93e-05	0 / 0
EG_SCALE_LARCALIB_GAIN	0 / 0	0 / 0	0 / 0	0.00229 / -0.00229	0.00449 / -0.00449	0.00143 / -0.00143	-0.000129 / 0.000129	8.21e-05 / -8.21e-05	0 / 0	0 / 0	0.00434 / -0.00434	0.00869 / -0.00869	0.00474 / -0.00474	0 / 0
EG_SCALE_L2GAIN	0 / 0	0 / 0	0 / 0	0.00083 / -0.00083	0.011 / -0.011	0.000793 / 0.000793	0.00143 / -0.00143	-2.3e-05 / 2.3e-05	0 / 0	0 / 0	0.00155 / -0.00155	-0.00112 / 0.00112	0.00163 / -0.00163	0 / 0
EG_SCALE_LARCALIB_ETABIN0	0 / 0	0 / 0	0 / 0	-0.000802 / 0.000802	0.000171 / -0.000171	0.00385 / -0.00385	-0.00147 / 0.00147	-2.07e-08 / -2.07e-08	0 / 0	0 / 0	-0.00273 / 0.00273	-0.00324 / 0.00324	-0.000554 / 0.000561	0 / 0
EG_SCALE_LARCALIB_ETABIN1	0 / 0	0 / 0	0 / 0	-0.000211 / 0.000211	-6.29e-05 / 6.29e-05	-0.00155 / 0.00155	7.61e-05 / -7.62e-05	-6.8e-05 / 6.8e-05	0 / 0	0 / 0	-0.0015 / 0.0015	-6.52e-06 / 6.53e-06	-0.000139 / 0.000143	0 / 0
EG_SCALE_LARELECCALIB	0 / 0	0 / 0	0 / 0	-0.000227 / 0.000227	9.77e-05 / -9.77e-05	0.00097 / -0.00097	-0.00023 / 0.00023	-0.0001 / 0.0001	-2.3e-05 / 2.3e-05	0 / 0	0.0163 / -0.0163	0.011 / -0.011	-2.7e-05 / 3.67e-05	0 / 0
EG_SCALE_LARELECUNCONV__ETABIN0	0 / 0	0 / 0	0 / 0	7.72e-05 / -7.72e-05	-0.00782 / 0.00782	0.00617 / -0.00617	-0.00167 / 0.00167	-0.00449 / 0.00449	0 / 0	0 / 0	-0.00557 / 0.00557	-0.00459 / 0.00459	-0.000619 / 0.000632	0 / 0
EG_SCALE_LARELECUNCONV__ETABIN1	0 / 0	0 / 0	0 / 0	0.000622 / -0.000622	0.0152 / -0.0152	-0.00109 / 0.00109	-0.000202 / 0.000202	-0.00524 / 0.00524	0 / 0	0 / 0	-0.00861 / 0.00861	0.00741 / -0.00741	-0.000376 / 0.000386	0 / 0
EG_SCALE_LARUNCONVCALIB__ETABIN0	0 / 0	0 / 0	0 / 0	4.15e-05 / -4.15e-05	2.58e-05 / -2.58e-05	0.000248 / -0.000248	0.0014 / -0.0014	0.0045 / -0.0045	0 / 0	0 / 0	0.00146 / -0.00146	0.00177 / -0.00177	0.000223 / -0.000223	0 / 0
EG_SCALE_LARUNCONVCALIB__ETABIN1	0 / 0	0 / 0	0 / 0	-0.000346 / 0.000346	-0.0142 / 0.0142	-0.00032 / 0.00032	-0.000704 / 0.000704	3.72e-07 / -4.14e-07	0 / 0	0 / 0	0.00631 / -0.00631	-0.00341 / 0.00341	8.97e-05 / -8.98e-05	0 / 0
EG_SCALE_MATCALO_ETABIN0	0 / 0	0 / 0	0 / 0	6.03e-05 / -6.03e-05	2.03e-05 / -2.03e-05	-1.33e-05 / 1.33e-05	2.91e-08 / 2.91e-08	-2.07e-08 / -2.07e-08	0 / 0	0 / 0	5.21e-06 / -5.24e-06	-3.87e-08 / -3.87e-08	-1.27e-05 / 1.27e-05	0 / 0
EG_SCALE_MATCALO_ETABIN1	0 / 0	0 / 0	0 / 0	-2.48e-05 / 2.48e-05	5.21e-09 / 5.21e-09	3.12e-05 / -3.12e-05	4.5e-06 / -4.52e-06	-2.07e-08 / -2.07e-08	0 / 0	0 / 0	-1.62e-08 / -1.62e-08	-3.87e-08 / -3.87e-08	-1.05e-05 / 1.05e-05	0 / 0
EG_SCALE_MATCALO_ETABIN10	0 / 0	0 / 0	0 / 0	1.97e-08 / 1.97e-08	5.21e-09 / 5.21e-09	-1.19e-10 / -1.19e-10	2.91e-08 / 2.91e-08	-2.07e-08 / -2.07e-08	0 / 0	0 / 0	-1.62e-08 / -1.62e-08	-3.87e-08 / -3.87e-08	9.49e-09 / 9.49e-09	0 / 0
EG_SCALE_MATCALO_ETABIN11	0 / 0	0 / 0	0 / 0	1.97e-08 / 1.97e-08	5.21e-09 / 5.21e-09	-1.19e-10 / -1.19e-10

	CR_{ll}	CR_{ll}	CR_{ll}	$W\gamma\gamma$	$Z\gamma$	$Z\gamma\gamma$	$tX\gamma$	$t\bar{t}$	Fake electrons	Fake muons	diboson	$W(\tau\nu)\gamma\gamma$	$W l\nu\gamma\gamma$	pileup	
Fake photon yield stat CRgj	0.0208 / -0.0208	0 / 0	0 / 0	0 / 0	0 / 0	0 / 0	0 / 0	0 / 0	0 / 0	0 / 0	0 / 0	0 / 0	0 / 0	0 / 0	
Fake photon yield sys	0.0575 / -0.0253	0.0575 / -0.0253	0.0575 / -0.0253	0 / 0	0 / 0	0 / 0	0 / 0	0 / 0	0 / 0	0 / 0	0 / 0	0 / 0	0 / 0	0 / 0	
Fake photon shape sys CRgj	0.13 / -0.132	0 / 0	0 / 0	0 / 0	0 / 0	0 / 0	0 / 0	0 / 0	0 / 0	0 / 0	0 / 0	0 / 0	0 / 0	0 / 0	
shape_FakePhotonShapeStat_gj_SignalRegion_bin_0	0.0326 / -0.0326	0 / 0	0 / 0	0 / 0	0 / 0	0 / 0	0 / 0	0 / 0	0 / 0	0 / 0	0 / 0	0 / 0	0 / 0	0 / 0	
shape_FakePhotonShapeStat_gj_SignalRegion_bin_1	0.0296 / -0.0296	0 / 0	0 / 0	0 / 0	0 / 0	0 / 0	0 / 0	0 / 0	0 / 0	0 / 0	0 / 0	0 / 0	0 / 0	0 / 0	
shape_FakePhotonShapeStat_gj_SignalRegion_bin_2	0.0263 / -0.0263	0 / 0	0 / 0	0 / 0	0 / 0	0 / 0	0 / 0	0 / 0	0 / 0	0 / 0	0 / 0	0 / 0	0 / 0	0 / 0	
shape_FakePhotonShapeStat_gj_SignalRegion_bin_3	0.0159 / -0.0159	0 / 0	0 / 0	0 / 0	0 / 0	0 / 0	0 / 0	0 / 0	0 / 0	0 / 0	0 / 0	0 / 0	0 / 0	0 / 0	
shape_FakePhotonShapeStat_gj_SignalRegion_bin_4	0.0307 / -0.0307	0 / 0	0 / 0	0 / 0	0 / 0	0 / 0	0 / 0	0 / 0	0 / 0	0 / 0	0 / 0	0 / 0	0 / 0	0 / 0	
Fake photon yield stat CRjj	0 / 0	0.0129 / -0.0129	0 / 0	0 / 0	0 / 0	0 / 0	0 / 0	0 / 0	0 / 0	0 / 0	0 / 0	0 / 0	0 / 0	0 / 0	
Fake photon shape sys CRjj	0 / 0	0.323 / -0.343	0 / 0	0 / 0	0 / 0	0 / 0	0 / 0	0 / 0	0 / 0	0 / 0	0 / 0	0 / 0	0 / 0	0 / 0	
shape_FakePhotonShapeStat_jg_SignalRegion_bin_0	0 / 0	0.0438 / -0.0438	0 / 0	0 / 0	0 / 0	0 / 0	0 / 0	0 / 0	0 / 0	0 / 0	0 / 0	0 / 0	0 / 0	0 / 0	
shape_FakePhotonShapeStat_jg_SignalRegion_bin_1	0 / 0	0.0402 / -0.0402	0 / 0	0 / 0	0 / 0	0 / 0	0 / 0	0 / 0	0 / 0	0 / 0	0 / 0	0 / 0	0 / 0	0 / 0	
shape_FakePhotonShapeStat_jg_SignalRegion_bin_2	0 / 0	0.0372 / -0.0372	0 / 0	0 / 0	0 / 0	0 / 0	0 / 0	0 / 0	0 / 0	0 / 0	0 / 0	0 / 0	0 / 0	0 / 0	
shape_FakePhotonShapeStat_jg_SignalRegion_bin_3	0 / 0	0.0225 / -0.0225	0 / 0	0 / 0	0 / 0	0 / 0	0 / 0	0 / 0	0 / 0	0 / 0	0 / 0	0 / 0	0 / 0	0 / 0	
shape_FakePhotonShapeStat_jg_SignalRegion_bin_4	0 / 0	0.042 / -0.042	0 / 0	0 / 0	0 / 0	0 / 0	0 / 0	0 / 0	0 / 0	0 / 0	0 / 0	0 / 0	0 / 0	0 / 0	
Fake photon yield stat CRjj	0 / 0	0 / 0	0.000993 / -0.000993	0 / 0	0 / 0	0 / 0	0 / 0	0 / 0	0 / 0	0 / 0	0 / 0	0 / 0	0 / 0	0 / 0	
Fake photon shape sys CRjj	0 / 0	0 / 0	0.167 / -0.167	0 / 0	0 / 0	0 / 0	0 / 0	0 / 0	0 / 0	0 / 0	0 / 0	0 / 0	0 / 0	0 / 0	
shape_FakePhotonShapeStat_jj_SignalRegion_bin_0	0 / 0	0 / 0	0.0492 / -0.0492	0 / 0	0 / 0	0 / 0	0 / 0	0 / 0	0 / 0	0 / 0	0 / 0	0 / 0	0 / 0	0 / 0	
shape_FakePhotonShapeStat_jj_SignalRegion_bin_1	0 / 0	0 / 0	0.0394 / -0.0394	0 / 0	0 / 0	0 / 0	0 / 0	0 / 0	0 / 0	0 / 0	0 / 0	0 / 0	0 / 0	0 / 0	
shape_FakePhotonShapeStat_jj_SignalRegion_bin_2	0 / 0	0 / 0	0.0255 / -0.0255	0 / 0	0 / 0	0 / 0	0 / 0	0 / 0	0 / 0	0 / 0	0 / 0	0 / 0	0 / 0	0 / 0	
shape_FakePhotonShapeStat_jj_SignalRegion_bin_3	0 / 0	0 / 0	0.0183 / -0.0183	0 / 0	0 / 0	0 / 0	0 / 0	0 / 0	0 / 0	0 / 0	0 / 0	0 / 0	0 / 0	0 / 0	
shape_FakePhotonShapeStat_jj_SignalRegion_bin_4	0 / 0	0 / 0	0.0593 / -0.0593	0 / 0	0 / 0	0 / 0	0 / 0	0 / 0	0 / 0	0 / 0	0 / 0	0 / 0	0 / 0	0 / 0	
$p_{T\gamma\gamma}$	0 / 0	0 / 0	0.158 / -0.157	0 / 0	0 / 0	0 / 0	0 / 0	0 / 0	0 / 0	0 / 0	0 / 0	0 / 0	0 / 0	0 / 0	
Luminosity	0 / 0	0 / 0	0.0169 / -0.0169	0.0169 / -0.0169	0.0169 / -0.0169	0.0169 / -0.0169	0.0169 / -0.0169	0.0169 / -0.0169	0 / 0	0 / 0	0.0169 / -0.0169	0.0169 / -0.0169	0.0169 / -0.0169	0.0169 / -0.0169	0.0337 / -0.0337
PDF Theory uncertainty Wgg	0 / 0	0 / 0	0 / 0	1.96-08 / 1.96-08	0 / 0	0 / 0	0 / 0	0 / 0	0 / 0	0 / 0	0 / 0	0 / 0	0 / 0	0 / 0	
Scale Theory uncertainty Wgg	0 / 0	0 / 0	0 / 0	1.95-08 / 1.91e-08	0 / 0	0 / 0	0 / 0	0 / 0	0 / 0	0 / 0	0 / 0	0 / 0	0 / 0	0 / 0	
α_S Theory uncertainty Wgg	0 / 0	0 / 0	0 / 0	1.97e-08 / 1.97e-08	0 / 0	0 / 0	0 / 0	0 / 0	0 / 0	0 / 0	0 / 0	0 / 0	0 / 0	0 / 0	
Modelling theory uncertainty Wgg	0 / 0	0 / 0	0 / 0	-5.55e-08 / 5.61e-08	0 / 0	0 / 0	0 / 0	0 / 0	0 / 0	0 / 0	0 / 0	0 / 0	0 / 0	0 / 0	
Electron identification eff.	0 / 0	0 / 0	0 / 0	0.00388 / -0.00388	0.00621 / -0.00621	0 / 0	0 / 0	0 / 0	0 / 0	0 / 0	0 / 0	0 / 0	0 / 0	0 / 0	
Electron isolation eff.	0 / 0	0 / 0	0 / 0	0.000591 / -0.000591	0.00104 / -0.00104	0 / 0	0 / 0	0 / 0	0 / 0	0 / 0	0 / 0	0 / 0	0 / 0	0 / 0	
Electron reconstruction eff.	0 / 0	0 / 0	0 / 0	0.000738 / -0.000738	0.00118 / -0.00118	0 / 0	0 / 0	0 / 0	0 / 0	0 / 0	0 / 0	0 / 0	0 / 0	0 / 0	
Electron Trigger eff.	0 / 0	0 / 0	0 / 0	1.97e-08 / 1.97e-08	5.21e-09 / 5.21e-09	0 / 0	0 / 0	0 / 0	0 / 0	0 / 0	0 / 0	0 / 0	0 / 0	0 / 0	
Photon identification eff.	0 / 0	0 / 0	0 / 0	0.0244 / -0.0244	0.0253 / -0.0254	0.0273 / -0.0273	0.0244 / -0.0244	0.027 / -0.0271	0 / 0	0 / 0	0 / 0	0.0259 / -0.0259	0.0233 / -0.0231	0.0171 / -0.0171	0 / 0
Photon isolation eff.	0 / 0	0 / 0	0 / 0	0.0244 / -0.0244	0.0288 / -0.0288	0.0259 / -0.0259	0.0259 / -0.0259	0.0281 / -0.0281	0 / 0	0 / 0	0 / 0	0.027 / -0.027	0.0235 / -0.0235	0.02 / -0.02	0 / 0
Photon Trigger eff.	0 / 0	0 / 0	0 / 0	0.00631 / -0.00631	0.000732 / -0.000732	0.00656 / -0.00656	0.00658 / -0.00658	0.00595 / -0.00595	0 / 0	0 / 0	0 / 0	0.00584 / -0.00584	0.00582 / -0.00582	0.00766 / -0.00766	0 / 0
Muon isolation eff. stat	0 / 0	0 / 0	0 / 0	0.000568 / -0.000568	2.74e-05 / -2.74e-05	0.000522 / -0.000522	0.000564 / -0.000564	0.000612 / -0.000612	0 / 0	0 / 0	0 / 0	0.000367 / -0.000368	0.000334 / -0.000334	0.000591 / -0.000591	0 / 0
Muon isolation eff. syst.	0 / 0	0 / 0	0 / 0	0.00363 / -0.00363	0.000618 / -0.000618	0.00357 / -0.00357	0.00299 / -0.00299	0.00333 / -0.00333	0 / 0	0 / 0	0 / 0	0.0032 / -0.0032	0.00506 / -0.00506	0.00299 / -0.00299	0 / 0
Muon reconstruction eff. stat	0 / 0	0 / 0	0 / 0	0.00023 / -0.00023	2.22e-05 / -2.21e-05	0.000248 / -0.000248	0.000235 / -0.000235	0.000191 / -0.000191	0 / 0	0 / 0	0 / 0	0.000144 / -0.000144	0.000182 / -0.000182	0.000234 / -0.000234	0 / 0
Muon reconstruction eff. low-pT stat.	0 / 0	0 / 0	0 / 0	1.97e-08 / 1.97e-08	5.21e-09 / 5.21e-09	-1.19e-10 / -1.19e-10	2.91e-08 / 2.91e-08	-2.07e-08 / -2.07e-08	0 / 0	0 / 0	0 / 0	-1.62e-08 / -1.62e-08	-3.87e-08 / -3.87e-08	9.49e-09 / 9.49e-09	0 / 0
Muon reconstruction eff. syst.	0 / 0	0 / 0	0 / 0	0.000068 / -0.000068	8.03e-08 / -8.03e-08	0.00119 / -0.00119	0.000944 / -0.000944	0.000853 / -0.000853	0 / 0	0 / 0	0 / 0	0.000706 / -0.000706	0.000663 / -0.000663	0.000976 / -0.000976	0 / 0
Muon reconstruction eff. low-pT syst.	0 / 0	0 / 0	0 / 0	1.97e-08 / 1.97e-08	5.21e-09 / 5.21e-09	-1.19e-10 / -1.19e-10	2.91e-08 / 2.91e-08	-2.07e-08 / -2.07e-08	0 / 0	0 / 0	0 / 0	-1.62e-08 / -1.62e-08	-3.87e-08 / -3.87e-08	9.49e-09 / 9.49e-09	0 / 0
Muon TTVA eff. stat	0 / 0	0 / 0	0 / 0	0.000135 / -0.000135	1.04e-05 / -1.04e-05	0.000135 / -0.000135	0.000137 / -0.000137	0.000128 / -0.000128	0 / 0	0 / 0	0 / 0	8.44e-05 / -8.44e-05	8.83e-05 / -8.84e-05	0.000142 / -0.000143	0 / 0
Muon TTVA eff. syst.	0 / 0	0 / 0	0 / 0	0.000175 / -0.000175	3.27e-06 / -3.27e-06	0.000172 / -0.000172	0.000171 / -0.000171	0.000176 / -0.000176	0 / 0	0 / 0	0 / 0	0.000101 / -0.000101	5.83e-05 / -5.83e-05	0.000177 / -0.000177	0 / 0
Muon trigger eff. stat	0 / 0	0 / 0	0 / 0	0.00156 / -0.00156	0.000124 / -0.000124	0.00149 / -0.00149	0.00151 / -0.00151	0.00149 / -0.00149	0 / 0	0 / 0	0 / 0	0.000993 / -0.000993	0.00164 / -0.00164	0.00155 / -0.00155	0 / 0
Muon trigger eff. syst.	0 / 0	0 / 0	0 / 0	0.0106 / -0.0106	0.0000937 / -0.0000937	0.00956 / -0.00956	0.0116 / -0.0116	0.0107 / -0.0107	0 / 0	0 / 0	0 / 0	0.0063 / -0.0063	0.00922 / -0.00922	0.0109 / -0.0109	0 / 0
Jet JVT eff.	0 / 0	0 / 0	0 / 0	0.000475 / 0.000475	0.000337 / -0.000337	0.00719 / 0.00719	-0.00719 / -0.00719	-0.0019 / 0.0019	-0.00198 / 0.00198	0 / 0	0 / 0	-0.00171 / 0.00171	0.00159 / -0.00159	-0.00631 / 0.00631	0 / 0
Flavour Tagging eff. B0	0 / 0	0 / 0	0 / 0	1.97e-08 / 1.97e-08	5.21e-09 / 5.21e-09	-1.19e-10 / -1.19e-10	2.91e-08 / 2.91e-08	-2.07e-08 / -2.07e-08	0 / 0	0 / 0	0 / 0	-1.62e-08 / -1.62e-08	-3.87e-08 / -3.87e-08	9.49e-09 / 9.49e-09	0 / 0
Flavour Tagging eff. B1	0 / 0	0 / 0	0 / 0	1.97e-08 / 1.97e-08	5.21e-09 / 5.21e-09	-1.19e-10 / -1.19e-10	2.91e-08 / 2.91e-08	-2.07e-08 / -2.07e-08	0 / 0	0 / 0	0 / 0	-1.62e-08 / -1.62e-08	-3.87e-08 / -3.87e-08	9.49e-09 / 9.49e-09	0 / 0
Flavour Tagging eff. B2	0 / 0	0 / 0	0 / 0	1.97e-08 / 1.97e-08	5.21e-09 / 5.21e-09	-1.19e-10 / -1.19e-10	2.91e-08 / 2.91e-08	-2.07e-08 / -2.07e-08	0 / 0	0 / 0	0 / 0	-1.62e-08 / -1.62e-08	-3.87e-08 / -3.87e-08	9.49e-09 / 9.49e-09	0 / 0
Flavour Tagging eff. B3	0 / 0	0 / 0	0 / 0	1.97e-08 / 1.97e-08	5.21e-09 / 5.21e-09	-1.19e-10 / -1.19e-10	2.91e-08 / 2.91e-08	-2.07e-08 / -2.07e-08	0 / 0	0 / 0	0 / 0	-1.62e-08 / -1.62e-08	-3.87e-08 / -3.87e-08	9.49e-09 / 9.49e-09	0 / 0
Flavour Tagging eff. B4	0 / 0	0 / 0	0 / 0	1.97e-08 / 1.97e-08	5.21e-09 / 5.21e-09	-1.19e-10 / -1.19e-10	2.91e-08 / 2.91e-08	-2.07e-08 / -2.07e-08	0 / 0	0 / 0	0 / 0	-1.62e-08 / -1.62e-08	-3.87e-08 / -3.87e-08	9.49e-09 / 9.49e-09	0 / 0
Flavour Tagging eff. B5	0 / 0	0 / 0	0 / 0	1.97e-08 / 1.97e-08	5.21e-09 / 5.21e-09	-1.19e-10 / -1.19e-10	2.91e-08 / 2.91e-08	-2.07e-08 / -2.07e-08	0 / 0	0 / 0	0 / 0	-1.62e-08 / -1.62e-08	-3.87e-08 / -3.87e-08	9.49e-09 / 9.49e-09	0 / 0
Flavour Tagging eff. B6	0 / 0	0 / 0	0 / 0	1.97e-08 / 1.97e-08	5.21e-09 / 5.21e-09	-1.19e-10 / -1.19e-10	2.91e-08 / 2.91e-08	-2.07e-08 / -2.07e-08	0 / 0	0 / 0	0 / 0	-1.62e-08 / -1.62e-08	-3.87e-08 / -3.87e-08	9.49e-09 / 9.49e-09	0 / 0
Flavour Tagging eff. B7	0 / 0	0 / 0	0 / 0	1.97e-08 / 1.97e-08	5.21e-09 / 5.21e-09	-1.19e-10 / -1.19e-10	2.91e-08 / 2.91e-08	-2.07e-08 / -2.07e-08	0 / 0	0 / 0	0 / 0	-1.62e-08 / -1.62e-08	-3.87e-08 / -3.87e-08	9.49e-09 / 9.49e-09	0 / 0
Flavour Tagging eff. B8	0 / 0	0 / 0	0 / 0	1.97e-08 / 1.97e-08	5.21e-09 / 5.21e-09	-1.19e-10 / -1.19e-10	2.91e-08 / 2.91e-08	-2.07e-08 / -2.07e-08	0 / 0	0 / 0	0 / 0	-1.62e-08 / -1.62e-08	-3.87e-08 / -3.87e-08	9.49e-09 / 9.49e-09	0 / 0
Flavour Tagging eff. C0	0 / 0	0 / 0	0 / 0	1.97e-08 / 1.97e-08	5.21e-09 / 5.21e-09	-1.19e-10 / -1.19e-10	2.91e-08 / 2.91e-08	-2.07e-08 / -2.07e-08	0 / 0	0 / 0	0 / 0	-1.62e-08 / -1.62e-08	-3.87e-08 / -3.87e-08	9.49e-09 / 9.49e-09	0 / 0
Flavour Tagging eff. C1	0 / 0	0 / 0	0 / 0	1.97e-08 / 1.97e-08	5.21e-09 / 5.21e-09	-1.19e-10 / -1.19e-10	2.91e-08 / 2.91e-08	-2.07e-08 / -2.07e-08	0 / 0	0 / 0	0 / 0	-1.62e-08 / -1.62e-08	-3.87e-08 / -3.87e-08	9.49e-09 / 9.49e-09	0 / 0
Flavour Tagging eff. C2	0 / 0	0 / 0	0 / 0	1.97e-08 / 1.97e-08	5.21e-09 / 5.21e-09	-1.19e-10 / -1.19e-10	2.91e-08 / 2.91e-08	-2.07e-08 / -2.07e-08	0 / 0	0 / 0	0 / 0	-1.62e-08 / -1.62e-08	-3.87e-08 / -3.87e-08	9.49e-09 / 9.49e-09	0 / 0
Flavour Tagging eff. C3	0 / 0	0 / 0	0 / 0	1.97e-08 / 1.97e-08	5.21e-09 / 5.21e-09	-1.19e-10 / -1.19e-10	2.91e-08 / 2.91e-08	-2.07e-08 / -2.07e-08	0 / 0	0 / 0	0 / 0	-1.62e-08 / -1.62e-08	-3.87e-08 / -3.87e-08	9.49e-09 / 9.49e-09	0 / 0
Flavour Tagging eff. Light0	0 / 0	0 / 0	0 / 0	1.97e-08 / 1.97e-08	5.21e-09 / 5.21e-09	-1.19e-10 / -1.19e-10	2.91e-08 / 2.91e-08	-2.07e-08 / -2.07e-08	0 / 0	0 / 0	0 / 0	-1.62e-08 / -1.62e-08	-3.87e-08 / -3.87e-08	9.49e-09 / 9.49e-09	0 / 0
Flavour Tagging eff. Light1	0 / 0	0 / 0	0 / 0	1.97e-08 / 1.97e-08	5.21e-09 / 5.21e-09	-1.19e-10 / -1.19e-10	2.91e-08 / 2.91e-08	-2.07e-08 / -2.07e-08	0 / 0	0 / 0	0 / 0	-1.62e-08 / -1.62e-08	-3.87e-08 / -3.87e-08	9.49e-09 / 9.49e-09	0 / 0
Flavour Tagging eff. Light2	0 / 0	0 / 0	0 / 0	1.97e-08 / 1.97e-08	5.21e-09 / 5.21e-09	-1.19e-10 / -1.19e-10	2.91e-08 / 2.91e-08	-2.07e-08 / -2.07e-08	0 / 0	0 / 0	0 / 0	-1.62e-08 / -1.62e-08	-3.87e-08 / -3.87e-08	9.49e-09 / 9.49e-09	0 / 0
Flavour Tagging eff. Light3	0 / 0	0 / 0	0 / 0	1.97e-08 / 1.97e-08	5.21e-09 / 5.21e-09	-1.19e-10 / -1.19e-10	2.91e-08 / 2.91e-08	-2.07e-08 / -2.07e-08	0 / 0	0 / 0	0 / 0	-1.62e-08 / -1.62e-08	-3.87e-08 / -3.87e-08	9.49e-09 / 9.49e-09	0 / 0
Flavour Tagging eff. extrapolation	0 / 0	0 / 0	0 / 0	1.97e-08 / 1.97e-08	5.21e-09 / 5.21e-09	-1.19e-10 / -1.19e-10	2.91e-08 / 2.91e-08	-2.07e-08 / -2.07e-08	0 / 0	0 / 0	0 / 0	-1.62e-08 / -1.62e-08	-3.87e-08 / -3.87e-08	9.49e-09 / 9.49e-09	0 / 0
Flavour Tagging eff. extrapolation from charm	0 / 0	0 / 0	0 / 0	1.97e-08 / 1.97e-08	5.21e-09 / 5.21e-09	-1.19e-10 / -1.19e-10	2.91e-08 / 2.91e-08	-2.07e-08 / -2.07e-08	0 / 0	0 / 0	0 / 0	-1.62e-08 / -1.62e-08	-3.87e-08 / -3.87e-08	9.49e-09 / 9.49e-09	0 / 0
EG_RESOLUTION_AF2	0 / 0	0 / 0	0 / 0	1.97e-08 / 1.97e-08	5.21e-09 / 5.21e-09	-1.19e-10 / -1.19e-10	2.91e-08 / 2.91e-08	-2.07e-08 / -2.07e-08	0 / 0	0 / 0	0 / 0	-1.62e-08 / -1.62e-08	-3.87e-08 / -3.87e-08	9.49e-09 / 9.49e-09	0 / 0
EG_RESOLUTION_MATERIALCALO	0 / 0	0 / 0	0 / 0	-0.00017 / 0.00017	2.41e-05 / -2.41e-05	0.00145 / -0.00145	-1.3e-05 / 1.3e-05	-2.05e-08 / -2.06e-08	0 / 0	0 / 0	0 / 0	0.0042 / -0.0042	4.46e-06 / -4.45e-06	-2.33e-05 / 2.34e-05	0 / 0
EG_RESOLUTION_MATERIALCRYO	0 / 0	0 / 0	0 / 0	0.000413 / -0.000413	0.000204 / -0.000204	0.000949 / -0.000949	0.000391 / -0.000391	6.76e-05 / -6.76e-05	0 / 0	0 / 0	0 / 0	0.00922 / -0.00922	0.00758 / -0.00758	5.37e-05 / -5.37e-05	0 / 0
EG_RESOLUTION_MATERIALGAP	0 / 0	0 / 0	0 / 0	0.000612 / -0.000612	-0.00366 / 0.00366	-1.69e-05 / 1.69e-05	-0.00277 / 0.00277	-2.05e-08 / -2.06e-08	0 / 0	0 / 0	0 / 0	0.0045 / -0.00451	0.00456 / -0.00456	8.82e-05 / -8.02e-05	0 / 0
EG_RESOLUTION_MATERIALIBL	0 / 0	0 / 0	0 / 0	0.00114 / -0.00114	0.00018 / -0.00018	0.0096 / -0.0096	-0.000438 / 0.000438	0.0126 / -0.0126	0 / 0	0 / 0	0 / 0	0.00412 / -0.00412	0.00418 / -0.00418	-5.89e-05 / 6.87e-05	0 / 0
EG_RESOLUTION_MATERIALID	0 / 0	0 / 0	0 / 0	0.00146 / -0.00146	0.00996 / -0.00996	0.00519 / -0.00519	-0.00141 / 0.00141	0.0127 / -0.0127	0 / 0	0 / 0	0 / 0	0.0162 / -0.0162	0.0109 / -0.0109	-2.68e-05 / 3.65e-05	0 / 0
EG_RESOLUTION_MATERIALPP0	0 / 0	0 / 0	0 / 0	0.00188 / -0.00188	0.00952 / -0.00952	-0.00426 / 0.00426	-0.00235 / 0.00235	9.12e-05 / -9.12e-05	0 / 0	0 / 0	0 / 0	0.00725 / -0.00725	0.00443 / -0.00443	0.000126 / -0.000126	0 / 0
EG_SCALE_AF2	0 / 0	0 / 0	0 / 0	1.97e-08 / 1.97e-08	5.21e-09 / 5.21e-09	-1.19e-10 / -1.19e-10	2.91e-08 / 2.91e-08	-2.07e-08 / -2.07e-08	0 / 0	0 / 0	0 / 0	-1.62e-08 / -1.62e-08	-3.87e-08 / -3.87e-08	9.49e-09 / 9.49e-09	0 / 0
EG_SCALE_E4SCINTILLATOR__ETABIN0	0 / 0	0 / 0	0 / 0	1.97e-08 / 1.97e-08	5.21e-09 / 5.21e-09	-1.19e-10 / -1.19e-10	2.91e-08 / 2.91e-08	-2.07e-08 / -2.07e-08	0 / 0	0 / 0	0 / 0	-1.62e-08 / -1.62e-08	-3.87e-08 / -3.87e-08	9.49e-09 / 9.49e-09	0 / 0
EG_SCALE_E4SCINTILLATOR__ETABIN1	0 / 0	0 / 0	0 / 0	-2.93e-05 / 2.92e-05	0.000135 / 0.000135	-2.69e-05 / 2.69e-05	2.91e-08 / 2.91e-08	-2.07e-08 / -2.07e-08	0 / 0	0 / 0	0 / 0	-1.62e-08 / -1.62e-08	-3.87e-08 / -3.87e-08	3.05e-07 / -3.6e-07	0 / 0
EG_SCALE_E4SCINTILLATOR__ETABIN2	0 / 0	0 / 0	0 / 0	-3.67e-05 / 3.68e-05	5.17e-09 / 5.17e-09	-0.000124 / 0.000124	-6.75e-05 / 6.75e-05	2.06e-08 / -2.06e-08	0 / 0	0 / 0	0 / 0	-8.42e-06 / 8.39e-06	-1.89e-06 / 1.9e-06	-4.24e-05 / 4.94e-05	0 / 0
EG_SCALE_G4	0 / 0	0 / 0	0 / 0	6.18e-05 / -6.19e-05	5.16e-09 / 5.18e-09	0.000867 / -0.000867	2.15e-05 / -2.16e-05	-2.05e-08 / -2.06e-08	0 / 0	0 / 0	0 / 0	0.000118 / -0.000118	-0.00321 / 0.00321	3.91e-05 / -3.91e-05	0 / 0
EG_SCALE_LARCALIN	0 / 0	0 / 0	0 / 0	0.00225 / -0.00228	0.00446 / -0.00446	0.00142 / -0.00142	-0.000128 / 0.000128	8.16e-05 / -8.16e-05	0 / 0	0 / 0	0 / 0	0.00431 / -0.00431	0.00864 / -0.00864	0.000471 / -0.000471	0 / 0
EG_SCALE_LARGAIN	0 / 0	0 / 0	0 / 0	0.000823 / -0.000823	0.0109 / -0.0109	-0.000787 / 0.000787	0.00142 / -0.00142	-2.28e-05 / 2.28e-05	0 / 0	0 / 0	0 / 0	0.00154 / -0.00154	-0.00111 / 0.00111	0.00161 / -0.00161	0 / 0
EG_SCALE_LARECLBPS	0 / 0	0 / 0	0 / 0	-0.000797 / 0.000797	0.00017 / -0.00017	0.00382 / -0.00382	-0.00146 / 0.00146	-2.03e-08 / -2.08e-08	0 / 0	0 / 0	0 / 0	-0.00271 / 0.00271	-0.00322 / 0.00322	-0.00055 / 0.000557	0 / 0
EG_SCALE_LARELECCALIB	0 / 0	0 / 0	0 / 0	-0.00021 / 0.00021	5.25e-05 / -5.25e-05	0.00154 / -0.00154	7.56e-05 / -7.57e-05	6.76e-05 / 6.76e-05	0 / 0	0 / 0	0 / 0	-0.00149 / 0.00149	-6.48e-06 / 6.49e-06	-0.000138 / 0.000142	0 / 0
EG_SCALE_LARELECCALIB	0 / 0	0 / 0	0 / 0	-0.000249 / 0.000249	-9.71e-05 / 9.71e-05	0.000963 / -0.000963	-9.97e-05 / 9.97e-05	-2.29e-05 / 2.28e-05	0 / 0	0 / 0	0 / 0	-0.000295 / 0.000295	1.2e-06 / -1.18e-06	2.37e-05 / -2.36e-05	0 / 0
EG_SCALE_LARELECUNCONV_ETABIN0	0 / 0	0 / 0	0 / 0	7.66e-05 / -7.67e-05	-0.00777 / 0.00776	0.00612 / -0.00613	-0.00165 / 0.00165	-0.00446 / 0.00446	0 / 0	0 / 0	0 / 0	-0.00553 / 0.00553	-0.00455 / 0.00455	-0.000614 / 0.000628	0 / 0
EG_SCALE_LARELECUNCONV_ETABIN1	0 / 0	0 / 0	0 / 0	0.000618 / -0.00188	0.00952 / -0.00952	-0.0151 / 0.0151	-0.00108 / 0.00108	-0.0002 / 0.0002	-0.0052 / 0.0052	0 / 0	0 / 0	-0.00855 / 0.00855	0.00736 / -0.00736	-0.000373 / 0.000384	0 / 0
EG_SCALE_LARUNCONVCALIB_ETABIN0	0 / 0	0 / 0	0 / 0	4.12e-05 / -4.12e-05	2.56e-05 / -2.56e-05	-0.00246 / 0.00246	0.00139 / -0.00139	0.00447 / -0.00447	0 / 0	0 / 0	0 / 0	-0.00145 / 0.00145	0.000176 / -0.000176	0.000222 / -0.000222	0 / 0
EG_SCALE_LARUNCONVCALIB_ETABIN1	0 / 0	0 / 0	0 / 0	-0.000343 / 0.000343	-0.0141 / 0.0141	-0.000318 / 0.000318	-0.000699 / 0.000699	3.7e-07 / -4.11e-07	0 / 0	0 / 0	0 / 0	0.00627 / -0.00627	-0.00339 / 0.00339	8.91e-05 / -8.92e-05	0 / 0
EG_SCALE_MATCALO_ETABIN0

	j-fake γ	$W\gamma\gamma$	$Z\gamma$	$Z\gamma\gamma$	$tX\gamma$	$t\bar{t}$	diboson	$W(\tau\nu)\gamma\gamma$	$WH\gamma\gamma$	$WH\gamma\gamma$
j-fake photon SF error	0.23 / -0.23	0 / 0	0 / 0	0 / 0	0 / 0	0 / 0	0 / 0	0 / 0	0 / 0	0 / 0
Luminosity	0 / 0	0.017 / -0.017	0.017 / -0.017	0.017 / -0.017	0.017 / -0.017	0.017 / -0.017	0.017 / -0.017	0.017 / -0.017	0.017 / -0.017	0 / 0
Electron identification eff.	0 / 0	0.00515 / -0.00515	0.00782 / -0.00782	0 / 0	0 / 0	0 / 0	0 / 0	0 / 0	0 / 0	0 / 0
Electron isolation eff.	0 / 0	0.000724 / -0.000724	0.00133 / -0.00133	0 / 0	0 / 0	0 / 0	0 / 0	0 / 0	0 / 0	0 / 0
Electron reconstruction eff.	0 / 0	0.000946 / -0.000946	0.00183 / -0.00183	0 / 0	0 / 0	0 / 0	0 / 0	0 / 0	0 / 0	0 / 0
Electron Trigger eff.	0 / 0	1.6e-10 / 1.6e-10	1.83e-08 / 1.83e-08	0 / 0	0 / 0	0 / 0	0 / 0	0 / 0	0 / 0	0 / 0
Photon identification eff.	0 / 0	0.0264 / -0.0264	0.0274 / -0.0274	0.0324 / -0.0324	0.0241 / -0.0241	0.0275 / -0.0275	0.0274 / -0.0274	0.0381 / -0.0381	0.0167 / -0.0167	0 / 0
Photon isolation eff.	0 / 0	0.0295 / -0.0295	0.0359 / -0.0359	0.027 / -0.027	0.0253 / -0.0253	0.0278 / -0.0278	0.0308 / -0.0308	0.034 / -0.034	0.0199 / -0.0199	0 / 0
Photon Trigger eff.	0 / 0	0.00666 / -0.00666	0.000286 / -0.000286	0.00829 / -0.00829	0.00636 / -0.00636	0.00644 / -0.00644	0.0108 / -0.0108	0.00383 / -0.00383	0.00747 / -0.00747	0 / 0
Muon isolation eff. stat	0 / 0	0.00056 / -0.00056	8.97e-06 / -9.02e-06	0.000822 / -0.000822	0.000595 / -0.000595	0.000494 / -0.000494	0.000605 / -0.000605	0.000118 / -0.000118	0.000605 / -0.000605	0 / 0
Muon isolation eff. syst.	0 / 0	0.00306 / -0.00306	0.000106 / -0.000106	0.00566 / -0.00566	0.00317 / -0.00317	0.00327 / -0.00327	0.00413 / -0.00413	0.0142 / -0.0142	0.00284 / -0.00284	0 / 0
Muon reconstruction eff. stat	0 / 0	0.000235 / -0.000235	1.28e-05 / -1.27e-05	0.000285 / -0.000285	0.000228 / -0.000228	0.000229 / -0.000229	0.000331 / -0.000331	0.000144 / -0.000144	0.000229 / -0.000229	0 / 0
Muon reconstruction eff. low-pT stat.	0 / 0	1.6e-10 / 1.6e-10	1.83e-08 / 1.83e-08	-3.04e-08 / -3.04e-08	1.64e-08 / 1.64e-08	3.79e-08 / 3.79e-08	-6.79e-09 / -6.79e-09	1.65e-08 / 1.65e-08	-3.88e-08 / -3.88e-08	0 / 0
Muon reconstruction eff. syst.	0 / 0	0.00121 / -0.00121	8.53e-05 / -8.52e-05	0.00116 / -0.00116	0.000978 / -0.000978	0.000886 / -0.000886	0.0026 / -0.0026	0.00105 / -0.00105	0.00104 / -0.00104	0 / 0
Muon reconstruction eff. low-pT syst.	0 / 0	1.6e-10 / 1.6e-10	1.83e-08 / 1.83e-08	-3.04e-08 / -3.04e-08	1.64e-08 / 1.64e-08	3.79e-08 / 3.79e-08	-6.79e-09 / -6.79e-09	1.65e-08 / 1.65e-08	-3.88e-08 / -3.88e-08	0 / 0
Muon TTVA eff. stat	0 / 0	0.000162 / -0.000162	5.19e-06 / -5.16e-06	0.000162 / -0.000162	0.000147 / -0.000146	0.000132 / -0.000132	0.000195 / -0.000195	0.000108 / -0.000108	0.00014 / -0.00014	0 / 0
Muon TTVA eff. syst.	0 / 0	0.000146 / -0.000146	1.97e-05 / -1.96e-05	0.000121 / -0.000121	0.000188 / -0.000188	0.000147 / -0.000147	0.000224 / -0.000224	4.13e-05 / -4.13e-05	0.000169 / -0.000169	0 / 0
Muon trigger eff. stat	0 / 0	0.00158 / -0.00158	6.24e-05 / -6.24e-05	0.0024 / -0.0024	0.00156 / -0.00156	0.00147 / -0.00147	0.0024 / -0.0024	0.00103 / -0.00103	0.00149 / -0.00149	0 / 0
Muon trigger eff. syst.	0 / 0	0.0118 / -0.0118	0.00132 / -0.00132	0.0169 / -0.0169	0.0102 / -0.0102	0.00959 / -0.00959	0.0192 / -0.0192	0.00377 / -0.00377	0.0105 / -0.0105	0 / 0
Jet JVT eff.	0 / 0	0.00151 / -0.00151	0.00168 / -0.00168	0.000333 / -0.000333	0.00118 / -0.00118	0.00193 / -0.00193	0.00418 / -0.00418	0.00522 / -0.00522	0.00161 / -0.00161	0 / 0
Flavour Tagging eff. B0	0 / 0	1.6e-10 / 1.6e-10	1.83e-08 / 1.83e-08	-3.04e-08 / -3.04e-08	1.64e-08 / 1.64e-08	3.79e-08 / 3.79e-08	-6.79e-09 / -6.79e-09	1.65e-08 / 1.65e-08	-3.88e-08 / -3.88e-08	0 / 0
Flavour Tagging eff. B1	0 / 0	1.6e-10 / 1.6e-10	1.83e-08 / 1.83e-08	-3.04e-08 / -3.04e-08	1.64e-08 / 1.64e-08	3.79e-08 / 3.79e-08	-6.79e-09 / -6.79e-09	1.65e-08 / 1.65e-08	-3.88e-08 / -3.88e-08	0 / 0
Flavour Tagging eff. B2	0 / 0	1.6e-10 / 1.6e-10	1.83e-08 / 1.83e-08	-3.04e-08 / -3.04e-08	1.64e-08 / 1.64e-08	3.79e-08 / 3.79e-08	-6.79e-09 / -6.79e-09	1.65e-08 / 1.65e-08	-3.88e-08 / -3.88e-08	0 / 0
Flavour Tagging eff. B3	0 / 0	1.6e-10 / 1.6e-10	1.83e-08 / 1.83e-08	-3.04e-08 / -3.04e-08	1.64e-08 / 1.64e-08	3.79e-08 / 3.79e-08	-6.79e-09 / -6.79e-09	1.65e-08 / 1.65e-08	-3.88e-08 / -3.88e-08	0 / 0
Flavour Tagging eff. B4	0 / 0	1.6e-10 / 1.6e-10	1.83e-08 / 1.83e-08	-3.04e-08 / -3.04e-08	1.64e-08 / 1.64e-08	3.79e-08 / 3.79e-08	-6.79e-09 / -6.79e-09	1.65e-08 / 1.65e-08	-3.88e-08 / -3.88e-08	0 / 0
Flavour Tagging eff. B5	0 / 0	1.6e-10 / 1.6e-10	1.83e-08 / 1.83e-08	-3.04e-08 / -3.04e-08	1.64e-08 / 1.64e-08	3.79e-08 / 3.79e-08	-6.79e-09 / -6.79e-09	1.65e-08 / 1.65e-08	-3.88e-08 / -3.88e-08	0 / 0
Flavour Tagging eff. B6	0 / 0	1.6e-10 / 1.6e-10	1.83e-08 / 1.83e-08	-3.04e-08 / -3.04e-08	1.64e-08 / 1.64e-08	3.79e-08 / 3.79e-08	-6.79e-09 / -6.79e-09	1.65e-08 / 1.65e-08	-3.88e-08 / -3.88e-08	0 / 0
Flavour Tagging eff. B7	0 / 0	1.6e-10 / 1.6e-10	1.83e-08 / 1.83e-08	-3.04e-08 / -3.04e-08	1.64e-08 / 1.64e-08	3.79e-08 / 3.79e-08	-6.79e-09 / -6.79e-09	1.65e-08 / 1.65e-08	-3.88e-08 / -3.88e-08	0 / 0
Flavour Tagging eff. B8	0 / 0	1.6e-10 / 1.6e-10	1.83e-08 / 1.83e-08	-3.04e-08 / -3.04e-08	1.64e-08 / 1.64e-08	3.79e-08 / 3.79e-08	-6.79e-09 / -6.79e-09	1.65e-08 / 1.65e-08	-3.88e-08 / -3.88e-08	0 / 0
Flavour Tagging eff. C0	0 / 0	1.6e-10 / 1.6e-10	1.83e-08 / 1.83e-08	-3.04e-08 / -3.04e-08	1.64e-08 / 1.64e-08	3.79e-08 / 3.79e-08	-6.79e-09 / -6.79e-09	1.65e-08 / 1.65e-08	-3.88e-08 / -3.88e-08	0 / 0
Flavour Tagging eff. C1	0 / 0	1.6e-10 / 1.6e-10	1.83e-08 / 1.83e-08	-3.04e-08 / -3.04e-08	1.64e-08 / 1.64e-08	3.79e-08 / 3.79e-08	-6.79e-09 / -6.79e-09	1.65e-08 / 1.65e-08	-3.88e-08 / -3.88e-08	0 / 0
Flavour Tagging eff. C2	0 / 0	1.6e-10 / 1.6e-10	1.83e-08 / 1.83e-08	-3.04e-08 / -3.04e-08	1.64e-08 / 1.64e-08	3.79e-08 / 3.79e-08	-6.79e-09 / -6.79e-09	1.65e-08 / 1.65e-08	-3.88e-08 / -3.88e-08	0 / 0
Flavour Tagging eff. C3	0 / 0	1.6e-10 / 1.6e-10	1.83e-08 / 1.83e-08	-3.04e-08 / -3.04e-08	1.64e-08 / 1.64e-08	3.79e-08 / 3.79e-08	-6.79e-09 / -6.79e-09	1.65e-08 / 1.65e-08	-3.88e-08 / -3.88e-08	0 / 0
Flavour Tagging eff. Light0	0 / 0	1.6e-10 / 1.6e-10	1.83e-08 / 1.83e-08	-3.04e-08 / -3.04e-08	1.64e-08 / 1.64e-08	3.79e-08 / 3.79e-08	-6.79e-09 / -6.79e-09	1.65e-08 / 1.65e-08	-3.88e-08 / -3.88e-08	0 / 0
Flavour Tagging eff. Light1	0 / 0	1.6e-10 / 1.6e-10	1.83e-08 / 1.83e-08	-3.04e-08 / -3.04e-08	1.64e-08 / 1.64e-08	3.79e-08 / 3.79e-08	-6.79e-09 / -6.79e-09	1.65e-08 / 1.65e-08	-3.88e-08 / -3.88e-08	0 / 0
Flavour Tagging eff. Light2	0 / 0	1.6e-10 / 1.6e-10	1.83e-08 / 1.83e-08	-3.04e-08 / -3.04e-08	1.64e-08 / 1.64e-08	3.79e-08 / 3.79e-08	-6.79e-09 / -6.79e-09	1.65e-08 / 1.65e-08	-3.88e-08 / -3.88e-08	0 / 0
Flavour Tagging eff. Light3	0 / 0	1.6e-10 / 1.6e-10	1.83e-08 / 1.83e-08	-3.04e-08 / -3.04e-08	1.64e-08 / 1.64e-08	3.79e-08 / 3.79e-08	-6.79e-09 / -6.79e-09	1.65e-08 / 1.65e-08	-3.88e-08 / -3.88e-08	0 / 0
Flavour Tagging eff. extrapolation	0 / 0	1.6e-10 / 1.6e-10	1.83e-08 / 1.83e-08	-3.04e-08 / -3.04e-08	1.64e-08 / 1.64e-08	3.79e-08 / 3.79e-08	-6.79e-09 / -6.79e-09	1.65e-08 / 1.65e-08	-3.88e-08 / -3.88e-08	0 / 0
Flavour Tagging eff. extrapolation from charm	0 / 0	1.6e-10 / 1.6e-10	1.83e-08 / 1.83e-08	-3.04e-08 / -3.04e-08	1.64e-08 / 1.64e-08	3.79e-08 / 3.79e-08	-6.79e-09 / -6.79e-09	1.65e-08 / 1.65e-08	-3.88e-08 / -3.88e-08	0 / 0
EG_RESOLUTION_AF2	0 / 0	1.6e-10 / 1.6e-10	1.83e-08 / 1.83e-08	-3.04e-08 / -3.04e-08	1.64e-08 / 1.64e-08	3.79e-08 / 3.79e-08	-6.79e-09 / -6.79e-09	1.65e-08 / 1.65e-08	-3.88e-08 / -3.88e-08	0 / 0
EG_RESOLUTION_MATERIALCALO	0 / 0	-3.24e-07 / 3.24e-07	1.83e-08 / 1.83e-08	0.000376 / -0.000376	-0.000217 / 0.000217	-2.48e-05 / 2.49e-05	0.00158 / -0.00158	1.65e-08 / 1.65e-08	-0.000352 / 0.000352	0 / 0
EG_RESOLUTION_MATERIALCRYO	0 / 0	-0.000286 / 0.000286	1.83e-08 / 1.83e-08	-0.0271 / 0.0271	-0.000729 / 0.000729	8.86e-05 / -8.85e-05	0.00158 / -0.00158	1.65e-08 / 1.65e-08	-0.000452 / 0.000452	0 / 0
EG_RESOLUTION_MATERIALGAP	0 / 0	-0.000215 / 0.000215	1.83e-08 / 1.83e-08	-0.0276 / 0.0276	-0.00112 / 0.00112	-0.000718 / 0.00718	-6.79e-09 / -6.79e-09	1.65e-08 / 1.65e-08	0.000136 / -0.000136	0 / 0
EG_RESOLUTION_MATERIALIBL	0 / 0	0.00666 / -0.00666	1.83e-08 / 1.83e-08	0.000588 / -0.000588	0.000804 / -0.000804	0.00227 / -0.00227	0.0029 / -0.0029	0.00114 / -0.00114	-7.1e-05 / 7.1e-05	0 / 0
EG_RESOLUTION_MATERIALID	0 / 0	0.000504 / -0.000504	1.83e-08 / 1.83e-08	-0.00362 / 0.00362	-0.000872 / 0.000872	0.00378 / -0.00378	0.00167 / -0.00167	0.00114 / -0.00114	-0.000303 / 0.000303	0 / 0
EG_RESOLUTION_MATERIALPP0	0 / 0	-0.00293 / 0.00293	-2.97e-05 / 2.97e-05	-0.0278 / 0.0278	-0.000306 / 0.000306	0.00634 / -0.00634	-2.55e-06 / 2.54e-06	1.65e-08 / 1.65e-08	0.000936 / -0.000936	0 / 0
EG_SCALE_AF2	0 / 0	1.6e-10 / 1.6e-10	1.83e-08 / 1.83e-08	-3.04e-08 / -3.04e-08	1.64e-08 / 1.64e-08	3.79e-08 / 3.79e-08	-6.79e-09 / -6.79e-09	1.65e-08 / 1.65e-08	-3.88e-08 / -3.88e-08	0 / 0
EG_SCALE_E4SCINTILLATOR__ETABIN0	0 / 0	1.6e-10 / 1.6e-10	1.83e-08 / 1.83e-08	-3.04e-08 / -3.04e-08	1.64e-08 / 1.64e-08	3.79e-08 / 3.79e-08	-6.79e-09 / -6.79e-09	1.65e-08 / 1.65e-08	-3.88e-08 / -3.88e-08	0 / 0
EG_SCALE_E4SCINTILLATOR__ETABIN1	0 / 0	1.6e-10 / 1.6e-10	1.83e-08 / 1.83e-08	-3.04e-08 / -3.04e-08	9.51e-05 / -9.51e-05	3.79e-08 / 3.79e-08	-6.79e-09 / -6.79e-09	1.65e-08 / 1.65e-08	-0.000739 / 0.000739	0 / 0
EG_SCALE_E4SCINTILLATOR__ETABIN2	0 / 0	-0.000215 / 0.000215	6.44e-05 / -6.44e-05	-0.0277 / 0.0277	-3.75e-05 / 3.75e-05	-1.02e-06 / 1e-06	6.79e-09 / -6.79e-09	1.65e-08 / 1.65e-08	-3.88e-08 / 6.05e-08	0 / 0
EG_SCALE_G4	0 / 0	8.91e-06 / -8.91e-06	1.83e-08 / 1.83e-08	5.93e-06 / -5.88e-06	0.00023 / -0.00023	-0.000123 / 0.000123	-2.99e-06 / 2.98e-06	1.65e-08 / 1.65e-08	0.000324 / -0.000324	0 / 0
EG_SCALE_L1GAIN	0 / 0	0.000612 / -0.000612	-0.0174 / 0.0174	6.1e-05 / -6.09e-05	0.00127 / -0.00127	0.00325 / -0.00325	2.54e-06 / -2.55e-06	1.65e-08 / 1.65e-08	0.000503 / -0.000502	0 / 0
EG_SCALE_L2GAIN	0 / 0	0.00049 / -0.00049	0.000339 / -0.000339	0.0276 / -0.0276	0.000596 / -0.000596	-0.00203 / 0.00203	0.00648 / -0.00648	9.57e-06 / -9.61e-06	0.00109 / -0.00109	0 / 0
EG_SCALE_LARCALIB_ETABIN0	0 / 0	-0.000282 / 0.000282	1.83e-08 / 1.83e-08	-1.35e-05 / 1.35e-05	-0.000307 / 0.000306	-3.66e-05 / 3.66e-05	2.98e-06 / -2.99e-06	-9.61e-06 / 9.57e-06	-0.00176 / 0.00176	0 / 0
EG_SCALE_LARCALIB_ETABIN1	0 / 0	-0.000406 / 0.000406	1.83e-08 / 1.83e-08	-0.0277 / 0.0277	-0.00056 / 0.00056	0.00191 / -0.00191	-2.55e-06 / 2.54e-06	1.65e-08 / 1.65e-08	-0.000205 / 0.000205	0 / 0
EG_SCALE_LARELECCALIB	0 / 0	0.000221 / -0.000221	1.83e-08 / 1.83e-08	5.11e-06 / -5.17e-06	0.000214 / -0.000214	-0.000854 / 0.000854	-6.79e-09 / -6.79e-09	1.65e-08 / 1.65e-08	0.000115 / -0.000115	0 / 0
EG_SCALE_LARELECUNCONV__ETABIN0	0 / 0	-0.000259 / 0.000259	-0.000176 / 0.000176	0.0237 / -0.0237	-0.000122 / 0.000121	0.000585 / -0.000585	0.000842 / -0.000842	0.00113 / -0.00113	-0.00128 / 0.00128	0 / 0
EG_SCALE_LARELECUNCONV__ETABIN1	0 / 0	-0.000226 / 0.000226	6.44e-05 / -6.44e-05	-0.0277 / 0.0277	-0.000591 / 0.000591	-0.00253 / 0.00253	-1.35e-05 / 1.35e-05	1.65e-08 / 1.65e-08	-0.000317 / 0.000317	0 / 0
EG_SCALE_LARUNCONVCALIB__ETABIN0	0 / 0	9.72e-06 / -9.72e-06	1.83e-08 / 1.83e-08	7.88e-07 / -7.32e-07	-0.000609 / 0.000609	0.000589 / -0.000589	-2.99e-06 / 2.98e-06	-0.00113 / 0.00113	0.0013 / -0.0013	0 / 0
EG_SCALE_LARUNCONVCALIB__ETABIN1	0 / 0	1.6e-10 / 1.6e-10	1.83e-08 / 1.83e-08	-3.04e-08 / -3.04e-08	-2.11e-05 / 2.1e-05	0.00108 / -0.00108	-6.79e-09 / -6.79e-09	1.65e-08 / 1.65e-08	0.000254 / -0.000254	0 / 0
EG_SCALE_MATCALO__ETABIN0	0 / 0	1.6e-10 / 1.6e-10	1.83e-08 / 1.83e-08	-3.04e-08 / -3.04e-08	-0.000184 / 0.000184	3.79e-08 / 3.79e-08	-6.79e-09 / -6.79e-09	1.65e-08 / 1.65e-08	8.2e-06 / -8.18e-06	0 / 0
EG_SCALE_MATCALO__ETABIN1	0 / 0	1.6e-10 / 1.6e-10	1.83e-08 / 1.83e-08	5.54e-07 / -4.98e-07	0.000208 / -0.000208	3.79e-08 / 3.79e-08	-6.79e-09 / -6.79e-09	1.65e-08 / 1.65e-08	0.000197 / -0.000197	0 / 0
EG_SCALE_MATCALO__ETABIN10	0 / 0	1.6e-10 / 1.6e-10	1.83e-08 / 1.83e-08	-3.04e-08 / -3.04e-08	1.64e-08 / 1.64e-08	3.79e-08 / 3.79e-08	-6.79e-09 / -6.79e-09	1.65e-08 / 1.65e-08	-3.88e-08 / -3.88e-08	0 / 0
EG_SCALE_MATCALO__ETABIN11	0 / 0	1.6e-10 / 1.6e-10	1.83e-08 / 1.83e-08	-3.04e-08 / -3.04e-08	1.64e-08 / 1.64e-08	3.79e-08 / 3.79e-08	-6.79e-09 / -6.79e-09	1.65e-08 / 1.65e-08	-3.88e-08 / -3.88e-08	0 / 0
EG_SCALE_MATCALO__ETABIN2	0 / 0	1.6e-10 / 1.6e-10	1.83e-08 / 1.83e-08	-3.04e-08 / -3.04e-08	9.23e-05 / -9.23e-05	3.79e-08 / 3.79e-08	-6.79e-09 / -6.79e-09	1.65e-08 / 1.65e-08	2.84e-06 / -2.82e-06	0 / 0
EG_SCALE_MATCALO__ETABIN3	0 / 0	3.24e-07 / -3.24e-07	1.83e-08 / 1.83e-08	3.59e-06 / -3.65e-06	-6.31e-05 / 6.32e-05	3.79e-08 / 3.79e-08	-6.79e-09 / -6.79e-09	1.65e-08 / 1.65e-08	0.000134 / -0.000134	0 / 0
EG_SCALE_MATCALO__ETABIN4	0 / 0	1.19e-05 / -1.19e-05	1.83e-08 / 1.83e-08	-3.04e-08 / -3.04e-08	-0.000203 / 0.000203	3.79e-08 / 3.79e-08	-6.79e-09 / -6.79e-09	1.65e-08 / 1.65e-08	2.94e-06 / -2.92e-06	0 / 0
EG_SCALE_MATCALO__ETABIN5	0 / 0	-4.54e-06 / 4.54e-06	1.83e-08 / 1.83e-08	2.03e-07 / -1.47e-07	-9.41e-05 / 9.42e-05	0.000589 / -0.000589	-6.79e-09 / -6.79e-09	-0.00114 / 0.00114	0.000615 / -0.000615	0 / 0
EG_SCALE_MATCALO__ETABIN6	0 / 0	2.03e-06 / -2.03e-06	1.83e-08 / 1.83e-08	-3.04e-08 / -3.04e-08	-0.000375 / 0.000375	-2.51e-07 / 2.3e-07	-2.99e-06 / 2.98e-06	9.57e-06 / -9.61e-06	0.000339 / -0.000339	0 / 0
EG_SCALE_MATCALO__ETABIN7	0 / 0	1.6e-10 / 1.6e-10	1.83e-08 / 1.83e-08	-3.04e-08 / -3.04e-08	0.000194 / -0.000194	3.79e-08 / 3.79e-08	-6.79e-09 / -6.79e-09	1.65e-08 / 1.65e-08	1.6e-07 / -2.37e-07	0 / 0
EG_SCALE_MATCALO__ETABIN8	0 / 0	1.6e-10 / 1.6e-10	1.83e-08 / 1.83e-08	-3.04e-08 / -3.04e-08	-9.36e-06 / 9.39e-06	0.00108 / -0.00108	-6.79e-09 / -6.79e-09	1.65e-08 / 1.65e-08	0.000251 / -0.000251	0 / 0
EG_SCALE_MATCALO__ETABIN9	0 / 0	1.6e-10 / 1.6e-10	1.83e-08 / 1.83e-08	-3.04e-08 / -3.04e-08	1.64e-08 / 1.64e-08	3.79e-08 / 3.79e-08	-6.79e-09 / -6.79e-09	1.65e-08 / 1.65e-08	-3.88e-08 / -3.88e-08	0 / 0
EG_SCALE_MATCRYO__ETABIN0	0 / 0	1.6e-10 / 1.6e-10	1.83e-08 / 1.83e-08	-3.04e-08 / -3.04e-08	-0.000185 / 0.000185	3.79e-08 / 3.79e-08	-6.79e-09 / -6.79e-09	1.65e-08 / 1.65e-08	8.2e-06 / -8.18e-06	0 / 0
EG_SCALE_MATCRYO__ETABIN1	0 / 0	1.6e-10 / 1.6e-10	1.83e-08 / 1.83e-08	0.000377 / -0.000377	0.00021 / -0.00021	3.79e-08 / 3.79e-08	0.00158 / -0.00158	1.65e-08 / 1.65e-08	0.000197 / -0.000197	0 / 0
EG_SCALE_MATCRYO__ETABIN10	0 / 0	0.000214 / -0.000214	1.83e-08 / 1.83e-08	1.1e-06 / -5.17e-06	0.000211 / -0.000211	-0.000854 / 0.000854	-6.79e-09 / -6.79e-09	6.56e-07 / -7.33e-07	0 / 0	0 / 0
EG_SCALE_MATCRYO__ETABIN11	0 / 0	4.94e-06 / -4.94e-06	1.83e-08 / 1.83e-08	2.03e-07 / -2.64e-07	2.9e-06 / -2.86e-06	3.79e-08 / 3.79e-08	-6.79e-09 / -6.79e-09	1.65e-08 / 1.65e-08	-3.88e-08 / -3.88e-08	0 / 0
EG_SCALE_MATCRYO__ETABIN2	0 / 0	1.6e-10 / 1.6e-10	1.83e-08 / 1.83e-08	-3.04e-08 / -3.04e-08	0.000194 / -0.000194	3.79e-08 / 3.79e-08	-6.79e-09 / -6.79e-09	1.65e-08 / 1.65e-08	2.84e-06 / -2.82e-06	0 / 0
EG_SCALE_MATCRYO__ETABIN3	0 / 0	0.00645 / -0.00645	1.83e-08 / 1.83e-08	3.59e-06 / -3.65e-06	-0.000223 / 0.000223	8.7e-06 / -8.72e-06	-6.79e-09 / -6.79e-09	1.65e-08 / 1.65e-08	0.000141 / -0.000141	0 / 0
EG_SCALE_MATCRYO__ETABIN4	0 / 0	1.19e-05 / -1.19e-05	1.83e-08 / 1.83e-08	-0.000208 / 0.000208	-0.000201 / 0.000201	3.79e-08 / 3.79e-08	-6.79e-09 / -6.79e-09	1.65e-08 / 1.65e-08	3.64e-05 / -3.65e-05	0 / 0
EG_SCALE_MATCRYO__ETABIN5	0 / 0	-4.54e-06 / 4.54e-06	1.83e-08 / 1.83e-08	2.03e-07 / -1.47e-07	-8.01e-05 / 8.01e-05	0.000587 / -0.000587	-6.79e-09 / -6.79e-09	-0.00114 / 0.00114	0.000614 / -0.000614	0 / 0
EG_SCALE_MATCRYO__ETABIN6	0 / 0	2.03e-06 / -2.03e-06	1.83e-08 / 1.83e-08	-3.04e-08 / -3.04e-08	-0.000375 / 0.000375	-6.36e-07 / 6.15e-07	-2.99e-06 / 2.98e-06	9.57e-06 / -9.61e-06	0.000339 / -0.000339	0 / 0
EG_SCALE_MATCRYO__ETABIN7	0 / 0	0.000134 / -0.000134	-6.44e-05 / 6.44e-05	-3.04e-08 / -3.04e-08	0.000335 / -0.000335	1.14e-05 / -1.13e-05	-6.79e-09 / -6.79e-09	1.65e-08 / 1.65e-08	0.000311 / -0.000311	0 / 0
EG_SCALE_MATCRYO__ETABIN8	0 / 0	2.94e-05 / -2.94e-05	1.83e-08 / 1.83e-08	-3.04e-08 / -3.04e-08	0.000183 / -0.000183	0.00279 / -0.00279	-6.79e-09 / -6.79e-09	1.65e-08 / 1.65e-08	0.000235 / -0.000235	0 / 0
EG_SCALE_MATCRYO__ETABIN9	0 / 0	7.05e-06 / -7.05e-06	1.83e-08 / 1.83e-08	-3.04e-08 / -3.04e-08	-4.52e-07 / 4.85e-07	3.79e-08 / 3.79e-08	-6.79e-09 / -6.79e-09	1.65e-08 / 1.65e-08	0.000115 / -0.000115	0 / 0
EG_SCALE_MATID__ETABIN0	0 / 0	6.97e-06 / -6.97e-06	1.83e-08 / 1.83e-08	7.88e-07 / -7.32e-07	0.000331 / -0.000331	0.000898 / -0.000898	6.79e-09 / -6.79e-09	-0.00114 / 0.00114	0.000628 / -0.000628	0 / 0
EG_SCALE_MATID__ETABIN1	0 / 0	2.35e-06 / -2.35e-06	1.83e-08 / 1.83e-08	-3.04e-08 / -3.04e-08	0.000462 / -0.000462	0.000341 / -0.000341	2.98e-06 / -2.99e-06	1.65e-08 / 1.65e-08	0.000346 / -0.000345	0 / 0
EG_SCALE_MATID__ETABIN2	0 / 0	7.29e-06 / -7.29e-06	1.83e-08 / 1.83e-08	0.0277 / -0.0277	0.0002 / -0.0002	0.00251 / -0.00251	-6.79e-09 / -6.79e-09	1.65e-08 / 1.65e-08	0.000611 / -0.000612	0 / 0
EG_SCALE_MATID__ETABIN3	0 / 0	1.6e-10 / 1.6e-10	1.83e-08 / 1.83e-08	-1.43e-05 / 1.42e-05	0.00023 / -0.00023	0.000854 / -0.000854	-6.79e-09 / -6.79e-09	1.65e-08 / 1.65e-08	-3.88e-08 / -3.88e-08	0 / 0
EG_SCALE_MATPP0__ETABIN0	0 / 0	1.39e-05 / -1.39e-05	1.83e-08 / 1.83e-08	7.88e-07 / -7.32e-07	-0.00017 / 0.00017	3.79e-08 / 3.79e-08	2.98e-06 / -2.99e-06	1.65e-08 / 1.65e-08	4.13e-06 / -4.11e-06	0 / 0
EG_SCALE_MATPP0__ETABIN1	0 / 0	0.000227 / -0.000227	1.83e-08 / 1.83e-08	0.0277 / -0.0277	0.000343 / -0.000343	0.00105 / -0.00105	2.54e-06 / -2.55e-06	1.65e-08 / 1.65e-08	0.000121 / -0.000121	0 / 0
EG_SCALE_PEDESTAL	0 / 0	0.000222 / 0.000224	1.83e-08 / 1.83e-08	-7.32e-07 / 7.88e-07	0.000515 / -0.000515	0.00104 / -0.00104	-6.79e-09 / -6.79e-09	1.65e-08 / 1.65e-08	-7.69e-05 / 7.69e-05	0 / 0
EG_SCALE_PS_BARREL_B12	0 / 0	-0.000277 / 0.000277	1.83e-08 / 1.83e-08	-1.35e-05 / 1.35e-05	-0.000525 / 0.000525	0.000289 / -0.000289	5.64e-06 / -5.65e-06	0.00113 / -0.00113	-0.00112 / 0.00112	0 / 0
EG_SCALE_PS_ETABIN0	0 / 0	1.6e-10 / 1.6e-10	1.83e-08 / 1.83e-08	-3.04e-08 / -3.04e-08	-4.99e-05 / 4.98e-05	3.79e-08 / 3.79e-08	-6.79e-09 / -6.79e-09	1.65e-08 / 1.65e-08	-8.97e-06 / 8.99e-06	0 / 0
EG_SCALE_PS_ETABIN1	0 / 0	1.6e-10 / 1.6e-10	1.83e-08 / 1.83e-08	-4.98e-07 / 5.54e-07	-0.000208 / 0.000208	3.79e-08 / 3.79e-08	-6.79e-09 / -6.79e-09	1.65e-08 / 1.65e-08	-0.000197 / 0.000197	0 / 0
EG_SCALE_PS_ETABIN2	0 / 0	1.6e-10 / 1.6e-10	1.83e-08 / 1.83e-08	-3.04e-08 / -3.04e-08	-0.000196 / 0.000196	3.79e-08 / 3.79e-08	-6.79e-09 / -6.79e-09	1.65e-08 / 1.65e-08	-2.82e-06 / 2.84e-06	0 / 0
EG_SCALE_PS_ETABIN3	0 / 0	-2.43e-07 / 2.43e-07	1.83e-08 / 1.83e-08	-3.

	j-fake γ	$W\gamma\gamma$	$Z\gamma$	$Z\gamma\gamma$	$tX\gamma$	$t\bar{t}$	diboson	$W(\tau\nu)\gamma\gamma$	$WH_{\gamma\gamma}$	$WH\gamma\gamma$
j-fake photon SF error	0.216 / -0.218	0 / 0	0 / 0	0 / 0	0 / 0	0 / 0	0 / 0	0 / 0	0 / 0	0 / 0
$\mu_{W\gamma\gamma}$	0 / 0	0.158 / -0.157	0 / 0	0 / 0	0 / 0	0 / 0	0 / 0	0 / 0	0 / 0	0 / 0
Luminosity	0 / 0	0.0169 / -0.0169	0.0169 / -0.0169	0.0169 / -0.0169	0.0169 / -0.0169	0.0169 / -0.0169	0.0169 / -0.0169	0.0169 / -0.0169	0.0169 / -0.0169	0 / 0
Electron identification eff.	0 / 0	0.00512 / -0.00512	0.00777 / -0.00777	0 / 0	0 / 0	0 / 0	0 / 0	0 / 0	0 / 0	0 / 0
Electron isolation eff.	0 / 0	0.00072 / -0.00072	0.00132 / -0.00132	0 / 0	0 / 0	0 / 0	0 / 0	0 / 0	0 / 0	0 / 0
Electron reconstruction eff.	0 / 0	0.00094 / -0.00094	0.00182 / -0.00182	0 / 0	0 / 0	0 / 0	0 / 0	0 / 0	0 / 0	0 / 0
Electron Trigger eff.	0 / 0	1.6e-10 / 1.6e-10	1.83e-08 / 1.83e-08	0 / 0	0 / 0	0 / 0	0 / 0	0 / 0	0 / 0	0 / 0
Photon identification eff.	0 / 0	0.026 / -0.026	0.0271 / -0.0271	0.032 / -0.032	0.0238 / -0.0238	0.0271 / -0.0271	0.0271 / -0.0271	0.0376 / -0.0376	0.0165 / -0.0165	0 / 0
Photon isolation eff.	0 / 0	0.0291 / -0.0292	0.0354 / -0.0354	0.0266 / -0.0267	0.025 / -0.025	0.0274 / -0.0274	0.0304 / -0.0304	0.0335 / -0.0336	0.0196 / -0.0196	0 / 0
Photon Trigger eff.	0 / 0	0.00662 / -0.00662	0.000284 / -0.000284	0.00824 / -0.00824	0.00631 / -0.00631	0.00639 / -0.00639	0.0107 / -0.0107	0.00381 / -0.00381	0.00742 / -0.00742	0 / 0
Muon isolation eff. stat	0 / 0	0.00056 / -0.00056	8.97e-06 / -9.02e-06	0.000822 / -0.000822	0.000595 / -0.000595	0.000494 / -0.000494	0.000605 / -0.000605	0.000118 / -0.000118	0.000605 / -0.000605	0 / 0
Muon isolation eff. syst.	0 / 0	0.00304 / -0.00304	0.000105 / -0.000105	0.00563 / -0.00563	0.00315 / -0.00315	0.00325 / -0.00325	0.00411 / -0.00411	0.0141 / -0.0141	0.00283 / -0.00283	0 / 0
Muon reconstruction eff. stat	0 / 0	0.000235 / -0.000235	1.28e-05 / -1.27e-05	0.000285 / -0.000285	0.000228 / -0.000228	0.000229 / -0.000229	0.000331 / -0.000331	0.000144 / -0.000144	0.000229 / -0.000229	0 / 0
Muon reconstruction eff. low-pT stat.	0 / 0	1.6e-10 / 1.6e-10	1.83e-08 / 1.83e-08	-3.04e-08 / -3.04e-08	1.64e-08 / 1.64e-08	3.79e-08 / 3.79e-08	-6.79e-09 / -6.79e-09	1.65e-08 / 1.65e-08	-3.88e-08 / -3.88e-08	0 / 0
Muon reconstruction eff. syst.	0 / 0	0.00121 / -0.00121	8.47e-05 / -8.47e-05	0.00115 / -0.00115	0.000972 / -0.000972	0.00088 / -0.00088	0.00258 / -0.00258	0.00104 / -0.00104	0.00103 / -0.00103	0 / 0
Muon reconstruction eff. low-pT syst.	0 / 0	1.6e-10 / 1.6e-10	1.83e-08 / 1.83e-08	-3.04e-08 / -3.04e-08	1.64e-08 / 1.64e-08	3.79e-08 / 3.79e-08	-6.79e-09 / -6.79e-09	1.65e-08 / 1.65e-08	-3.88e-08 / -3.88e-08	0 / 0
Muon TTVA eff. stat	0 / 0	0.000162 / -0.000162	5.19e-06 / -5.16e-06	0.000162 / -0.000162	0.000147 / -0.000146	0.000132 / -0.000132	0.000195 / -0.000195	0.000108 / -0.000108	0.00014 / -0.00014	0 / 0
Muon TTVA eff. syst.	0 / 0	0.000146 / -0.000146	1.97e-05 / -1.96e-05	0.000121 / -0.000121	0.000188 / -0.000188	0.000147 / -0.000147	0.000224 / -0.000224	4.13e-05 / -4.13e-05	0.000169 / -0.000169	0 / 0
Muon trigger eff. stat	0 / 0	0.00157 / -0.00157	6.19e-05 / -6.2e-05	0.00239 / -0.00239	0.00155 / -0.00155	0.00146 / -0.00146	0.00239 / -0.00239	0.00102 / -0.00102	0.00148 / -0.00148	0 / 0
Muon trigger eff. syst.	0 / 0	0.0117 / -0.0117	0.00131 / -0.00131	0.0168 / -0.0168	0.0101 / -0.0101	0.00952 / -0.00952	0.019 / -0.019	0.00375 / -0.00375	0.0104 / -0.0104	0 / 0
Jet JVT eff.	0 / 0	0.0015 / -0.0015	0.00167 / -0.00167	0.00033 / -0.00033	0.00117 / -0.00117	0.00192 / -0.00192	0.00415 / -0.00415	0.00519 / -0.00519	0.0016 / -0.0016	0 / 0
Flavour Tagging eff. B0	0 / 0	1.6e-10 / 1.6e-10	1.83e-08 / 1.83e-08	-3.04e-08 / -3.04e-08	1.64e-08 / 1.64e-08	3.79e-08 / 3.79e-08	-6.79e-09 / -6.79e-09	1.65e-08 / 1.65e-08	-3.88e-08 / -3.88e-08	0 / 0
Flavour Tagging eff. B1	0 / 0	1.6e-10 / 1.6e-10	1.83e-08 / 1.83e-08	-3.04e-08 / -3.04e-08	1.64e-08 / 1.64e-08	3.79e-08 / 3.79e-08	-6.79e-09 / -6.79e-09	1.65e-08 / 1.65e-08	-3.88e-08 / -3.88e-08	0 / 0
Flavour Tagging eff. B2	0 / 0	1.6e-10 / 1.6e-10	1.83e-08 / 1.83e-08	-3.04e-08 / -3.04e-08	1.64e-08 / 1.64e-08	3.79e-08 / 3.79e-08	-6.79e-09 / -6.79e-09	1.65e-08 / 1.65e-08	-3.88e-08 / -3.88e-08	0 / 0
Flavour Tagging eff. B3	0 / 0	1.6e-10 / 1.6e-10	1.83e-08 / 1.83e-08	-3.04e-08 / -3.04e-08	1.64e-08 / 1.64e-08	3.79e-08 / 3.79e-08	-6.79e-09 / -6.79e-09	1.65e-08 / 1.65e-08	-3.88e-08 / -3.88e-08	0 / 0
Flavour Tagging eff. B4	0 / 0	1.6e-10 / 1.6e-10	1.83e-08 / 1.83e-08	-3.04e-08 / -3.04e-08	1.64e-08 / 1.64e-08	3.79e-08 / 3.79e-08	-6.79e-09 / -6.79e-09	1.65e-08 / 1.65e-08	-3.88e-08 / -3.88e-08	0 / 0
Flavour Tagging eff. B5	0 / 0	1.6e-10 / 1.6e-10	1.83e-08 / 1.83e-08	-3.04e-08 / -3.04e-08	1.64e-08 / 1.64e-08	3.79e-08 / 3.79e-08	-6.79e-09 / -6.79e-09	1.65e-08 / 1.65e-08	-3.88e-08 / -3.88e-08	0 / 0
Flavour Tagging eff. B6	0 / 0	1.6e-10 / 1.6e-10	1.83e-08 / 1.83e-08	-3.04e-08 / -3.04e-08	1.64e-08 / 1.64e-08	3.79e-08 / 3.79e-08	-6.79e-09 / -6.79e-09	1.65e-08 / 1.65e-08	-3.88e-08 / -3.88e-08	0 / 0
Flavour Tagging eff. B7	0 / 0	1.6e-10 / 1.6e-10	1.83e-08 / 1.83e-08	-3.04e-08 / -3.04e-08	1.64e-08 / 1.64e-08	3.79e-08 / 3.79e-08	-6.79e-09 / -6.79e-09	1.65e-08 / 1.65e-08	-3.88e-08 / -3.88e-08	0 / 0
Flavour Tagging eff. B8	0 / 0	1.6e-10 / 1.6e-10	1.83e-08 / 1.83e-08	-3.04e-08 / -3.04e-08	1.64e-08 / 1.64e-08	3.79e-08 / 3.79e-08	-6.79e-09 / -6.79e-09	1.65e-08 / 1.65e-08	-3.88e-08 / -3.88e-08	0 / 0
Flavour Tagging eff. C0	0 / 0	1.6e-10 / 1.6e-10	1.83e-08 / 1.83e-08	-3.04e-08 / -3.04e-08	1.64e-08 / 1.64e-08	3.79e-08 / 3.79e-08	-6.79e-09 / -6.79e-09	1.65e-08 / 1.65e-08	-3.88e-08 / -3.88e-08	0 / 0
Flavour Tagging eff. C1	0 / 0	1.6e-10 / 1.6e-10	1.83e-08 / 1.83e-08	-3.04e-08 / -3.04e-08	1.64e-08 / 1.64e-08	3.79e-08 / 3.79e-08	-6.79e-09 / -6.79e-09	1.65e-08 / 1.65e-08	-3.88e-08 / -3.88e-08	0 / 0
Flavour Tagging eff. C2	0 / 0	1.6e-10 / 1.6e-10	1.83e-08 / 1.83e-08	-3.04e-08 / -3.04e-08	1.64e-08 / 1.64e-08	3.79e-08 / 3.79e-08	-6.79e-09 / -6.79e-09	1.65e-08 / 1.65e-08	-3.88e-08 / -3.88e-08	0 / 0
Flavour Tagging eff. C3	0 / 0	1.6e-10 / 1.6e-10	1.83e-08 / 1.83e-08	-3.04e-08 / -3.04e-08	1.64e-08 / 1.64e-08	3.79e-08 / 3.79e-08	-6.79e-09 / -6.79e-09	1.65e-08 / 1.65e-08	-3.88e-08 / -3.88e-08	0 / 0
Flavour Tagging eff. Light0	0 / 0	1.6e-10 / 1.6e-10	1.83e-08 / 1.83e-08	-3.04e-08 / -3.04e-08	1.64e-08 / 1.64e-08	3.79e-08 / 3.79e-08	-6.79e-09 / -6.79e-09	1.65e-08 / 1.65e-08	-3.88e-08 / -3.88e-08	0 / 0
Flavour Tagging eff. Light1	0 / 0	1.6e-10 / 1.6e-10	1.83e-08 / 1.83e-08	-3.04e-08 / -3.04e-08	1.64e-08 / 1.64e-08	3.79e-08 / 3.79e-08	-6.79e-09 / -6.79e-09	1.65e-08 / 1.65e-08	-3.88e-08 / -3.88e-08	0 / 0
Flavour Tagging eff. Light2	0 / 0	1.6e-10 / 1.6e-10	1.83e-08 / 1.83e-08	-3.04e-08 / -3.04e-08	1.64e-08 / 1.64e-08	3.79e-08 / 3.79e-08	-6.79e-09 / -6.79e-09	1.65e-08 / 1.65e-08	-3.88e-08 / -3.88e-08	0 / 0
Flavour Tagging eff. Light3	0 / 0	1.6e-10 / 1.6e-10	1.83e-08 / 1.83e-08	-3.04e-08 / -3.04e-08	1.64e-08 / 1.64e-08	3.79e-08 / 3.79e-08	-6.79e-09 / -6.79e-09	1.65e-08 / 1.65e-08	-3.88e-08 / -3.88e-08	0 / 0
Flavour Tagging eff. extrapolation	0 / 0	1.6e-10 / 1.6e-10	1.83e-08 / 1.83e-08	-3.04e-08 / -3.04e-08	1.64e-08 / 1.64e-08	3.79e-08 / 3.79e-08	-6.79e-09 / -6.79e-09	1.65e-08 / 1.65e-08	-3.88e-08 / -3.88e-08	0 / 0
Flavour Tagging eff. extrapolation from charm	0 / 0	1.6e-10 / 1.6e-10	1.83e-08 / 1.83e-08	-3.04e-08 / -3.04e-08	1.64e-08 / 1.64e-08	3.79e-08 / 3.79e-08	-6.79e-09 / -6.79e-09	1.65e-08 / 1.65e-08	-3.88e-08 / -3.88e-08	0 / 0
EG_RESOLUTION_AF2	0 / 0	1.6e-10 / 1.6e-10	1.83e-08 / 1.83e-08	-3.04e-08 / -3.04e-08	1.64e-08 / 1.64e-08	3.79e-08 / 3.79e-08	-6.79e-09 / -6.79e-09	1.65e-08 / 1.65e-08	-3.88e-08 / -3.88e-08	0 / 0
EG_RESOLUTION_MATERIALCALO	0 / 0	-3.22e-07 / 3.22e-07	1.82e-08 / 1.82e-08	0.000373 / -0.000373	-0.000216 / 0.000216	-2.46e-05 / 2.47e-05	0.00157 / -0.00157	1.63e-08 / 1.64e-08	-0.00035 / 0.00035	0 / 0
EG_RESOLUTION_MATERIALCRYO	0 / 0	-0.000284 / 0.000284	1.82e-08 / 1.82e-08	-0.0269 / 0.0269	-0.000724 / 0.000724	8.8e-05 / -8.79e-05	0.00157 / -0.00157	1.64e-08 / 1.64e-08	-0.000449 / 0.000448	0 / 0
EG_RESOLUTION_MATERIALGAP	0 / 0	-0.000213 / 0.000213	1.81e-08 / 1.83e-08	-0.0274 / 0.0274	-0.00112 / 0.00112	-0.000713 / 0.000713	6.72e-09 / -6.77e-09	1.63e-08 / 1.64e-08	0.000135 / -0.000135	0 / 0
EG_RESOLUTION_MATERIALIBL	0 / 0	0.00662 / -0.00662	1.82e-08 / 1.82e-08	0.000583 / -0.000583	0.000799 / -0.000798	0.00225 / -0.00225	0.00288 / -0.00288	0.00113 / -0.00113	-7.05e-05 / 7.05e-05	0 / 0
EG_RESOLUTION_MATERIALID	0 / 0	0.0005 / -0.0005	1.79e-08 / 1.84e-08	-0.00359 / 0.00359	-0.000865 / 0.000865	0.00375 / -0.00375	0.00166 / -0.00166	0.00113 / -0.00113	-0.000301 / 0.000301	0 / 0
EG_RESOLUTION_MATERIALPP0	0 / 0	-0.00291 / 0.00291	-2.95e-05 / 2.95e-05	-0.0276 / 0.0276	-0.000304 / 0.000303	0.00629 / -0.00629	-2.53e-06 / 2.52e-06	1.65e-08 / 1.62e-08	0.00093 / -0.00093	0 / 0
EG_SCALE_AF2	0 / 0	1.6e-10 / 1.6e-10	1.83e-08 / 1.83e-08	-3.04e-08 / -3.04e-08	1.64e-08 / 1.64e-08	3.79e-08 / 3.79e-08	-6.79e-09 / -6.79e-09	1.65e-08 / 1.65e-08	-3.88e-08 / -3.88e-08	0 / 0
EG_SCALE_E4SCINTILLATOR_ETABIN0	0 / 0	1.6e-10 / 1.6e-10	1.83e-08 / 1.83e-08	-3.04e-08 / -3.04e-08	1.64e-08 / 1.64e-08	3.79e-08 / 3.79e-08	-6.79e-09 / -6.79e-09	1.65e-08 / 1.65e-08	-3.88e-08 / -3.88e-08	0 / 0
EG_SCALE_E4SCINTILLATOR_ETABIN1	0 / 0	1.6e-10 / 1.6e-10	1.83e-08 / 1.83e-08	-3.04e-08 / -3.04e-08	9.51e-05 / -9.51e-05	3.79e-08 / 3.79e-08	-6.79e-09 / -6.79e-09	1.65e-08 / 1.65e-08	-0.000739 / 0.000739	0 / 0
EG_SCALE_E4SCINTILLATOR_ETABIN2	0 / 0	-0.000213 / 0.000213	6.4e-05 / -6.4e-05	-0.0275 / 0.0275	-3.73e-05 / 3.73e-05	-1.01e-06 / 9.93e-07	-6.75e-09 / 6.74e-09	1.64e-08 / 1.64e-08	-3.85e-08 / 6.01e-08	0 / 0
EG_SCALE_G4	0 / 0	8.85e-06 / -8.85e-06	1.81e-08 / 1.82e-08	5.89e-06 / -5.84e-06	0.000229 / -0.000229	-0.000122 / 0.000122	-2.97e-06 / 2.96e-06	1.63e-08 / 1.64e-08	0.000322 / -0.000322	0 / 0
EG_SCALE_L1GAIN	0 / 0	0.000608 / -0.000608	-0.0172 / 0.0172	6.06e-05 / -6.05e-05	0.00126 / -0.00126	0.00323 / -0.00323	2.52e-06 / -2.53e-06	1.64e-08 / 1.64e-08	0.000499 / -0.000499	0 / 0
EG_SCALE_L2GAIN	0 / 0	0.000486 / -0.000486	0.000337 / -0.000337	0.0274 / -0.0274	0.000592 / -0.000592	-0.00202 / 0.00202	0.00643 / -0.00643	9.5e-06 / -9.54e-06	0.00108 / -0.00108	0 / 0
EG_SCALE_LARCALIB_ETABIN0	0 / 0	-0.000281 / 0.000281	1.8e-08 / 1.84e-08	-1.34e-05 / 1.34e-05	-0.000304 / 0.000304	-3.64e-05 / 3.63e-05	2.96e-06 / -2.97e-06	-9.55e-06 / 9.51e-06	-0.00175 / 0.00175	0 / 0
EG_SCALE_LARCALIB_ETABIN1	0 / 0	-0.000403 / 0.000403	1.82e-08 / 1.82e-08	-0.0275 / 0.0275	-0.000556 / 0.000556	0.00189 / -0.00189	-2.53e-06 / 2.52e-06	1.64e-08 / 1.64e-08	-0.000204 / 0.000204	0 / 0
EG_SCALE_LARELECCALIB	0 / 0	0.00022 / -0.00022	1.82e-08 / 1.82e-08	5.08e-06 / -5.14e-06	0.000213 / -0.000213	-0.000848 / 0.000848	-6.74e-09 / 6.75e-09	1.63e-08 / 1.64e-08	0.000114 / -0.000114	0 / 0
EG_SCALE_LARELECUNCONV__ETABIN0	0 / 0	-0.000258 / 0.000258	-0.000175 / 0.000175	0.0236 / -0.0236	-0.000121 / 0.000121	0.000581 / -0.000581	0.000836 / -0.000836	0.00112 / -0.00112	-0.00127 / 0.00127	0 / 0
EG_SCALE_LARELECUNCONV__ETABIN1	0 / 0	-0.000224 / 0.000224	6.4e-05 / -6.39e-05	-0.0275 / 0.0275	-0.000587 / 0.000587	-0.00251 / 0.00251	-1.34e-05 / 1.34e-05	1.63e-08 / 1.64e-08	-0.000314 / 0.000314	0 / 0
EG_SCALE_LARUNCONVCALIB__ETABIN0	0 / 0	9.66e-06 / -9.66e-06	1.81e-08 / 1.83e-08	7.82e-07 / -7.27e-07	-0.000605 / 0.000605	0.000585 / -0.000585	-2.97e-06 / 2.96e-06	-0.00112 / 0.00112	0.00129 / -0.00129	0 / 0
EG_SCALE_LARUNCONVCALIB__ETABIN1	0 / 0	1.58e-10 / 1.58e-10	1.82e-08 / 1.82e-08	-3.02e-08 / -3.02e-08	-2.09e-05 / 2.09e-05	0.00107 / -0.00107	-6.74e-09 / 6.75e-09	1.63e-08 / 1.64e-08	0.000252 / -0.000252	0 / 0
EG_SCALE_MATCALO_ETABIN0	0 / 0	1.6e-10 / 1.6e-10	1.83e-08 / 1.83e-08	-3.04e-08 / -3.04e-08	-0.000184 / 0.000184	3.79e-08 / 3.79e-08	-6.79e-09 / -6.79e-09	1.65e-08 / 1.65e-08	8.2e-06 / -8.18e-06	0 / 0
EG_SCALE_MATCALO_ETABIN1	0 / 0	1.6e-10 / 1.6e-10	1.83e-08 / 1.83e-08	5.54e-07 / -4.98e-07	0.000208 / -0.000208	3.79e-08 / 3.79e-08	-6.79e-09 / -6.79e-09	1.65e-08 / 1.65e-08	0.000197 / -0.000197	0 / 0
EG_SCALE_MATCALO_ETABIN10	0 / 0	1.6e-10 / 1.6e-10	1.83e-08 / 1.83e-08	-3.04e-08 / -3.04e-08	1.64e-08 / 1.64e-08	3.79e-08 / 3.79e-08	-6.79e-09 / -6.79e-09	1.65e-08 / 1.65e-08	-3.88e-08 / -3.88e-08	0 / 0
EG_SCALE_MATCALO_ETABIN11	0 / 0	1.6e-10 / 1.6e-10	1.83e-08 / 1.83e-08	-3.04e-08 / -3.04e-08	1.64e-08 / 1.64e-08	3.79e-08 / 3.79e-08	-6.79e-09 / -6.79e-09	1.65e-08 / 1.65e-08	-3.88e-08 / -3.88e-08	0 / 0
EG_SCALE_MATCALO_ETABIN2	0 / 0	1.6e-10 / 1.6e-10	1.83e-08 / 1.83e-08	-3.04e-08 / -3.04e-08	9.23e-05 / -9.23e-05	3.79e-08 / 3.79e-08	-6.79e-09 / -6.79e-09	1.65e-08 / 1.65e-08	2.84e-06 / -2.82e-06	0 / 0
EG_SCALE_MATCALO_ETABIN3	0 / 0	3.24e-07 / -3.24e-07	1.83e-08 / 1.83e-08	3.59e-06 / -3.65e-06	-6.31e-05 / 6.32e-05	3.79e-08 / 3.79e-08	-6.79e-09 / -6.79e-09	1.65e-08 / 1.65e-08	0.000134 / -0.000134	0 / 0
EG_SCALE_MATCALO_ETABIN4	0 / 0	1.19e-05 / -1.19e-05	1.83e-08 / 1.83e-08	-3.04e-08 / -3.04e-08	-0.000203 / 0.000203	3.79e-08 / 3.79e-08	-6.79e-09 / -6.79e-09	1.65e-08 / 1.65e-08	2.94e-06 / -2.92e-06	0 / 0
EG_SCALE_MATCALO_ETABIN5	0 / 0	-4.51e-06 / 4.51e-06	1.82e-08 / 1.82e-08	2.02e-07 / -1.46e-07	-9.35e-05 / 9.35e-05	0.000585 / -0.000585	-6.74e-09 / -6.75e-09	-0.00113 / 0.00113	0.000611 / -0.000611	0 / 0
EG_SCALE_MATCALO_ETABIN6	0 / 0	2.01e-06 / -2.01e-06	1.82e-08 / 1.82e-08	-3.02e-08 / -3.02e-08	-0.000372 / 0.000372	-2.49e-07 / 2.29e-07	-2.97e-06 / 2.96e-06	9.51e-06 / -9.55e-06	0.000337 / -0.000337	0 / 0
EG_SCALE_MATCALO_ETABIN7	0 / 0	1.6e-10 / 1.6e-10	1.83e-08 / 1.83e-08	-3.04e-08 / -3.04e-08	0.000194 / -0.000194	3.79e-08 / 3.79e-08	-6.79e-09 / -6.79e-09	1.65e-08 / 1.65e-08	1.6e-07 / -2.37e-07	0 / 0
EG_SCALE_MATCALO_ETABIN8	0 / 0	1.59e-10 / 1.59e-10	1.82e-08 / 1.82e-08	-3.02e-08 / -3.02e-08	-9.3e-06 / 9.33e-06	0.00107 / -0.00107	-6.74e-09 / -6.75e-09	1.64e-08 / 1.64e-08	0.000249 / -0.000249	0 / 0
EG_SCALE_MATCALO_ETABIN9	0 / 0	1.6e-10 / 1.6e-10	1.83e-08 / 1.83e-08	-3.04e-08 / -3.04e-08	1.64e-08 / 1.64e-08	3.79e-08 / 3.79e-08	-6.79e-09 / -6.79e-09	1.65e-08 / 1.65e-08	-3.88e-08 / -3.88e-08	0 / 0
EG_SCALE_MATCRYO_ETABIN0	0 / 0	1.6e-10 / 1.6e-10	1.83e-08 / 1.83e-08	-3.04e-08 / -3.04e-08	-0.000185 / 0.000185	3.79e-08 / 3.79e-08	-6.79e-09 / -6.79e-09	1.65e-08 / 1.65e-08	8.2e-06 / -8.18e-06	0 / 0
EG_SCALE_MATCRYO_ETABIN1	0 / 0	1.59e-10 / 1.59e-10	1.82e-08 / 1.82e-08	0.000374 / -0.000375	0.000209 / -0.000209	3.77e-08 / 3.77e-08	0.00157 / -0.00157	1.64e-08 / 1.64e-08	0.000196 / -0.000196	0 / 0
EG_SCALE_MATCRYO_ETABIN10	0 / 0	0.000213 / -0.000213	1.82e-08 / 1.82e-08	5.88e-06 / -5.14e-06	0.00021 / -0.00021	-0.000848 / 0.000848	-6.74e-09 / 6.75e-09	1.63e-08 / 1.64e-08	6.52e-07 / -7.29e-07	0 / 0
EG_SCALE_MATCRYO_ETABIN11	0 / 0	4.94e-06 / -4.94e-06	1.83e-08 / 1.83e-08	2.03e-07 / -2.64e-07	2.9e-06 / -2.86e-06	3.79e-08 / 3.79e-08	-6.79e-09 / -6.79e-09	1.65e-08 / 1.65e-08	-3.88e-08 / -3.88e-08	0 / 0
EG_SCALE_MATCRYO_ETABIN2	0 / 0	1.6e-10 / 1.6e-10	1.83e-08 / 1.83e-08	-3.04e-08 / -3.04e-08	0.000194 / -0.000194	3.79e-08 / 3.79e-08	-6.79e-09 / -6.79e-09	1.65e-08 / 1.65e-08	2.84e-06 / -2.82e-06	0 / 0
EG_SCALE_MATCRYO_ETABIN3	0 / 0	0.00641 / -0.00641	1.82e-08 / 1.82e-08	3.57e-06 / -3.63e-06	-0.000222 / 0.000222	8.64e-06 / -8.66e-06	-6.75e-09 / 6.74e-09	1.64e-08 / 1.63e-08	0.000141 / -0.000141	0 / 0
EG_SCALE_MATCRYO_ETABIN4	0 / 0	1.19e-05 / -1.19e-05	1.83e-08 / 1.83e-08	-0.000208 / 0.000208	-0.000201 / 0.000201	3.79e-08 / 3.79e-08	-6.79e-09 / -6.79e-09	1.65e-08 / 1.65e-08	3.64e-05 / -3.65e-05	0 / 0
EG_SCALE_MATCRYO_ETABIN5	0 / 0	-4.51e-06 / 4.51e-06	1.82e-08 / 1.82e-08	2.02e-07 / -1.46e-07	-7.96e-05 / 7.96e-05	0.000583 / -0.000583	-6.74e-09 / 6.75e-09	-0.00113 / 0.00113	0.00061 / -0.00061	0 / 0
EG_SCALE_MATCRYO_ETABIN6	0 / 0	2.01e-06 / -2.01e-06	1.82e-08 / 1.82e-08	-3.02e-08 / -3.02e-08	-0.000373 / 0.000373	-6.31e-07 / 6.11e-07	-2.97e-06 / 2.96e-06	9.51e-06 / -9.55e-06	0.000337 / -0.000337	0 / 0
EG_SCALE_MATCRYO_ETABIN7	0 / 0	0.000133 / -0.000133	-6.39e-05 / 6.4e-05	-3.02e-08 / -3.03e-08	0.000333 / -0.000333	1.13e-05 / -1.12e-05	-6.74e-09 / -6.75e-09	1.64e-08 / 1.64e-08	0.000309 / -0.000309	0 / 0
EG_SCALE_MATCRYO_ETABIN8	0 / 0	2.92e-05 / -2.92e-05	1.82e-08 / 1.82e-08	-3.02e-08 / -3.03e-08	0.000181 / -0.000181	0.00277 / -0.00277	-6.74e-09 / 6.75e-09	1.63e-08 / 1.64e-08	0.000233 / -0.000233	0 / 0
EG_SCALE_MATCRYO_ETABIN9	0 / 0	7.05e-06 / -7.05e-06	1.83e-08 / 1.83e-08	-3.04e-08 / -3.04e-08	-4.52e-07 / 4.85e-07	3.79e-08 / 3.79e-08	-6.79e-09 / -6.79e-09	1.65e-08 / 1.65e-08	0.000115 / -0.000115	0 / 0
EG_SCALE_MATID__ETABIN0	0 / 0	6.92e-06 / -6.92e-06	1.82e-08 / 1.82e-08	7.83e-07 / -7.27e-07	0.000329 / -0.000329	0.000892 / -0.000893	-6.74e-09 / 6.75e-09	-0.00113 / 0.00113	0.000624 / -0.000624	0 / 0
EG_SCALE_MATID__ETABIN1	0 / 0	2.33e-06 / -2.33e-06	1.82e-08 / 1.82e-08	-3.02e-08 / -3.02e-08	0.000459 / -0.000459	0.000339 / -0.000339	2.96e-06 / -2.97e-06	1.64e-08 / 1.64e-08	0.000343 / -0.000343	0 / 0
EG_SCALE_MATID__ETABIN2	0 / 0	7.24e-06 / -7.24e-06	1.82e-08 / 1.82e-08	0.0275 / -0.0275	0.000198 / -0.000198	0.00249 / -0.00249	-6.74e-09 / 6.75e-09	1.64e-08 / 1.64e-08	0.000607 / -0.000607	0 / 0
EG_SCALE_MATID__ETABIN3	0 / 0	1.59e-10 / 1.58e-10	1.82e-08 / 1.82e-08	-1.42e-05 / 1.41e-05	0.000229 / -0.000229	0.000848 / -0.000848	-6.75e-09 / 6.74e-09	1.64e-08 / 1.63e-08	-3.86e-08 / -3.85e-08	0 / 0
EG_SCALE_MATPP0__ETABIN0	0 / 0	1.38e-05 / -1.38e-05	1.82e-08 / 1.82e-08	7.83e-07 / -7.27e-07	-0.000169 / 0.000169	3.77e-08 / 3.77e-08	2.96e-06 / -2.97e-06	1.64e-08 / 1.64e-08	4.1e-06 / -4.08e-06	0 / 0
EG_SCALE_MATPP0__ETABIN1	0 / 0	0.000226 / -0.000226	1.82e-08 / 1.82e-08	0.0275 / -0.0275	0.000341 / -0.000341	0.00104 / -0.00104	2.52e-06 / -2.53e-06	1.63e-08 / 1.64e-08	0.00012 / -0.00012	0 / 0
EG_SCALE_PEDESTAL	0 / 0	-0.000222 / 0.000222	1.81e-08 / 1.83e-08	7.27e-07 / 7.83e-07	0.000512 / -0.000512	0.00104 / -0.00104	-6.79e-09 / 6.77e-09	1.63e-08 / 1.64e-08	-7.64e-05 / 7.64e-05	0 / 0
EG_SCALE_PS_BARREL_B12	0 / 0	-0.000275 / 0.000275	1.81e-08 / 1.83e-08	-1.34e-05 / 1.34e-05	-0.000521 / 0.000521	0.000287 / -0.000287	5.6e-06 / -5.61e-06	0.00112 / -0.00112	-0.00111 / 0.00111	0 / 0
EG_SCALE_PS__ETABIN0	0 / 0	1.6e-10 / 1.6e-10	1.83e-08 / 1.83e-08	-3.04e-08 / -3.04e-08	-4.99e-05 / 4.98e-05	3.79e-08 / 3.79e-08	-6.79e-09 / -6.79e-09	1.65e-08 / 1.65e-08	-8.97e-06 / 8.99e-06	0 / 0
EG_SCALE_PS__ETABIN1	0 / 0	1.6e-10 / 1.6e-10	1.83e-08 / 1.83e-08	-4.98e-07 / 5.54e-07	-0.000208 / 0.000208	3.79e-08 / 3.79e-08	-6.79e-09 / -6.79e-09	1.65e-08 / 1.65e-08	-0.000197 / 0.000197	0 / 0
EG_SCALE_PS__ETABIN2	0 / 0	1.6e-10 / 1.6e-10	1.83e-08 / 1.83e-08	-3.04e-08 / -3.04e-08	-0.000196 / 0.000196	3.79e-08 / 3.79e-08

	j-fake γ	$W\gamma\gamma$	$Z\gamma$	$Z\gamma\gamma$	$t\bar{X}\gamma$	$t\bar{t}$	diboson	$W(\tau\nu)\gamma\gamma$	$WH_{\gamma\gamma}$	$WH_{\gamma\gamma}$
j-fake photon SF error	0.23 / -0.23	0 / 0	0 / 0	0 / 0	0 / 0	0 / 0	0 / 0	0 / 0	0 / 0	0 / 0
Luminosity	0 / 0	0.017 / -0.017	0.017 / -0.017	0.017 / -0.017	0.017 / -0.017	0.017 / -0.017	0.017 / -0.017	0.017 / -0.017	0.017 / -0.017	0 / 0
Electron identification eff.	0 / 0	0.00405 / -0.00405	0.0131 / -0.0131	0 / 0	0 / 0	0 / 0	0 / 0	0 / 0	0 / 0	0 / 0
Electron isolation eff.	0 / 0	0.000723 / -0.000723	0.00106 / -0.00106	0 / 0	0 / 0	0 / 0	0 / 0	0 / 0	0 / 0	0 / 0
Electron reconstruction eff.	0 / 0	0.000658 / -0.000658	0.00195 / -0.00195	0 / 0	0 / 0	0 / 0	0 / 0	0 / 0	0 / 0	0 / 0
Electron Trigger eff.	0 / 0	0 / 0	0 / 0	0 / 0	0 / 0	0 / 0	0 / 0	0 / 0	0 / 0	0 / 0
Photon identification eff.	0 / 0	0.0329 / -0.0329	0.0242 / -0.0242	0.0297 / -0.0297	0.0251 / -0.0251	0.0246 / -0.0246	0.0244 / -0.0244	0.0308 / -0.0308	0.0179 / -0.0179	0 / 0
Photon isolation eff.	0 / 0	0.0325 / -0.0325	0.0257 / -0.0257	0.0325 / -0.0325	0.0259 / -0.0259	0.0255 / -0.0255	0.0202 / -0.0202	0.0298 / -0.0298	0.0206 / -0.0206	0 / 0
Photon Trigger eff.	0 / 0	0.00431 / -0.00431	0.000218 / -0.000218	0.00445 / -0.00445	0.00689 / -0.00689	0.0061 / -0.0061	0.00735 / -0.00735	0 / 0	0.00528 / -0.00528	0 / 0
Muon isolation eff. stat	0 / 0	0.000265 / -0.000265	0.000304 / -0.000304	0.000281 / -0.000281	0.00043 / -0.00043	0.000492 / -0.000492	0.000489 / -0.000489	0 / 0	0.000455 / -0.000455	0 / 0
Muon isolation eff. syst.	0 / 0	0.0023 / -0.0023	3.92e-05 / -3.92e-05	0.00438 / -0.00438	0.00418 / -0.00418	0.00496 / -0.00496	0.0011 / -0.0011	0 / 0	0.002 / -0.002	0 / 0
Muon reconstruction eff. stat	0 / 0	0.000241 / -0.000241	1.37e-05 / -1.37e-05	0.000163 / -0.000163	0.000236 / -0.000236	0.00027 / -0.00027	0.000154 / -0.000154	0 / 0	0.000192 / -0.000192	0 / 0
Muon reconstruction eff. low-pT stat.	0 / 0	0 / 0	0 / 0	0 / 0	0 / 0	0 / 0	0 / 0	0 / 0	0 / 0	0 / 0
Muon reconstruction eff. syst.	0 / 0	0.000668 / -0.000668	0.000181 / -0.000181	0.000364 / -0.000364	0.000826 / -0.000826	0.000528 / -0.000528	0.000528 / -0.000528	0 / 0	0.0008 / -0.0008	0 / 0
Muon reconstruction eff. low-pT syst.	0 / 0	0 / 0	0 / 0	0 / 0	0 / 0	0 / 0	0 / 0	0 / 0	0 / 0	0 / 0
Muon TTVA eff. stat	0 / 0	8.86e-05 / -8.86e-05	1.47e-05 / -1.47e-05	7.42e-05 / -7.42e-05	0.000124 / -0.000124	0.000111 / -0.000111	0.00015 / -0.00015	0 / 0	0.000131 / -0.000131	0 / 0
Muon TTVA eff. syst.	0 / 0	0.000111 / -0.000111	6.33e-05 / -6.33e-05	6.31e-05 / -6.31e-05	0.000187 / -0.000187	7.88e-05 / -7.88e-05	0.000556 / -0.000556	0 / 0	0.000181 / -0.000181	0 / 0
Muon trigger eff. stat	0 / 0	0.00135 / -0.00135	5.42e-05 / -5.42e-05	0.0011 / -0.0011	0.00167 / -0.00167	0.00165 / -0.00165	0.00141 / -0.00141	0 / 0	0.00128 / -0.00128	0 / 0
Muon trigger eff. syst.	0 / 0	0.00988 / -0.00988	0.000108 / -0.000108	0.00612 / -0.00612	0.0107 / -0.0107	0.0111 / -0.0111	0.00486 / -0.00486	0 / 0	0.0116 / -0.0116	0 / 0
Jet JVT eff.	0 / 0	0.00354 / -0.00354	0.00379 / -0.00379	0.00373 / -0.00373	0.0037 / -0.0037	0.00613 / -0.00613	0.00693 / -0.00693	0.00367 / -0.00367	0.00221 / -0.00221	0 / 0
Flavour Tagging eff. B0	0 / 0	0 / 0	0 / 0	0 / 0	0 / 0	0 / 0	0 / 0	0 / 0	0 / 0	0 / 0
Flavour Tagging eff. B1	0 / 0	0 / 0	0 / 0	0 / 0	0 / 0	0 / 0	0 / 0	0 / 0	0 / 0	0 / 0
Flavour Tagging eff. B2	0 / 0	0 / 0	0 / 0	0 / 0	0 / 0	0 / 0	0 / 0	0 / 0	0 / 0	0 / 0
Flavour Tagging eff. B3	0 / 0	0 / 0	0 / 0	0 / 0	0 / 0	0 / 0	0 / 0	0 / 0	0 / 0	0 / 0
Flavour Tagging eff. B4	0 / 0	0 / 0	0 / 0	0 / 0	0 / 0	0 / 0	0 / 0	0 / 0	0 / 0	0 / 0
Flavour Tagging eff. B5	0 / 0	0 / 0	0 / 0	0 / 0	0 / 0	0 / 0	0 / 0	0 / 0	0 / 0	0 / 0
Flavour Tagging eff. B6	0 / 0	0 / 0	0 / 0	0 / 0	0 / 0	0 / 0	0 / 0	0 / 0	0 / 0	0 / 0
Flavour Tagging eff. B7	0 / 0	0 / 0	0 / 0	0 / 0	0 / 0	0 / 0	0 / 0	0 / 0	0 / 0	0 / 0
Flavour Tagging eff. B8	0 / 0	0 / 0	0 / 0	0 / 0	0 / 0	0 / 0	0 / 0	0 / 0	0 / 0	0 / 0
Flavour Tagging eff. C0	0 / 0	0 / 0	0 / 0	0 / 0	0 / 0	0 / 0	0 / 0	0 / 0	0 / 0	0 / 0
Flavour Tagging eff. C1	0 / 0	0 / 0	0 / 0	0 / 0	0 / 0	0 / 0	0 / 0	0 / 0	0 / 0	0 / 0
Flavour Tagging eff. C2	0 / 0	0 / 0	0 / 0	0 / 0	0 / 0	0 / 0	0 / 0	0 / 0	0 / 0	0 / 0
Flavour Tagging eff. C3	0 / 0	0 / 0	0 / 0	0 / 0	0 / 0	0 / 0	0 / 0	0 / 0	0 / 0	0 / 0
Flavour Tagging eff. Light0	0 / 0	0 / 0	0 / 0	0 / 0	0 / 0	0 / 0	0 / 0	0 / 0	0 / 0	0 / 0
Flavour Tagging eff. Light1	0 / 0	0 / 0	0 / 0	0 / 0	0 / 0	0 / 0	0 / 0	0 / 0	0 / 0	0 / 0
Flavour Tagging eff. Light2	0 / 0	0 / 0	0 / 0	0 / 0	0 / 0	0 / 0	0 / 0	0 / 0	0 / 0	0 / 0
Flavour Tagging eff. Light3	0 / 0	0 / 0	0 / 0	0 / 0	0 / 0	0 / 0	0 / 0	0 / 0	0 / 0	0 / 0
Flavour Tagging eff. extrapolation	0 / 0	0 / 0	0 / 0	0 / 0	0 / 0	0 / 0	0 / 0	0 / 0	0 / 0	0 / 0
Flavour Tagging eff. extrapolation from charm	0 / 0	0 / 0	0 / 0	0 / 0	0 / 0	0 / 0	0 / 0	0 / 0	0 / 0	0 / 0
EG_RESOLUTION_AF2	0 / 0	0 / 0	0 / 0	0 / 0	0 / 0	0 / 0	0 / 0	0 / 0	0 / 0	0 / 0
EG_RESOLUTION_MATERIALCALO	0 / 0	0 / 0	0 / 0	0 / 0	-0.000968 / 0.000968	0 / 0	0 / 0	0 / 0	-0.00174 / 0.00174	0 / 0
EG_RESOLUTION_MATERIALCRYO	0 / 0	0 / 0	4.47e-06 / -4.47e-06	1.96e-07 / -1.96e-07	-0.00096 / 0.00096	0.000168 / -0.000168	0.0245 / -0.0245	0 / 0	-0.00175 / 0.00175	0 / 0
EG_RESOLUTION_MATERIALGAP	0 / 0	0 / 0	0 / 0	1.96e-07 / -1.96e-07	-0.00299 / 0.00299	0.00012 / -0.00012	0.00125 / -0.00125	0 / 0	-1.54e-05 / 1.54e-05	0 / 0
EG_RESOLUTION_MATERIALIBL	0 / 0	-0.0198 / 0.0198	0 / 0	0.0019 / -0.0019	0.000407 / -0.000407	-0.000673 / 0.000673	0.0245 / -0.0245	0 / 0	-0.0061 / 0.0061	0 / 0
EG_RESOLUTION_MATERIALID	0 / 0	0.0154 / -0.0154	0.00249 / -0.00249	-0.00776 / 0.00776	0.00405 / -0.00405	-0.000505 / 0.000505	0.0958 / -0.0958	0 / 0	-0.0145 / 0.0145	0 / 0
EG_RESOLUTION_MATERIALPP0	0 / 0	0.000246 / -0.000246	0.00246 / -0.00246	1.16e-05 / -1.16e-05	0.00338 / -0.00338	0.0162 / -0.0162	0.00125 / -0.00125	0 / 0	-0.00285 / 0.00285	0 / 0
EG_SCALE_AF2	0 / 0	0 / 0	0 / 0	0 / 0	0 / 0	0 / 0	0 / 0	0 / 0	0 / 0	0 / 0
EG_SCALE_E4SCINTILLATOR_ETABIN0	0 / 0	0 / 0	0 / 0	0 / 0	0 / 0	0 / 0	0 / 0	0 / 0	0 / 0	0 / 0
EG_SCALE_E4SCINTILLATOR_ETABIN1	0 / 0	0 / 0	0 / 0	0 / 0	0 / 0	0 / 0	0 / 0	0 / 0	0 / 0	0 / 0
EG_SCALE_E4SCINTILLATOR_ETABIN2	0 / 0	0 / 0	0 / 0	0 / 0	-2.5e-05 / 2.5e-05	0 / 0	0 / 0	0 / 0	-1.49e-05 / 1.49e-05	0 / 0
EG_SCALE_G4	0 / 0	0 / 0	0 / 0	0 / 0	2.04e-05 / -2.04e-05	0 / 0	0 / 0	0 / 0	1.35e-05 / -1.35e-05	0 / 0
EG_SCALE_L1GAIN	0 / 0	-0.00269 / 0.00269	-4.47e-06 / 4.47e-06	5.6e-06 / -5.6e-06	0.00154 / -0.00154	0 / 0	1.54e-05 / -1.54e-05	0 / 0	0.00218 / -0.00218	0 / 0
EG_SCALE_L2GAIN	0 / 0	0.0461 / -0.0461	-0.0402 / 0.0402	0.000594 / -0.000594	0.00519 / -0.00519	-0.00012 / 0.00012	0.07 / -0.07	0 / 0	-0.00265 / 0.00265	0 / 0
EG_SCALE_LARCALIB_ETABIN0	0 / 0	-0.0311 / 0.0311	-4.47e-06 / 4.47e-06	0 / 0	-0.00105 / 0.00105	0 / 0	-0.07 / 0.07	0 / 0	0.0017 / -0.0017	0 / 0
EG_SCALE_LARCALIB_ETABIN1	0 / 0	0 / 0	4.47e-06 / -4.47e-06	-5.74e-06 / 5.74e-06	0.000235 / -0.000235	0.00012 / -0.00012	0 / 0	0 / 0	-1.22e-05 / 1.22e-05	0 / 0
EG_SCALE_LARELECCALIB	0 / 0	0 / 0	0 / 0	0 / 0	8.67e-06 / -8.67e-06	0 / 0	0 / 0	0 / 0	0 / 0	0 / 0
EG_SCALE_LARELECUNCONV_ETABIN0	0 / 0	0.00392 / -0.00392	-4.47e-06 / 4.47e-06	-3.95e-06 / 3.95e-06	-0.00533 / 0.00533	0 / 0	0 / 0	0 / 0	0.000142 / -0.000142	0 / 0
EG_SCALE_LARELECUNCONV_ETABIN1	0 / 0	0 / 0	4.47e-06 / -4.47e-06	1.96e-07 / -1.96e-07	0.000424 / -0.000424	0.00012 / -0.00012	-0.00125 / 0.00125	0 / 0	-0.00076 / 0.00076	0 / 0
EG_SCALE_LARUNCONVCALIB_ETABIN0	0 / 0	-0.00394 / 0.00394	4.47e-06 / -4.47e-06	0 / 0	2.97e-05 / -2.97e-05	0 / 0	0 / 0	0 / 0	-0.0017 / 0.0017	0 / 0
EG_SCALE_LARUNCONVCALIB_ETABIN1	0 / 0	0 / 0	0 / 0	-1.96e-07 / 1.96e-07	-0.000478 / 0.000478	-0.00012 / 0.00012	0 / 0	0 / 0	9.99e-06 / -9.99e-06	0 / 0
EG_SCALE_MATCALO_ETABIN0	0 / 0	0 / 0	0 / 0	0 / 0	0 / 0	0 / 0	0 / 0	0 / 0	6.65e-06 / -6.65e-06	0 / 0
EG_SCALE_MATCALO_ETABIN1	0 / 0	0 / 0	0 / 0	0 / 0	2.69e-08 / -2.69e-08	0 / 0	0 / 0	0 / 0	-3.66e-05 / 3.66e-05	0 / 0
EG_SCALE_MATCALO_ETABIN10	0 / 0	0 / 0	0 / 0	0 / 0	0 / 0	0 / 0	0 / 0	0 / 0	0 / 0	0 / 0
EG_SCALE_MATCALO_ETABIN11	0 / 0	0 / 0	0 / 0	0 / 0	0 / 0	0 / 0	0 / 0	0 / 0	0 / 0	0 / 0
EG_SCALE_MATCALO_ETABIN2	0 / 0	0 / 0	0 / 0	0 / 0	0.000983 / -0.000983	0 / 0	0 / 0	0 / 0	-4.02e-06 / 4.02e-06	0 / 0
EG_SCALE_MATCALO_ETABIN3	0 / 0	0 / 0	4.47e-06 / -4.47e-06	0 / 0	0 / 0	0 / 0	0 / 0	0 / 0	-1.16e-16 / 1.16e-16	0 / 0
EG_SCALE_MATCALO_ETABIN4	0 / 0	0 / 0	0 / 0	0 / 0	0 / 0	0 / 0	0 / 0	0 / 0	0 / 0	0 / 0
EG_SCALE_MATCALO_ETABIN5	0 / 0	0 / 0	0 / 0	0 / 0	1.16e-05 / -1.16e-05	0 / 0	0 / 0	0 / 0	-0.0017 / 0.0017	0 / 0
EG_SCALE_MATCALO_ETABIN6	0 / 0	-0.00394 / 0.00394	0 / 0	0 / 0	8.76e-06 / -8.76e-06	0 / 0	0 / 0	0 / 0	5.99e-06 / -5.99e-06	0 / 0
EG_SCALE_MATCALO_ETABIN7	0 / 0	0 / 0	0 / 0	0 / 0	6.49e-06 / -6.49e-06	0 / 0	0 / 0	0 / 0	9.99e-06 / -9.99e-06	0 / 0
EG_SCALE_MATCALO_ETABIN8	0 / 0	0 / 0	0 / 0	0 / 0	-0.00167 / 0.00167	-0.00012 / 0.00012	0 / 0	0 / 0	0 / 0	0 / 0
EG_SCALE_MATCALO_ETABIN9	0 / 0	0 / 0	0 / 0	0 / 0	0 / 0	0 / 0	0 / 0	0 / 0	0 / 0	0 / 0
EG_SCALE_MATCRYO_ETABIN0	0 / 0	0 / 0	0 / 0	0 / 0	0 / 0	0 / 0	0 / 0	0 / 0	6.65e-06 / -6.65e-06	0 / 0
EG_SCALE_MATCRYO_ETABIN1	0 / 0	0 / 0	0 / 0	0 / 0	2.69e-08 / -2.69e-08	0 / 0	0 / 0	0 / 0	-3.66e-05 / 3.66e-05	0 / 0
EG_SCALE_MATCRYO_ETABIN10	0 / 0	0 / 0	0 / 0	0 / 0	8.67e-06 / -8.67e-06	0 / 0	0 / 0	0 / 0	0 / 0	0 / 0
EG_SCALE_MATCRYO_ETABIN11	0 / 0	0 / 0	0 / 0	0 / 0	0 / 0	0 / 0	0 / 0	0 / 0	0 / 0	0 / 0
EG_SCALE_MATCRYO_ETABIN2	0 / 0	0 / 0	0 / 0	0 / 0	0.000983 / -0.000983	0 / 0	0 / 0	0 / 0	-4.02e-06 / 4.02e-06	0 / 0
EG_SCALE_MATCRYO_ETABIN3	0 / 0	0 / 0	4.47e-06 / -4.47e-06	0 / 0	0 / 0	0 / 0	0 / 0	0 / 0	-1.16e-16 / 1.16e-16	0 / 0
EG_SCALE_MATCRYO_ETABIN4	0 / 0	0 / 0	0 / 0	0 / 0	0.00144 / -0.00144	0 / 0	0 / 0	0 / 0	-1.07e-05 / 1.07e-05	0 / 0
EG_SCALE_MATCRYO_ETABIN5	0 / 0	0 / 0	0 / 0	0 / 0	1.16e-05 / -1.16e-05	0 / 0	0 / 0	0 / 0	-0.0017 / 0.0017	0 / 0
EG_SCALE_MATCRYO_ETABIN6	0 / 0	-0.00394 / 0.00394	0 / 0	0 / 0	1.03e-05 / -1.03e-05	0 / 0	0 / 0	0 / 0	5.99e-06 / -5.99e-06	0 / 0
EG_SCALE_MATCRYO_ETABIN7	0 / 0	0 / 0	0 / 0	0 / 0	0.00128 / -0.00128	0 / 0	0.00125 / -0.00125	0 / 0	9.99e-06 / -9.99e-06	0 / 0
EG_SCALE_MATCRYO_ETABIN8	0 / 0	0 / 0	0 / 0	0 / 0	-0.00195 / 0.00195	-0.00012 / 0.00012	0 / 0	0 / 0	-0.0021 / 0.0021	0 / 0
EG_SCALE_MATCRYO_ETABIN9	0 / 0	0 / 0	0 / 0	0 / 0	0 / 0	0 / 0	0 / 0	0 / 0	0 / 0	0 / 0
EG_SCALE_MATID_ETABIN0	0 / 0	0 / 0	0 / 0	0 / 0	2.1e-05 / -2.1e-05	0 / 0	0 / 0	0 / 0	-0.00171 / 0.00171	0 / 0
EG_SCALE_MATID_ETABIN1	0 / 0	2.94e-06 / -2.94e-06	0 / 0	0 / 0	-6.53e-07 / 6.53e-07	0 / 0	0 / 0	0 / 0	-2.45e-06 / 2.45e-06	0 / 0
EG_SCALE_MATID_ETABIN2	0 / 0	0 / 0	0 / 0	-1.96e-07 / 1.96e-07	0.00166 / -0.00166	-0.00012 / 0.00012	0 / 0	0 / 0	-0.000627 / 0.000627	0 / 0
EG_SCALE_MATID_ETABIN3	0 / 0	0 / 0	0 / 0	0 / 0	-0.000276 / 0.000276	0 / 0	0 / 0	0 / 0	0 / 0	0 / 0
EG_SCALE_MATPP0_ETABIN0	0 / 0	0 / 0	0 / 0	0 / 0	2.03e-05 / -2.03e-05	0 / 0	0 / 0	0 / 0	3.51e-06 / -3.51e-06	0 / 0
EG_SCALE_MATPP0_ETABIN1	0 / 0	0 / 0	4.47e-06 / 4.47e-06	-1.96e-07 / 1.96e-07	-0.000253 / 0.000253	-0.00012 / 0.00012	0 / 0	0 / 0	-0.00266 / 0.00266	0 / 0
EG_SCALE_PEDESTAL	0 / 0	0 / 0	0 / 0	1.96e-07 / -1.96e-07	0.000247 / -0.000247	0 / 0	0 / 0	0 / 0	-3.51e-06 / 3.51e-06	0 / 0
EG_SCALE_PS_BARREL_B12	0 / 0	0.00394 / -0.00394	4.47e-06 / 4.47e-06	-3.44e-06 / 3.44e-06	-0.001 / 0.001	0 / 0	0 / 0	0 / 0	-0.000587 / 0.000587	0 / 0
EG_SCALE_PS_ETABIN0	0 / 0	0 / 0	0 / 0	0 / 0	-1.6e-06 / 1.6e-06	0 / 0	0 / 0	0 / 0	-2.8e-05 / 2.8e-05	0 / 0
EG_SCALE_PS_ETABIN1	0 / 0	0 / 0	0 / 0	0 / 0	-2.69e-08 / 2.69e-08	0 / 0	0 / 0	0 / 0	3.06e-07 / -3.06e-07	0 / 0
EG_SCALE_PS_ETABIN2	0 / 0	0 / 0	0 / 0	0 / 0	-0.000983 / 0.000983	0 / 0	0 / 0	0 / 0	4.02e-06 / -4.02e-06	0 / 0
EG_SCALE_PS_ETABIN3	0 / 0	0 / 0	4.47e-06 / 4.47e-06	0 / 0	-2.12e-16 / 2.12e-16	0 / 0	0 / 0	0 / 0	0 / 0	0 / 0
EG_SCALE_PS_ETABIN4	0 / 0	0 / 0	0 / 0	0 / 0	0 / 0	0 / 0	0 / 0	0 / 0	0 / 0	0 / 0
EG_SCALE_PS_ETABIN5	0 / 0	0 / 0	0 / 0	0 / 0	-1.16e-05 / 1.16e-05	0 / 0	0 / 0	0 / 0	0.0017 / -0.0017	0 / 0
EG_SCALE_PS_ETABIN6	0 / 0	0.00377 / -0.00377	0 / 0	-1.18e-05 / 1.18e-05	-0.000561 / 0.000561	-5.17e-05 / 5.17e-05	-0.000465 / 0.000465	0 / 0	-0.00353 / 0.00353	0 / 0
EG_SCALE_PS_ETABIN7	0 / 0	0 / 0	0 / 0	0 / 0	0 / 0	0 / 0	0 / 0	0 / 0	0 / 0	0 / 0
EG_SCALE_PS_ETABIN8	0 / 0	0 / 0	0 / 0	1.96e-07 / -1.96e-07	-1.02e-05 / 1.02e-05	0.00012 / -0.00012	0 / 0	0 / 0	-1.49e-05 / 1.49e-05	0 / 0
EG_SCALE_S12_ETABIN0	0 / 0	-0.035 / 0.035	0 / 0	0 / 0	-0.00227 / 0.00227	0 / 0	-0.07 / 0.07	0 / 0	1.26e-05 / -1.26e-05	0 / 0
EG_SCALE_S12_ETABIN1	0 / 0	0.00394 / -0.00394	-4.47e-06 / 4.47e-06	0 / 0	0.00123 / -0.00123	0 / 0	0 / 0	0 / 0	0.0017 / -0.0017	0 / 0
EG_SCALE_S12_ETABIN2	0 / 0	0 / 0	0 / 0	0 / 0	0 / 0	0 / 0	0 / 0	0 / 0	0 / 0	0 / 0
EG_SCALE_S12_ETABIN3	0 / 0	0 / 0	4.47e-06 / -4.47e-06	-5.4e-06 / 5.4e-06	-3.82e-05 / 3.82e-05	0.00012 / -0.00012	0 / 0	0 / 0	-0.00212 / 0.00212	0 / 0
EG_SCALE_S12_ETABIN4	0 / 0	0 / 0	0 / 0	0 / 0	-0.000272 / 0.000272	0 / 0	0 / 0	0 / 0	0 / 0	0 / 0
EG_SCALE_TOPOCLUSTER_THRES	0 / 0	0 / 0	0 / 0	-1.96e-07 / 1.96e-07	8.76e-06 / -8.76e-06	0 / 0	0 / 0	0 / 0	-1.16e-16 / 1.16e-16	0 / 0
EG_SCALE_WTOTS1	0 / 0	0.000981 / -0.000981	0 / 0	3.63e-06 / -3.63e-06	0.00227 / -0.00227	-0.00012 / 0.00012	0.00125 / -0.00125	0 / 0	0.0026 / -0.0026	0 / 0
EG_SCALE_ZEESTAT	0 / 0	0 / 0	0 / 0	0 / 0	0 / 0	0 / 0	0 / 0	0 / 0	0 / 0	0 / 0
EG_SCALE_ZEESYST	0 / 0	-0.00394 / 0.00394	-1.27e-07 / 1.27e-07	-1.96e-07 / 1.96e-07	0.000194 / -0.000194	6.21e-05 / -6.21e-05	0 / 0	0 / 0	-0.00338 / 0.00338	0 / 0
JES GroupedNP - NP 1	0 / 0	0.00811 / -0.00811	0 / 0	0.000254 / -0.000254	6.83e-05 / -6.83e-05	-0.000224 / 0.000224	0.0531 / -0.0531	0 / 0	0.00742 / -0.00742	0 / 0
JES GroupedNP - NP 2	0 / 0	0.00811 / -0.00811	0 / 0	-1.75e-05 / 1.75e-05	0.000108 / -0.000108	-4.42e-05 / 4.42e-05	0.0531 / -0.0531	0 / 0	0.00586 / -0.00586	0 / 0
JES GroupedNP - NP 3	0 / 0	-0.00123 / 0.00123	0 / 0	0 / 0	-3.37e-05 / 3.37e-05	0 / 0	0 / 0	0 / 0	0.00217 / -0.00217	0 / 0
Jet flavour response	0 / 0	-0.00812 / 0.00812	0 / 0	0 / 0	-0.000307 / 0.000307	0.000184 / -0.000184	-0.0201 / 0.0201	0 / 0	-0.00385 / 0.00385	0 / 0
MET soft track ResoPara	0 / 0	0 / 0	-7e-07 / 7e-07	-1.24e-06 / 1.24e-06	-2.39e-07 / 2.39e-07	-9.4e-07 / 9.4e-07	-0.000191 / 0.000191	-6.47e-06 / 6.47e-06	-0.000267 / 0.000267	0 / 0
MET soft track ResoPerp	0 / 0	0 / 0	-7e-07 / 7e-07	-1.24e-06 / 1.24e-06	-2.39e-07 / 2.39e-07	-9.4e-07 / 9.4e-07	-0.000191 / 0.000191	-6.47e-06 / 6.47e-06	-0.000267 / 0.000267	0 / 0
MET soft track scale	0 / 0	0 / 0	0 / 0	0 / 0	0 / 0	0 / 0	0 / 0	0 / 0	0 / 0	0 / 0
Muon ID track	0 / 0	-0.0107 / 0.0107	0 / 0	-0.00227 / 0.00227	0.00316 / -0.00316	0.0177 / -0.0177	0.0245 / -0.0245	0 / 0	0.00375 / -0.00375	0 / 0
Muon MS track	0 / 0	0.00245 / -0.00245	0 / 0	-0.00288 / 0.00288	-0.000976 / 0.000976	0.0179 / -0.0179	0 / 0	0 / 0	0.00311 / -0.00311	0 / 0
Muon Sagitta resolution bias	0 / 0	0 / 0	0 / 0	0 / 0	8.98e-05 / -8.98e-05	0 / 0	0 / 0	0 / 0	-0.0049 / 0.0049	0 / 0
Muon sagitta rho	0 / 0	0 / 0	0 / 0	0 / 0	0 / 0	0 / 0	0 / 0	0 / 0	0 / 0	0 / 0
Muon scale	0 / 0	0 / 0	0 / 0	-0.00033 / 0.00033	0.000438 / -0.000438	-0.0179 / 0.0179	-0.0245 / 0.0245	0 / 0	0.00311 / -0.00311	0 / 0
JET_JER_DataVsMC_MC16	0 / 0	0 / 0	0 / 0	0 / 0	0 / 0	0 / 0	0 / 0	0 / 0	0 / 0	0 / 0
JET_JER_EffectiveNP_1	0 / 0	0 / 0	0 / 0	0 / 0	0 / 0	0 / 0	0 / 0	0 / 0	0 / 0	0 / 0
JET_JER_EffectiveNP_2	0 / 0	0 / 0	0 / 0	0 / 0	0 / 0	0 / 0	0 / 0	0 / 0	0 / 0	0 / 0
JET_JER_EffectiveNP_3	0 / 0	0 / 0	0 / 0	0 / 0	0 / 0	0 / 0	0 / 0	0 / 0	0 / 0	0 / 0
JET_JER_EffectiveNP_4	0 / 0	0 / 0	0 / 0	0 / 0	0 / 0	0 / 0	0 / 0	0 / 0	0 / 0	0 / 0
JET_JER_EffectiveNP_5	0 / 0	0 / 0	0 / 0	0 / 0	0 / 0	0 / 0	0 / 0	0 / 0	0 / 0	0 / 0
JET_JER_EffectiveNP_6	0 / 0	0 / 0	0 / 0	0 / 0	0 / 0	0 / 0	0 / 0	0 / 0	0 / 0	0 / 0
JET_JER_EffectiveNP_7restTerm	0 / 0	0 / 0	0 / 0	0 / 0	0 / 0	0 / 0	0 / 0	0 / 0	0 / 0	0 / 0
Jet eta intercalibration non-closure 2018 data	0 / 0	-0.00123 / 0.00123	0 / 0	0 / 0	-6.49e-06 / 6.49e-06	0 / 0	0 / 0	0 / 0	0.00217 / -0.00217	0 / 0
Jet eta intercalibration non-closure high E	0 / 0	0 / 0	0 / 0	0 / 0	0 / 0	0 / 0	0 / 0	0 / 0	0 / 0	0 / 0
Jet eta intercalibration non-closure eta ¿ 0	0 / 0	0 / 0	0 / 0	0 / 0	-1.11e-05 / 1.11e-05	0 / 0	0 / 0	0 / 0	0 / 0	0 / 0
Jet eta intercalibration non-closure eta ¿0	0 / 0	0 / 0	0 / 0	0 / 0	0 / 0	0 /

	j-fake γ	$W\gamma\gamma$	$Z\gamma$	$Z\gamma\gamma$	$tX\gamma$	$t\bar{t}$	diboson	$W(\tau\nu)\gamma\gamma$	$WH\gamma\gamma$	$WH\gamma\gamma$
j-fake photon SF error	0.216 / -0.218	0 / 0	0 / 0	0 / 0	0 / 0	0 / 0	0 / 0	0 / 0	0 / 0	0 / 0
$\mu_{t\bar{t}W\gamma\gamma}$	0 / 0	0.158 / -0.157	0 / 0	0 / 0	0 / 0	0 / 0	0 / 0	0 / 0	0 / 0	0 / 0
Luminosity	0 / 0	0.0169 / -0.0169	0.0169 / -0.0169	0.0169 / -0.0169	0.0169 / -0.0169	0.0169 / -0.0169	0.0169 / -0.0169	0.0169 / -0.0169	0.0169 / -0.0169	0 / 0
Electron identification eff.	0 / 0	0.00403 / -0.00403	0.013 / -0.013	0 / 0	0 / 0	0 / 0	0 / 0	0 / 0	0 / 0	0 / 0
Electron isolation eff.	0 / 0	0.000719 / -0.000719	0.00105 / -0.00105	0 / 0	0 / 0	0 / 0	0 / 0	0 / 0	0 / 0	0 / 0
Electron reconstruction eff.	0 / 0	0.000654 / -0.000654	0.00194 / -0.00194	0 / 0	0 / 0	0 / 0	0 / 0	0 / 0	0 / 0	0 / 0
Electron Trigger eff.	0 / 0	0 / 0	0 / 0	0 / 0	0 / 0	0 / 0	0 / 0	0 / 0	0 / 0	0 / 0
Photon identification eff.	0 / 0	0.0325 / -0.0325	0.0239 / -0.0239	0.0293 / -0.0293	0.0247 / -0.0247	0.0242 / -0.0242	0.0241 / -0.0241	0.0304 / -0.0304	0.0177 / -0.0177	0 / 0
Photon isolation eff.	0 / 0	0.0321 / -0.0321	0.0254 / -0.0254	0.0321 / -0.0321	0.0256 / -0.0256	0.0252 / -0.0252	0.0199 / -0.0199	0.0294 / -0.0294	0.0204 / -0.0204	0 / 0
Photon Trigger eff.	0 / 0	0.00428 / -0.00428	0.000217 / -0.000217	0.00442 / -0.00442	0.00684 / -0.00684	0.00606 / -0.00606	0.0073 / -0.0073	0 / 0	0.00524 / -0.00524	0 / 0
Muon isolation eff. stat	0 / 0	0.000265 / -0.000265	0.000304 / -0.000304	0.000281 / -0.000281	0.00043 / -0.00043	0.000492 / -0.000492	0.000489 / -0.000489	0 / 0	0.000455 / -0.000455	0 / 0
Muon isolation eff. syst.	0 / 0	0.00229 / -0.00229	3.89e-05 / -3.89e-05	0.00435 / -0.00435	0.00416 / -0.00416	0.00492 / -0.00492	0.00109 / -0.00109	0 / 0	0.00199 / -0.00199	0 / 0
Muon reconstruction eff. stat	0 / 0	0.000241 / -0.000241	1.37e-05 / -1.37e-05	0.000163 / -0.000163	0.000236 / -0.000236	0.00027 / -0.00027	0.000154 / -0.000154	0 / 0	0.000192 / -0.000192	0 / 0
Muon reconstruction eff. low-pT stat.	0 / 0	0 / 0	0 / 0	0 / 0	0 / 0	0 / 0	0 / 0	0 / 0	0 / 0	0 / 0
Muon reconstruction eff. syst.	0 / 0	0.000664 / -0.000664	0.00018 / -0.00018	0.000361 / -0.000361	0.00082 / -0.00082	0.000525 / -0.000525	0.000525 / -0.000525	0 / 0	0.000795 / -0.000795	0 / 0
Muon reconstruction eff. low-pT syst.	0 / 0	0 / 0	0 / 0	0 / 0	0 / 0	0 / 0	0 / 0	0 / 0	0 / 0	0 / 0
Muon TTVA eff. stat	0 / 0	8.86e-05 / -8.86e-05	1.47e-05 / -1.47e-05	7.42e-05 / -7.42e-05	0.000124 / -0.000124	0.000111 / -0.000111	0.00015 / -0.00015	0 / 0	0.000131 / -0.000131	0 / 0
Muon TTVA eff. syst.	0 / 0	0.000111 / -0.000111	6.33e-05 / -6.33e-05	6.31e-05 / -6.31e-05	0.000187 / -0.000187	7.88e-05 / -7.88e-05	0.000556 / -0.000556	0 / 0	0.000181 / -0.000181	0 / 0
Muon trigger eff. stat	0 / 0	0.00134 / -0.00134	5.39e-05 / -5.39e-05	0.0011 / -0.0011	0.00166 / -0.00166	0.00164 / -0.00164	0.0014 / -0.0014	0 / 0	0.00128 / -0.00128	0 / 0
Muon trigger eff. syst.	0 / 0	0.00981 / -0.00981	0.000107 / -0.000107	0.00608 / -0.00608	0.0106 / -0.0106	0.011 / -0.011	0.00483 / -0.00483	0 / 0	0.0116 / -0.0116	0 / 0
Jet JVT eff.	0 / 0	0.00352 / -0.00352	0.00377 / -0.00377	0.00371 / -0.00371	0.00367 / -0.00367	0.00608 / -0.00608	0.00689 / -0.00689	0.00364 / -0.00364	0.0022 / -0.0022	0 / 0
Flavour Tagging eff. B0	0 / 0	0 / 0	0 / 0	0 / 0	0 / 0	0 / 0	0 / 0	0 / 0	0 / 0	0 / 0
Flavour Tagging eff. B1	0 / 0	0 / 0	0 / 0	0 / 0	0 / 0	0 / 0	0 / 0	0 / 0	0 / 0	0 / 0
Flavour Tagging eff. B2	0 / 0	0 / 0	0 / 0	0 / 0	0 / 0	0 / 0	0 / 0	0 / 0	0 / 0	0 / 0
Flavour Tagging eff. B3	0 / 0	0 / 0	0 / 0	0 / 0	0 / 0	0 / 0	0 / 0	0 / 0	0 / 0	0 / 0
Flavour Tagging eff. B4	0 / 0	0 / 0	0 / 0	0 / 0	0 / 0	0 / 0	0 / 0	0 / 0	0 / 0	0 / 0
Flavour Tagging eff. B5	0 / 0	0 / 0	0 / 0	0 / 0	0 / 0	0 / 0	0 / 0	0 / 0	0 / 0	0 / 0
Flavour Tagging eff. B6	0 / 0	0 / 0	0 / 0	0 / 0	0 / 0	0 / 0	0 / 0	0 / 0	0 / 0	0 / 0
Flavour Tagging eff. B7	0 / 0	0 / 0	0 / 0	0 / 0	0 / 0	0 / 0	0 / 0	0 / 0	0 / 0	0 / 0
Flavour Tagging eff. B8	0 / 0	0 / 0	0 / 0	0 / 0	0 / 0	0 / 0	0 / 0	0 / 0	0 / 0	0 / 0
Flavour Tagging eff. C0	0 / 0	0 / 0	0 / 0	0 / 0	0 / 0	0 / 0	0 / 0	0 / 0	0 / 0	0 / 0
Flavour Tagging eff. C1	0 / 0	0 / 0	0 / 0	0 / 0	0 / 0	0 / 0	0 / 0	0 / 0	0 / 0	0 / 0
Flavour Tagging eff. C2	0 / 0	0 / 0	0 / 0	0 / 0	0 / 0	0 / 0	0 / 0	0 / 0	0 / 0	0 / 0
Flavour Tagging eff. C3	0 / 0	0 / 0	0 / 0	0 / 0	0 / 0	0 / 0	0 / 0	0 / 0	0 / 0	0 / 0
Flavour Tagging eff. Light0	0 / 0	0 / 0	0 / 0	0 / 0	0 / 0	0 / 0	0 / 0	0 / 0	0 / 0	0 / 0
Flavour Tagging eff. Light1	0 / 0	0 / 0	0 / 0	0 / 0	0 / 0	0 / 0	0 / 0	0 / 0	0 / 0	0 / 0
Flavour Tagging eff. Light2	0 / 0	0 / 0	0 / 0	0 / 0	0 / 0	0 / 0	0 / 0	0 / 0	0 / 0	0 / 0
Flavour Tagging eff. Light3	0 / 0	0 / 0	0 / 0	0 / 0	0 / 0	0 / 0	0 / 0	0 / 0	0 / 0	0 / 0
Flavour Tagging eff. extrapolation	0 / 0	0 / 0	0 / 0	0 / 0	0 / 0	0 / 0	0 / 0	0 / 0	0 / 0	0 / 0
Flavour Tagging eff. extrapolation from charm	0 / 0	0 / 0	0 / 0	0 / 0	0 / 0	0 / 0	0 / 0	0 / 0	0 / 0	0 / 0
EG_RESOLUTION_AF2	0 / 0	0 / 0	0 / 0	0 / 0	0 / 0	0 / 0	0 / 0	0 / 0	0 / 0	0 / 0
EG_RESOLUTION_MATERIALCALO	0 / 0	0 / 0	0 / 0	0 / 0	-0.000961 / 0.000961	0 / 0	0 / 0	0 / 0	-0.00173 / 0.00173	0 / 0
EG_RESOLUTION_MATERIALCRYO	0 / 0	0 / 0	4.44e-06 / -4.44e-06	1.95e-07 / -1.95e-07	-0.000953 / 0.000953	0.000167 / -0.000167	0.0243 / -0.0243	0 / 0	-0.00174 / 0.00174	0 / 0
EG_RESOLUTION_MATERIALGAP	0 / 0	0 / 0	0 / 0	1.94e-07 / -1.94e-07	-0.00297 / 0.00297	0.000119 / -0.000119	0.00124 / -0.00124	0 / 0	-1.53e-05 / 1.53e-05	0 / 0
EG_RESOLUTION_MATERIALIBL	0 / 0	-0.0197 / 0.0197	0 / 0	0.00188 / -0.00188	0.000404 / -0.000404	-0.000668 / 0.000668	0.0243 / -0.0243	0 / 0	-0.00606 / 0.00606	0 / 0
EG_RESOLUTION_MATERIALID	0 / 0	0.0153 / -0.0153	0.00247 / -0.00247	-0.0077 / 0.0077	0.00401 / -0.00401	-0.000501 / 0.000501	0.0951 / -0.0952	0 / 0	-0.0144 / 0.0144	0 / 0
EG_RESOLUTION_MATERIALPP0	0 / 0	0.000244 / -0.000244	0.00245 / -0.00245	1.15e-05 / -1.15e-05	0.00336 / -0.00336	0.016 / -0.016	0.00124 / -0.00124	0 / 0	-0.00283 / 0.00283	0 / 0
EG_SCALE_AF2	0 / 0	0 / 0	0 / 0	0 / 0	0 / 0	0 / 0	0 / 0	0 / 0	0 / 0	0 / 0
EG_SCALE_E4SCINTILLATOR__ETABIN0	0 / 0	0 / 0	0 / 0	0 / 0	0 / 0	0 / 0	0 / 0	0 / 0	0 / 0	0 / 0
EG_SCALE_E4SCINTILLATOR__ETABIN1	0 / 0	0 / 0	0 / 0	0 / 0	0 / 0	0 / 0	0 / 0	0 / 0	0 / 0	0 / 0
EG_SCALE_E4SCINTILLATOR__ETABIN2	0 / 0	0 / 0	0 / 0	0 / 0	-2.48e-05 / 2.48e-05	0 / 0	0 / 0	0 / 0	-1.48e-05 / 1.48e-05	0 / 0
EG_SCALE_G4	0 / 0	0 / 0	0 / 0	0 / 0	2.02e-05 / -2.02e-05	0 / 0	0 / 0	0 / 0	1.34e-05 / -1.34e-05	0 / 0
EG_SCALE_L1GAIN	0 / 0	-0.00267 / 0.00267	-4.44e-06 / 4.44e-06	5.56e-06 / -5.56e-06	0.00153 / -0.00153	0 / 0	1.53e-05 / -1.53e-05	0 / 0	0.00217 / -0.00217	0 / 0
EG_SCALE_L2GAIN	0 / 0	0.0457 / -0.0457	-0.0399 / 0.0399	0.00059 / -0.00059	0.00515 / -0.00515	-0.000119 / 0.000119	0.0694 / -0.0695	0 / 0	-0.00263 / 0.00263	0 / 0
EG_SCALE_LARCALIB__ETABIN0	0 / 0	-0.0309 / 0.0309	-4.44e-06 / 4.44e-06	0 / 0	-0.00104 / 0.00104	0 / 0	-0.0696 / 0.0695	0 / 0	0.00169 / -0.00169	0 / 0
EG_SCALE_LARCALIB__ETABIN1	0 / 0	0 / 0	4.44e-06 / -4.44e-06	-5.7e-06 / 5.7e-06	0.000234 / -0.000234	0.000119 / -0.000119	0 / 0	0 / 0	-1.21e-05 / 1.21e-05	0 / 0
EG_SCALE_LARELECCALIB	0 / 0	0 / 0	0 / 0	0 / 0	8.61e-06 / -8.61e-06	0 / 0	0 / 0	0 / 0	0 / 0	0 / 0
EG_SCALE_LARELECUNCONV__ETABIN0	0 / 0	0.00389 / -0.00389	-4.44e-06 / 4.44e-06	-3.92e-06 / 3.92e-06	-0.00529 / 0.00529	0 / 0	0 / 0	0 / 0	0.000141 / -0.000141	0 / 0
EG_SCALE_LARELECUNCONV__ETABIN1	0 / 0	0 / 0	4.44e-06 / -4.44e-06	1.94e-07 / -1.94e-07	0.000421 / -0.000421	0.000119 / -0.000119	-0.00124 / 0.00124	0 / 0	-0.000755 / 0.000755	0 / 0
EG_SCALE_LARUNCONVCALIB__ETABIN0	0 / 0	-0.00391 / 0.00391	4.44e-06 / -4.44e-06	0 / 0	2.95e-05 / -2.95e-05	0 / 0	0 / 0	0 / 0	-0.00169 / 0.00169	0 / 0
EG_SCALE_LARUNCONVCALIB__ETABIN1	0 / 0	0 / 0	0 / 0	-1.94e-07 / 1.94e-07	-0.000475 / 0.000475	-0.000119 / 0.000119	0 / 0	0 / 0	9.92e-06 / -9.92e-06	0 / 0
EG_SCALE_MATCALO__ETABIN0	0 / 0	0 / 0	0 / 0	0 / 0	0 / 0	0 / 0	0 / 0	0 / 0	6.65e-06 / -6.65e-06	0 / 0
EG_SCALE_MATCALO__ETABIN1	0 / 0	0 / 0	0 / 0	0 / 0	2.69e-08 / -2.69e-08	0 / 0	0 / 0	0 / 0	-3.66e-05 / 3.66e-05	0 / 0
EG_SCALE_MATCALO__ETABIN10	0 / 0	0 / 0	0 / 0	0 / 0	0 / 0	0 / 0	0 / 0	0 / 0	0 / 0	0 / 0
EG_SCALE_MATCALO__ETABIN11	0 / 0	0 / 0	0 / 0	0 / 0	0 / 0	0 / 0	0 / 0	0 / 0	0 / 0	0 / 0
EG_SCALE_MATCALO__ETABIN2	0 / 0	0 / 0	0 / 0	0 / 0	0.000983 / -0.000983	0 / 0	0 / 0	0 / 0	-4.02e-06 / 4.02e-06	0 / 0
EG_SCALE_MATCALO__ETABIN3	0 / 0	0 / 0	4.47e-06 / -4.47e-06	0 / 0	0 / 0	0 / 0	0 / 0	0 / 0	0 / 2.32e-16	0 / 0
EG_SCALE_MATCALO__ETABIN4	0 / 0	0 / 0	0 / 0	0 / 0	0 / 0	0 / 0	0 / 0	0 / 0	0 / 0	0 / 0
EG_SCALE_MATCALO__ETABIN5	0 / 0	0 / 0	0 / 0	0 / 0	1.15e-05 / -1.15e-05	0 / 0	0 / 0	0 / 0	-0.00169 / 0.00169	0 / 0
EG_SCALE_MATCALO__ETABIN6	0 / 0	-0.00391 / 0.00391	0 / 0	0 / 0	8.7e-06 / -8.7e-06	0 / 0	0 / 0	0 / 0	5.95e-06 / -5.95e-06	0 / 0
EG_SCALE_MATCALO__ETABIN7	0 / 0	0 / 0	0 / 0	0 / 0	6.49e-06 / -6.49e-06	0 / 0	0 / 0	0 / 0	9.99e-06 / -9.99e-06	0 / 0
EG_SCALE_MATCALO__ETABIN8	0 / 0	0 / 0	0 / 0	-1.95e-07 / 1.95e-07	-0.00166 / 0.00166	-0.000119 / 0.000119	0 / 0	0 / 0	0 / 0	0 / 0
EG_SCALE_MATCALO__ETABIN9	0 / 0	0 / 0	0 / 0	0 / 0	0 / 0	0 / 0	0 / 0	0 / 0	0 / 0	0 / 0
EG_SCALE_MATCRYO__ETABIN0	0 / 0	0 / 0	0 / 0	0 / 0	0 / 0	0 / 0	0 / 0	0 / 0	6.65e-06 / -6.65e-06	0 / 0
EG_SCALE_MATCRYO__ETABIN1	0 / 0	0 / 0	0 / 0	0 / 0	2.67e-08 / -2.67e-08	0 / 0	0 / 0	0 / 0	-3.63e-05 / 3.63e-05	0 / 0
EG_SCALE_MATCRYO__ETABIN10	0 / 0	0 / 0	0 / 0	0 / 0	8.61e-06 / -8.61e-06	0 / 0	0 / 0	0 / 0	0 / 0	0 / 0
EG_SCALE_MATCRYO__ETABIN11	0 / 0	0 / 0	0 / 0	0 / 0	0 / 0	0 / 0	0 / 0	0 / 0	0 / 0	0 / 0
EG_SCALE_MATCRYO__ETABIN2	0 / 0	0 / 0	0 / 0	0 / 0	0.000983 / -0.000983	0 / 0	0 / 0	0 / 0	-4.02e-06 / 4.02e-06	0 / 0
EG_SCALE_MATCRYO__ETABIN3	0 / 0	0 / 0	4.44e-06 / -4.44e-06	0 / 0	0 / 0	0 / 0	0 / 0	0 / 0	0 / 2.32e-16	0 / 0
EG_SCALE_MATCRYO__ETABIN4	0 / 0	0 / 0	0 / 0	0 / 0	0.00144 / -0.00144	0 / 0	0 / 0	0 / 0	-1.07e-05 / 1.07e-05	0 / 0
EG_SCALE_MATCRYO__ETABIN5	0 / 0	0 / 0	0 / 0	0 / 0	1.15e-05 / -1.15e-05	0 / 0	0 / 0	0 / 0	-0.00169 / 0.00169	0 / 0
EG_SCALE_MATCRYO__ETABIN6	0 / 0	-0.00391 / 0.00391	0 / 0	0 / 0	1.02e-05 / -1.02e-05	0 / 0	0 / 0	0 / 0	5.95e-06 / -5.95e-06	0 / 0
EG_SCALE_MATCRYO__ETABIN7	0 / 0	0 / 0	0 / 0	0 / 0	0.00127 / -0.00127	0 / 0	0.00124 / -0.00124	0 / 0	9.92e-06 / -9.92e-06	0 / 0
EG_SCALE_MATCRYO__ETABIN8	0 / 0	0 / 0	0 / 0	0 / 0	-0.00194 / 0.00194	-0.000119 / 0.000119	0 / 0	0 / 0	-0.00208 / 0.00208	0 / 0
EG_SCALE_MATCRYO__ETABIN9	0 / 0	0 / 0	0 / 0	0 / 0	0 / 0	0 / 0	0 / 0	0 / 0	0 / 0	0 / 0
EG_SCALE_MATID__ETABIN0	0 / 0	0 / 0	0 / 0	0 / 0	2.08e-05 / -2.08e-05	0 / 0	0 / 0	0 / 0	-0.0017 / 0.0017	0 / 0
EG_SCALE_MATID__ETABIN1	0 / 0	2.92e-06 / -2.92e-06	0 / 0	0 / 0	-6.49e-07 / 6.49e-07	0 / 0	0 / 0	0 / 0	-2.43e-06 / 2.43e-06	0 / 0
EG_SCALE_MATID__ETABIN2	0 / 0	0 / 0	0 / 0	-1.95e-07 / 1.95e-07	0.00165 / -0.00165	-0.000119 / 0.000119	0 / 0	0 / 0	-0.000623 / 0.000623	0 / 0
EG_SCALE_MATID__ETABIN3	0 / 0	0 / 0	0 / 0	0 / 0	-0.000274 / 0.000274	0 / 0	0 / 0	0 / 0	0 / 0	0 / 0
EG_SCALE_MATPP0__ETABIN0	0 / 0	0 / 0	0 / 0	0 / 0	2.02e-05 / -2.02e-05	0 / 0	0 / 0	0 / 0	3.48e-06 / -3.48e-06	0 / 0
EG_SCALE_MATPP0__ETABIN1	0 / 0	0 / 0	4.44e-06 / 4.44e-06	-1.95e-07 / 1.95e-07	-0.000251 / 0.000251	-0.000119 / 0.000119	0 / 0	0 / 0	-0.00264 / 0.00264	0 / 0
EG_SCALE_PEDESTAL	0 / 0	0 / 0	0 / 0	1.95e-07 / -1.95e-07	0.000245 / -0.000245	0 / 0	0 / 0	0 / 0	-3.48e-06 / 3.48e-06	0 / 0
EG_SCALE_PS_BARREL_B12	0 / 0	0.00391 / -0.00391	-4.44e-06 / 4.44e-06	-3.41e-06 / 3.41e-06	-0.000998 / 0.000998	0 / 0	0 / 0	0 / 0	-0.000584 / 0.000584	0 / 0
EG_SCALE_PS_ETABIN0	0 / 0	0 / 0	0 / 0	0 / 0	-1.6e-06 / 1.6e-06	0 / 0	0 / 0	0 / 0	-2.8e-05 / 2.8e-05	0 / 0
EG_SCALE_PS_ETABIN1	0 / 0	0 / 0	0 / 0	0 / 0	-2.69e-08 / 2.69e-08	0 / 0	0 / 0	0 / 0	3.06e-07 / -3.06e-07	0 / 0
EG_SCALE_PS_ETABIN2	0 / 0	0 / 0	0 / 0	0 / 0	-0.000983 / 0.000983	0 / 0	0 / 0	0 / 0	4.02e-06 / -4.02e-06	0 / 0
EG_SCALE_PS_ETABIN3	0 / 0	0 / 0	-4.44e-06 / 4.44e-06	0 / 0	-1.63e-16 / 1.63e-16	0 / 0	0 / 0	0 / 0	0 / 0	0 / 0
EG_SCALE_PS_ETABIN4	0 / 0	0 / 0	0 / 0	0 / 0	0 / 0	0 / 0	0 / 0	0 / 0	0 / 0	0 / 0
EG_SCALE_PS_ETABIN5	0 / 0	0 / 0	0 / 0	0 / 0	-1.15e-05 / 1.15e-05	0 / 0	0 / 0	0 / 0	0.00169 / -0.00169	0 / 0
EG_SCALE_PS_ETABIN6	0 / 0	0.00374 / -0.00374	0 / 0	-1.17e-05 / 1.17e-05	-0.000557 / 0.000557	-5.14e-05 / 5.14e-05	-0.000461 / 0.000461	0 / 0	-0.00351 / 0.00351	0 / 0
EG_SCALE_PS_ETABIN7	0 / 0	0 / 0	0 / 0	0 / 0	0 / 0	0 / 0	0 / 0	0 / 0	0 / 0	0 / 0
EG_SCALE_PS_ETABIN8	0 / 0	0 / 0	0 / 0	1.95e-07 / -1.95e-07	-1.02e-05 / 1.02e-05	0.000119 / -0.000119	0 / 0	0 / 0	-1.48e-05 / 1.48e-05	0 / 0
EG_SCALE_S12__ETABIN0	0 / 0	-0.0348 / 0.0348	0 / 0	0 / 0	-0.00225 / 0.00225	0 / 0	-0.0696 / 0.0696	0 / 0	1.25e-05 / -1.25e-05	0 / 0
EG_SCALE_S12__ETABIN1	0 / 0	0.00391 / -0.00391	-4.44e-06 / 4.44e-06	0 / 0	0.00122 / -0.00122	0 / 0	0 / 0	0 / 0	0.00169 / -0.00169	0 / 0
EG_SCALE_S12__ETABIN2	0 / 0	0 / 0	0 / 0	0 / 0	0 / 0	0 / 0	0 / 0	0 / 0	0 / 0	0 / 0
EG_SCALE_S12__ETABIN3	0 / 0	0 / 0	4.44e-06 / -4.44e-06	-5.37e-06 / 5.37e-06	-3.8e-05 / 3.8e-05	0.000119 / -0.000119	0 / 0	0 / 0	-0.00211 / 0.00211	0 / 0
EG_SCALE_S12__ETABIN4	0 / 0	0 / 0	0 / 0	0 / 0	-0.00027 / 0.00027	0 / 0	0 / 0	0 / 0	0 / 0	0 / 0
EG_SCALE_TOPOCLUSTER_THRES	0 / 0	0 / 0	0 / 0	-1.95e-07 / 1.95e-07	8.7e-06 / -8.7e-06	0 / 0	0 / 0	0 / 0	0 / 2.32e-16	0 / 0
EG_SCALE_WTOTS1	0 / 0	0.000974 / -0.000974	0 / 0	3.61e-06 / -3.61e-06	0.00226 / -0.00226	-0.000119 / 0.000119	0.00124 / -0.00124	0 / 0	0.00258 / -0.00258	0 / 0
EG_SCALE_ZEESTAT	0 / 0	0 / 0	0 / 0	0 / 0	0 / 0	0 / 0	0 / 0	0 / 0	0 / 0	0 / 0
EG_SCALE_ZEESYST	0 / 0	-0.00391 / 0.00391	-1.26e-07 / 1.26e-07	-1.94e-07 / 1.94e-07	0.000193 / -0.000193	6.17e-05 / -6.17e-05	0 / 0	0 / 0	-0.00336 / 0.00336	0 / 0
JES GroupedNP - NP 1	0 / 0	0.00805 / -0.00805	0 / 0	0.000252 / -0.000252	6.79e-05 / -6.79e-05	-0.000222 / 0.000222	0.0527 / -0.0528	0 / 0	0.00737 / -0.00737	0 / 0
JES GroupedNP - NP 2	0 / 0	0.00805 / -0.00805	0 / 0	1.74e-05 / 1.74e-05	0.000107 / -0.000107	-4.39e-05 / 4.39e-05	0.0527 / -0.0528	0 / 0	0.00582 / -0.00582	0 / 0
JES GroupedNP - NP 3	0 / 0	-0.00122 / 0.00122	0 / 0	0 / 0	-3.35e-05 / 3.35e-05	0 / 0	0 / 0	0 / 0	0.00216 / -0.00216	0 / 0
Jet flavour response	0 / 0	-0.00807 / 0.00807	0 / 0	0 / 0	-0.000305 / 0.000305	0.000183 / -0.000183	-0.02 / 0.02	0 / 0	-0.00383 / 0.00383	0 / 0
MET soft track ResoPara	0 / 0	0 / 0	-7e-07 / 7e-07	-1.24e-06 / 1.24e-06	-2.39e-07 / 2.39e-07	-9.4e-07 / 9.4e-07	-0.000191 / 0.000191	-6.47e-06 / 6.47e-06	-0.000267 / 0.000267	0 / 0
MET soft track ResoPerp	0 / 0	0 / 0	-7e-07 / 7e-07	-1.24e-06 / 1.24e-06	-2.39e-07 / 2.39e-07	-9.4e-07 / 9.4e-07	-0.000191 / 0.000191	-6.47e-06 / 6.47e-06	-0.000267 / 0.000267	0 / 0
MET soft track scale	0 / 0	0 / 0	0 / 0	0 / 0	0 / 0	0 / 0	0 / 0	0 / 0	0 / 0	0 / 0
Muon ID track	0 / 0	-0.0106 / 0.0106	0 / 0	-0.00226 / 0.00226	0.00314 / -0.00314	0.0175 / -0.0175	0.0244 / -0.0244	0 / 0	0.00372 / -0.00372	0 / 0
Muon MS track	0 / 0	0.00243 / -0.00243	0 / 0	-0.00287 / 0.00287	-0.000969 / 0.000969	0.0178 / -0.0178	0 / 0	0 / 0	0.00309 / -0.00309	0 / 0
Muon Sagitta resolution bias	0 / 0	0 / 0	0 / 0	0 / 0	8.98e-05 / -8.98e-05	0 / 0	0 / 0	0 / 0	-0.0049 / 0.0049	0 / 0
Muon sagitta rho	0 / 0	0 / 0	0 / 0	0 / 0	0 / 0	0 / 0	0 / 0	0 / 0	0 / 0	0 / 0
Muon scale	0 / 0	0 / 0	0 / 0	-0.000328 / 0.000328	0.000435 / -0.000435	-0.0178 / 0.0178	-0.0244 / 0.0244	0 / 0	0.00309 / -0.00309	0 / 0
JET_JER_DataVsMC_MC16	0 / 0	0 / 0	0 / 0	0 / 0	0 / 0	0 / 0	0 / 0	0 / 0	0 / 0	0 / 0
JET_JER_EffectiveNP_1	0 / 0	0 / 0	0 / 0	0 / 0	0 / 0	0 / 0	0 / 0	0 / 0	0 / 0	0 / 0
JET_JER_EffectiveNP_2	0 / 0	0 / 0	0 / 0	0 / 0	0 / 0	0 / 0	0 / 0	0 / 0	0 / 0	0 / 0
JET_JER_EffectiveNP_3	0 / 0	0 / 0	0 / 0	0 / 0	0 / 0	0 / 0	0 / 0	0 / 0	0 / 0	0 / 0
JET_JER_EffectiveNP_4	0 / 0	0 / 0	0 / 0	0 / 0	0 / 0	0 / 0	0 / 0	0 / 0	0 / 0	0 / 0
JET_JER_EffectiveNP_5	0 / 0	0 / 0	0 / 0	0 / 0	0 / 0	0 / 0	0 / 0	0 / 0	0 / 0	0 / 0
JET_JER_EffectiveNP_6	0 / 0	0 / 0	0 / 0	0 / 0	0 / 0	0 / 0	0 / 0	0 / 0	0 / 0	0 / 0
JET_JER_EffectiveNP_7restTerm	0 / 0	0 / 0	0 / 0	0 / 0	0 / 0	0 / 0	0 / 0	0 / 0	0 / 0	0 / 0
Jet eta intercalibration non-closure 2018 data	0 / 0	-0.00123 / 0.00123	0 / 0	0 / 0	-6.49e-06 / 6.49e-06	0 / 0	0 / 0	0 / 0	0.00217 / -0.00217	0 / 0
Jet eta intercalibration non-closure high E	0 / 0	0 / 0	0 / 0	0 / 0	0 / 0	0 / 0	0 / 0	0 / 0	0 / 0	0 / 0
Jet eta intercalibration non-closure eta _j 0	0 / 0	0 / 0	0 / 0	0 / 0	-1.11e-05 / 1.11

E.1 Propagating theory uncertainties in 2D template

The 2D template method used to estimate the fake photons from jets uses both data and MC simulations. The simulated samples are used to remove backgrounds other than fake photons from the control regions used both to compute the templates and to compute the final fit. Uncertainties on the MC modelling could therefore affect the 2D template results. This effect was measured and judged negligible.

A variation of $\pm 30\%$ was imposed on the background subtraction. It corresponds to the maximum theory uncertainty measured for the simulated samples. The variation in the 2D template results is of less than 1% for the signal and jj background estimation and of 2% for the γj and jγ backgrounds. The full propagation of the theoretical uncertainties was therefore judged unnecessary.

	MC -30%	Nominal	MC+ 30%
$\gamma\gamma$	0.70 ± 0.04	0.70 ± 0.12	0.70 ± 0.08
γj	0.13 ± 0.01	0.12 ± 0.06	0.11 ± 0.05
jγ	0.14 ± 0.02	0.15 ± 0.06	0.16 ± 0.05
jj	0.025 ± 0.001	0.027 ± 0.002	0.030 ± 0.002

Table E.1: Effect of simulated background subtraction variation on the 2D template results.

E.2 Comparison between MadGraph and SHERPA

The nominal SHERPA signal Monte Carlo was compared to the MadGraph generated $W\gamma\gamma$ sample. Both generator show good agreement in terms of distribution shapes in all variables of interest. Comparisons are shown for the signal region (Figure E.8) and for baseline events (Figure E.8). A slight normalisation difference was observed. The difference between the two samples was added as a signal modelling uncertainty (see Section 7.3).

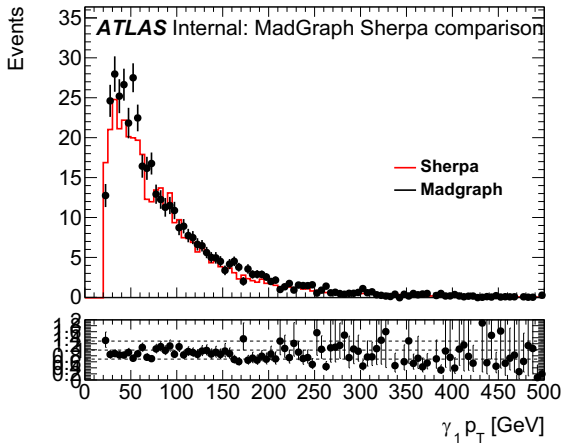

(a) Leading photon p_{T}

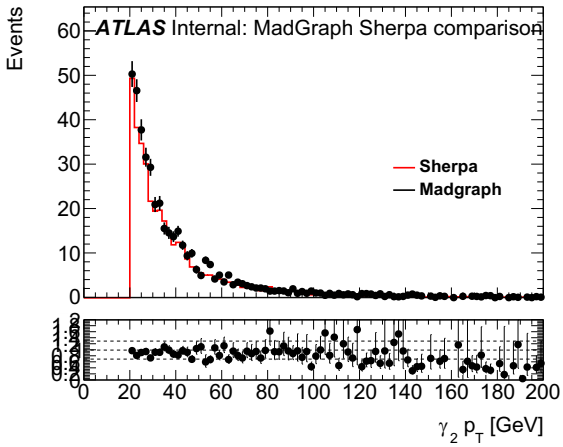

(b) Subleading photon p_{T}

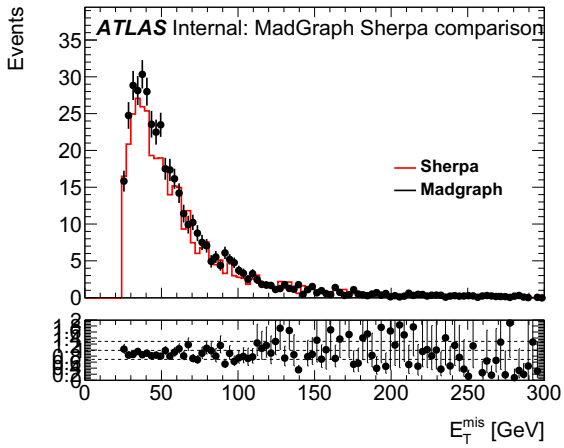

(c) Missing transverse energy

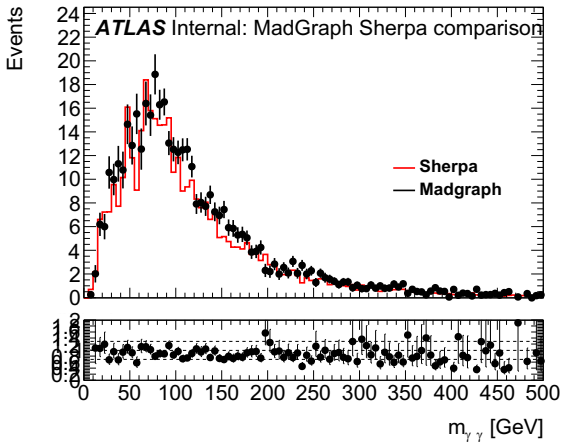

(d) Diphoton invariant mass

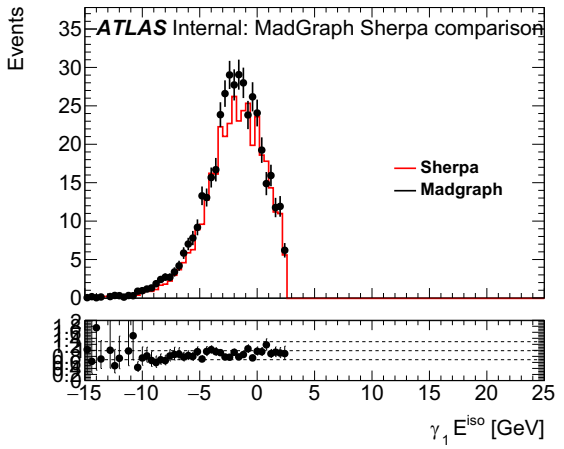

(e) Leading photon isolation energy

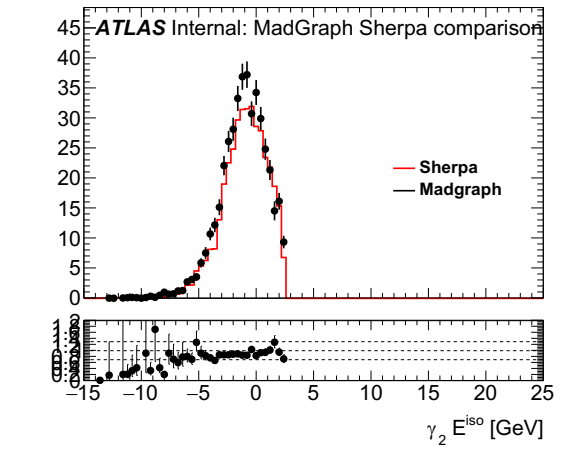

(f) Subleading photon isolation energy

Figure E.8: comparison between MadGraph SHERPA in the Signal Region. The theoretically calculated cross-sections are $\sigma_{\mathrm{SHERPA}} = 388$ fb and $\sigma_{\mathrm{MadGraph}} = 433$ fb.

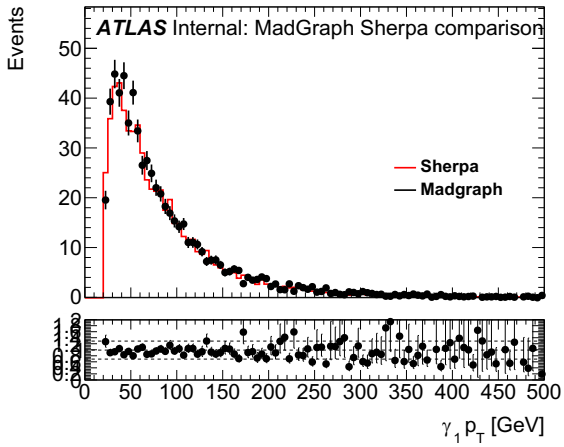

(a) Leading photon p_{T}

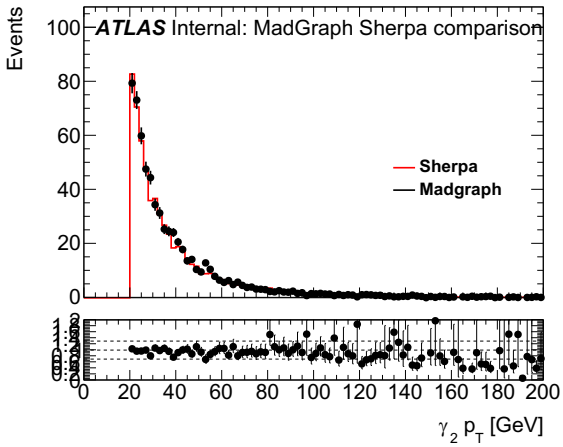

(b) Subleading photon p_{T}

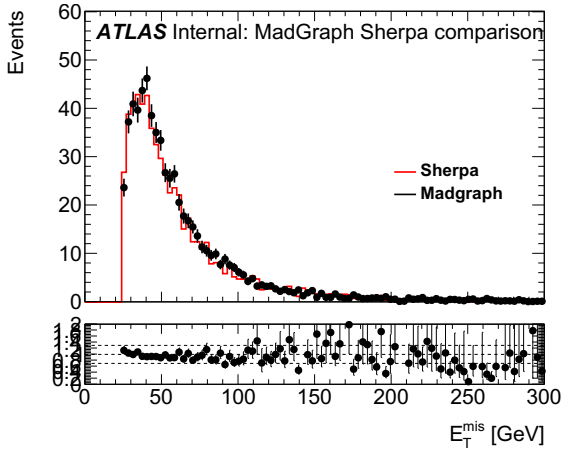

(c) Missing transverse energy

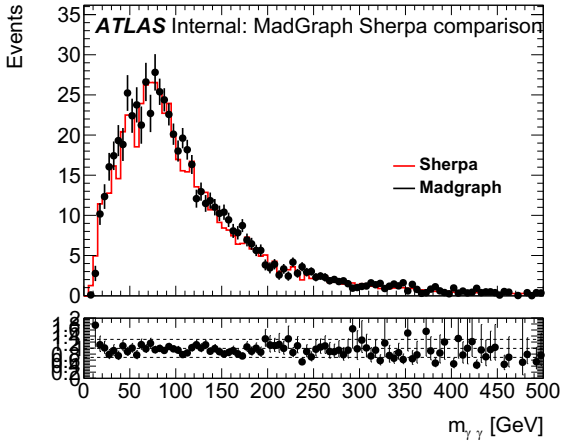

(d) Diphoton invariant mass

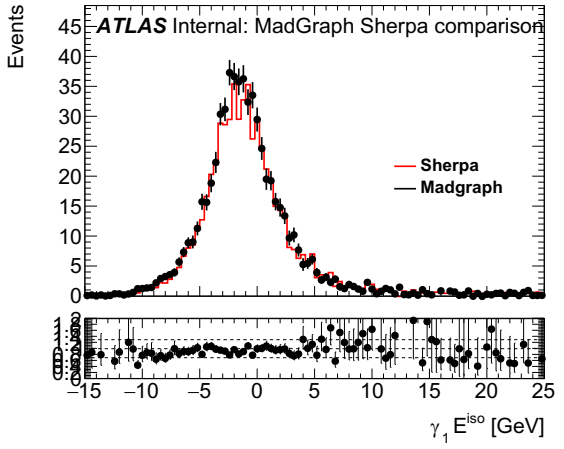

(e) Leading photon isolation energy

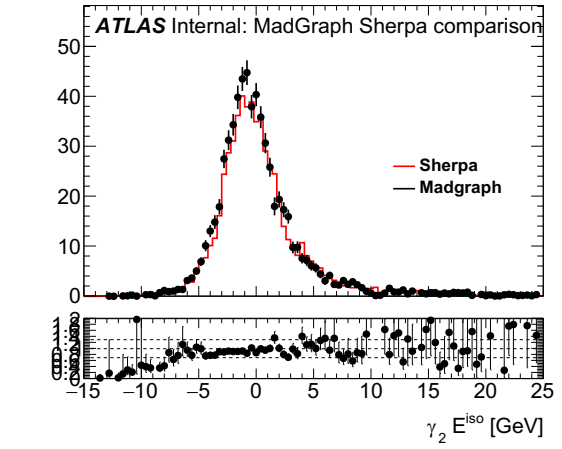

(f) Subleading photon isolation energy

Figure E.9: comparison between MadGraph Sherpa for baseline events. The theoretically calculated cross-sections are $\sigma_{\mathrm{SHERPA}} = 2360$ fb and $\sigma_{\mathrm{MadGraph}} = 2404$ fb